Entropic Forces on Bio-Molecules

Von der Fakultät für Mathematik und Physik der Universität Stuttgart zur Erlangung der Würde eines Doktors der Naturwissenschaften (Dr. rer. nat.) genehmigte Abhandlung

Vorgelegt von

Hendrik Hansen-Goos

aus Gifhorn

Hauptberichter:	Prof. Dr. S. Dietrich
Mitberichter:	Prof. Dr. U. Seifert

Tag der Einreichung:	9. Mai 2008
Tag der mündlichen Prüfung:	2. Juli 2008

Institut für Theoretische und Angewandte Physik
Universität Stuttgart

Max-Planck-Institut für Metallforschung
Stuttgart

2008

Contents

Chapter 1

Introduction

Proteins are the workhorses of the cell. The wealth of functions exerted by proteins includes the catalysis of biochemical reactions and the binding of molecules either as a switch which induces a specific biochemical response or as a means for transporting the ligand to other locations in the body. On the macroscopic scale, the action of proteins gets visible when motor proteins, which are capable of generating mechanical forces, cause muscles to contract. Structural proteins fulfill functions which are critical to maintaining the shape of the body such as actin and tubulin forming the cytoskeleton which stabilizes the shape and the size of the cell while hard structures as hair and nails are built of keratin. In view of the enormous diversity of protein function, this list could be widely extended.

Historically, structural proteins are of some importance as the two principal secondary motifs of proteins derive their names from an early experiment which was performed with keratin by Astbury [1] who had his results published in 1931. X-ray photographs of bundles of hair revealed two markedly different interference figures depending on whether the hair was extended or not. Astbury termed the figures belonging to the unextended hair as α-form which was gradually replaced upon extention by what he called the β-form. It was, however, not until 1951 that thanks to the work of Pauling [2,3] the observed keratin forms were related to the correct structure in an atomic model. Pauling showed that the α-form corresponds to a helical conformation of the protein polypeptide chain while the β-form could be identified to have the structure of a pleated sheet. With Pauling's seminal work, the principal secondary motifs of proteins had been discovered: α-helices and β-sheets (see Fig. 1.1).

Under physiological conditions, a protein adopts a well-defined compact native state, the so-called tertiary structure or fold, where different parts of the polypeptide chain arrange according to different secondary motifs and the latter are situated at

Figure 1.1: Ribbon representation of the H119A variant of the protein Ribonuclease A. The protein backbone forms three α-helices (shown in red) and several β-sheets (shown in yellow), which are two principal secondary motifs of protein folding. The picture was generated from data obtained via x-ray diffraction by Park *et al.* [4] using the visualization program Rasmol [5].

fixed positions in space relative to one another. The phenomenon of protein folding gains its interest from the intimate link which exists between protein fold and protein function [6] as well as from the observation that, once in the native state, the protein, except for minor conformational changes due to its functioning, is in general rather stable and difficult to unfold. Moreover, during the last years, researchers have been challenged by the fact that although the chemical structure of a given protein can be expressed as a sequence of the 20 amino acids (the protein primary structure), and hence the input for algorithms that predict protein structures is a simple list, the task of assigning the correct secondary (and tertiary) structure to an amino acid sequence has still not been resolved satisfactorily [7]. Today, there exists a large testing ground for structure predictions thanks to protein tertiary structures obtained by x-ray crystallography and NMR spectroscopy. In 2006, the Protein Data Bank (www.rcsb.org) contained about 35,000 protein structures [8]. Interestingly, the large number of proteins can be grouped together in families which share the

same fold and have moreover sequence and functional similarities suggesting that proteins of one family are descended from a common ancestor [9]. With an estimated one thousand, the number of these families is relatively small compared to the total number of different proteins. Taking further into account that these basic folds are obtained from the various secondary motifs according to a set of "constructional rules" and that they are robust against short-term deformations due to molecular turbulence of the cell as well as against long-term evolutionary changes in the amino acid sequences, has lead researchers to consider them as primary natural forms which are governed by generative physical laws [10]. Based thereon, it has been argued that, despite of Darwin's evolution theory, certain traits of nature might be described with a Platonian model which assumes a finite set of immutable natural forms supplemented by certain "laws of form" reigning their assembly [10].

Guided by the idea of robust "Platonian" folds which are to some extent stable against changes in the amino acid sequence, Banvar and Maritan have set up a simplified model for protein folding [11, 12]. They model the protein backbone as a flexible, impenetrable tube with finite radius which can be pictured as a garden hose. The features implied in the tube representation are, on the one hand, that it supplies space which is required by the side chains of the amino acids which protrude from the protein backbone and, on the other hand, that the local direction of the backbone is encoded in the local tube axis which has to be contrasted with other simplified models representing the backbone as a chain of tethered spheres. The tendency of a protein to assume a compact native state, which allows for burying hydrophobic side chains inside the folded protein [13], is modeled by Banavar and Maritan via the introduction of an effective attractive potential acting between different segments of the tube. By tuning the tube thickness and the range of the attractive potential to a critical ratio, the model protein can be driven to its so-called marginally compact phase where it assumes secondary structural motifs such as helices, hairpins, and sheetlike structures [11, 12]. The fact that the Banavar-Maritan model does not include the chemical details of specific proteins makes them universal in the sense that they may be considered as primary, immutable forms which serve as the building blocks for protein folds.

A shortcome of the approach by Banavar and Maritan is that the presence of the solvent, which in the cell is to a first approximation water, and which via the hydrophobic effect supports proteins to adopt a compact state, enters into the model only *indirectly* through the effective attractive interaction between different parts of the tube. The purpose of the present work is to examine the tube model for proteins *directly* under the influence of a solvent liquid and to describe to which extent differ-

ent solvent configurations can lead to a favoring or not of certain secondary motifs. When the present investigation was started a first step in this direction had just been undertaken by Snir and Kamien [14, 15]. They concentrated on entropic effects of the solvent on chain-like molecules represented in the tube model by considering a simple hard-sphere solvent in the dilute limit. In this limit it becomes possible to obtain the solvent entropy (which is the only relevant free energetic contribution for hard spheres) within the Asakura-Oosawa model [16] which was designed originally in order to yield depletion forces between two parallel plates mediated, e.g., by a polymer solution. Snir and Kamien found that increasing the size of the solvent particles would cause a helically bent tube to unwind with the consequence that sheetlike conformations would be energetically favored in the presence of large solvent particles. However, their results are strictly valid only in the limit of infinite dilution so that it seemed worthwhile to extend these investigations into the range of more realistic solvent densities.

In the present work we[1] do so by using the methods of density functional theory (DFT) of classical fluids [17–19] which we embed into the context of the so-called morphological thermodynamics which is a concept based on integral geometry and dating from the 1990's [20]. DFT has proved to be an excellent tool for the investigation of spatially inhomogeneous classical fluids since the 1970's and it has served, just to mention a few examples, for the description of crystals, fluids in confined geometries, liquid-vapor interfaces, and wetting and drying of different substrates (see Ref. [21] for a recent review). In principle, DFT provides an exact method. However, for almost all fluids of practical interest only approximations for the corresponding density functional are known. Fortunately, for the hard-sphere fluid these approximations are particularly reliable and can be derived beautifully as a merit of Rosenfeld who introduced his fundamental measure theory (FMT) for the hard-sphere fluid in 1989 [22]. More complex interactions, such as an attraction between the fluid particles which comes on top of a hard-core repulsion, can be included into a DFT description by using perturbation theory. Performing full three-dimensional DFT calculations for a non-trivial solvent which contains the protein (represented within the tube model) and scanning a variety of protein conformations is, however, computationally extremely costly and can hardly be performed with the necessary accuracy. These problems can be overcome by applying the concept of morphological thermodynamics to the solvation free energy F_{sol} of proteins. The morphometric approach to F_{sol}, which has, for very large solutes, the property of being extensive,

[1] Throughout this work I employ *pluralis modestiae* instead of the first person singular. This facilitates the use of the active voice while avoiding the "I" and "my" which are rather unusual in scientific texts as they are often associated with the expression of subjective, personal views.

is based on a suitable generalization of extensivity to finite-sized solutes. Exploiting the analogy with Hadwiger's theorem [23] from integral geometry yields an *approximate* morphological form of F_{sol} which allows for obtaining F_{sol} by computing solvent properties in a simple test geometry and, *separately*, a set of four geometric measures depending on the given protein conformation. As a result, we are able to calculate the free energetically favorable secondary motifs for a wide configuration range of the hard-sphere solvent, including the high density regime. Moreover, results for a solvent with a simple intermolecular attractive potential, which allows for a study of the hydrophobic effect, are readily derived with our method. It should be mentioned that, while hydrophobicity of certain amino acids as a driving force for protein folding has already been discussed for a long time [13], the gain in solvent entropy upon folding has been emphasized more recently [24]. The methodology, which we employ in the present work, covers these two aspects.

In order to orient the reader, we mention that our results concerning the biologically motivated treatment of solvation effects of proteins as represented within the tube model are contained in Chapter 5, which is the chapter preceding the summary and outlook. Chapters 2 to 4 deal with work which can be viewed as preparatory to the study of protein solvation although their content, which is related to more fundamental aspects touching upon the construction of density functionals, stands independently of the biological application. We start this work in Chapter 2 with a calculation of the statistical mechanics of a classical system of particles which are confined to one spatial dimension (1D). The 1D systems are particularly appealing as they allow for exact results even for particles with non-trivial interactions. This predestinates the analytical results to be compared with experimental data of colloidal particles. In the laboratory of Prof. Bechinger in Stuttgart experiments have been performed in which the confinement of micron-sized colloidal particles to 1D was accomplished with the help of an optical tweezer. Obviously, the size of the colloidal particles defines a characteristic lengthscale which is by several orders of magnitude larger than in the case of protein solvation. Nevertheless, DFT is also perfectly suited for treating colloidal systems where the actual solvent enters the calculations only indirectly insofar as it mediates effective interactions and allows the colloids to perform Brownian motion and equilibrate thermally. Besides this connection to experimental results, the 1D setting enables us to introduce the field of DFT for classical fluids by presenting, as an example, the density functional for hard-spheres confined to 1D which is known exactly, contrary to the 2D and 3D counterparts. The examination of the 1D hard-sphere functional serves as an excellent preparation for the derivation of Rosenfeld's FMT [22] for the hard-sphere fluid in 3D which is a subject of Chapter 3.

While providing a very good account of many aspects of the structure of the inhomogeneous fluid, Rosenfeld's FMT suffers from an inaccuracy of the underlying equation of state in the high-density regime. This has been partly cured by subsequent modifications of the theory [25, 26] which are aimed at incorporating a more accurate equation of state into the framework of FMT. However, this gain in accuracy has to be paid for by a slight inconsistency between the modified FMT and an exact relation from scaled-particle theory [27,28]. The observation of this shortcoming has triggered our efforts of constructing a novel equation of state for the hard-sphere mixture based on the requirement of enhancing the degree of consistency. It turns out that such a consistency-based construction leads indeed to an equation of state which is in line with scaled-particle theory if the one-component hard-sphere fluid is considered and which yields a significantly better description of ternary hard-sphere mixtures as can be shown by comparison with simulation data (see Section 3.2). Based on the improved equation of state, a new version of FMT can be put forward (Section 3.3) which, due to its high degree of consistency, proves to be greatly beneficial within the context of morphological thermodynamics (see Section 5.1). The link between FMT and morphological thermodynamics can, however, only be fully established if FMT is generalized to fluids which are composed of hard particles with arbitrary shape (including mixtures of different components). This so-called general hard-body fluid is treated in Chapter 4 which starts with a presentation of Rosenfeld's extention of his FMT to fluids of non-spherical particles [29, 30]. The theory is based on rather heuristic arguments and it has the serious drawback that it is unable to predict a stable nematic phase which is observed in hard-rod fluids. We can cure this deficiency by pursuing more systematically Rosenfeld's ideas, which consist in rewriting the known low-density limit of the free energy functional with the help of the Gauss-Bonnet theorem from differential geometry [31]. The resulting FMT gives a good account of the isotropic-nematic transition in a rod fluid. In addition, the description of the structure of the isotropic *inhomogeneous* hard-rod fluid is enhanced with respect to Rosenfeld's FMT as we show by comparison with data from Monte-Carlo simulations which we have performed for the hard-spherocylinder fluid in contact with a hard wall (see Section 4.2).

As we have mentioned earlier, the results of Chapters 2 to 4 are essential to properly setting up the morphological thermodynamics for the solvation free energy of proteins in the tube model (see Chapter 5). In this respect, the new FMT with increased consistency is particularly valuable as it provides us with accurate *analytical* results for the properties of the hard-sphere solvent which, in turn, guarantees us that the biologically motivated questions can be tackled most efficiently.

Finally, we summarize our results in Chapter 6 where we also discuss issues of interest for future research, which naturally emerge from the questions addressed in this work.

The results contained in this thesis have been published or are planned to be published in the following articles:

- H. Hansen-Goos, C. Lutz, C. Bechinger, and R. Roth, *From pair correlations to pair interactions: An exact relation in one-dimensional systems*, Europhys. Lett. **74**, 8 (2006).

- H. Hansen-Goos and R. Roth, *A new generalization of the Carnahan-Starling equation of state to additive mixtures of hard spheres*, J. Chem. Phys. **124**, 154506 (2006).

- H. Hansen-Goos and R. Roth, *Density functional theory for hard-sphere mixtures: the White Bear version Mark II*, J. Phys.: Condens. Matter **18**, 8413 (2006).

- H. Hansen-Goos, R. Roth, K. Mecke, and S. Dietrich, *Solvation of proteins: linking thermodynamics to geometry*, Phys. Rev. Lett. **99**, 128101 (2007).

- H. Hansen-Goos and K. Mecke, *Extended fundamental measure theory for the inhomogeneous hard-body fluid*, in preparation.

- H. Hansen-Goos, R. Roth, K. Mecke, and S. Dietrich, *Morphological thermodynamics of protein solvation – influence of hydrophobicity*, in preparation.

Chapter 2

Colloids in one dimension

The study of one dimensional (1D) systems has a long standing history in physics in particular as theoretical approaches are concerned [32]. The reasons for this are manifold. The obvious advantage of 1D systems is that they allow for complete analytical treatments in many respects, e.g., when equilibrium properties are required. This makes 1D systems a natural candidate for investigations of dynamic properties such as for instance relaxation processes in lattice gases (a collection of many aspects of non-equilibrium 1D systems can be found in Ref. [33]). For these systems approximate descriptions of the dynamics are based on the solid ground provided by the known statics. Another complex and rich field of studies is provided by driven systems [34] which exhibit a steady state rather than an equilibrium state and are not governed by a Hamiltonian. A prominent example of these models is the totally asymmetric simple exclusion process [35, 36] which is defined in one dimension where it already (in contrast to 1D equilibrium systems with short-ranged interactions) displays different phases. Thus for these driven systems reduced dimensionality allows for an exhaustive study of the phenomenology which becomes rather vast if the dimension is increased. But this is of course not the only motivation for using 1D models. Many experimental setups involve quasi 1D transport such as liquid or gas flow through carbon nanotubes [37, 38] or single-file diffusion of molecular fluids in zeolites of 1D channel structure [39]. A different experimental context, which we consider in the following, is provided by colloidal suspensions with a scanning laser tweezer creating a confining potential. It has been shown experimentally that these colloidal 1D systems are governed by anomalous diffusion [40, 41]. A further important reason for broad interest in 1D equilibrium systems is that while being analytically solvable their structure is in many respects (excluding phase transitions) complex enough to provide indications how suitable approximations for the treatment of 2D and 3D systems can be constructed. For instance, approximations for the

equilibrium properties of the hard-sphere fluid in 2D and 3D can be derived within the so-called fundamental measure theory [22] (see Chapter 3) the structure of which is largely inspired by the exact result in 1D.

In this chapter, we present a brief calculation of the exact pair correlation function in a 1D system with arbitrary interaction potential between next neighbors. The results are used in connection with the experimental setup involving colloidal particles, which we have mentioned earlier, where they serve for solving the inverse problem of recovering the interaction potential from the pair distribution function. Contrary to systems in higher dimensions a remarkably simple relationship can be derived allowing for an unambiguous inversion. Finally, we establish a connection to the theory of hard-sphere fluids by determining an effective hard-sphere radius for the colloidal particles. In this context we present the exact solution for the general mixture of differently-sized hard spheres confined to 1D and introduce the basic notations of density functional theory (DFT). This sets the stage for the extension of the 1D DFT to hard-sphere fluids in 3D which is the subject of the subsequent Chapter 3.

2.1 Calculation of the pair distribution function

Consider a 1D system which contains N identical particles with positions denoted by $r_1, \ldots, r_N$. The particles are assumed to interact only with their nearest neighbors via the potential $V(r)$ where r denotes the distance between two neighboring particles. Interaction with the next-nearest neighbor and more distant neighbors are not included in our calculation. Therefore our results can only be applied to physical systems with interactions which are either relatively short ranged or alternatively screened by the presence of the two direct neighbors. Suppose the particles are required to remain inside the interval $[0, L]$ which is realized by fixing two additional particles of the same kind as the given N particles at positions $r_0 = 0$ and $r_{N+1} = L$. The Hamiltonian of the 1D system is given by

$$H = \sum_{i=1}^{N} \frac{p_i^2}{2m} + \sum_{i=0}^{N} V(r_{i+1} - r_i)\,, \tag{2.1}$$

where m denotes the mass of an individual particle. In the calculation of the canonical partition function Z the momenta integrations can be carried out so that one obtains

$$Z = \left(\frac{2\pi m}{\beta h^2}\right)^{N/2} Q(L, N)\,, \tag{2.2}$$

where h is Planck's constant, $\beta = 1/(k_{\mathrm{B}}T)$ is the inverse temperature, and Q denotes the configurational part of the partition function. As all the particles are identical

one can assume for the calculation of Q that they remain in the given order $r_0 \leq r_1 \leq \cdots \leq r_N \leq r_{N+1}$. Thus Q can be written as

$$\begin{aligned} Q = \int_0^L \mathrm{d}r_N e^{-\beta V(L-r_N)} \int_0^{r_N} \mathrm{d}r_{N-1} e^{-\beta V(r_N - r_{N-1})} \\ \cdots \int_0^{r_3} \mathrm{d}r_2 e^{-\beta V(r_3-r_2)} \int_0^{r_2} \mathrm{d}r_1 e^{-\beta V(r_2-r_1)} e^{-\beta V(r_1)} \,. \end{aligned} \tag{2.3}$$

It was observed by Gürsey [42] that this integral is the N-fold convolution of the function $e^{-\beta V(r)}$. It is therefore worthwhile to take the Laplace transform of Q which simplifies the convolution product into an ordinary product. Using moreover the formula for the inverse Laplace transform one can rewrite Q as

$$Q = Q(L,N) = \frac{1}{2\pi i} \int_{c-i\infty}^{c+i\infty} e^{Ls} [F(s)]^{N+1} \mathrm{d}s \,, \tag{2.4}$$

where the constant c has to be chosen greater than the real parts of all the singularities of $F(s)$, the Laplace transform of the function $f(r) = e^{-\beta V(r)}$, i.e.,

$$F(s) = \int_0^\infty e^{-sr - \beta V(r)} \mathrm{d}r \,. \tag{2.5}$$

Obviously, as any meaningful interaction potential fulfills $V(r \to \infty) = 0$ the function $F(s)$ has no singularity as long as $s > 0$ while it diverges for $s \to 0$. We must therefore require $c > 0$.

In the thermodynamic limit $N \to \infty$ the integral (2.4) can be evaluated in an asymptotic expansion which utilizes the method of steepest decent. Defining the more general expression

$$M = \frac{1}{2\pi i} \int_{c-i\infty}^{c+i\infty} e^{(N+1)G(s)} \chi(s) \mathrm{d}s \,, \tag{2.6}$$

with $G(s) = Ls/(N+1) + \ln F(s)$, the leading term of the large-N-expansion is [43]

$$M e^{-(N+1)G(c)} \sim \frac{\chi(c)}{(2\pi(N+1)G''(c))^{\frac{1}{2}}} \tag{2.7}$$

where the constant c must be chosen according to the saddle point criterion

$$(G'(s))_{s=c} = 0 \,. \tag{2.8}$$

The physical meaning of c becomes immediately clear if one calculates the pressure p which is exerted by the bulk particles (i.e. the N mobile particles in the limit $N \to \infty$) onto the fixed boundary particles. Using the thermodynamic relation between

the pressure and the system's free energy and applying the asymptotic expansion (2.7) in order to proceed to the thermodynamic limit $N \to \infty$ we find that

$$\beta p = \frac{\partial \ln Q}{\partial L} \overset{(2.4)}{=} \frac{\int_{c-i\infty}^{c+i\infty} s e^{Ls} [F(s)]^{N+1} \mathrm{d}s}{\int_{c-i\infty}^{c+i\infty} e^{Ls} [F(s)]^{N+1} \mathrm{d}s} \overset{N\to\infty}{=} c\,, \tag{2.9}$$

where c on the r.h.s. of the equation has to be chosen according to Eq. (2.8). Defining the bulk particle number density in the 1D system as $\rho_\mathrm{b} = \frac{N}{L}$ we can now rewrite Eq. (2.8) for a large system by using the definition of $G(s)$. The result is

$$\rho_\mathrm{b} = -\left(\frac{F(s)}{F'(s)}\right)_{s=\beta p}\,, \tag{2.10}$$

which is the *equation of state* of the 1D system under consideration. As a simple test case one can consider the ideal gas which has the trivial interaction potential $V(r) \equiv 0$. From Eq. (2.5) it follows that $F(s) = s^{-1}$ and thus Eq. (2.10) yields $\beta p = \rho_\mathrm{b}$, as expected. A simple non-trivial case is provided by a hard-sphere fluid which is confined to one dimension. Denoting the sphere diameter by σ_hs the interaction potential reads

$$V(r) = V_\mathrm{hs}(r) = \begin{cases} \infty & \text{for } r < \sigma_\mathrm{hs} \\ 0 & \text{for } r \geq \sigma_\mathrm{hs} \end{cases} \tag{2.11}$$

and from Eq. (2.10) one obtains the 1D hard-sphere equation of state

$$\beta p = \frac{\rho_\mathrm{b}}{1 - \sigma_\mathrm{hs}\rho_\mathrm{b}} \tag{2.12}$$

which predicts a divergence of the pressure as ρ_b increases towards the close packing density σ_hs^{-1}.

We now come to the main issue of this section which is the calculation of the pair distribution function. To this end we follow Salsburg *et al.* [43] and note that the thermal average $\langle\varphi\rangle$ of an observable φ depending only on the spacial coordinates of the particles and being invariant under interchange of particles can be calculated as

$$\begin{aligned} \langle\varphi\rangle = Q^{-1} \int_0^L \mathrm{d}r_N e^{-\beta V(L-r_N)} \int_0^{r_N} \mathrm{d}r_{N-1} e^{-\beta V(r_N - r_{N-1})} \\ \cdots \int_0^{r_3} \mathrm{d}r_2 e^{-\beta V(r_3-r_2)} \int_0^{r_2} \mathrm{d}r_1 e^{-\beta V(r_2-r_1)} e^{-\beta V(r_1)} \varphi(r_1, \ldots, r_N)\,. \end{aligned} \tag{2.13}$$

In the 1D system the pair distribution function $g(r)$ is related to the density distribution $\rho(r)$, which denotes the average probability per unit length that a particle is located at position r. This is a consequence of bounding the system at $r_0 = 0$ by a fixed particle of the same kind as the bulk particles. Therefore taking into

account that $g(r \to \infty) = 1$ leads to the relation that $\rho(r) = \rho_\mathrm{b} g(r)$. The observable belonging to the density distribution $\rho(r)$ in the system containing N particles is $\varphi = \sum_{k=1}^{N} \delta(r_k - r)$. Taking the average of φ according to Eq. (2.13) yields the quantity $\rho(r)$. As for the derivation of Eq. (2.4) we also use the Laplace transform and its inverse in order to obtain the intermediate result [43] (with Q from Eq. (2.4))

$$\rho(r) = Q(L,N)^{-1} \sum_{k=1}^{N} Q(r,k-1) Q(L-r, N-k)\,. \tag{2.14}$$

This results has an easy intuitive interpretation. The product $Q(r,k-1)Q(L-r,N-k)$ equals the statistical weight of all the configurations with one particle fixed at position r (in addition to the boundary particles at $r = 0$ and $r = L$) and $k-1$ particles in the interval $[0,r]$ and $N-k$ particles in the interval $[r,L]$. Each of the N particles can play the role of the particle which is held fixed at position r, hence the sum. The factor $Q(L,N)^{-1}$ normalizes the statistical weight in order to yield a probability. The asymptotic expansion, Eq. (2.7), can be used to obtain the result for $\rho(r)$ in the thermodynamic limit,

$$\rho(r) \overset{N\to\infty}{=} \sum_{k=1}^{\infty} \frac{e^{-\beta p r}}{[F(\beta p)]^k} Q(r,k-1) \tag{2.15}$$

$$= \sum_{k=1}^{\infty} \frac{1}{2\pi} \int_{-\infty}^{+\infty} \left[\frac{F(\beta p + it)}{F(\beta p)}\right]^k e^{irt} \mathrm{d}t\,. \tag{2.16}$$

In the second step we have inserted the expression for Q from Eq. (2.4) and shifted the integration path onto the real axis.

We conclude this section with the observation that for particles interacting via a hard core with diameter σ plus some "soft" potential $V(r)$, i.e.,

$$V_\mathrm{hc}(r) = \begin{cases} \infty & \text{for } r < \sigma \\ V(r) & \text{for } r \geq \sigma\,, \end{cases} \tag{2.17}$$

the integrals in Eq. (2.16) can be shown to vanish for r below certain values using the theory of residues. More precisely,

$$\frac{1}{2\pi} \int_{-\infty}^{+\infty} \left[\frac{F(\beta p + it)}{F(\beta p)}\right]^k e^{irt} \mathrm{d}t = 0 \quad \text{for} \quad r < k\sigma\,, \tag{2.18}$$

which reflects the fact that the k-th term of the sum in Eq. (2.16) corresponds to a particle contributing from the k-th correlation shell onwards. This can also been inferred from Eq. (2.14) as $Q(r,k-1) = 0$ for $r < k\sigma$ which means that an interval carrying $k-1$ particles with diameter σ must have a length of at least $k\sigma$ (the bounding particles occupy $\sigma/2$ of the interval each).

2.2 From pair correlations to pair interactions

The pair distribution function $g(r)$, or the closely related pair correlation function $h(r) = g(r) - 1$ can be obtained by analyzing real space data from experiments which allow for direct visualization of the interacting particles. This is for instance the case for investigations involving colloidal suspensions where the (μm-sized) colloids can be observed by optical microscopy. The solvent constituents are of atomic size and therefore cannot be traced using direct visualization. Their presence is reflected through the solvent-specific interaction potential between the colloidal particles. Due to the presence of the solvent, chemical groups dissociate from the surface of the colloidal particles leaving them charged. With increasing ion concentration the resulting electrostatic interaction is more and more screened. At high salt concentrations two colloids can approach so closely that they experience dispersion forces which eventually make them aggregate. If the screening length is large enough to prevent colloid aggregation a colloidal suspension is termed electrostatically stabilized.

In this section, we aim to apply the previously found analytical results for the relation between the pair distribution function $g(r)$ and the interaction potential $V(r)$ to a system of charge-stabilized, μm-sized colloids as it has been realized experimentally in the group of Prof. Bechinger in Stuttgart. The confinement to 1D is induced by a scanning laser tweezer which effectively creates a quasi-static potential constraining the colloids to a line. As we shall see in the following, our statistical mechanics treatment of the 1D system gives us a simple relation between $g(r)$ and $V(r)$ which for short-ranged pair interaction potentials $V(r)$ allows to solve the inverse problem (i.e. extracting $V(r)$ from $g(r)$) *without* resorting to any approximation. It should be noted in this context that common approaches to the inverse problem in 2D or 3D such as density functional theory [44], Ornstein-Zernike formalism (OZ) [45], and inverse Monte-Carlo (IMC) simulations [46] require more or less far-reaching assumptions which can have uncontrolled effects on the derived pair interaction potentials. The solution of the OZ integral equations requires additional closure relations whose accuracy depends on the range of $V(r)$. In case of IMC, an arbitrarily chosen cut-off in the pair potential has to be introduced. It has been demonstrated that this can lead to artificial features (e.g. a minimum in $V(r)$ for entirely repulsive systems) [47]. Another complication which concerns even the formulation of the inverse problem is due to the influence of many-body contributions to the particle interactions. It has been shown also for colloidal suspensions that the interactions between three colloidal particles *cannot* always be decomposed into only pair-wise interaction potentials [48, 49]. For 1D systems with rather short-ranged interactions as in the experimental realization which we discuss in this section the assumption that only

nearest neighbors interact is valid and, as a consequence, many-body contributions to the interaction potential can be ruled out.

For the purpose of the practical application let us examine the analytical result for the 1D density distribution $\rho(r)$ [Eq. (2.16)] more closely. We remind the reader that the simple relation $\rho(r) = \rho_\mathrm{b} g(r)$ holds. The integrals in Eq. (2.16) are of the Fourier type and a simple calculation shows that the expression for $\rho(r)$ can be written as

$$\rho(r) = \sum_{k=1}^{\infty} \mathcal{F}_\mathrm{p}^{-1} \left\{ \mathcal{F}_\mathrm{p} \left\{ \exp[-\beta p r' - \beta V_\mathrm{hc}(r')]/F(\beta p) \right\}^k \right\}. \tag{2.19}$$

Here, we have introduce the Fourier transform $\mathcal{F}_\mathrm{p}$ which is restricted to positive arguments of the transformed function and its inverse $\mathcal{F}_\mathrm{p}^{-1}$. They are explicitly given by

$$\mathcal{F}_\mathrm{p}\{f(r')\} = \int_0^\infty e^{-itr'} f(r') \mathrm{d}r' \tag{2.20}$$

$$\text{and} \quad \mathcal{F}_\mathrm{p}^{-1}\{q(t)\} = \frac{1}{2\pi} \int_{-\infty}^{+\infty} e^{itr} q(t) \mathrm{d}t \,. \tag{2.21}$$

For an interaction potential $V_\mathrm{hc}(r)$ [see Eq. (2.17)] and a bulk particle density ρ_b given as input, having $\rho(r)$ in the form of Eq. (2.19) allows for efficient numerical computations using fast Fourier transform. In the numerical procedure we solve, in a first step, Eq. (2.10) for the pressure βp. Then we calculate the function $q(t) = \mathcal{F}_\mathrm{p} \left\{ \exp[-\beta p r' - \beta V_\mathrm{hc}(r')]/F(\beta p) \right\}$. We know from Eq. (2.18) that, for the calculation of $\rho(r)$ at $r \leq r_\mathrm{max}$, only the first $n_\mathrm{max} = \lfloor r_\mathrm{max}/\sigma \rfloor$ integrals in Eq. (2.19) are required. Therefore we can simplify Eq. (2.19) for $r \leq r_\mathrm{max}$ according to

$$\begin{aligned} \rho(r) &= \sum_{k=1}^{n_\mathrm{max}} \mathcal{F}_\mathrm{p}^{-1} \left\{ q(t)^k \right\} = \mathcal{F}_\mathrm{p}^{-1} \left\{ \sum_{k=1}^{n_\mathrm{max}} q(t)^k \right\} \\ &= \mathcal{F}_\mathrm{p}^{-1} \left\{ \frac{q(t)(1 - q(t)^{n_\mathrm{max}})}{1 - q(t)} \right\} . \end{aligned} \tag{2.22}$$

The calculation of $\rho(r)$ according to Eq. (2.22) concludes the numerical procedure in which we obtain $\rho(r)$ for the given $V_\mathrm{hc}(r)$ and ρ_b. It turns out that Eq. (2.22) with a finite n_max (chosen depending on the interval in which $\rho(r)$ is required) stabilizes the numerical procedure compared to using $\rho(r) = \mathcal{F}_\mathrm{p}^{-1}\{q(t)/(1 - q(t))\}$ where the limit $n_\mathrm{max} \to \infty$ has been taken. This is due to the divergence of $q(t)/(1 - q(t))$ as $t \to 0$ which is required in order to ensure that $\rho(r \to \infty) = \rho_\mathrm{b}$, i.e. that the bulk value of the density is recovered for large distances from the fixed particle at $r = 0$.

While the calculation of the exact $\rho(r)$ can be performed easily for arbitrary distance r *numerically*, it is most instructive to take a closer look at the analytical

expression for $\rho(r)$ in the interval $[0, 2\sigma]$ (cf. Ref. [50]). In this interval only the term $k = 1$ in the sum of Eq. (2.19) contributes and for this term we can make use of the fact that $\mathcal{F}_{\mathrm{p}}^{-1}$ inverts $\mathcal{F}_{\mathrm{p}}$. Using moreover Eq. (2.17), which defines $V_{\mathrm{hc}}(r)$, we obtain the simple result that

$$\begin{aligned} \rho(r) &= 0 && \text{for } 0 \leq r < \sigma, \\ \rho(r) &= \exp[-\beta p r - \beta V(r)]/F(\beta p) && \text{for } \sigma \leq r \leq 2\sigma \ . \end{aligned} \tag{2.23}$$

The first equation expresses the core condition. The second identity is very simple due to the fact that in the interval $\sigma \leq r \leq 2\sigma$ one can find only the nearest neighbor. This particle feels on the one side the external field $V(r)$ exerted by the fixed particle at $r = 0$ and on the other side the rest of the system that pushes it toward the origin with the pressure p.

Obviously, Eq. (2.23) provides an excellent tool for extracting *both* the interaction potential and the equation of state *directly* from pair distribution functions measured in experiments, provided that the range of $V_{\mathrm{hc}}(r)$ is below 2σ. In this case, we can employ the analytical result Eq. (2.23) in order to extract βp and $F(\beta p)$ from a linear fit to $\ln(\rho(r))$ in the interval where the short-ranged $V_{\mathrm{hc}}(r)$ vanishes, i.e. for $r \lesssim 2\sigma$. With the knowledge of βp and $F(\beta p)$ Eq. (2.23) can be directly solved for the unknown pair potential $V(r)$. In higher dimensions the pair distribution function even at small separations cannot be described in such simple terms because multiple particle interactions are important already in the first correlation shell. Therefore, as we have mentioned above, no exact method yielding the pair potential from the pair distribution function is available.

It is worthwhile noting that the constant $F(\beta p)$ obtained from the linear fit is related to the chemical potential μ via $\beta\mu = -\ln(F(\beta p)/\Lambda)$, where Λ is the thermal wavelength. Thus both the pressure p and the chemical potential μ of a system with a given bulk density ρ_{b} can be gained in a simple way from experimental pair correlations by making use of Eq. (2.23). Therefore, the method could be applied for an experimental test of the Gibbs-Duhem relation which, at constant temperature, states that $\partial p/\partial\mu = \rho_{\mathrm{b}}$. A further interesting implication arises for experiments in which no direct visualization of the particles is feasible so that one has to turn to scattering techniques. Then the static structure factor $S(t)$ is measured instead of $\rho(r)$. However, the two quantities are related through $S(t) = 1 + \int \exp(-itr)\rho(r)\mathrm{d}r$ [45]. For our 1D system one finds that $S(t) = 1 + 2\,\mathrm{Re}\{q(t)/(1 - q(t))\}$. It should, however, be noted that 1D scattering experiments are difficult to realize due to the small number of particles involved which leads to low scattering intensities.

We have now provided the analytical tools which are required for analyzing the data obtained experimentally. Let us therefore present the experimental setup in

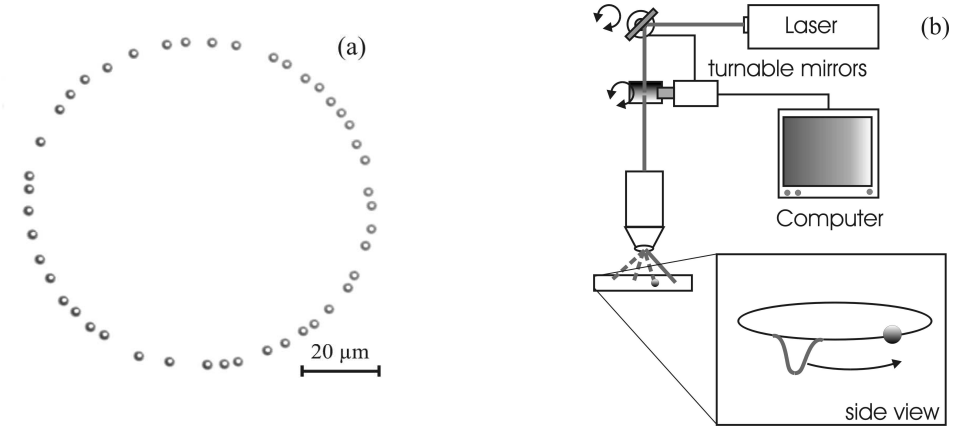

Figure 2.1: (a) Snapshot of $N = 45$ electrostatically stabilized, polystyrene spheres with diameter $\sigma = 2.9\mu$m in deionized water. The particle motion is limited to a circular line by a circular optical trap. (b) Experimental setup.

detail. The system investigated by Lutz and Bechinger (cf. Ref. [40]) consists of a dilute aqueous suspension of electrostatically stabilized, polystyrene spheres with a diameter of $\sigma = 2.9\mu$m [see Fig. 2.1(a)]. The particles are imaged by means of an inverted microscope and particle positions are recorded by video microscopy [51]. The particle motion is confined to a 1D optical trap which is created with an optical tweezer. For this purpose, a single laser beam is continuously deflected by a pair of galvanometric mirrors with a frequency f=330Hz thus forming a circular line [see Fig. 2.1(b)]. The circle is projected with a microscope objective into the sample cell which consists of two 200μm-spaced, flat glass substrates. The negatively charged particles are forced towards the likely charged lower glass wall by gravity and the vertically incident laser tweezer. Therefore the equilibrium position of the particles is typically located about 50nm above the glass plate. Vertical particle fluctuations are on the order of 5% of the particle diameter.

Figure 2.2(a) shows the averaged particle density in the presence of a scanning laser focus. As can be seen, the colloids are effectively confined to a 1D toroidal trap with a rather uniform density distribution along the circumference [Fig. 2.2(a)]. It has been demonstrated by Faucheux *et al.* [52] that at sufficiently high scanning frequencies the particles experience an effective quasi-static potential. Accordingly, the scanning frequency used in the experiments, i.e. 330Hz, is large enough such that the particles are in thermal equilibrium and diffuse freely along the laser trap. From the radial particle distribution the radial trap potential $V_{\mathrm{radial}}(R)$ acting on the colloids can be obtained [Fig. 2.2(b)]. When comparing the width of the potential with the particle diameter, it becomes clear that the spheres cannot pass each other and that indeed the experiment is an excellent realization of a 1D trap. As expected

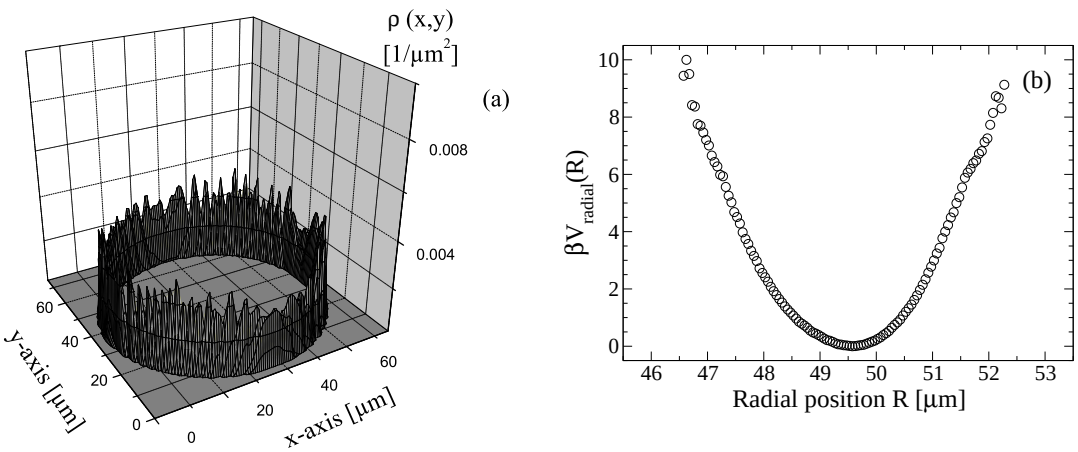

Figure 2.2: (a) Particle density distribution $\rho(x, y)$ for one of the measurements. The particles distribute only, and there equally, along the circular line drawn by the laser focus. (b) An averaged light potential perpendicular to the scanning direction, sampled by the particles due to Brownian motion.

for such systems, the mean-square displacement at large times follows the well-known square-root time dependence which is a unique signature of 1D systems [40, 41].

In order to vary the line density of particles inside the trap, measurements were performed with $N = 45$ colloids trapped on circles with different radii $R \simeq 35.5\mu$m, 39.0μm, 42.5μm and 46.0μm, respectively. The density distribution $\rho(r)$ is obtained from the position data of the colloids as a histogram of the distances with the normalization $1/(NM\Delta r)$, where N is the number of colloids in the trap, M the number of evaluated snapshots and Δr the spacial resolution of the histogram. The distances are measured along the circular confining region which is drawn by the scanning laser beam. The deviation from a straight line is negligible because on the range of the particle interaction (approx. $2\sigma \simeq 5.8\mu$m) the true distance of interacting particles differs from that measured along the circle by less than 0.1%, even for the smallest radius of the trap. Concerning finite size effects, we remark that the correlation length ξ is below 2σ even for the highest density as we have checked using the exact solution for $\rho(r)$. Given the length of the circular line it is therefore justified to regard the system with periodic boundary conditions as having infinite extension.

An application of the analytical results requires the knowledge of the bulk particle number density ρ_b. We determine ρ_b from the value to which the density distribution $\rho(r)$ converges for large argument r (which equals the distance from the fixed particle). The values extracted from the experimental data of the four measurements are $\rho_\mathrm{b} \simeq 0.202\mu\mathrm{m}^{-1}$, $0.183\mu\mathrm{m}^{-1}$, $0.168\mu\mathrm{m}^{-1}$ and $0.155\mu\mathrm{m}^{-1}$.

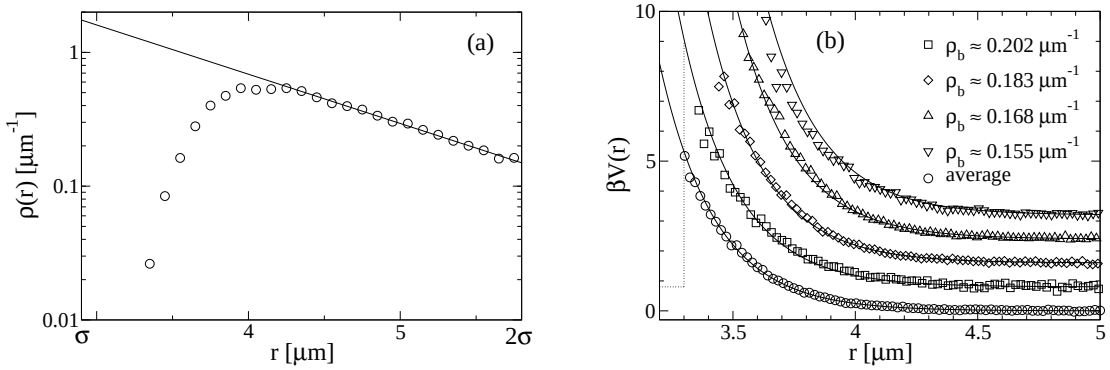

Figure 2.3: (a) Logarithmic plot of $\rho(r)$ for $\rho_\mathrm{b} \simeq 0.202\mu\mathrm{m}^{-1}$. The linear behavior of $\ln(\rho(r))$ confirms that the pair potential $V(r)$ is short ranged. (b) Individual and averaged pair potentials from the measurements. The full lines correspond to the best fit of $V_\mathrm{DLVO}(r)$ to the averaged pair potential (circles). The curves have been shifted for clarity along both axes (see dotted line).

In order to verify the short range of the particle interaction, we confirm for the different measurements that $\ln(\rho(r))$ displays linear behavior at least on the last μm of the interval $[\sigma, 2\sigma]$. As an example, we show $\ln(\rho(r))$ for $\rho_\mathrm{b} \simeq 0.202\mu\mathrm{m}^{-1}$ in Fig. 2.3(a). For each density, this linearization yields the osmotic pressure βp of the colloids and the constant $F(\beta p)$. Equation (2.23) can then be inverted directly to yield unambiguously $V(r)$, as shown in Fig. 2.3(b). The potentials from the four measurements agree very well. Only the result for $\rho_\mathrm{b} \simeq 0.155\mu\mathrm{m}^{-1}$, which was the last measurement in a series of measurements performed with the same sample, shows slight deviations. This is most likely due to the slow increase of airborne ions in the solvent during the measurement.

We aim at finding a *single* pair potential that describes *all* measurements. This would enable us to calculate the equation of state and the particle density distribution for any given bulk density ρ_b. The interaction of charged spherical colloids in a bulk solution (for a review see Ref. [53]) has been described by various approaches which are valid in different regimes [54–56]. According to Derjaguin-Landau-Verwey-Overbeek (DLVO) theory [55], the interaction between two charge stabilized colloids can be described using a screened Coulomb potential:

$$\beta V_\mathrm{DLVO}(r) = \frac{1}{4}\phi^2 \frac{\sigma^2}{\ell_\mathrm{B} r} \exp[-\kappa(r-\sigma)]\,, \tag{2.24}$$

where $\ell_\mathrm{B} \simeq 7$Å is the Bjerrum length in water at room temperature. The Debye screening length κ^{-1} and the normalized surface potential ϕ depend on the properties of the solvent and the colloidal particles.

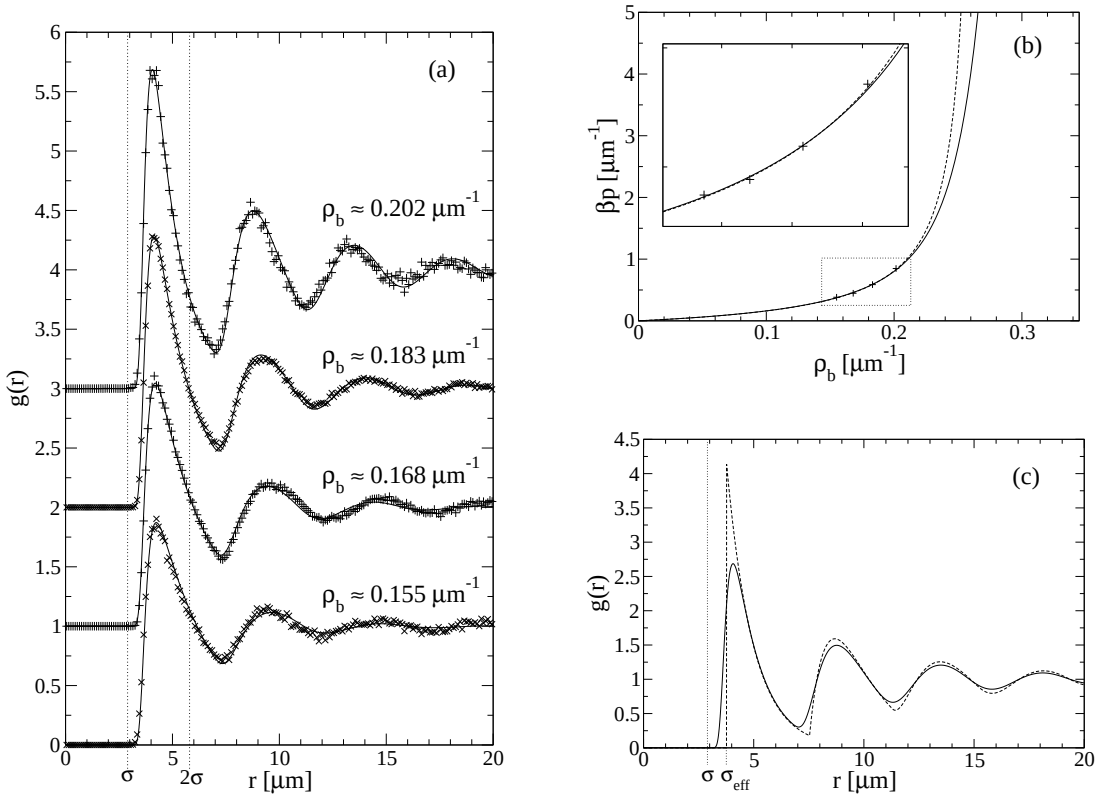

Figure 2.4: (a) Pair-distribution function $g(r)$ from the measurements compared with the analytical calculation (full lines). The curves have been shifted vertically for clarity. σ is the particle diameter. (b) Pressure of the colloids with interaction V_{DLVO} (full line). Fit of the equation of state for hard spheres (dashed line). The points represent the pressure obtained from the four measurements through Eq. (2.23). (c) $g(r)$ of the system with interaction V_{DLVO} (full line) compared to that of a hard-sphere system with effective diameter σ_{eff} (dashed line) at a bulk density $\rho_{\mathrm{b}} \simeq 0.202\mu\mathrm{m}^{-1}$.

The best fit of $V_{\mathrm{DLVO}}(r)$ to the averaged pair potential from the four measurements is obtained for $\kappa^{-1} \simeq 244\mathrm{nm}$ and $\phi \simeq 0.174$, and is in good agreement with the experimental data [see full lines and circles in Fig. 2.3(b)]. The effective charge of the colloids is given by the relation $Z^{\mathrm{eff}} = \ell_{\mathrm{B}}^{-1}(\sigma/2)(1+\kappa\sigma/2)\phi$ [57]. For our data, we obtain $Z^{\mathrm{eff}} \simeq 2500$ which is in good agreement with the result of an independent measurement ($Z^{\mathrm{eff}} \simeq 2250$) where the pair potential was obtained from $g(r)$ by inverting the Ornstein-Zernike equation in 2D [58].

Using the fitted pair potential $V_{\mathrm{DLVO}}(r)$, we can now calculate the equation of state and the density distribution $\rho(r)$ for arbitrary values of ρ_{b} as described previously. The results for the pair-distribution function $g(r) = \rho(r)/\rho_{\mathrm{b}}$ are shown in Fig. 2.4(a). The analytical curves are in very good agreement with the experimental data. We

have marked the interval $[\sigma, 2\sigma]$ in order to emphasize that only experimental data from this interval have been used for determining the common pair potential and hence the analytical curves for the whole function $g(r)$.

The result for the equation of state is shown in Fig. 2.4(b). As a consistency check, we show the results for βp as obtained from the four measurements via Eq. (2.23). We have also checked that similar agreement holds for the chemical potentials determined on the one hand side from the measured $g(r)$ [using Eq. (2.23) together with $\beta\mu = -\ln(F(\beta p)/\Lambda)$] and, on the other hand side, from the function $F(\beta p)$ as it follows when the fitted pair potential $V_{\mathrm{DLVO}}(r)$ is used. Finally, we compare results for a system with DLVO interaction to that of a hard-sphere system, where particles interact via the potential $V_{\mathrm{hs}}(r)$ defined in Eq. (2.11). The corresponding equation of state, Eq. (2.12), can be fitted to the experimentally measured data points for $p(\rho_{\mathrm{b}})$. The fitting parameter is the hard-sphere diameter σ_{hs} and the best fit yields the effective diameter $\sigma_{\mathrm{eff}} = \sigma_{\mathrm{hs}} \simeq 3.76\mu$m belonging to the hard-sphere system which is expected to behave in a most similar way compared to the colloidal system under consideration. As far as bulk properties are concerned, the experimental system can hardly be distinguished from the effective hard-sphere system in a wide range of densities ρ_{b} [see Fig. 2.4(b)]. When microscopic structural properties are compared, it turns out that the effective hard-sphere system displays results which differ significantly from the experimental findings, as can be seen from Fig. 2.4(c). The mapping onto an effective hard-sphere system has been carried out previously for charge stabilized colloids in 2D [59] with qualitatively similar agreement.

After having demonstrated that the exact analytical solution for the 1D system with arbitrary next neighbor interaction, in particular the simple Eq. (2.23), provides a valuable tool for solving the inverse problem (i.e. recovering the interaction potential from the pair correlations) in 1D, we shall discuss in the next section the special case of a 1D hard-sphere system in some detail. Above, the hard-sphere system has been shown to provide a reference system which is partly capable of yielding features of a system with more complex interactions. In many theoretical treatments, the well understood hard-sphere system serves as a solid foundation on which more elaborate model fluids (or solids) can be investigated. Moreover, in the next section we shall introduce the basic traits of density functional theory which constitutes the major tool which we shall use throughout this work.

2.3 Density functional theory for hard spheres in one dimension

Using the theory of residues it can be easily shown that for a 1D system of hard spheres (diameter $\sigma_{\rm hs}$) interacting via the potential $V_{\rm hs}(r)$ [see Eq. (2.11)] the density distribution $\rho(r)$ as given in Eq. (2.16) takes the explicit form

$$\rho(r) = \beta p \sum_{k=1}^{\infty} \Theta(r - k\sigma_{\rm hs}) \frac{[\beta p(r - k\sigma_{\rm hs})]^{k-1}}{(k-1)!} \, e^{-\beta p(r - k\sigma_{\rm hs})} \, . \tag{2.25}$$

While this is a nice result due to its relative simplicity, in many relevant cases one is interested in fluids which experience an external potential allowing to model, e.g., adsorption of fluid particles at an attractive wall or fluids confined in narrow pores where phenomena like capillary condensation or evaporation can occur in 2D and 3D systems. In this context, Eq. (2.25) can be viewed as the density distribution $\rho(r)$ of hard spheres in 1D in contact with a hard "wall" located at $r = \sigma_{\rm hs}/2$ which is mimicked by the fixed boundary particle at $r = 0$.

A very versatile tool for the investigation of inhomogeneous fluids, i.e. fluids which are subject to a spatially inhomogeneous external potential, is provided by density functional theory (DFT) for systems obeying classical statistical mechanics. DFT goes back to the work by Hohenberg, Kohn, and Mermin [60,61] where it was initially formulated for quantum systems before the method was transfered to the field of classical fluids [17–19] and later on also to crystalline (see Ref. [62] and references therein) and glassy solids [63]. The basis of DFT as we employ it throughout this work can be stated in the following concise form. Consider a fluid consisting of ν different particle species, also termed components in the following, which behave classically and interact according to the potential energy U which is a function of the coordinates of all particles in the fluid. For given U one can construct the so-called excess free energy functional $\mathcal{F}_{\rm ex}[\rho_1, \ldots, \rho_\nu]$ depending on the density distributions $\rho_1(\mathbf{r}), \ldots, \rho_\nu(\mathbf{r})$ which are functions of the spacial coordinates $\mathbf{r}$ (reducing to r in the 1D system). As they provide a direct generalization of the density distributions defined earlier for the 1D system, the combinations $\rho_i(\mathbf{r})\mathrm{d}\mathbf{r}$ give the probability that a particle of species i is contained in the infinitesimal volume $\mathrm{d}\mathbf{r}$ at position $\mathbf{r}$. The functional $\mathcal{F}_{\rm ex}$ is uniquely determined by the requirement that the density functional

$$\begin{aligned} \Omega[\rho_1, \ldots, \rho_\nu] \; = \; & \mathcal{F}_{\rm id}[\rho_1, \ldots, \rho_\nu] + \mathcal{F}_{\rm ex}[\rho_1, \ldots, \rho_\nu] \\ & - \sum_{i=1}^{\nu} \int \mathrm{d}\mathbf{r} \rho_i(\mathbf{r})(\mu_i - V_i^{\rm ext}(\mathbf{r})) \end{aligned} \tag{2.26}$$

be minimized by the density distributions $\rho_1(\mathbf{r}), \ldots, \rho_\nu(\mathbf{r})$ which the system assumes in thermal *equilibrium*. It should be emphasized that this minimization property has to be required for *any* set of chemical potentials $\mu_1, \ldots, \mu_\nu$ and external potentials $V_1^{\text{ext}}(\mathbf{r}), \ldots, V_\nu^{\text{ext}}(\mathbf{r})$ which apply to the respective fluid component. The dependence on the inverse temperature β comes into play through $\mathcal{F}_{\text{id}}$ which is the functional of the free energy of the ideal gas (i.e. for $\mathcal{F}_{\text{ex}} \equiv 0$). In d dimensions, this part is given by

$$\mathcal{F}_{\text{id}}[\rho_1, \ldots, \rho_\nu] = \beta^{-1} \sum_{i=1}^{\nu} \int \mathrm{d}\mathbf{r} \rho_i(\mathbf{r}) (\ln(\Lambda_i^d \rho_i(\mathbf{r})) - 1) \tag{2.27}$$

with the thermal wavelengths $\Lambda_i = (\beta h^2 / 2\pi m_i)^{1/2}$ which depend on the mass m_i of a particle of species i. In addition, $\mathcal{F}_{\text{ex}}$ is temperature-dependent.

When the functional given in Eq. (2.26) is evaluated for the equilibrium density distributions one can identify the following quantities: Ω is the system's grand potential, $\mathcal{F}_{\text{id}}$ is the ideal gas part of the internal free energy and $\mathcal{F}_{\text{ex}}$ is the contribution to the intrinsic free energy due to the presence of nontrivial interactions between the fluid particles (the index ex stands for excess, i.e. over ideal gas, free energy).

We can phrase the defining property of $\mathcal{F}_{\text{ex}}$ differently: once the excess free energy density functional $\mathcal{F}_{\text{ex}}$ is known, minimizing the functional Ω [Eq. (2.26)] yields the equilibrium density distributions $\rho_i(\mathbf{r})$ for any given chemical potentials μ_i and external potentials $V_i^{\text{ext}}(\mathbf{r})$. The external potentials are a crucial ingredient of the DFT as they induce the spacial inhomogeneities which give rise to non-trivial density distributions $\rho_i(\mathbf{r})$. Examples for such sources of inhomogeneities in physical systems include for instance a container with the fluid inside, a porous medium filled with the fluid, and a (large) molecule being immersed in the fluid which acts as a solvent. The latter example will be treated in this work in the context of a simple model for protein solvation (see Chapter 5). One of the simplest test geometries occurs when the fluid is in contact with a planar hard wall. The equilibrium density distribution $\rho(r)$ in the analogous 1D geometry (where the term "wall" refers to a pointlike obstacle) is given in a closed analytical form by Eq. (2.25). For more complicated external potentials, however, calculating $\rho(r)$ analytically is—even in 1D—not an amenable task. It is advisable to use the functional Ω for the computation of equilibrium properties instead. The minimization of Ω [Eq. (2.26)] leads to solving the set of Euler-Lagrange equations $\delta\Omega/\delta\rho_i = 0$, $i = 1, \ldots, \nu$ which are equivalent to the equations

$$\rho_i(\mathbf{r}) = \rho_i^{\text{b}} \exp\left\{-\beta V_i^{\text{ext}}(\mathbf{r}) + c_i^{(1)}[\rho_1, \ldots, \rho_\nu; \mathbf{r}] + \beta\mu_i^{\text{ex}}\right\} \quad , \quad i = 1, \ldots, \nu. \tag{2.28}$$

Here we have splitted the chemical potentials into two parts: $\mu_i = \mu_i^{\text{id}} + \mu_i^{\text{ex}}$. The ideal gas part of μ_i is connected with the bulk density ρ_i^{b} of component i (i.e. the

density in the unperturbed system far away from the inhomogeneities) via the relation $\mu_i^{\mathrm{id}} = \beta^{-1} \ln(\Lambda_i^d \rho_i^{\mathrm{b}})$. The one point direct correlation function is defined as

$$c_i^{(1)}[\rho_1, \ldots, \rho_\nu; \mathbf{r}] = -\beta \frac{\delta \mathcal{F}_{\mathrm{ex}}[\rho_1, \ldots, \rho_\nu]}{\delta \rho_i(\mathbf{r})} \,. \tag{2.29}$$

The excess free energy density in the bulk fluid can be obtained as $f_{\mathrm{ex}}^{\mathrm{b}}(\rho_1^{\mathrm{b}}, \ldots, \rho_\nu^{\mathrm{b}}) = \mathcal{F}_{\mathrm{ex}}[\rho_1 = \rho_1^{\mathrm{b}}, \ldots, \rho_\nu = \rho_\nu^{\mathrm{b}}]/V$ from which we calculate the excess chemical potential μ_i^{ex} through the relation

$$\mu_i^{\mathrm{ex}} = \frac{\partial f_{\mathrm{ex}}^{\mathrm{b}}}{\partial \rho_i^{\mathrm{b}}} \,. \tag{2.30}$$

Obviously, for the bulk fluid the relation $c_i^{(1)} = -\beta \mu_i^{\mathrm{ex}}$ holds, which guarantees the consistency of Eq. (2.28). We mention as an aside that, in analogy to Eq. (2.29), higher order direct correlation functions are defined by means of higher order functional derivatives [19]. Thus, once the equilibrium density profiles are obtained by solving Eq. (2.28) the whole equilibrium microscopic structure of the fluid in the given external potentials follows from functional derivatives of $\mathcal{F}_{\mathrm{ex}}$.

In conclusion, DFT yields a versatile framework for the calculation of equilibrium properties of fluids (and solids), not only on the level of density profiles and correlation functions. Also values for free energies, which are difficult to access by means of numerical simulations, are readily obtained from the theory. It should, however, be noted that the bottleneck of DFT is the knowledge of the excess free energy functional $\mathcal{F}_{\mathrm{ex}}$. We have not mentioned so far *how* $\mathcal{F}_{\mathrm{ex}}$ can be derived given a fluid with specified microscopic interaction. And, not surprisingly, for systems lacking an exact statistical mechanics solution, only approximations for $\mathcal{F}_{\mathrm{ex}}$ are available. We shall come back to the construction of such approximations several times in this work. In particular for the hard-sphere fluid in 3D (Chapter 3) and the general hard-body fluid (Chapter 4), i.e. a 3D fluid consisting of hard particles of arbitrary shape. For the hard-sphere fluid in 1D, however, the functional $\mathcal{F}_{\mathrm{ex}}$ is known exactly [64]. Given that this exact result exhibits already several structural features which we shall encounter in the following chapters during the construction of the approximative 3D functionals, we conclude the chapter with a brief presentation and discussion of the 1D functional.

Consider a system of hard spheres with centers confined to a straight line. Let the 1D system be composed of ν different species which are characterized by their radii R_i, $i = 1, \ldots, \nu$. The thermodynamic bulk state of the system is specified by the chemical potentials μ_i or, alternatively, the bulk densities ρ_i^{b} of the different components. Using the density distributions $\rho_i(\mathbf{r})$ the following two *weighted densities*

can be defined:

$$n_0(r) = \sum_{i=1}^{\nu} \frac{1}{2} \left(\rho_i(r - R_i) + \rho_i(r + R_i) \right) \tag{2.31}$$

$$n_1(r) = \sum_{i=1}^{\nu} \int_{r-R_i}^{r+R_i} \rho_i(r) \mathrm{d}r \, . \tag{2.32}$$

The weighted densities constitute quantities which are non-local in the sense that they contain information about the density profile at more than a single point in space. If one imagines a particle of species i which is located at the position r one can easily see that the combination $\frac{1}{2} \left(\rho_i(r - R_i) + \rho_i(r + R_i) \right)$ weights the density profile according to the *surface* (i.e. two points in 1D) of sphere i while the integral $\int_{r-R_i}^{r+R_i} \rho_i(r) \mathrm{d}r$ corresponds to weighting $\rho_i(r)$ over the *volume* (i.e. a line in 1D) of the particle. In the bulk fluid, Eqs. (2.31) and (2.32) reduce to $n_0 = \sum_{i=1}^{\nu} \rho_i^{\mathrm{b}}$, which equals the total particle number density N_{tot}/V, and $n_1 = \sum_{i=1}^{\nu} 2R_i \rho_i^{\mathrm{b}}$, which is the total packing fraction, i.e. the fraction of the rectilinear system which is covered by the 1D spheres.

The excess free energy density Φ_{1D} of the system is given as a simple *function* of the weighted densities,

$$\Phi_{\mathrm{1D}}(r) = -n_0(r) \ln \left(1 - n_1(r) \right) \, , \tag{2.33}$$

from which the excess free energy function $\mathcal{F}_{\mathrm{ex}}$ is obtained as

$$\beta \mathcal{F}_{\mathrm{ex}}^{\mathrm{1D}}[\rho_1, \ldots, \rho_\nu] = \int \mathrm{d}r \, \Phi_{\mathrm{1D}}(r) \, . \tag{2.34}$$

We want to analyze the remarkably simple expression Eq. (2.33) in the limit of dilute systems, i.e. $\rho_i(r) \to 0$. Then one obtains from Eq. (2.33) that $\Phi_{\mathrm{1D}}(r) \to n_0(r) n_1(r)$ to lowest order in the densities $\rho_i(r)$. Plugging this low-density expression into Eq. (2.34) we obtain the lowest order result[1] for the functional $\mathcal{F}_{\mathrm{ex}}^{\mathrm{1D}}$,

$$\begin{aligned} \beta \mathcal{F}_{\mathrm{ex}}^{\mathrm{1D}} &\xrightarrow{\text{l.d.l.}} \int \mathrm{d}r \, n_0(r) n_1(r) \\ &= \frac{1}{2} \sum_{i,j=1}^{\nu} \iint \mathrm{d}r_i \mathrm{d}r_j \rho_i(r_i) \rho_j(r_j) (\omega_i^{(0)} \otimes \omega_j^{(1)} + \omega_j^{(0)} \otimes \omega_i^{(1)}) \, . \end{aligned} \tag{2.35}$$

For the rewriting in the last step we use the so-called weight functions

$$\omega_i^{(0)}(r) \doteq \frac{1}{2} \delta(R_i - |r|) \quad \text{and} \quad \omega_i^{(1)}(r) \doteq \Theta(R_i - |r|) \tag{2.36}$$

[1] We refer to the limiting case $\rho_i(r) \to 0$ in which we expand the density functional up to second order in the densities $\rho_i(r)$ as the low-density limit (l.d.l.).

which generate the weighted densities, Eqs. (2.31) and (2.32), according to the formula

$$n_\alpha(r) = \sum_{i=1}^{\nu} \int \mathrm{d}r' \rho_i(r') \omega_i^{(\alpha)}(r - r') \,, \quad \alpha = 0, 1 \,. \tag{2.37}$$

The convolution product $\otimes$ in Eq. (2.35) is defined by

$$\omega_i^{(\alpha)} \otimes \omega_j^{(\gamma)} \doteq \int \mathrm{d}r \, \omega_i^{(\alpha)}(r - r_i) \omega_j^{(\gamma)}(r - r_j) \,, \tag{2.38}$$

which obviously is a function only of the difference $r_j - r_i$ or, more precisely, of $|r_j - r_i|$ as follows from the form of the weight functions from Eq. (2.36).

The purpose of rewriting the low-density expression for $\mathcal{F}_{\mathrm{ex}}^{\mathrm{1D}}$ in the form of Eq. (2.35) is to identify the second order virial expansion. To this end we examine the combination

$$-f_{ij}(|r_j - r_i|) = \omega_i^{(0)} \otimes \omega_j^{(1)} + \omega_j^{(0)} \otimes \omega_i^{(1)} \tag{2.39}$$

using the Fourier transform which transforms the convolution products appearing in Eq. (2.39) into usual products. In Fourier space, the weight functions as defined in Eq. (2.36) become

$$\tilde{\omega}_i^{(0)}(k) = \int_{-\infty}^{\infty} \mathrm{d}r \, \omega_i^{(0)}(r) e^{-ikr} = \cos(kR_i) \tag{2.40}$$

$$\tilde{\omega}_i^{(1)}(k) = \int_{-\infty}^{\infty} \mathrm{d}r \, \omega_i^{(1)}(r) e^{-ikr} = \frac{2\sin(kR_i)}{k} \,. \tag{2.41}$$

With these results we obtain Eq. (2.39) in Fourier space as

$$\begin{aligned} -\tilde{f}_{ij}(k) &= \tilde{\omega}_i^{(0)}(k) \tilde{\omega}_j^{(1)}(k) + \tilde{\omega}_j^{(0)}(k) \tilde{\omega}_i^{(1)}(k) \\ &= \frac{2}{k} \big(\cos(kR_i) \sin(kR_j) + \cos(kR_j) \sin(kR_i) \big) \\ &= \frac{2 \sin\big(k(R_i + R_j)\big)}{k} \,, \end{aligned} \tag{2.42}$$

where we have used the appropriate angle sum identity in the last step. Considering Eqs. (2.36), (2.41), and (2.42) it follows that f_{ij} can be written in the form

$$f_{ij}(|r_j - r_i|) = -\Theta(R_i + R_j - |r_j - r_i|) \tag{2.43}$$

in real space, which is obviously equivalent to writing

$$f_{ij}(|r_j - r_i|) \equiv \exp\big[-\beta V_{ij}(|r_j - r_i|) \big] - 1 \tag{2.44}$$

with the potential

$$V_{ij}(|r_j - r_i|) = \begin{cases} \infty & \text{for } |r_j - r_i| < R_i + R_j \\ 0 & \text{for } |r_j - r_i| \geq R_i + R_j \end{cases} \tag{2.45}$$

describing the interaction between two hard spheres of species i and j.

Equation (2.44) is precisely the definition of the Mayer f-function and thus we have explicitly shown that Eq. (2.35) is nothing else but the second order virial expansion

$$\beta\mathcal{F}_{\rm ex}^{\rm 1D} \stackrel{\rm l.d.l.}{\longrightarrow} -\frac{1}{2}\sum_{i,j=1}^{\nu}\iint {\rm d}r_i{\rm d}r_j\rho_i(r_i)\rho_j(r_j)f_{ij}(|r_j-r_i|)\,. \tag{2.46}$$

It is very interesting to note that Eq. (2.46) holds not only in 1D but provides also the exact low-density limit for hard-body fluids in 2D and 3D (after adapting the expression to higher dimensional space). Therefore, as we shall see in the next chapter, Eq. (2.46) provides an excellent starting point for the *construction* of approximate functionals $\mathcal{F}_{\rm ex}$ for the hard-body fluid in 3D. The calculation above, which has led us from $\mathcal{F}_{\rm ex}^{\rm 1D}$ as given without derivation in Eq. (2.33) to the low-density expression in Eq. (2.46), has to be "reversed" in some sense in order to construct the approximate functionals. In this context, the reasoning in terms of weight functions, convolutions thereof, and Fourier transforms as presented above will prove most useful. This makes the detailed study of the exact 1D result so valuable.

While the deconvolution of the Mayer f-function in analogy to Eq. (2.39) provides one key for the construction of hard-body density functionals which is microscopically based as the interaction between two particles is taken into account explicitly, the second key is provided by arguments concerning a *bulk* property of the fluid, namely the pressure. According to thermodynamics, the pressure p of the 1D hard-sphere fluid can be obtained from the excess free energy density $\Phi_{\rm 1D}$, evaluated in the bulk fluid, via

$$\beta p - n_0 = -\frac{\partial(V\Phi_{\rm 1D})}{\partial V} = -\Phi_{\rm 1D} + \sum_{i=1}^{\nu}\frac{\partial\Phi_{\rm 1D}}{\partial\rho_i}\rho_i = -\Phi_{\rm 1D} + \frac{\partial\Phi_{\rm 1D}}{\partial n_0}n_0 + \frac{\partial\Phi_{\rm 1D}}{\partial n_1}n_1\,, \tag{2.47}$$

where, on the l.h.s., we have subtracted n_0 which equals the ideal gas contribution to βp. With the expression from Eq. (2.33) we find

$$\beta p = \frac{n_0}{1-n_1} \tag{2.48}$$

which generalizes the 1D hard-sphere equation of state obtained in Eq. (2.12) to multi-component systems.

An alternative route to the pressure p makes explicit use of the fact that $\Phi_{\rm 1D}$ provides a formulation for multi-component mixtures. The excess chemical potential $\mu_i^{\rm ex}$ of species i, which is the reversible work required for inserting such a particle into the given fluid mixture, can be calculated as

$$\beta\mu_i^{\rm ex} = \frac{\partial\Phi_{\rm 1D}}{\partial\rho_i} = \frac{\partial\Phi_{\rm 1D}}{\partial n_1}2R_i + \frac{\partial\Phi_{\rm 1D}}{\partial n_0}\,. \tag{2.49}$$

In the limit of an inserted particle which is very large, the required work is dominated by the work against the bulk pressure p which is needed to create a cavity which is large enough to hold the inserted particle. More precisely, we know from scaled-particle theory [27, 28] that $\lim_{R_i\to\infty} \mu_i^{\mathrm{ex}}/(2R_i) = p$ and we can therefore identify

$$\beta p = \frac{\partial \Phi_{1\mathrm{D}}}{\partial n_1} \overset{(2.33)}{=} \frac{n_0}{1-n_1}\,. \tag{2.50}$$

As required, the two routes to the pressure lead to the same result. The requirement of consistency of the results for p provides, in addition to the deconvolution of the Mayer f-function, the second crucial resource in the context of the construction of hard-body density functionals. We will come back to these two aspects frequently in the following Chapters 3 and 4. The simplicity and shortness of the expressions for the 1D system have allowed us to present calculations explicitly, which, in the cases where direct analogies occur, will permit us to spare the reader certain lengthy details in the context of the more complex 3D functionals.

Chapter 3

Hard-sphere fluid in three dimensions

In the last section of the previous chapter we have introduced density functional theory (DFT) as a tool for the study of the microscopic structure of fluids subject to arbitrary external potentials. Moreover, DFT is capable of yielding free energies of equilibrium systems which makes it a powerful approach to calculate solvation free energies. The latter can be obtained by minimizing the functional Ω [Eq. (2.26)] for the fluid with and without the solute (being modeled by an appropriate external potential), which will be discussed in detail in Chapter 5 of this work.

So far we have presented the exact density functional for 1D hard-sphere systems only (see Section 2.3). For the general case of a fluid in 3D with interacting particles there are no exact density functionals known, except for formal multi-particle expansions involving an infinite number of terms [45]. These expressions are of no practical use for concrete calculations as they contain multiple integrals which cannot be evaluated systematically within reasonable computational time and accuracy. It is obviously more useful to find an expression for Ω in 3D which is as compact as the 1D functional [Eq. (2.34) supplemented with Eq. (2.33)], i.e., which does not require the evaluation of an infinite number of terms but which is rather based on a restricted set of weighted densities which can be computed easily. The construction of density functionals for the 3D hard-sphere fluid goes back to the work of Tarazona and others from the late 70's and early 80's [65] but only with the work of Rosenfeld [22, 66], who constructed the so-called *fundamental measure theory* (FMT) for the hard-sphere fluid, a functional was set up which makes use of the beautifully simple 1D result while it is more accurate than the previous theories (cf. Refs. [67,68]). Moreover, FMT is the first workable theory for the general inhomogeneous hard-sphere mixture (cf. Ref. [69]). In this chapter, we present a derivation of FMT which uses the close anal-

ogy to the 1D functional (Section 3.1). We further construct an improved version of FMT (Section 3.3) which makes use of a new generalization of the Carnahan-Starling equation of state to hard-sphere mixtures (Section 3.2). The new DFT, which we refer to as the White Bear version of FMT Mark II (WBII), will prove especially useful in the context of *morphological thermodynamics* (see Section 5.1) where its high degree of self-consistency allows for obtaining accurate analytical results for thermodynamic solvent properties (surface tension, bending rigidities). Therefore, the WBII density functional enables us to perform calculations of solvation free energies of biomolecules within morphological thermodynamics both efficiently *and* accurately. We shall elaborate on this application in the context of the biologically inspirated model which we treat in Chapter 5.

3.1 Rosenfeld's fundamental measure theory

In 1989, Rosenfeld presented in a seminal paper his FMT [22] which is based on ideas originating in his "scaled field particle theory" where he obtained a representation of the Percus-Yevick (PY) direct correlation function of a hard-particle fluid in terms of the (fundamental) geometric measures such as volume and surface area of the intersection body [70]. The approach connects the PY results [71–73] to the scaled-particle theory of Reiss *et al.* [27, 28]. It allowed Rosenfeld to construct a density functional on the basis of purely geometric arguments which, unlike previous DFTs, does not require the PY results as an input but rather *outputs* them. At the time when FMT was constructed, the exact 1D result which we presented in Section 2.3 was not yet published in the literature. However, as the analogy of the 1D functional with the approximative functionals in higher dimension is so striking we choose to exploit it for our presentation of Rosenfeld's FMT.

As in the case of the 1D density functional the non-trivial part of the grand potential functional Ω [Eq. (2.26)] is contained in the excess free energy functional $\mathcal{F}_{\text{ex}}^{\text{3D}}$ which encodes the interactions between the particles. For the 1D expression $\mathcal{F}_{\text{ex}}^{\text{1D}}$ we have shown that in the low-density limit the functional reduces to a double integral over the density distributions which are coupled by the Mayer f-function [see Eq. (2.46)]. It is known from the theory of diagrammatic expansions [45] that the corresponding low-density limit (l.d.l.) in higher dimension assumes the same form. Thus, for the ν-component hard-sphere fluid in 3D (with radii R_i and density distributions $\rho_i(\mathbf{r})$) we have

$$\beta\mathcal{F}_{\text{ex}}^{\text{3D}} \xrightarrow{\text{l.d.l.}} -\frac{1}{2}\sum_{i,j=1}^{\nu}\int \mathrm{d}\mathbf{r}_i\mathrm{d}\mathbf{r}_j\rho_i(\mathbf{r}_i)\rho_j(\mathbf{r}_j)f_{ij}(|\mathbf{r}_i-\mathbf{r}_j|)\,. \tag{3.1}$$

The Mayer f-function f_{ij} is defined, like in the 1D case [see Eq. (2.44)], by

$$f_{ij}(|\mathbf{r}_i - \mathbf{r}_j|) \doteq \exp[-\beta V_{ij}(|\mathbf{r}_i - \mathbf{r}_j|)] - 1\,, \tag{3.2}$$

which uses the interaction potential V_{ij} of the hard spheres. The latter is given explicitly by

$$V_{ij}(|\mathbf{r}|) = \begin{cases} \infty & \text{for } |\mathbf{r}| < R_i + R_j \\ 0 & \text{for } |\mathbf{r}| \geq R_i + R_j \end{cases} \tag{3.3}$$

expressing the fact that the hard spheres are not allowed to overlap.

In order to identify suitable weighted densities [the analog of n_0 and n_1, see Eqs. (2.31) and (2.32)] from which we can construct $\mathcal{F}_{\text{ex}}^{\text{3D}}$, one can proceed like for the 1D system where a deconvolution of the Mayer f-function f_{ij} in terms of weight functions $\omega_i^{(\alpha)}$ was formulated [see Eq. (2.39)]. Rosenfeld came up with a deconvolution of the Mayer f-function which is valid in 3D. In contrast to the deconvolution in 1D a total number of six (instead of two) weight functions is required, four of which are scalar and two are vector valued. The deconvolution reads

$$\begin{aligned} -f_{ij}(|\mathbf{r}_j - \mathbf{r}_i|) \;=\; & \omega_i^{(0)} \otimes \omega_j^{(3)} + \omega_j^{(0)} \otimes \omega_i^{(3)} + \omega_i^{(1)} \otimes \omega_j^{(2)} + \omega_j^{(1)} \otimes \omega_i^{(2)} \\ & - \overrightarrow{\omega}_i^{(1)} \otimes \overrightarrow{\omega}_j^{(2)} - \overrightarrow{\omega}_j^{(1)} \otimes \overrightarrow{\omega}_i^{(2)} \end{aligned} \tag{3.4}$$

with

$$\omega_i^{(3)}(\mathbf{r}) = \Theta(R_i - |\mathbf{r}|)\,, \quad \omega_i^{(2)}(\mathbf{r}) = \delta(R_i - |\mathbf{r}|)\,, \quad \overrightarrow{\omega}_i^{(2)}(\mathbf{r}) = \frac{\mathbf{r}}{|\mathbf{r}|}\,\delta(R_i - |\mathbf{r}|)\,, \tag{3.5}$$

and $\omega_i^{(1)}(\mathbf{r}) = \omega_i^{(2)}(\mathbf{r})/(4\pi R_i)$, $\omega_i^{(0)}(\mathbf{r}) = \omega_i^{(2)}(\mathbf{r})/(4\pi R_i^2)$, and $\overrightarrow{\omega}_i^{(1)}(\mathbf{r}) = \overrightarrow{\omega}_i^{(2)}(\mathbf{r})/(4\pi R_i)$. The convolution product $\otimes$ is defined, in complete analogy to the 1D case, by the integral

$$\omega_i^{(\alpha)} \otimes \omega_j^{(\gamma)} \doteq \int \mathrm{d}\mathbf{r}\, \omega_i^{(\alpha)}(\mathbf{r} - \mathbf{r}_i)\omega_j^{(\gamma)}(\mathbf{r} - \mathbf{r}_j)\,, \tag{3.6}$$

which is, again, a function only of the difference vector $\mathbf{r}_j - \mathbf{r}_i$. It is important to remark that our notation $\omega_i^{(\alpha)}$ for an arbitrary weight function *includes* the vector valued weight functions. The convolution of two vectorial weight functions requires to employ the scalar product of vectors on the r.h.s. of Eq. (3.6) which, in our notation, is not distinguished from the usual product of two scalars.

The validity of the deconvolution, Eq. (3.4), can be checked most conveniently by mapping the expression to Fourier space were the convolutions reduce to usual products. The corresponding calculation resembles the one which we have performed explicitly in the 1D case [see Eq. (2.42)] though the expressions are more cumbersome.

The 3D deconvolution Eq. (3.4) can be plugged into the expression for the exact low density limit, Eq. (3.1), which can then be recast to the form

$$\beta\mathcal{F}^{\text{ex}} \xrightarrow{\text{l.d.l.}} \int \mathrm{d}\mathbf{r}\big(n_0(\mathbf{r})n_3(\mathbf{r}) + n_1(\mathbf{r})n_2(\mathbf{r}) - \overrightarrow{n}_1(\mathbf{r})\overrightarrow{n}_2(\mathbf{r})\big) \tag{3.7}$$

with the weighted densities n_α which are defined by

$$n_\alpha(\mathbf{r}) = \sum_{i=1}^{\nu} \int \mathrm{d}\mathbf{r}' \rho_i(\mathbf{r}')\omega_i^{(\alpha)}(\mathbf{r}-\mathbf{r}')\,. \tag{3.8}$$

From Eq. (3.7) we can read off that in the low-density limit the excess free energy density $\Phi_{3\text{D}}$ behaves like $\Phi_{3\text{D}}(\mathbf{r}) \to n_0(\mathbf{r})n_3(\mathbf{r}) + n_1(\mathbf{r})n_2(\mathbf{r}) - \overrightarrow{n}_1(\mathbf{r})\overrightarrow{n}_2(\mathbf{r})$ which can be compared with the 1D low-density limit $\Phi_{1\text{D}}(r) \to n_0(r)n_1(r)$ as derived from the exact expression for $\Phi_{1\text{D}}$ given in Eq. (2.33). This observation constitutes a strong motivation to construct $\Phi_{3\text{D}}$ as a *function* of only the six weighted densities defined in Eq. (3.8) with the weight functions given in and below Eq. (3.5). In the first place, this procedure allows us to match $\Phi_{3\text{D}}$ with the exact expression for the low-density limit [Eq. (3.7)] which itself can be written as a function of the weighted densities. Moreover, it is interesting to consider that the exact 1D excess free energy density $\Phi_{1\text{D}}$ is a function of the 1D weighted densities n_0 and n_1, which can be identified from the low-density limit of $\Phi_{1\text{D}}$. We can, however, not expect that the assumption $\Phi_{3\text{D}} = \Phi_{3\text{D}}(\{n_\alpha\})$ is valid in 3D as it is in 1D and it can be shown that the assumption is in fact incorrect. It seems nevertheless worthwhile to construct an *approximation* for $\Phi_{3\text{D}}$ as a function of the weighted densities. Indeed, it turns out that using a suitable extrapolation of the low-density expression towards higher densities, an approximative $\Phi_{3\text{D}}$ can be constructed as a function of the weighted densities such that the hard-sphere fluid is well described even in the high-density regime, i.e. at packing fractions as large as 49% above which the one-component hard-sphere system starts to crystallize. For the fcc hard-sphere crystal the functional, which we derive in the following, fails. A functional which is suitable to describe the high-density phase shall be discussed in the context of the general hard-body fluid (see Chapter 4) in which other "building blocks" in addition to the present weighted densities can be identified.

The extrapolation of the exact low-density limit $\Phi_{3\text{D}} \to n_0n_3 + n_1n_2 - \overrightarrow{n}_1\overrightarrow{n}_2$ to higher densities goes as follows. We consider the case of a homogeneous hard-sphere mixture with constant density distributions $\rho_i(\mathbf{r}) \equiv \rho_i = N_i/V$. N_i is the number or spheres of species i in the volume V. The part of the pressure of a fluid mixture which arises from the interactions between the particles, i.e. the excess pressure p^{ex},

can be obtained from the excess free energy density Φ_{3D} via

$$\beta p^{\text{ex}} = -\frac{\partial(V\Phi_{3D})}{\partial V} = -\Phi_{3D} + \sum_{i=1}^{\nu} \frac{\partial \Phi_{3D}}{\partial \rho_i}\rho_i = -\Phi_{3D} + \sum_{\alpha} \frac{\partial \Phi_{3D}}{\partial n_\alpha} n_\alpha \,. \tag{3.9}$$

Note that the vectorial weighted densities actually vanish in the uniform fluid. Nonetheless, we formally include them in the above sum. The ideal gas contribution to the pressure is $\beta p^{\text{id}} = \sum_i \rho_i$, which in terms of the weighted densities reduces to $\beta p^{\text{id}} = n_0$. Hence, according to thermodynamics (TD), the total pressure within FMT can be written as

$$\beta p_{\text{TD}} = n_0 - \Phi_{3D} + \sum_{\alpha} \frac{\partial \Phi_{3D}}{\partial n_\alpha} n_\alpha \,. \tag{3.10}$$

This is the 3D analog of Eq. (2.47) for the pressure in the 1D system.

On the other hand, the pressure can be accessed using an exact result from scaled-particle theory [27, 28] for the excess chemical potential μ_i^{ex} of species i which equals the reversible work required for the creation of a cavity that is large enough so that it can hold a sphere of species i. For a very large sphere ($R_i \to \infty$) scaled-particle (SP) theory states that $\mu_i^{\text{ex}}/V_i \to p_{\text{SP}}$, where $V_i = \frac{4\pi}{3}R_i^3$ equals the volume of the large sphere. We denote the total pressure of the fluid mixture by p_{SP} in order to distinguish it from the pressure p_{TD} as obtained above from thermodynamic arguments. Assuming $\Phi_{3D} = \Phi_{3D}(\{n_\alpha\})$ and using that in the homogeneous bulk fluid the weighted densities reduce to

$$n_0 = \sum_{i=1}^{\nu} \rho_i \,, \quad n_1 = \sum_{i=1}^{\nu} \rho_i R_i \,, \quad n_2 = \sum_{i=1}^{\nu} \rho_i A_i \,, \quad n_3 = \sum_{i=1}^{\nu} \rho_i V_i \,, \quad \vec{n}_1 = \vec{n}_2 = 0 \,, \tag{3.11}$$

we find for the excess chemical potential

$$\beta\mu_i^{\text{ex}} = \frac{\partial \Phi_{3D}}{\partial \rho_i} = \frac{\partial \Phi_{3D}}{\partial n_3} V_i + \frac{\partial \Phi_{3D}}{\partial n_2} A_i + \frac{\partial \Phi_{3D}}{\partial n_1} R_i + \frac{\partial \Phi_{3D}}{\partial n_0} \,, \tag{3.12}$$

where we denote the surface area of the sphere i by $A_i = 4\pi R_i^2$. This result is the 3D analog of Eq. (2.49) for μ_i^{ex} of the hard sphere fluid in 1D. There, the leading term is $\frac{\partial \Phi_{1D}}{\partial n_1} 2R_i$ where $2R_i$ corresponds to the "volume" of a hard sphere in 1D, which can be viewed as a blocked interval of length $2R_i$ on a straight line. For the 3D system considered here, the relation $\lim_{R_i \to \infty} \mu_i^{\text{ex}}/V_i = p_{\text{SP}}$ allows us to identify p_{SP} from Eq. (3.12) which yields

$$\beta p_{\text{SP}} = \frac{\partial \Phi_{3D}}{\partial n_3} \,. \tag{3.13}$$

As both p_{TD} and p_{SP} were calculated from exact relations they have to be equal and therefore we obtain the following differential equation for Φ_{3D} by equating Eqs. (3.10)

and (3.13):

$$\frac{\partial \Phi_{3D}}{\partial n_3} = n_0 - \Phi_{3D} + \sum_\alpha \frac{\partial \Phi_{3D}}{\partial n_\alpha} n_\alpha \tag{3.14}$$

Rosenfeld introduced this differential equation [22] and he obtained a solution $\Phi_{3D} = \Phi_{RF}$ by using the ansatz

$$\Phi_{RF} = f_1(n_3)n_0 + f_2(n_3)n_1 n_2 + f_3(n_3)\,\vec{n}_1\,\vec{n}_2 + f_4(n_3)n_2^3 + f_5(n_3)n_2\,\vec{n}_2\,\vec{n}_2\,, \tag{3.15}$$

with $f_1, \ldots, f_5$ being functions of the dimensionless weighted density n_3. The ansatz Eq. (3.15) makes a linear combination of all products of the weighted densities which share the dimension of Φ_{3D}, i.e. $(\text{length})^{-3}$. From the definitions of the weighted densities it can be easily shown that the dimension of n_α is $(\text{length})^{\alpha-3}$.

Plugging the ansatz Eq. (3.15) into Eq. (3.14) leads to a set of decoupled differential equations for the functions $f_1, \ldots, f_5$ which can be easily solved. The integration constants of f_1, f_2, and f_3 can be fixed by matching Φ_{RF} with the low-density limit $\Phi_{RF} \to n_0 n_3 + n_1 n_2 - \vec{n}_1\,\vec{n}_2$. The integration constant of f_4 is determined by the requirement that for the one-component uniform hard-sphere fluid the correct third virial coefficient, which is known analytically [45], is reproduced. Finally, the integration constant of f_5 is enforced by the requirement that the pair direct correlation function $c^{(2)}(r)$ is regular in the limit $r \to 0$ (for a related calculation of $c^{(2)}(r)$ see Ref. [25]). The result is

$$\Phi_{RF} = -n_0 \ln(1 - n_3) + \frac{n_1 n_2 - \vec{n}_1\,\vec{n}_2}{1 - n_3} + \frac{n_2^3 - 3n_2\,\vec{n}_2\,\vec{n}_2}{24\pi(1 - n_3)^2}\,. \tag{3.16}$$

Based on a derivation which makes use of a minimal number of prerequisites, Rosenfeld's excess free energy density Φ_{RF} gives a remarkably good account of many aspects of nonuniform hard-sphere fluids, pure [67, 68] or mixtures [69]. However, it does not predict freezing, which is actually observed for the pure hard-sphere fluid at a packing fraction $\eta \simeq 0.494$ [74]. This deficiency can be resolved empirically by modifying the third term in Eq. (3.16) [75, 76], or, more systematically, by the approach of Tarazona [77] who introduced an additional tensorial weighted density in the last term of Φ_{RF}. As we have mentioned earlier in this section, the latter modification will be discussed in Chapter 4 in the context of the general hard-body fluid. Another interesting property of Φ_{RF} is that it yields the PY direct pair correlation function (cf. Ref. [22]) although the derivation of Φ_{RF} does not make use of *any* of the PY "ingredients" (i.e. the Ornstein-Zernike relation supplemented with the PY closure [45]). The equation of state which follows from Φ_{RF} can be obtained using Eq. (3.10) or, equivalently, Eq. (3.13). Taking into account the fact that the vectorial

weighted densities vanish in the bulk fluid, one finds the pressure to be

$$\beta p_{\mathrm{PY}} = \frac{n_0}{1-n_3} + \frac{n_1 n_2}{(1-n_3)^2} + \frac{n_2^3}{12\pi(1-n_3)^3}\,, \tag{3.17}$$

which is the compressibility expression from the solution of the PY integral equation [73]. The PY pressure is in good agreement with simulations for the pure hard-sphere fluid at low packing fractions but close to the freezing transition it overestimates the pressure by about 7%. More accurate and yet simple equations of state for the hard-sphere mixture are available and can be incorporated within the context of FMT. In the next section we present a systematic derivation of several such equations of state one of which has not appeared in the previous literature to our knowledge. The new equation of state will be shown to improve upon previous ones by comparison with simulation data. In Section 3.3, which concludes this chapter, we will formulate an improved FMT free energy density which is based on the new equation of state.

3.2 Improved equation of state for the hard-sphere mixture

Let us examine the PY compressibility equation of state [Eq. (3.17)] for the case of a single component hard-sphere fluid. The weighted densities are then given by Eq. (3.11) with the additional simplification that $\nu = 1$. Denoting the hard-sphere packing fraction and number density by η and ρ, respectively, and using that $n_3 = \eta$, Eq. (3.17) takes the simple form

$$\frac{\beta p_{\mathrm{PY}}}{\rho} = \frac{1+\eta+\eta^2}{(1-\eta)^3}\,. \tag{3.18}$$

The PY equation of state, albeit very simple, is in good agreement with the outcome from simulation data for the hard-sphere fluid at moderate packing fractions. We have, however, already mentioned that with increasing packing fraction the PY equation of state starts to deviate significantly from simulation data such that the use of a more accurate expression is in order. In principle, such an expression can be obtained by some intelligent fitting to the numerical data and this has indeed been widely done (for an example of related work which includes binary mixtures see Ref. [78]). However, these approaches have several drawbacks. In the first place, the resulting equations of state are rather cumbersome and involve extended sets of numerical prefactors which makes them unsuitable for many analytical calculations. Perhaps more importantly, the numerical fits are limited to mixtures with only very few components of not too different sizes while for many application purposes, in

particular experiments, polydispersity and strong size asymmetry have to be tackled. A very successful equation of state for the single component hard-sphere fluid which is both simple and accurate has been suggested empirically by Carnahan and Starling (CS) [79]. Their expression cures the overestimation of the pressure by the PY equation of state with a small but efficient modification. The CS equation of state reads

$$\frac{\beta p_{\mathrm{CS}}}{\rho} = \frac{1+\eta+\eta^2-\eta^3}{(1-\eta)^3}\,. \tag{3.19}$$

The question remains, however, how this equation, which has proved very useful for the one-component fluid, can be generalized to arbitrary mixtures of hard spheres *without* making use of fitting to numerical data. Our answer to this question is based on using the requirement of consistency between the two routes to the pressure presented in the previous Section 3.1. By equating p_{TD}, which was obtained by considerations based on thermodynamics, and p_{SP}, which followed from an exact relation from scaled-particle theory, we have shown that the PY pressure p_{PY} is the only mixture equation of state which guarantees full consistency of the two routes. The deviation of p_{PY} from simulation data is thus due to the fact that we have limited ourselves to the set of the weighted densities $n_0,\ldots,n_3$ (neglecting the vectorial weighted densities which do not contribute in the bulk fluid) as variables of the excess free energy density Φ_{3D}. With the "complete" (but unknown) set of variables, the requirement $p_{\mathrm{TD}} = p_{\mathrm{SP}}$ would lead to the exact equation of state. Having only the variables $n_0,\ldots,n_3$ at hand, we can never reach perfect consistency between p_{TD} and p_{SP} for any equation of state other than p_{PY}. Therefore, we shall base our following calculations, in which we seek to generalize p_{CS} to mixtures, on the requirement of *maximizing* consistency between the two results for the pressure under the constraint that p_{CS} is recovered in the case of a pure (i.e. one-component) fluid. It will turn out that demanding consistency up to different orders in the particle density yields different mixture equations of state, the quality of which increases with increasing consistency.

Considering that for the fluid mixture the weighted density n_3 plays the role of the total packing fraction (which is denoted η for the pure fluid) it is instructive to bring Eq. (3.17) to a common denominator such that it can be compared with Eq. (3.19). The PY equation of state then reads

$$\beta p_{\mathrm{PY}} = \frac{n_0 + n_1 n_2 + \frac{1}{12\pi} n_2^3 - (2n_0 + n_1 n_2) n_3 + n_0 n_3^2}{(1-n_3)^3}\,. \tag{3.20}$$

In order to make the analogy with Eq. (3.19) clearer, it should be kept in mind that the weighted density n_0 in the mixture corresponds to the particle density ρ of the

pure fluid. This explains why the numerator in Eq. (3.19) starts with 1 while it starts with n_0 in Eq. (3.20) (note that Eq. (3.19) has been divided by ρ).

The key idea of our derivation is to consider the numerator of Eq. (3.20) as the starting point for a systematic expansion in powers of n_3 (which is the sole dimensionless weighted density) with coefficients that are linear combinations of n_0, $n_1 n_2$ and n_2^3 (which have the dimension of βp). For the purpose of our derivation, the expansion is pursued up to third order, i.e. as the most general ansatz for the mixture equation of state we use

$$\beta p_{\mathrm{TD}}^{(3)} = \Big\{ n_0 + n_1 n_2 + \tfrac{1}{12\pi} n_2^3 - \left(2n_0 + n_1 n_2 + c_1 n_2^3\right) n_3 + \left(n_0 + b_2 n_1 n_2 + c_2 n_2^3\right) n_3^2 + \left(a_3 n_0 + b_3 n_1 n_2 + c_3 n_2^3\right) n_3^3 \Big\} \Big/ (1-n_3)^3 \,. \tag{3.21}$$

In order to simplify the following expressions, we make two preliminary remarks on the coefficients. Since $p_{\mathrm{TD}}^{(3)}$ is intended to be a generalization to mixtures of the CS equation of state, Eq. (3.19), we require that it reduces to p_{CS} in the case of a one-component fluid. This condition implies immediately that $c_3 = 0$ as the corresponding term is $\propto \rho^6$, whereas the highest power in the numerator of p_{CS} is $\propto \rho^4$. It also follows that $b_3 = -12\pi c_2$ in order to assure that the terms $\propto \rho^5$ in the numerator of $p_{\mathrm{TD}}^{(3)}$ compensate.

For additional conditions on the unknown constants in Eq. (3.21) we now turn to the excess free energy density $\Phi^{(3)}$ which corresponds to $p_{\mathrm{TD}}^{(3)}$ by solving the differential equation (3.10) (omitting the vectorial weighted densities) with $p_{\mathrm{TD}} \doteq p_{\mathrm{TD}}^{(3)}$. Again, the solution is obtained using the ansatz $\Phi^{(3)} = f_1(n_3) n_0 + f_2(n_3) n_1 n_2 + f_4(n_3) n_2^3$ and choosing integration constants such that the additional part to Φ_{RF} is at least of forth order in the densities ρ_i as $\rho_i \to 0$. This assures that the low-density behavior of Φ_{RF}, which for the pure fluid is exact up to third order in the density, is not affected. We obtain

$$\Phi^{(3)} = \Phi_{\mathrm{RF}} + \phi_4(n_3) \left(-c_1 n_2^3 n_3 + b_2 n_1 n_2 n_3^2 + a_3 n_0 n_3^3\right) + \phi_5(n_3) c_2 \left(n_2^3 n_3^2 - 12\pi n_1 n_2 n_3^3\right) \tag{3.22}$$

where

$$\phi_4(n_3) = \frac{\frac{3}{2} n_3^2 - n_3 - (1-n_3)^2 \ln(1-n_3)}{n_3^3 (1-n_3)^2} = \frac{1}{3} + \frac{3}{4} n_3 + \mathcal{O}(n_3^2) \tag{3.23}$$

and

$$\phi_5(n_3) = \frac{\frac{9}{2} n_3^2 - n_3^3 - 3n_3 - 3(1-n_3)^2 \ln(1-n_3)}{n_3^4 (1-n_3)^2} = \frac{1}{4} + \frac{3}{5} n_3 + \mathcal{O}(n_3^2) \,. \tag{3.24}$$

In the following, we will examine the consistency of $\Phi^{(3)}$ with the scaled-particle theory relation for the pressure p_{SP} [Eq. (3.13)] while pursuing the n_3-expansion of the numerator of Eq. (3.21) to increasing orders.

First order n_3-expansion

In the case of a first order expansion in n_3, the pressure $p_{\rm TD}^{(1)}$ and the excess free energy density $\Phi^{(1)}$ are obtained from the general expressions, Eqs. (3.21) and (3.22), by setting $b_2 = c_2 = a_3 = b_3 = c_3 = 0$. The remaining free parameter c_1 can be determined from the condition that $p_{\rm TD}^{(1)}$ has to reduce to $p_{\rm CS}$ for the one-component fluid. We find $c_1 = 1/(36\pi)$. The resulting expression for $p_{\rm TD}^{(1)}$ is precisely the Boublík-Mansoori-Carnahan-Starling-Leland (BMCSL) equation of state [80, 81]

$$\beta p_{\rm TD}^{(1)} = \beta p_{\rm PY} - \frac{n_2^3 n_3}{36\pi(1-n_3)^3} \equiv \beta p_{\rm BMCSL}\,. \tag{3.25}$$

It is interesting to note that $p_{\rm BMCSL}$, which originally was obtained from an empirical mixing of two thirds of the PY compressibility equation of state with one third of the PY virial pressure, can also be derived within the present framework although the latter does not require the analytical solution of the PY integral equation for the hard-sphere fluid as an input.

The degree of consistency of the scaled-particle theory relation Eq. (3.13) with the pressure $p_{\rm TD}^{(1)}$ can be inferred by expanding $p_{\rm TD}^{(1)}$ and $p_{\rm SP}^{(1)} = \beta^{-1}\partial\Phi^{(1)}/\partial n_3$, as they figure for the one-component fluid, in powers of $\eta = n_3$:

$$\frac{\beta p_{\rm TD}^{(1)}}{\rho} = 1 + 4\eta + 10\eta^2 + 18\eta^3 + 28\eta^4 + 40\eta^5 + 54\eta^6 + \cdots \tag{3.26}$$

$$\frac{\beta p_{\rm SP}^{(1)}}{\rho} = 1 + 4\eta + 9.67\eta^2 + 17.50\eta^3 + 27.40\eta^4 + 39.33\eta^5 + 53.29\eta^6 + \cdots . \tag{3.27}$$

Second order n_3-expansion

The pressure $p_{\rm TD}^{(2)}$ and the excess free energy density $\Phi^{(2)}$ in the second order expansion in n_3 can be obtained from Eqs. (3.21) and (3.22) by setting the constants $a_3 = b_3 = c_3 = 0$. In order to assure that $p_{\rm TD}^{(2)}$ reduces to the CS pressure for the pure fluid there are constraints on c_1, c_2 and b_2. First, c_2 has to vanish since the corresponding term is the only term $\propto \rho^5$ and therefore cannot be compensated (note that in the numerator of $p_{\rm CS}$ [cf. Eq. (3.19)] the density occurs only up to order four). In addition, c_1 and b_2 must obey the relation $36\pi c_1 - 3b_2 = 1$. The remaining degree of freedom can be used in order to increase the degree of consistency between $p_{\rm TD}^{(2)}$ from Eq. (3.21) and $p_{\rm SP}^{(2)}$ from Eq. (3.13). By evaluating $p_{\rm SP}^{(2)}$ for the one-component fluid we obtain

$$\frac{\beta p_{\rm SP}^{(2)}}{\rho} = \frac{1}{\rho}\frac{\partial\Phi^{(2)}}{\partial n_3} = 1 + 4\eta + \left(10 + 2b_2 - 12\pi c_1\right)\eta^2 + \left(19 + \tfrac{27}{4}b_2 - 54\pi c_1\right)\eta^3 + \cdots , \tag{3.28}$$

which results in a second relation between c_1 and b_2, namely $b_2 - 6\pi c_1 = 0$, in order to enforce consistency of $p_{\rm SP}^{(2)}$ with $p_{\rm TD}^{(2)}$ up to the quadratic η term (the coefficient of which must amount to 10). Both conditions on c_1 and b_2 are satisfied by setting $c_1 = 1/(18\pi)$ and $b_2 = 1/3$. Interestingly, the resulting equation of state is the so-called extended CS (eCS) equation of state

$$\beta p^{(2)} = \beta p_{\rm PY} - \frac{n_2^3 n_3}{18\pi(1-n_3)^3} + \frac{n_1 n_2 n_3^2}{3(1-n_3)^3} \equiv \beta p_{\rm eCS}, \tag{3.29}$$

which has been introduced by Santos *et al.* [82] and which was found to be slightly more accurate, when compared to data from computer simulations, than the BMCSL equation of state. The eCS equation of state was obtained by the use of an extrapolation formula for the contact value of the radial distribution function of the one-component fluid towards mixtures. From this formula for the contact values, which was inspired by the analytic solution of the PY equation, a corresponding equation of state can be derived. When substantiated with the CS result for the one-component fluid the method outputs the eCS equation of state. It is striking to see that our present approach is able to yield within a unifying framework the BMCSL and the eCS equation of state, which where derived previously by obviously different techniques.

For the above choice of parameters, consistency of $p_{\rm TD}^{(2)}$ and $p_{\rm SP}^{(2)}$ up to the term $\propto \eta^2$ in the case of the one-component fluid can be seen from the expansions

$$\frac{\beta p_{\rm TD}^{(2)}}{\rho} = 1 + 4\eta + 10\eta^2 + 18\eta^3 + 28\eta^4 + 40\eta^5 + 54\eta^6 + \cdots \tag{3.30}$$

$$\frac{\beta p_{\rm SP}^{(2)}}{\rho} = 1 + 4\eta + 10\eta^2 + 18.25\eta^3 + 28.60\eta^4 + 41.00\eta^5 + 55.43\eta^6 + \cdots . \tag{3.31}$$

Third order n_3-expansion

The third order expansion in n_3 for the pressure $p_{\rm TD}^{(3)}$ and the excess free energy density $\Phi^{(3)}$ are given by Eqs. (3.21) and (3.22) with $c_3 = 0$ and $b_3 = -12\pi c_2$. In addition, $a_3 = 36\pi c_1 - 3b_2 - 1$ is required in order to ensure that $p_{\rm TD}^{(3)} = p_{\rm CS}$ for the one-component fluid. It turns out that for $b_2 = 24\pi c_1 - 1$ and $c_2 = 1/(36\pi)$ the description of the one-component fluid (ocf) through the equation of state $p_{\rm TD}^{(3)}$ [Eq. (3.21)] is fully consistent with the scaled-particle theory relation [Eq. (3.13)], i.e. we have

$$\left(p_{\rm TD}^{(3)}\right)_{\rm ocf} = \left(p_{\rm SP}^{(3)}\right)_{\rm ocf} \quad \text{with} \quad \beta p_{\rm SP}^{(3)} = \frac{\partial \Phi^{(3)}}{\partial n_3}\,. \tag{3.32}$$

Note, however, that the equality does not hold for mixtures, i.e. in terms of the weighted densities $n_0, \ldots, n_3$.

One of the parameters c_1, b_2 and a_3 can still be chosen freely. It seems natural to attempt to extend the requirement of consistency between $p_{\mathrm{TD}}^{(3)}$ and $p_{\mathrm{SP}}^{(3)}$ to binary mixtures in a first step. However, the virial expansions of $p_{\mathrm{TD}}^{(3)}$ and $p_{\mathrm{SP}}^{(3)}$ show that there is no suitable choice of the parameters which could increase the degree of consistency for the binary mixture. On the other hand, a_3 can be chosen such that the exact low-density result for the surface tension [83] is reproduced (see also the section below where we compare the equations of state with simulation data). The corresponding equation of state, however, performs worse than the BMCSL and eCS equations of state. Therefore, we set $a_3 = 0$ for the simplicity of the resulting equation of state and find our choice justified *a posteriori* by the agreement with simulation data. An additional argument for choosing $a_3 = 0$ can be provided by considering the FMT density functional which implements $p_{\mathrm{TD}}^{(3)}$ (see Section 3.3) in the limit of a zero dimensional cavity (cf. Ref. [84]). It can be shown that $a_3 = 0$ guarantees that in the zero dimensional limit the exact free energy is recovered. The whole set of parameters then reads: $c_1 = 1/(18\pi)$, $b_2 = 1/3$, $c_2 = 1/(36\pi)$, $a_3 = 0$, $b_3 = -1/3$ and $c_3 = 0$. Accordingly, the pressure arising from the third order expansion is related to the eCS formula by

$$\beta p_{\mathrm{TD}}^{(3)} = \beta p_{\mathrm{eCS}} + \frac{n_2^3 n_3^2}{36\pi(1-n_3)^3} - \frac{n_1 n_2 n_3^3}{3(1-n_3)^3}\,, \tag{3.33}$$

and can be written in a simple compact form:

$$\beta p_{\mathrm{TD}}^{(3)} = \frac{n_0}{1-n_3} + \frac{n_1 n_2\left(1+\frac{1}{3}n_3^2\right)}{(1-n_3)^2} + \frac{n_2^3\left(1-\frac{2}{3}n_3+\frac{1}{3}n_3^2\right)}{12\pi(1-n_3)^3}. \tag{3.34}$$

Comparison with simulation data

In Table 3.1 we compare the compressibility $z = \beta p/\rho$ of binary hard-sphere mixtures obtained by computer simulations to those calculated from p_{BMCSL}, p_{eCS} and the new equation of state $p_{\mathrm{TD}}^{(3)}$. First we note that the BMCSL equation of state has a general tendency to slightly underestimate the pressure. At closer examination, the eCS equation of state tends to systematically overestimate the pressure slightly. This becomes most visible in the data for $\eta = 0.45$ or $\eta = 0.49$. While it is fair to say that all three equations are in good agreement with the simulations for binary mixtures, we find that the pressure $p_{\mathrm{TD}}^{(3)}$ derived in this work is always between p_{BMCSL} and p_{eCS} and describes the numerical data most reliably. This is substantiated by the fact that the deviation of $z_{\mathrm{TD}}^{(3)}$ from the simulation data is always below five times the error of the simulation data whereas z_{BMCSL} and z_{eCS} deviate by about ten times the numerical error for several data points.

The small systematic deviations of p_{BMCSL} and p_{eCS} which show up for the binary mixtures are more pronounced in the case of ternary mixtures [87]. This led the

Table 3.1: Compressibility $z = \beta p/\rho$ for binary hard-sphere mixtures from simulations and the deviations of $\beta p_{\mathrm{BMSCL}}/\rho$, $\beta p_{\mathrm{eCS}}/\rho$ and $\beta p^{(3)}_{\mathrm{TD}}/\rho$ from the simulation data. The data for radii $R_2/R_1 = 0.3$ are taken from Ref. [85] and for $R_2/R_1 = \frac{1}{3}$ and $R_2/R_1 = 0.5$ from Ref. [86]. The number densities of the components are $\rho_1 = x_1\rho$ and $\rho_2 = (1 - x_1)\rho$. η is the total packing fraction. The connection to the weighted densities is established via the relations $\rho = n_0$ and $\eta = n_3$.

x_1	η	z	$\Delta z_{\mathrm{BMCSL}}$	Δz_{eCS}	$\Delta z^{(3)}_{\mathrm{TD}}$
$R_2/R_1 = 0.3$					
0.0625	0.40	4.410 ± 0.003	-0.035	0.013	-0.006
	0.45	5.722 ± 0.005	-0.063	0.027	-0.013
	0.49	7.158 ± 0.007	-0.081	0.065	-0.007
0.125	0.40	4.204 ± 0.003	-0.029	0.015	-0.003
	0.45	5.421 ± 0.004	-0.044	0.038	0.001
	0.49	6.773 ± 0.006	-0.070	0.061	-0.003
0.25	0.40	4.396 ± 0.003	-0.025	0.010	-0.004
	0.45	5.704 ± 0.004	-0.035	0.030	0.001
	0.49	7.160 ± 0.005	-0.054	0.052	0.000
0.50	0.40	5.176 ± 0.003	-0.027	-0.005	-0.014
	0.45	6.831 ± 0.003	-0.029	0.013	-0.006
	0.49	8.691 ± 0.004	-0.042	0.025	-0.008
0.75	0.40	6.045 ± 0.003	-0.021	-0.010	-0.014
	0.45	8.097 ± 0.003	-0.022	-0.002	-0.011
	0.49	10.415 ± 0.006	-0.037	-0.004	-0.021
$R_2/R_1 = \frac{1}{3}$					
0.25	0.35	3.613 ± 0.002	-0.016	0.003	-0.004
	0.40	4.615 ± 0.002	-0.024	0.012	-0.003
	0.45	6.006 ± 0.004	-0.020	0.045	0.016
0.50	0.35	4.083 ± 0.002	-0.016	-0.004	-0.008
	0.40	5.294 ± 0.002	-0.018	0.005	-0.005
	0.45	6.994 ± 0.004	-0.009	0.033	0.014
0.75	0.35	4.638 ± 0.002	-0.013	-0.007	-0.009
	0.40	6.099 ± 0.003	-0.015	-0.004	-0.008
	0.45	8.159 ± 0.005	0.002	0.023	0.013
$R_2/R_1 = 0.5$					
0.25	0.35	4.370 ± 0.002	-0.017	-0.003	-0.008
	0.40	5.702 ± 0.003	-0.019	0.007	-0.004
	0.45	7.590 ± 0.004	-0.022	0.025	0.004
0.50	0.35	4.536 ± 0.002	-0.014	-0.005	-0.008
	0.40	5.957 ± 0.005	-0.027	-0.008	-0.016
	0.45	7.942 ± 0.004	-0.010	0.024	0.009
0.75	0.35	4.852 ± 0.002	-0.013	-0.008	-0.010
	0.40	6.409 ± 0.003	-0.016	-0.007	-0.011
	0.45	8.623 ± 0.005	-0.016	0.001	-0.007

Table 3.2: The excess chemical potentials $\mu_i^{\rm ex}$ of small, medium and large spheres in ternary hard-sphere mixtures as obtained in simulations [87]. The deviations from the simulation data of the excess chemical potentials according to the BMCSL, eCS, and the new equation of state [Eq. (3.34)] are shown. The size ratios are $R_2/R_1 = 2$ and $R_3/R_1 = 3$. The following compositions are considered: (a) $x_1 = 0.70$, $x_2 = 0.20$, $x_3 = 0.10$; (b) $x_1 = 0.60$, $x_2 = 0.20$, $x_3 = 0.20$; (c) $x_1 = 0.85$, $x_2 = 0.05$, $x_3 = 0.10$.

Size	η	$\mu_i^{\rm ex}$	$\Delta\mu_{\rm BMCSL}^{\rm ex}$	$\Delta\mu_{\rm eCS}^{\rm ex}$	$\Delta\mu_{\rm TD}^{(3),\,\rm ex}$
Composition (a)					
small	0.40	2.86 ± 0.02	-0.02	0.00	-0.01
	0.45	3.68 ± 0.04	-0.02	0.01	0.00
	0.49	4.51 ± 0.05	-0.01	0.04	0.02
medium	0.40	9.52 ± 0.06	-0.05	0.01	-0.01
	0.45	12.87 ± 0.07	-0.07	0.04	-0.01
	0.49	16.48 ± 0.07	-0.07	0.10	0.01
large	0.40	22.88 ± 0.07	-0.11	0.08	0.01
	0.45	31.69 ± 0.03	-0.18	0.18	0.02
	0.49	41.44 ± 0.06	-0.25	0.34	0.05
Composition (b)					
small	0.40	2.36 ± 0.01	-0.01	0.01	0.00
	0.45	3.03 ± 0.01	-0.02	0.00	-0.01
	0.49	3.68 ± 0.03	-0.01	0.03	0.01
medium	0.40	7.26 ± 0.06	-0.02	0.01	0.00
	0.45	9.77 ± 0.04	-0.07	0.00	-0.03
	0.49	12.41 ± 0.06	-0.06	0.04	-0.01
large	0.40	16.80 ± 0.03	-0.08	0.03	-0.01
	0.45	23.13 ± 0.05	-0.14	0.07	-0.03
	0.49	30.05 ± 0.07	-0.16	0.17	0.01
Composition (c)					
small	0.40	3.05 ± 0.03	-0.02	0.01	0.00
	0.45	3.95 ± 0.05	-0.03	0.01	-0.01
	0.49	4.84 ± 0.04	-0.02	0.04	0.02
medium	0.40	10.54 ± 0.06	-0.05	0.03	0.00
	0.45	14.26 ± 0.07	-0.09	0.07	0.00
	0.49	18.26 ± 0.07	-0.10	0.15	0.03
large	0.40	25.81 ± 0.03	-0.15	0.14	0.02
	0.45	35.67 ± 0.08	-0.23	0.31	0.07
	0.49	46.58 ± 0.07	-0.32	0.54	0.12

authors of Ref. [87] to speculate that an arithmetic average of the BMCSL and eCS equations of state would lead to improved results. The interpolation between BMCSL and eCS pressures is realized by the equation of state $p_{\mathrm{TD}}^{(3)}$ through physically motivated concepts, rather than just by an empirical fitting to numerical data. In Table 3.2 we show simulation data for the excess chemical potentials μ_i^{ex} with $i = s, m, l$ for the small, medium, and large spheres in ternary mixtures together with the deviations of the chemical potentials as obtained from the three equations of state according to Eq. (3.12). The quality of the new equation of state $p_{\mathrm{TD}}^{(3)}$, Eq. (3.34), is clearly visible from the excellent agreement with the numerical data. Except for one data point, the deviation is always within the statistical error while the pressures p_{BMCSL} and p_{eCS} are systematically in error.

After the comparison with simulation data concerning the homogeneous bulk fluid (pressure, excess chemical potential) we now turn to properties of the one-component bulk fluid in the presence of an inhomogeneity which is caused by the presence of a planar hard wall. Thermodynamic quantities which are of interest in this setup are the *wall-fluid surface tension* and the *excess adsorption*. The surface tension can be calculated following Ref. [88]. The authors consider a homogeneous hard-sphere fluid into which a single big hard sphere of radius R_b is inserted. The change in grand potential due to the insertion of the big sphere is described by its excess chemical potential. Considering Eq. (3.12) in the limit of $R_b \to \infty$ it becomes clear that in addition to the expression from scaled-particle theory, Eq. (3.13), which identifies the pressure with $\partial\Phi_{\mathrm{3D}}/\partial n_3$, it is also possible to give a physical meaning to the derivative of the excess free energy density Φ_{3D} with respect to the weighted density n_2. One finds that [88]

$$\beta\sigma_w = \frac{\partial\Phi_{\mathrm{3D}}}{\partial n_2}, \tag{3.35}$$

is the wall-fluid surface tension of a hard-sphere fluid at a planar hard wall. Note that the value of the wall-fluid surface tension depends on the definition of the dividing interface. By construction, Eq. (3.35) chooses the dividing interface to be the physical wall, which is the reason for choosing the index w. In order to be able to compare this prediction to other results, it is useful to also specify the surface tension σ with respect to the dividing surface which limits the space which is accessible to the centers of the hard spheres. This surface lies parallel to the physical wall at a distance R (hard-sphere radius) and hence it follows from the definition of σ (for details see Section 5.1) that

$$\beta\sigma = \frac{\partial\Phi_{\mathrm{3D}}}{\partial n_2} - R\frac{\partial\Phi_{\mathrm{3D}}}{\partial n_3}\,. \tag{3.36}$$

From the different approximations of the excess free energy density $\Phi_{\mathrm{3D}} = \Phi^{(i)}$,

$i = 1, \ldots, 3$, considered above, we can calculate the corresponding approximations for the wall-fluid surface tension, which we denote by $\sigma^{(1)}$, $\sigma^{(2)}$ and $\sigma^{(3)}$. To be concise, we give the explicit expression only for $\sigma^{(3)}$:

$$\frac{\beta\sigma^{(3)}}{R\rho} = -\frac{1 + 2\eta + 8\eta^2 - 5\eta^3}{3(1-\eta)^3} - \frac{\ln(1-\eta)}{3\,\eta}\,. \tag{3.37}$$

Here ρ and η are the hard-sphere fluid particle number density and packing fraction, respectively. For the surface tension of the hard-sphere fluid there exists an empirical expression,

$$\frac{\beta\sigma_{\mathrm{HP}}}{R\rho} = -\frac{3}{2}\,\eta\,\frac{1 + \frac{44}{35}\eta - \frac{4}{5}\eta^2}{(1-\eta)^3}\,, \tag{3.38}$$

by Henderson and Plischke [89], which is often quoted as a quasi-exact description of the wall-fluid surface tension and which was obtained by fitting to data from molecular dynamics (MD) simulations [90]. In order to compare our result with σ_{HP} we consider the expansion

$$-\frac{2}{3}\frac{(1-\eta)^3}{\eta}\frac{\beta\sigma^{(3)}}{R\rho} = 1 + \frac{37}{27}\eta - \frac{19}{18}\eta^2 + \frac{1}{90}\eta^3 + \frac{1}{270}\eta^4 + \frac{1}{630}\eta^5 + \cdots\,. \tag{3.39}$$

The smallness of the contributions from third and higher order terms leads us to define the following approximation to $\sigma^{(3)}$:

$$\frac{\beta\tilde{\sigma}^{(3)}}{R\rho} = -\frac{3}{2}\,\eta\,\frac{1 + \frac{37}{27}\eta - \frac{19}{18}\eta^2}{(1-\eta)^3}\,, \tag{3.40}$$

which confirms the empirical *form* of the Henderson-Plischke surface tension although the numerical coefficients in σ_{HP} and $\tilde{\sigma}^{(3)}$ are clearly different. Note that the coefficient 44/35 in the Henderson-Plischke expression is imposed if one requires to recover the exact low-density limit [83]. This limit can also be achieved on the level of the third order n_3-expansion by choosing $a_3 = 107/70$ instead of $a_3 = 0$. This choice, however, would significantly worsen the equation of state $p_{\mathrm{TD}}^{(3)}$ as we checked by comparison with the pressure and excess chemical potential from simulations of the binary and ternary mixture.

An examination of the different expressions for σ, which we plot in Fig. 3.1, shows that $\sigma^{(3)}$ (and its approximation $\tilde{\sigma}^{(3)}$) deviate from σ_{HP} by at most 1%. For high values of η the relative deviation is even less than 0.5%. In contrast, the deviation of $\sigma^{(1)}$ and $\sigma^{(2)}$ from σ_{HP} grows with increasing packing fraction and reaches 4.75% and 2.75%, respectively, at $\eta = 0.494$. Actually, due to the scatter and error bars in the available MD [90][1] and Monte-Carlo (MC) [91] simulation data for the surface tension it is

[1]The error bars for the surface tension as given in Ref. [90] are too large by a factor of 3 (J.R. Henderson, *private communication*). We have corrected this error for the data shown in Fig. 3.1.

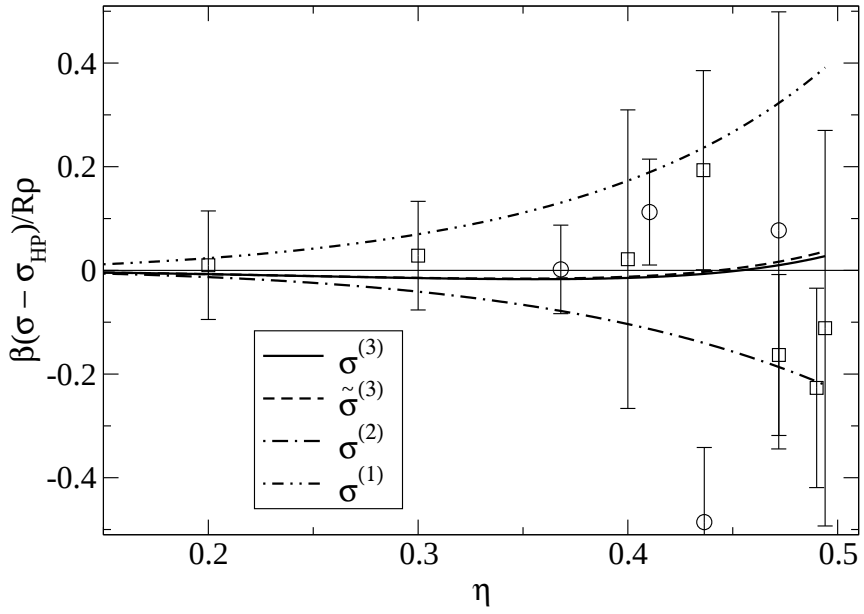

Figure 3.1: Absolute deviation of the various expressions for the wall-fluid surface tension σ from the empirical fit σ_{HP} by Henderson and Plischke [89] as a function of the hard-sphere packing fraction η. $\sigma^{(1)}$ and $\sigma^{(2)}$ are calculated from the BMCSL and eCS equations of state, $\sigma^{(3)}$ from the new equation of state [Eq. (3.34)]. Circles denote MD data from Ref. [90], while squares denote MC data from Ref. [91]. Using the CS equation of state, the MC data have been converted to the definition of the dividing interface as it is common in scaled-particle theory [92].

impossible to decide whether σ_{HP} or $\sigma^{(3)}$ is more accurate at high densities. In the low-density regime σ_{HP}, which is exact up to third order in η, yields a more accurate description than $\sigma^{(3)}$.

Another quantity studied in simulations is the excess adsorption Γ at a planar wall which is defined as the excess (over bulk) number of adsorbed particles per unit surface. It is calculated according to

$$\Gamma = \int_0^\infty \mathrm{d}z(\rho(z) - \rho_{\mathrm{b}})\,, \tag{3.41}$$

where $z = -R$ corresponds to the location of the physical wall, $\rho(z)$ is the equilibrium density profile, and ρ_{b} denotes the density in the bulk. In the case of a planar hard wall, Γ can be calculated from Gibbs' adsorption theorem:

$$\Gamma = -\left(\frac{\partial\sigma}{\partial\mu}\right)_{T,V}\,. \tag{3.42}$$

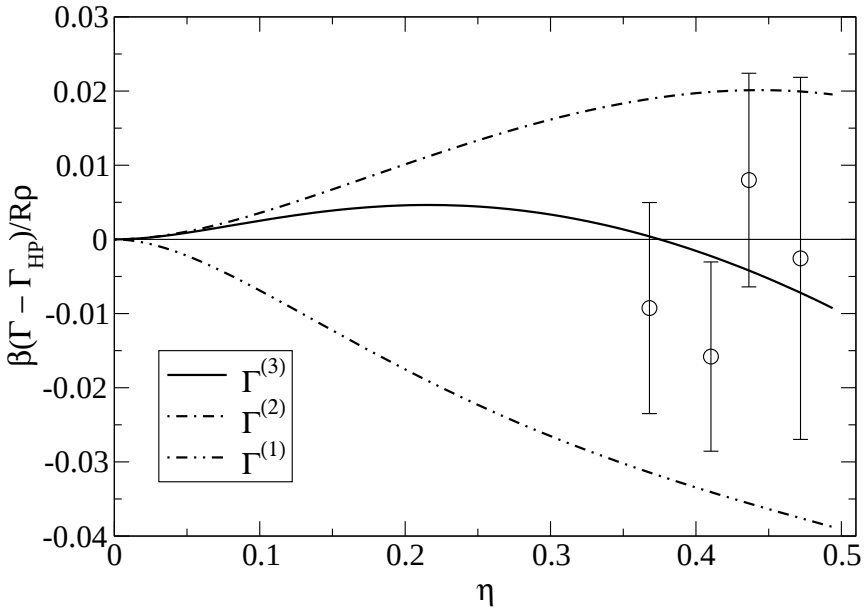

Figure 3.2: Absolute deviation for the planar wall excess adsorption Γ from the empirical result Γ_{HP} according to Ref. [89] as a function of the packing fraction η. $\Gamma^{(1)}$ and $\Gamma^{(2)}$ were obtained from the BMCSL and eCS equations of state, $\Gamma^{(3)}$ from the new equation of state [Eq. (3.34)]. The circles denote MD simulation data from Ref. [90].

In Fig. 3.2 we compare the results for Γ as obtained from the surface tensions $\sigma^{(1)}$, $\sigma^{(2)}$, and $\sigma^{(3)}$ with the result Γ_{HP}, calculated from the empirical σ_{HP}. Again, the comparison to MD simulation data [90] does not allow one to decide whether Γ_{HP} or $\Gamma^{(3)}$ is more accurate. The conclusion which can be drawn from the study of Γ is that both expressions are more accurate than $\Gamma^{(1)}$ and $\Gamma^{(2)}$. This can be stated since the error bars for Γ are smaller than the deviations between the various expressions which was not the case for the results for the surface tension σ considered in Fig. 3.1. For large packing fractions $\eta \lesssim 0.494$ the relative deviation from Γ_{HP} is about 5.0% for $\Gamma^{(1)}$, 2.5% for $\Gamma^{(2)}$ and 1.0% for $\Gamma^{(3)}$.

Summary

We have introduced an expansion of the equation of state for the hard-sphere mixture in powers of the total packing fraction n_3 with prefactors depending on the weighted densities n_0, n_1 and n_2 [see Eq. (3.11)]. We consider the first three orders of the expansion and determine the coefficients by maximizing the consistency of the respective equation of state with an exact relation from scaled-particle theory

[Eq. (3.13)]. Additionally, we require that the CS equation of state [Eq. (3.19)] is recovered in the limiting case of a one-component fluid. The first and second order results that follow unambiguously from the method turn out to be the BMCSL and eCS equations of state [Eqs. (3.25) and (3.29)] which are two results frequently used for the hard-sphere mixture which have the merit of being both simple and accurate. The third order expansion leads us to the definition of a new equation of state [Eq. (3.34)] which possesses the nice property of being fully consistent with scaled particle theory in the case of the one-component fluid. Moreover, we find by comparing with simulation data for binary and ternary mixtures that the new equation of state is more accurate than the BMCSL and eCS results.

Besides the equations of state, we have derived expressions for the bulk excess free energy density belonging to the different orders of the expansion. These lead to results for the wall-fluid surface tension and excess adsorption of a hard-sphere fluid at a planar hard wall which we compare to simulation data. We have shown that the quantities calculated from the new equation of state [Eq. (3.34)] are close to a previous empirical result [89] which is often quoted as quasi-exact. The available simulation data, however, do not allow to decide which of the two descriptions is more accurate.

In the next section we shall implement the new equation of state $p_{\mathrm{TD}}^{(3)}$ into the context of FMT for the inhomogeneous hard-sphere fluid the basics of which we have introduced in Section 3.1. As $p_{\mathrm{TD}}^{(3)}$ can be written as a function of the weighted densities $n_0, \ldots, n_3$ it is possible to follow the lines of Refs. [25] and [26] for the setup of a FMT based density functional. Moreover, the new excess free energy density $\Phi^{(3)}$ will prove useful for investigations within the context of morphological thermodynamics [93, 94] which we undertake in Chapter 5 where we use several quantities derived from $\Phi^{(3)}$ for the calculation of solvation free energies of a model protein.

3.3 Density functional based on the new equation of state

We have seen in Section 3.1 that FMT provides a context in which a free energy for the inhomogeneous hard-sphere fluid can be derived from a minimal number of prerequisites. These are (i) the exact low-density limit of the excess free energy from which upon close inspection the building blocks of the FMT, namely the weighted densities n_α [Eq. (3.8) with Eq. (3.5)], could be identified; (ii) the expression for the pressure p_{TD} [Eq. (3.10)] as it follows from thermodynamics assuming that the excess free energy density Φ_{3D} is a function only of the weighted densities; and (iii) an exact

relation for the pressure p_{SP} [Eq. (3.13)] from scaled-particle theory as it follows from considerations concerning the reversible work which is required in order to insert a large sphere into a given hard-sphere fluid mixture (composed of smaller spheres). We have shown that requiring p_{TD} and p_{SP} to be equal for all possible hard-sphere mixtures leads to the PY compressibility equation of state [73]. This finding, which goes back to the work of Rosenfeld [22, 66], is remarkable insofar as none of the PY results serves as an input for the derivation of the FMT free energy and no use of the PY integral equation is made. The PY equation of state, however, does not yield an accurate description of the fluid in the high density regime. This has motivated our efforts in generalizing the very accurate and nonetheless simple CS equation of state [Eq. (3.19)] to hard-sphere *mixtures*. Understandably, efforts have been undertaken in order to combine the merits of FMT, which provides the appropriate tools for the treatment of *inhomogeneous* hard-sphere fluids, with the high accuracy of CS-based mixture equations of state.

Some years ago, Roth *et al.* [25] and Yu and Wu [26] have incorporated the pressure p_{BMCSL} into FMT. They use the fact that p_{BMCSL} is a function of the weighted densities $n_0, \ldots, n_3$. This allows one to solve the differential equation for the excess free energy $\Phi_{\mathrm{3D}} = \Phi_{\mathrm{WB}}$ which is obtained by equating p_{BMCSL} and the thermodynamic expression p_{TD} as given in Eq. (3.10). Note that for the implementation of this approach a *bulk* fluid mixture is considered for which the vectorial weighted densities vanish. Hence, the solution of the resulting differential equation is obtained by using the dimensional ansatz Eq. (3.15) without the vectorial contributions. For this ansatz there is a unique solution if two additional requirements are made: (i) the result Φ_{WB} must be compatible with the low-density limit Eq. (3.7) and (ii) for the pure hard-sphere fluid the third virial coefficient must be recovered. Unlike in Rosenfeld's derivation of Φ_{RF} the vectorial contributions have to be incorporated at a later stage. In analogy to Φ_{RF} the substitutions $n_1 n_2 \to n_1 n_2 - \vec{n}_1 \vec{n}_2$ and $n_2^3 \to n_2^3 - 3 n_2 \vec{n}_2 \vec{n}_2$ are made in Φ_{WB}. The resulting functional Φ_{WB} is called the White-Bear version of FMT [25]. In virtue of these substitutions, Φ_{WB} has the correct low-density limit Eq. (3.7) and the regularity of the pair direct correlation function for $r \to 0$ is guaranteed.

The White-Bear version of FMT has been shown to inherit all the good properties of Rosenfeld's FMT for the description of the inhomogeneous hard-sphere fluid and to improve the predictions of thermodynamic quantities due to the more accurate underlying equation of state. This becomes particularly apparent in the contact densities at a hard wall which equal βp according to a sum rule (for a comparison with simulation data see, e.g., Ref. [95]). Moreover, one finds that the prediction of the

freezing transition of the pure hard-sphere system agrees very well with simulations [25]. A drawback of $\Phi_{\rm WB}$ is, however, that the scaled-particle relation Eq. (3.13) is violated, i.e. one finds that $\partial\Phi_{\rm WB}/\partial n_3 \neq p_{\rm BMCSL}$. This is of course not surprising as the equality $p_{\rm TD} = p_{\rm SP}$ unambiguously leads to Rosenfeld's expression $\Phi_{\rm RF}$, if we assume that the free energy density is a function only of the weighted densities $n_0, \ldots, n_3$, and $\overrightarrow{n}_1$ and $\overrightarrow{n}_2$. Despite this inconsistency of the White-Bear version, the quality of the resulting density distributions is high [96]. However, analytical results obtained from the free energy density $\Phi_{\rm WB}$ within the context of morphological thermodynamics are affected [97].

We conclude that there is some room for improvement with respect to the self-consistency of the free energy density. The basis for this improvement is the new equation of state $p_{\rm TD}^{(3)}$ [Eq. (3.34)] which we have derived in Section 3.2 and which, like the BMCSL equation of state, generalizes the CS pressure to hard-sphere mixtures. By following the recipe for the derivation of the original White-Bear version [25, 26], described above, we calculate a new functional based on the pressure $p_{\rm TD}^{(3)}$:

$$\begin{aligned}\Phi_{\rm WBII} &= -n_0\ln(1-n_3) + \left(1+\tfrac{1}{9}n_3^2\phi_2(n_3)\right)\frac{n_1n_2 - \overrightarrow{n}_1\overrightarrow{n}_2}{1-n_3} \\ &\quad + \left(1-\tfrac{4}{9}n_3\phi_3(n_3)\right)\frac{n_2^3 - 3n_2\overrightarrow{n}_2\overrightarrow{n}_2}{24\pi(1-n_3)^2}\end{aligned} \tag{3.43}$$

with

$$\begin{aligned}\phi_2(n_3) &= \left(6n_3 - 3n_3^2 + 6(1-n_3)\ln(1-n_3)\right)/n_3^3 = 1 + \tfrac{1}{2}n_3 + \mathcal{O}(n_3^2)\,, \\ \phi_3(n_3) &= \left(6n_3 - 9n_3^2 + 6n_3^3 + 6(1-n_3)^2\ln(1-n_3)\right)/(4n_3^3) = 1 - \tfrac{1}{8}n_3 + \mathcal{O}(n_3^2)\,.\end{aligned} \tag{3.44}$$

The new functional improves upon the White Bear version of FMT, as we shall show in Section 5.1 within the context of morphological thermodynamics. The index WBII is chosen to indicate that the new functional is Mark II of the White Bear functional. Note that in the bulk fluid, where the vectorial weighted densities vanish, $\Phi_{\rm WBII}$ reduces to $\Phi^{(3)}$ from Eq. (3.22) with the numerical coefficients which correspond to the pressure $p_{\rm TD}^{(3)}$.

For comparison we mention that in the above notation the original White-Bear functional $\Phi_{\rm WB}$ is recovered with $\phi_2^{\rm WB}(n_3) \equiv 0$ and

$$\phi_3^{\rm WB}(n_3) = \left(9n_3^2 - 6n_3 - 6(1-n_3)^2\ln(1-n_3)\right)/(4n_3^3) = \tfrac{1}{2} + \tfrac{1}{8}n_3 + \mathcal{O}(n_3^2)\,. \tag{3.45}$$

We have compared predictions of our new version of FMT with corresponding results obtained by the original White-Bear version for a pure hard-sphere fluid and a binary mixture close to a planar hard wall. We have found that the density distributions resulting from numerical minimization of the functional Eq. (2.26) with

Φ_{WB} or Φ_{WBII}, respectively, differ very little. For the pure hard-sphere fluid, this can be expected from the fact that the underlying bulk equation of state is then the same for both versions of FMT and hence the contact densities at the wall have to be identical. Comparison with density distributions from Monte-Carlo simulations revealed that the very small deviations of the DFT results from the simulation data are clearly more significant than the mutual deviations between the two FMT versions. We conclude that the limitations of FMT-based density functionals cannot be considerably pushed forward by increasing the quality of the underlying bulk equation of state but are rather determined by the structure of FMT itself, i.e. the set of weight functions which are employed and hence the restriction to one-center convolutions. For a discussion of the intrinsic limitations of FMT see Ref. [98]. A slight improvement through the WBII version is indeed found for the description of the pair direct correlation function as can be inferred from comparison with simulation data.

We shall see in Section 5.1 that one main benefit of the new functional Φ_{WBII} appears in the context of morphological thermodynamics. There, the self-consistency of Φ_{WBII} on the level of the pressure, i.e. the equality of p_{TD} from Eq. (3.10) and p_{SP} from Eq. (3.13) in the case of the pure fluid, is crucial for the accuracy of analytical expressions obtained within the morphological theory. In order to establish the link between FMT and morphological thermodynamics, which is based on Hadwiger's theorem from integral geometry [23], it is necessary to formulate FMT for fluids which are composed of hard particles of *arbitrary* shape. This task is the purpose of the following Chapter 4.

Chapter 4

General hard-body fluid

In view of our study of the solvation free energy of proteins, which we elaborate on in Chapter 5, we shall establish a connection between density functional theory (DFT) of classical fluids [19] and Hadwiger's theorem from integral geometry [23]. This will lead us to use the concept of morphological thermodynamics presented in Section 5.1 which allows for very efficient calculations of solvation free energies of complexly shaped solutes. However, concerning the required DFT background it turns out that the FMT for hard spheres, which we have presented and developed further in Chapter 3, is insufficient. Given that solutes with shapes different from the spherical one are ubiquitous in applications to biological systems there is a need to extend FMT to fluids which are composed of hard particles with *arbitrary* shape. In this chapter we present a FMT for fluids of non-spherical particles and improve the existing theory.

Besides the applications to biologically inspired problems, where the DFT describes the fluid on the molecular scale (i.e. the hard particles considered in FMT correspond to the solvent molecules), a more direct connection between the FMT and experimental realizations can be established for suspensions of colloidal particles. There, the colloidal particles (nano or micron sized) are represented by the hard FMT particles while the (molecular sized) particles of the solvent which contains the colloids are not taken into account explicitly and only act as a medium which enables the colloids to perform Brownian motion. Colloidal suspensions occur in many applications and have become an object of extensive theoretical and experimental studies [99, 100]. With the advance in particle synthesis non-spherical colloids can be designed, exposing degrees of complexity in shape which range from silica-coated boehmite rods [101] and gibbsite platelets [102] to conical, triangular, and diamond-like particles composed of polymerized polystyrene spheres [103]. These suspensions can display rich phase behavior including isotropic, nematic, and differ-

ent crystalline phases (see, e.g., Ref. [104] for phase diagrams of tobacco mosaic virus solutions). An even broader phenomenology can be observed in the case of mixtures of differently shaped colloidal particles (for experiments with rod-sphere mixtures see Refs. [105, 106]), as well as for rods interacting via polymer-induced attraction or for rods which dimerize (for theoretical and simulational studies of the latter examples see Refs. [107, 108]).

In many experimental realizations, however, it is possible to prepare the colloids in a way that their mutual interactions are essentially those of hard bodies [101, 102] such that these systems are entirely governed by entropy. The first study of entropic effects in systems of non-spherical colloidal particles was undertaken in 1949 by Onsager who derived the isotropic-nematic phase transition of hard spherocylinders (i.e. a hard cylinder being capped by two hard hemispheres) from the second order virial expansion of the excess (over ideal gas) free energy [109]. The theory is assumed to become exact in the so-called Onsager limit which corresponds to very long spherocylinders with a length-to-diameter ratio tending to infinity (for a comprehensive treatment of Onsager's virial theory see the review [110]). Using a decoupling approximation [111] in which higher order virial coefficients are approximated by recurring to a suitable reference system (here, the hard-sphere fluid) Onsager's theory has been modified by Parsons and Lee [112,113] such that it yields the accurate location of the isotropic-nematic transition also for short spherocylinders with length-to-diameter ratios ≈ 3 (see Ref. [114] for a comparison of Onsager, Parsons-Lee, and simulation results). For a description of the smectic and crystalline phases, however, as well as for other studies involving the inhomogeneous fluid, e.g., the isotropic-nematic interface or a nematic fluid anchoring to a surface, it becomes necessary to deal with particle density distributions which depend both on particle orientations *and* particle positions. For the description of these phases a treatment of inhomogeneous systems is required which can be tackled using DFT. The extention of Onsager's work to inhomogeneous fluids started in the late 1980's with the DFT proposed by Hołyst and Poniewierski [115] and a wealth of related DFTs which are also based on the Onsager limit with some generalized decoupling approximation have emerged subsequently. These early developments of DFT for general hard bodies have been review by Tarazona [116]. For a more recent DFT, a modified weighted-density approximation for hard spherocylinders, see Ref. [117]. While the early DFTs yield good results for the properties of inhomogeneous fluids of long rods [118] (as it is expected from the fact that Onsager theory is accurate then) they perform poorly for short spherocylinders or at least the interpolation between Onsager's limit and the underlying DFT for spherical particles is realized in a rather empirical and eclectic manner as often are

the DFTs for spherical particles of that time too.

A powerful DFT for the hard-sphere fluid became available with the FMT introduced by Rosenfeld in 1989 (see Ref. [22] and Chapter 3). Subsequently, Rosenfeld has generalized FMT for arbitrarily shaped hard bodies [29, 30]. However, this original non-spherical FMT (onFMT) has the drawback that it does not reproduce the correct second virial coefficient for the non-isotropic fluid. Even worse, it does *not* yield a stable nematic phase for a rod fluid. This failure has understandably triggered some effort during the last years which was devoted to the construction of modified FMTs being compatible with the Onsager limit while providing the virtues inherent to FMT for spheres. The collection of FMTs exhibiting the correct second order virial expansion (and hence the correct Mayer f-function) includes a FMT for mixtures of parallel hard cubes [119], a FMT for mixtures of colloidal spheres and infinitely thin needles [120, 121] and a FMT for the general hard-body fluid [114]. The latter is, however, not based on one-center convolutions for the weighted densities, which makes is computationally more demanding. Later, the work from Refs. [120, 121] was extended toward rods of finite thickness (adding one order to the expansion of the second virial coefficient in terms of the rod thickness) but at the expense of markedly increasing the total number of weighted densities [122]. Recently, FMTs involving thin hard platelets have been put forward (see Ref. [123] and references therein).

While in the above work generically new weight functions depending on the properties of *several* species (e.g. sphere and needle) are constructed from geometric arguments which apply only in certain limiting cases (e.g. vanishing thickness) in this chapter we devise an approach which sets out from the *exact* expression for the Mayer f-function of arbitrary hard bodies, formulated in terms of appropriate integrals extending over the surface of intersections of hard bodies. Using this expression, as in Rosenfeld's FMT [22], we construct a deconvolution of the Mayer f-function which becomes exact if an infinite number of (tensorial) one-center weight functions, depending each on the properties of only one species of the fluid components, is employed. The FMT which we suggest adds two tensorial weighted densities to those of onFMT [29, 30] one of which has already been used in the context of FMT for hard-sphere crystals [77] and a new one which is non-zero only for non-spherical particles. As a consequence, our theory reduces to the former FMTs for spheres [22, 77] while it cures one major defect of onFMT as it leads to a stable nematic phase.

This chapter starts with a presentation of Rosenfeld's onFMT (Section 4.1.1) which we keep rather short as onFMT is based on the notions which have been already introduced in Chapter 3 where we have discussed Rosenfeld's FMT for hard spheres. This is followed by the calculation of an appropriate expression of the Mayer

f-function which is based on the Gauss-Bonnet formula (Section 4.1.2) and which is deconvoluted using a suitable approximation (Section 4.1.3). In Section 4.1.4 the approximate deconvolution serves as a basis for the construction of a new excess free energy functional for the hard-body fluid which we refer to as extended-deconvolution FMT (edFMT). In this context we also make reference to the concept of multicavity expansions which allows us to establish the connection of the extended deconvolution with Tarazona's functional for the hard-sphere crystal [77]. The two following sections are devoted to applications of edFMT to the hard-spherocylinder fluid. In Section 4.2.1 we study the ability of edFMT to describe the isotropic-nematic transition. In Section 4.2.2 we test the onFMT and edFMT predictions for the density profiles of the isotropic hard-spherocylinder fluid in contact with a hard planar wall by comparison with data from Monte-Carlo simulations. Concluding remarks can be found in Section 4.3.

4.1 Derivation of the new density functional

4.1.1 Rosenfeld's fundamental measure theory

Rosenfeld's extention of FMT to arbitrarily shaped hard particles is based on the observation that the deconvolution Eq. (3.4) of the Mayer f-function for hard spheres is merely a special case of the Gauss-Bonnet theorem, which we shall introduce in Section 4.1.2. This alternative interpretation of the deconvolution allows for replacing the radius R_i appearing in some of the hard-sphere weight functions by the local mean and Gaussian curvatures which are also meaningful for non-spherical surfaces and reduce to $1/R_i$ and $1/R_i^2$, respectively, in the case of spheres. The description is completed by generalizing $\mathbf{r}/|\mathbf{r}|$ in the vectorial weight functions to the outward surface normal of the arbitrarily shaped particle and adapting the Θ- and δ-functions to the non-spherical shape. To this end we parametrize a given hard body $\mathcal{B}_i$ with respect to some reference point C_i, e.g., the center of mass of $\mathcal{B}_i$. This is achieved by the vector $\mathbf{R}_i(\hat{\mathbf{r}})$ which points from C_i to the point on the surface of $\mathcal{B}_i$ which lies in the direction of the unit vector $\hat{\mathbf{r}} = \mathbf{r}/|\mathbf{r}|$ (see Fig. 4.1). Obviously, such a parametrization is possible only for convex $\mathcal{B}_i$. Note, however, that this restriction is a consequence of the concern about a transparent notation alone. With some straightforward generalization, the following expressions can also be used for non-convex particles. We are now prepared to introduce Rosenfeld's proposal for the weight functions for non-spherical particles[1] [29, 30]:

[1]It should be noted that the weight functions involving δ-functions contain a factor $(\mathbf{n}_i(\hat{\mathbf{r}})\hat{\mathbf{r}})^{-1}$ which does not appear in Rosenfeld's original proposal [29, 30]. This factor, which is a consequence

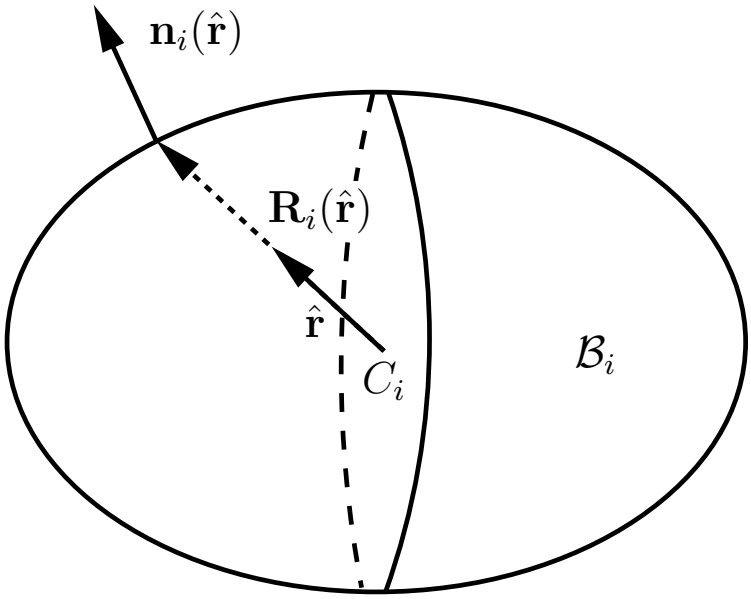

Figure 4.1: Parametrization of a convex body $\mathcal{B}_i$ via $\mathbf{R}_i(\hat{\mathbf{r}})$. The vector $\mathbf{R}_i(\hat{\mathbf{r}})$ connects the reference point C_i of $\mathcal{B}_i$ with the point of the surface $\partial\mathcal{B}_i$ which lies in the direction of the unit vector $\hat{\mathbf{r}}$. The surface point is characterized by its surface normal $\mathbf{n}_i(\hat{\mathbf{r}})$ as well as its mean curvature $H_i(\hat{\mathbf{r}})$ and its Gaussian curvature $K_i(\hat{\mathbf{r}})$.

$$
\begin{aligned}
&\omega_i^{(3)}(\mathbf{r}) = \Theta(|\mathbf{R}_i(\hat{\mathbf{r}})| - |\mathbf{r}|)\,, \\
&\omega_i^{(2)}(\mathbf{r}) = \delta(|\mathbf{R}_i(\hat{\mathbf{r}})| - |\mathbf{r}|)/(\mathbf{n}_i(\hat{\mathbf{r}})\hat{\mathbf{r}})\,, \\
&\omega_i^{(1)}(\mathbf{r}) = \frac{H_i(\hat{\mathbf{r}})}{4\pi}\,\omega_i^{(2)}(\mathbf{r})\,, \quad \omega_i^{(0)}(\mathbf{r}) = \frac{K_i(\hat{\mathbf{r}})}{4\pi}\,\omega_i^{(2)}(\mathbf{r})\,, \\
&\overrightarrow{\omega}_i^{(2)}(\mathbf{r}) = \mathbf{n}_i(\hat{\mathbf{r}})\delta(|\mathbf{R}_i(\hat{\mathbf{r}})| - |\mathbf{r}|)/(\mathbf{n}_i(\hat{\mathbf{r}})\hat{\mathbf{r}})\,, \quad \overrightarrow{\omega}_i^{(1)}(\mathbf{r}) = \frac{H_i(\hat{\mathbf{r}})}{4\pi}\overrightarrow{\omega}_i^{(2)}(\mathbf{r})\,.
\end{aligned}
\tag{4.1}
$$

Here $\mathbf{n}_i(\hat{\mathbf{r}})$ denotes the outward normal to the surface of $\mathcal{B}_i$ at the surface point indicated by $\hat{\mathbf{r}}$. The mean and Gaussian curvature at that surface point are denoted by $H_i(\hat{\mathbf{r}})$ and $K_i(\hat{\mathbf{r}})$, respectively. They are obtained from the local principal curvatures κ_i^I and κ_i^{II} according to $H_i = \frac{1}{2}(\kappa_i^I + \kappa_i^{II})$ and $K_i = \kappa_i^I\kappa_i^{II}$. For spheres, $\kappa_i^I = \kappa_i^{II} = 1/R_i$ and therefore the weight functions in Eq. (4.1) reduce to those of the hard-sphere fluid. Apart from the weight functions, the free energy model for nonspherical particles is identical to that for the hard spheres, i.e. the weighted densities are calculated according to Eq. (3.8) and the excess free energy density is given by

of parametrizing $\mathcal{B}_i$ by $\mathbf{R}_i(\hat{\mathbf{r}})$, guarantees that the contributions from the surface of $\mathcal{B}_i$ are weighted according to the surface area (for a related calculation see Appendix B).

Eq. (3.16). We refer to the model (with some slight additional modification which we discuss in Section 4.1.4) as the original FMT for non-spherical particles (onFMT). It should be noted that the particle $\mathcal{B}_i$ in the above considerations has *fixed* orientation. Freely orientating particles are realized in the theory by considering them as different components (each of them having a given fixed orientation) of a mixture with infinitely many components. In virtue of the applicability of FMT to mixtures this is feasible simply by transforming the summation over the components in Eq. (3.8) into an integral over the orientations. Along these lines it is of course also possible to treat a mixture of differently shaped freely orientating particles. Making the dependence of the weight functions and the density profiles on the particle orientation ϖ explicit, the generalization of Eq. (3.8) for the weighted densities reads

$$n_\alpha(\mathbf{r}) = \sum_{i=1}^{\nu} \iint \mathrm{d}\varpi \mathrm{d}\mathbf{r}' \rho_i(\mathbf{r}', \varpi) \omega_i^{(\alpha)}(\mathbf{r} - \mathbf{r}', \varpi) \,. \tag{4.2}$$

The onFMT has several valuable properties. First, in the case of isotropic fluids it yields the exact result for the second virial coefficient [29, 30] and a good approximation for the third virial coefficient, which, interestingly, is different from the prediction according to scaled-particle theory [124]. Recently, onFMT has been shown to fit perfectly into the context of morphological thermodynamics which allows for an efficient calculation of free energies of fluids in contact with complexly shaped walls [93]. Moreover, the successful description of structural properties of the inhomogeneous hard-sphere fluid by FMT makes onFMT a promising tool for investigations of the general inhomogeneous hard-body fluid. A good performance is expected for particles with small deviations from sphericity. However, it has been observed that the theory has severe drawbacks when it is applied to particles with large aspect ratios such as extended rigid rods. The deconvolution Eq. (3.4) of the Mayer f-function is no longer exact for general hard bodies, except in special cases such as the parallel hard ellipsoid fluid which can be related to the hard-sphere system via an anisotropic mapping [29, 30]. As a consequence, onFMT does not yield the correct low-density limit, Eq. (3.1), which for the bulk fluid coincides with Onsager theory [109]. The latter gives an accurate description of very long and thin hard rods, revealing the presence of a nematic phase at higher densities (see, e.g., Ref. [110]). In this respect, onFMT fails. This becomes obvious when we consider a bulk fluid where the density $\rho(\varpi) = \rho f(\varpi)$, with $\int \mathrm{d}\varpi f(\varpi) = 1$, is a function of the particle orientation ϖ only. The weighted densities are then obtained as $n_\alpha = \int \mathrm{d}\varpi n_\alpha(\varpi)$, where $n_\alpha(\varpi)$ is the weighted density which takes only the particles with orientation ϖ into account. Using Gauss's divergence theorem, it follows immediately that $\overrightarrow{n_2}(\varpi) \equiv 0$ for all ϖ. Thus in the bulk fluid the terms in Φ_{RF} [Eq. (3.16)] involving vectorial weight

functions do not contribute. The scalar weight functions can obviously be written as $n_\alpha(\varpi) = \rho(\varpi)c_\alpha$ with constants c_α which do not depend on ϖ. It follows that $n_\alpha = \rho c_\alpha$, which implies that the weighted densities, and hence Φ_{RF}, are independent of the orientational distribution $f(\varpi)$ of the particles. Consequently, onFMT does not capture the tendency of non-spherical particles to adopt a phase other than the isotropic one.

Our plan is to remediate this failure by improving the description of the low-density limit by extending the deconvolution Eq. (3.4) such that contributions arising from curvature asymmetry are taken into account. To this end we employ two additional *tensorial* weight functions. These allow for a modification of the excess free energy density Φ_{RF} such that it becomes capable of describing a stable nematic phase. In a first step, we derive a representation of the Mayer f-function in terms of integrals over the surface of the intersection of two hard bodies.

4.1.2 Exact decomposition of the Mayer f-function f_{ij}

Consider two orientated hard bodies $\mathcal{B}_i$ and $\mathcal{B}_j$ located at $\mathbf{r}_i$ and $\mathbf{r}_j$ and denote their intersection (which depends on the vector $\mathbf{r}_j - \mathbf{r}_i$) by $\mathcal{B}_i \cap \mathcal{B}_j$. Then, in analogy to the case of hard spheres discussed in Chapter 3, the Mayer f-function f_{ij} is given by

$$f_{ij}(\mathbf{r}_j - \mathbf{r}_i) = \begin{cases} 0 & \text{if } \mathcal{B}_i \cap \mathcal{B}_j = \varnothing \\ -1 & \text{if } \mathcal{B}_i \cap \mathcal{B}_j \neq \varnothing \end{cases} . \tag{4.3}$$

As it has been observed by Rosenfeld in the derivation of onFMT [29, 30] the Gauss-Bonnet theorem from differential geometry [31] can be used to rewrite f_{ij} in terms of integrals of the Gaussian curvature K. For a closed curve $\mathcal{C}$ with arc-length s which bounds a simply connected portion S of a surface the Gauss-Bonnet theorem states that

$$\int_S K \,\mathrm{d}A + \int_{\mathcal{C}} \kappa^{\mathrm{g}} \,\mathrm{d}s = 2\pi \,. \tag{4.4}$$

Here K is the Gaussian curvature of the surface and κ^{g} denotes the geodesic curvature of $\mathcal{C}$ on the surface (for the sign convention of κ^{g} see Appendix A). In the case where $\mathcal{B}_i$ and $\mathcal{B}_j$ are both convex, the surface of the intersection $\mathcal{B}_i \cap \mathcal{B}_j$ consist of two surfaces: $\partial\mathcal{B}_i \cap \mathcal{B}_j$ which is contained in $\mathcal{B}_j$ and $\mathcal{B}_i \cap \partial\mathcal{B}_j$ which is contained in $\mathcal{B}_i$. The two surfaces are bounded by the same closed curve $\partial\mathcal{B}_i \cap \partial\mathcal{B}_j$. Applying the Gauss-Bonnet theorem Eq. (4.4) to each bounded surface separately and adding up the results leads to

$$\int_{\partial\mathcal{B}_i \cap \mathcal{B}_j} K_i \mathrm{d}A_i + \int_{\mathcal{B}_i \cap \partial\mathcal{B}_j} K_j \mathrm{d}A_j + \int_{\partial\mathcal{B}_i \cap \partial\mathcal{B}_j} (\kappa_i^{\mathrm{g}} + \kappa_j^{\mathrm{g}}) \mathrm{d}s = 4\pi \,. \tag{4.5}$$

This equation is valid of course only in the cases where $\mathcal{B}_i \cap \mathcal{B}_j \neq \varnothing$. Otherwise the l.h.s. of Eq. (4.5) vanishes as the integrations are performed over empty sets. Thus we can express Eq. (4.3) with the help of the Gauss-Bonnet theorem as follows:

$$-f_{ij}(\mathbf{r}_j - \mathbf{r}_i) = \int\limits_{\partial\mathcal{B}_i\cap\mathcal{B}_j} \frac{K_i}{4\pi}\mathrm{d}A_i + \int\limits_{\mathcal{B}_i\cap\partial\mathcal{B}_j} \frac{K_j}{4\pi}\mathrm{d}A_j + \int\limits_{\partial\mathcal{B}_i\cap\partial\mathcal{B}_j} \frac{\kappa_i^{\mathrm{g}} + \kappa_j^{\mathrm{g}}}{4\pi}\mathrm{d}s \tag{4.6}$$

$$= \int\limits_{\partial\mathcal{B}_i\cap\mathcal{B}_j} \frac{K_i}{4\pi}\mathrm{d}A_i + \int\limits_{\partial\mathcal{B}_i\cap\partial\mathcal{B}_j} \frac{H_i}{4\pi}\frac{\mathrm{d}s}{|\mathbf{n}_i\times\mathbf{n}_j|} - \int\limits_{\partial\mathcal{B}_i\cap\partial\mathcal{B}_j} \frac{H_i\mathbf{n}_i\mathbf{n}_j}{4\pi}\frac{\mathrm{d}s}{|\mathbf{n}_i\times\mathbf{n}_j|}$$
$$- \int\limits_{\partial\mathcal{B}_i\cap\partial\mathcal{B}_j} \frac{\Delta\kappa_i}{4\pi}\frac{(\mathbf{v}_i^I\mathbf{n}_j)^2 - (\mathbf{v}_i^{II}\mathbf{n}_j)^2}{(1+\mathbf{n}_i\mathbf{n}_j)}\frac{\mathrm{d}s}{|\mathbf{n}_i\times\mathbf{n}_j|} + (i\leftrightarrow j)\,. \tag{4.7}$$

In the last step, we have used the result for $\kappa_i^{\mathrm{g}} + \kappa_j^{\mathrm{g}}$ [Eq. (A.17)] which we derive in Appendix A. In the formula $(i \leftrightarrow j)$ stands for the previous terms with exchanged indices i and j. Apart from the local mean curvature H_i, the local Gaussian curvature K_i, and the surface normal $\mathbf{n}_i$, which we have already introduced above, the expression involves the deviatoric curvature $\Delta\kappa_i = \frac{1}{2}(\kappa_i^I - \kappa_i^{II})$, which is a measure for the deviation from sphericity ($\Delta\kappa_i = 0$ for spheres). The unit vectors $\mathbf{v}_i^I$ and $\mathbf{v}_i^{II}$ lie in the tangent plane (i.e. the plane perpendicular to $\mathbf{n}_i$) and point into the directions of the principal curvatures κ_i^I and κ_i^{II}. The directions of principal curvatures are perpendicular, thus $\mathbf{v}_i^I$, $\mathbf{v}_i^{II}$, and $\mathbf{n}_i$ constitute an orthonormal basis of $\mathbb{R}^3$.

4.1.3 Properties of an approximate deconvolution of f_{ij}

The connection between Eq. (4.7) and the deconvolution Eq. (3.4), which is exact only for spheres, becomes obvious when we realize that the first three integrals of Eq. (4.7) can be rewritten as follows:

$$\int\limits_{\partial\mathcal{B}_i\cap\mathcal{B}_j} \frac{K_i}{4\pi}\mathrm{d}A_i = \omega_i^{(0)} \otimes \omega_j^{(3)}\,, \tag{4.8}$$

$$\int\limits_{\partial\mathcal{B}_i\cap\partial\mathcal{B}_j} \frac{H_i}{4\pi}\frac{\mathrm{d}s}{|\mathbf{n}_i\times\mathbf{n}_j|} = \omega_i^{(1)} \otimes \omega_j^{(2)}\,, \tag{4.9}$$

$$\int\limits_{\partial\mathcal{B}_i\cap\partial\mathcal{B}_j} \frac{H_i\mathbf{n}_i\mathbf{n}_j}{4\pi}\frac{\mathrm{d}s}{|\mathbf{n}_i\times\mathbf{n}_j|} = \overrightarrow{\omega}_i^{(1)} \otimes \overrightarrow{\omega}_j^{(2)}\,. \tag{4.10}$$

The calculations concerning the latter two equalities are carried out in Appendix B. However, the last integral in Eq. (4.7),

$$I_{\Delta\kappa} = \int\limits_{\partial\mathcal{B}_i\cap\partial\mathcal{B}_j} \frac{\Delta\kappa_i}{4\pi}\frac{(\mathbf{v}_i^I\mathbf{n}_j)^2 - (\mathbf{v}_i^{II}\mathbf{n}_j)^2}{(1+\mathbf{n}_i\mathbf{n}_j)}\frac{\mathrm{d}s}{|\mathbf{n}_i\times\mathbf{n}_j|}\,, \tag{4.11}$$

cannot be written as a convolution of weight functions depending only on the properties of one species each. This is obviously a consequence of the fact that the integrand (without the factor $|\mathbf{n}_i \times \mathbf{n}_j|^{-1}$) is no longer a polynomial in the components of unit vectors. One can, however, expand the integrand in a Taylor series in powers of the components of unit vectors. In the present case this amounts to using the expansion $(1 + \mathbf{n}_i\mathbf{n}_j)^{-1} = 1 - \mathbf{n}_i\mathbf{n}_j + (\mathbf{n}_i\mathbf{n}_j)^2 - \ldots$. Pursuing the expansion up to order n allows for a deconvolution of $I_{\Delta\kappa}$ in terms of *tensorial* weight functions of rank up to $n + 2$. In the simplest possible scenario we take $n = 0$, meaning that we use the approximation $(1 + \mathbf{n}_i\mathbf{n}_j)^{-1} = \zeta$, where we have introduced the constant ζ which can be different from 1 in order to compensate for the error arising from the omission of higher order terms in the expansion. Below, we shall determine appropriate values of ζ for the hard-spherocylinder fluid. The deconvolution of $I_{\Delta\kappa}$ corresponding to an expansion of order $n = 0$ reads

$$\begin{aligned} I_{\Delta\kappa} &\approx \zeta \int\limits_{\partial\mathcal{B}_i \cap \partial\mathcal{B}_j} \frac{\Delta\kappa_i}{4\pi} \left((\mathbf{v}_i^I \mathbf{n}_j)^2 - (\mathbf{v}_i^{II} \mathbf{n}_j)^2 \right) \frac{\mathrm{d}s}{|\mathbf{n}_i \times \mathbf{n}_j|} \\ &= \zeta \overleftrightarrow{\omega}_i^{(1)} \otimes \overleftrightarrow{\omega}_j^{(2)} , \end{aligned} \tag{4.12}$$

where

$$\overleftrightarrow{\omega}_i^{(1)} = \frac{\Delta\kappa_i(\hat{\mathbf{r}})}{4\pi} \left(\mathbf{v}_i^I(\hat{\mathbf{r}}) \mathbf{v}_i^I(\hat{\mathbf{r}})^{\mathrm{T}} - \mathbf{v}_i^{II}(\hat{\mathbf{r}}) \mathbf{v}_i^{II}(\hat{\mathbf{r}})^{\mathrm{T}} \right) \delta(|\mathbf{R}_i(\hat{\mathbf{r}})| - |\mathbf{r}|) \,/\, (\mathbf{n}_i(\hat{\mathbf{r}})\hat{\mathbf{r}}) , \tag{4.13}$$

$$\overleftrightarrow{\omega}_i^{(2)} = \mathbf{n}_i(\hat{\mathbf{r}}) \mathbf{n}_i(\hat{\mathbf{r}})^{\mathrm{T}} \, \delta(|\mathbf{R}_i(\hat{\mathbf{r}})| - |\mathbf{r}|) \,/\, (\mathbf{n}_i(\hat{\mathbf{r}})\hat{\mathbf{r}}) . \tag{4.14}$$

These tensorial weight functions can be represented as 3×3-matrices and the dyadic product $\mathbf{a}\mathbf{b}^{\mathrm{T}}$ stands for the matrix with entries $(\mathbf{a}\mathbf{b}^{\mathrm{T}})_{ij} = a_i b_j$. The definition of the convolution product [Eq. (3.6)] must be extended to the tensorial weight functions. To this end, we introduce as an appropriate scalar product of matrices $\overleftrightarrow{A}$ and $\overleftrightarrow{B}$ the trace of the result of matrix multiplication: $\mathrm{Tr}[\overleftrightarrow{A}\overleftrightarrow{B}] = \sum_{i,j} A_{ij} B_{ji}$. This adds a third meaning to the multiplication of the weight functions in Eq. (3.6) which was already defined as the usual product for the scalar weight functions and as the vector scalar product for the vectorial weight functions.

With these steps we are lead to an extension of the deconvolution of the Mayer f-function f_{ij} which goes beyond Eq. (3.4) but, for non-spherical particles, is still approximate:

$$-f_{ij}(\mathbf{r}_i - \mathbf{r}_j) \approx \omega_i^{(0)} \otimes \omega_j^{(3)} + \omega_i^{(1)} \otimes \omega_j^{(2)} - \overrightarrow{\omega}_i^{(1)} \otimes \overrightarrow{\omega}_j^{(2)} - \zeta \overleftrightarrow{\omega}_i^{(1)} \otimes \overleftrightarrow{\omega}_j^{(2)} + (i \leftrightarrow j) . \tag{4.15}$$

In the case of spheres the term $\zeta \overleftrightarrow{\omega}_i^{(1)} \otimes \overleftrightarrow{\omega}_j^{(2)}$ does not contribute as the deviatoric curvature $\Delta\kappa_i$ vanishes and therefore $\overleftrightarrow{\omega}_i^{(1)} \equiv 0$. Thus the exact deconvolution for

spheres is not altered by our extention. Rosenfeld's decomposition for non-spherical particles underlying onFMT [29, 30] is recovered in the special case $\zeta = 0$.

The question arises to which extend the additional term in the deconvolution does in fact improve our expression for f_{ij}. In a first step we show that the additional term does not contribute in the isotropic bulk fluid. Thus the extended deconvolution inherits the property of onFMT ($\zeta = 0$) to yield the exact second virial coefficient B_2 for the *isotropic* bulk fluid. Denoting the excess free energy density belonging to the extended deconvolution with Φ_{ed}, the relation $\Phi_{\text{ed}} = B_2\rho^2 + \mathcal{O}(\rho^3)$ holds in the isotropic bulk fluid. We proceed analogously to the derivation of Eq. (3.7) in order to obtain the low-density limit of Φ_{ed} as imposed by the extended deconvolution Eq. (4.15) of f_{ij}. The result is

$$\Phi_{\text{ed}} = n_0 n_3 + n_1 n_2 - \overrightarrow{n}_1 \overrightarrow{n}_2 - \zeta \text{Tr}[\overleftrightarrow{n}_1 \overleftrightarrow{n}_2] + \mathcal{O}(\rho^3)\,, \tag{4.16}$$

where we have introduced the new weighted densities $\overleftrightarrow{n}_1$ and $\overleftrightarrow{n}_2$ which are calculated according to Eq. (4.2) with the weight functions $\overleftrightarrow{\omega}_1$ and $\overleftrightarrow{\omega}_2$.

One can see easily that the trace of $\overleftrightarrow{n}_1$ vanishes, $\text{Tr}\overleftrightarrow{n}_1 = 0$, no matter what the underlying density distributions $\rho_i(\mathbf{r}, \varpi)$ are. This is simply a consequence of the normalization of the directions of principal curvatures: $|\mathbf{v}_i^I(\hat{\mathbf{r}})| = |\mathbf{v}_i^{II}(\hat{\mathbf{r}})| = 1$. In the special case of an isotropic bulk fluid the weighted density $\overleftrightarrow{n}_2$ is of the simple diagonal form $\overleftrightarrow{n}_2 = \frac{1}{3} n_2 \mathbb{1}$, where $\mathbb{1}$ is the unit matrix and n_2 is the scalar weighted density as defined above. This result can be obtained in a simple calculation from Eq. (4.2) by realizing that the integration over the orientational degrees of freedom yields the same result for every point of the surface of a given body, namely $\frac{1}{3}\mathbb{1}$. A subsequent integration over the surface of the given body yields the above result. From the properties of $\overleftrightarrow{n}_1$ and $\overleftrightarrow{n}_2$ it follows immediately that $\text{Tr}[\overleftrightarrow{n}_1 \overleftrightarrow{n}_2]$ vanishes in the isotropic bulk fluid. Therefore, our additional term does not cause a FMT with the low-density limit Eq. (4.16) to deviate from the exact result for the second virial coefficient of the isotropic bulk fluid. The explicit construction of such a FMT is postponed to Section 4.1.4. For the moment we only introduce the notion of extended-deconvolution FMT (edFMT) for a suitable FMT which is based on the low-density limit Eq. (4.16) with $\zeta \neq 0$.

What is the situation when a non-isotropic bulk fluid is considered? The second virial coefficient B_2 then depends on the orientational distribution $f(\varpi)$ according to

$$B_2 = \frac{1}{2} \iint \mathrm{d}\varpi \mathrm{d}\varpi' f(\varpi) f(\varpi') v(\varpi, \varpi')\,, \tag{4.17}$$

where $v(\varpi, \varpi')$ is the volume which is excluded by a particle of orientation ϖ to another particle of orientation ϖ' (or vice-versa, equivalently).

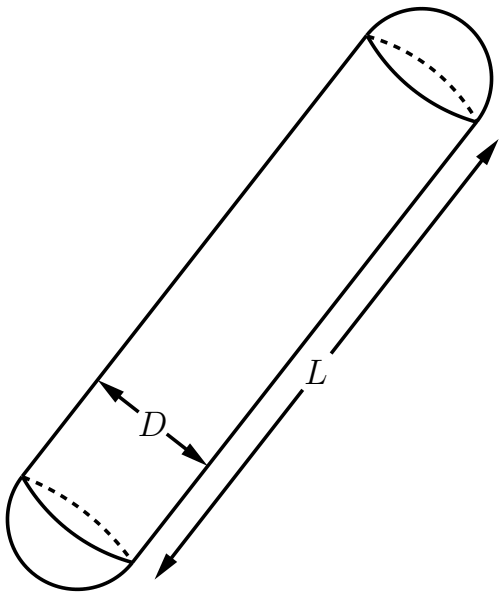

Figure 4.2: Sketch of a spherocylinder, which consists of a solid cylinder with diameter D and length L being capped by two solid hemispheres with diameter D. In the limit $L \to 0$ the geometry of a sphere with diameter D is recovered.

Let us consider the specific case of a fluid which is composed of hard spherocylinders with length L and diameter D (see Fig. 4.2). The excluded volume $v(\varpi, \varpi')$ is then given by [109]

$$v(\varpi, \varpi') = 2L^2 D \sin\gamma + 2\pi L D^2 + \frac{4}{3}\pi D^3 \,, \tag{4.18}$$

where $\gamma \in [0, \pi]$ is the angle between the two spherocylinders.

On the other hand, edFMT provides an approximation to $v(\varpi, \varpi')$ which can be derived on the basis of Eq. (4.16) together with the relation that $\Phi_{\mathrm{ed}} = B_2\rho^2 + \mathcal{O}(\rho^3)$, see Appendix C. The result is

$$v_{\mathrm{FMT}}(\varpi, \varpi') = 2L^2 D \left(\frac{\pi}{4} + \zeta\frac{\pi}{8}\left(\frac{3}{2}\sin^2\gamma - 1\right)\right) + 2\pi L D^2 + \frac{4}{3}\pi D^3 \,. \tag{4.19}$$

We first observe that $v_{\mathrm{FMT}}(\varpi, \varpi')$ is correct up to linear order in L, only the quadradic term in L does not agree with the exact result from Eq. (4.18). Our aim is to determine the value of ζ such that in the isotropic fluid the average deviation of $v_{\mathrm{FMT}}(\varpi, \varpi')$ from the exact result is minimal. This is achieved by the least squares criterion which requires that

$$\int_0^\pi \mathrm{d}\gamma \sin\gamma (v_{\mathrm{FMT}}(\varpi, \varpi') - v(\varpi, \varpi'))^2 \quad \longrightarrow \quad \text{minimum} \,. \tag{4.20}$$

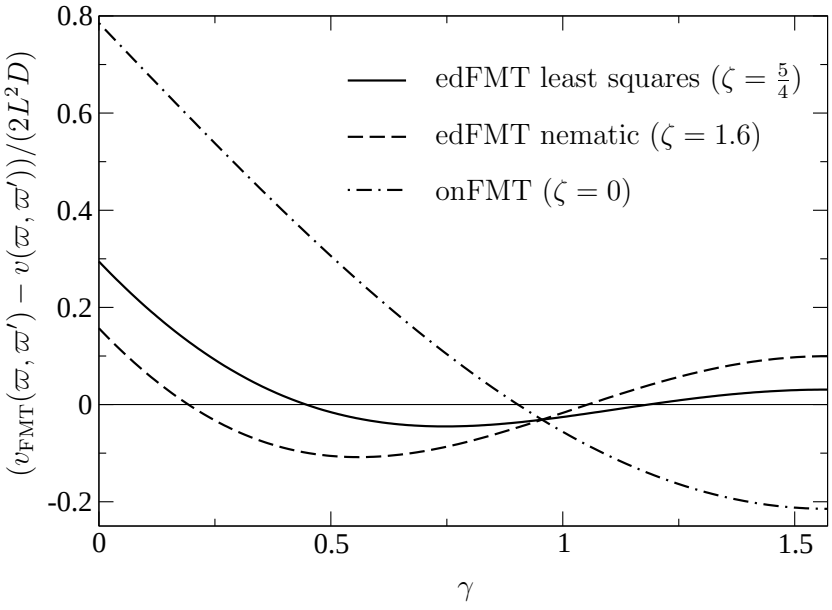

Figure 4.3: Different FMT approximations $v_{\mathrm{FMT}}(\varpi, \varpi')$ to the volume $v(\varpi, \varpi')$ which is excluded by a spherocylinder (length L, diameter D) of orientation ϖ to a spherocylinder of orientation ϖ' with the same aspect ratio. Shown are the deviations from the exact result. γ is the angle between the orientations ϖ and ϖ'.

The calculation can be performed easily and leads to a value of $\zeta = \frac{5}{4}$. We have plotted the different FMT approximations to $v(\varpi, \varpi')$ in Fig. 4.3. Obviously, our edFMT result $v_{\mathrm{FMT}}(\varpi, \varpi')$ with $\zeta = \frac{5}{4}$ improves significantly upon Rosenfeld's onFMT result which has $\zeta = 0$ and which therefore does not contain any γ-dependence. However, in particular for spherocylinders which are aligned in the same direction (i.e. γ is small) the deviation is pronounced even for the edFMT with $\zeta = \frac{5}{4}$. While in the isotropic fluid the case of small γ has a relatively small weight, this is clearly different for the fluid in the nematic phase. It is thus not surprising that this phase is better described by $\zeta > \frac{5}{4}$. This is indeed what we observe when we compare edFMT with computer simulation data for the isotropic-nematic transition (see Section 4.2.1). There, we find that the transition for not too large L is best described with $\zeta = 1.6$. The corresponding curve is also included in Fig. 4.3 and yields indeed a better description of the low γ range. Finally, we mention that 2 is an upper bound for ζ. By choosing $\zeta = 2$ we can reproduce the exact result for B_2 in the case that spherocylinders with fixed orientation ($\gamma = 0$) are considered. $\zeta > 2$ would cause an unphysical situation where B_2 becomes negative for small γ in the case of elongated spherocylinders for which the quadratic term in L dominates.

4.1.4 Extrapolation to finite particle densities

Similar to the derivation of Rosenfeld's excess free energy density Φ_{RF} [Eq. (3.16)] we need to extrapolate the low-density limit Eq. (4.16) to higher densities in order to describe the dense fluid (and potentially solid phases) appropriately. Using the same arguments as for the derivation of Φ_{RF} (see Section 3.1) the extrapolation of Eq. (4.16) can be easily shown to yield the edFMT excess free energy density

$$\Phi_{\mathrm{ed}} = -n_0 \ln(1-n_3) + \frac{n_1 n_2 - \overrightarrow{n}_1 \overrightarrow{n}_2 - \zeta \mathrm{Tr}[\overleftrightarrow{n}_1 \overleftrightarrow{n}_2]}{1-n_3} + \frac{\phi(n_2, \overrightarrow{n}_2, \overleftrightarrow{n}_2)}{(1-n_3)^2} \,. \tag{4.21}$$

Interestingly, a dimensional analysis of the possible products of the weighted densities shows that ϕ, the numerator of the third term, which has to be of order 3 in the weighted densities, can depend not only on the scalar n_2 and the vectorial $\overrightarrow{n}_2$ but also on the tensor $\overleftrightarrow{n}_2$. If the latter possibility is not considered one obtains ϕ from Φ_{RF} [Eq. (3.16)], i.e., $\phi = \phi(n_2, \overrightarrow{n}_2) = \frac{1}{24\pi}(n_2^3 - 3 n_2 \overrightarrow{n}_2 \overrightarrow{n}_2)$. It has, however, turned out that this expression for ϕ is problematic as the resulting third term of Φ_{RF} spoils the (exactly known) result for one dimensional density distributions and causes a strong negative divergency of the free energy for strongly peaked density distributions (see, e.g., Ref. [84]). As a consequence, the hard-sphere crystal is dramatically overstabilized. This deficiency has been cured first by an empirical modification of the third term [75, 76]. Subsequently, a systematic construction of the free energy functional became possible which was based on zero dimensional cavities and correct dimensional crossover [84]. The method led Tarazona [77] to introducing the weighted density $\overleftrightarrow{n}_2$ and constructing ϕ as

$$\phi(n_2, \overrightarrow{n}_2, \overleftrightarrow{n}_2) = \frac{3}{16\pi} \left(\overrightarrow{n}_2^{\mathrm{T}} \overleftrightarrow{n}_2 \overrightarrow{n}_2 - n_2 \overrightarrow{n}_2 \overrightarrow{n}_2 - \mathrm{Tr}[\overleftrightarrow{n}_2^3] + n_2 \mathrm{Tr}[\overleftrightarrow{n}_2^2] \right) . \tag{4.22}$$

In contrast to Rosenfeld's Φ_{RF} from Eq. (3.16), the version by Tarazona yields the exact result for monocomponent hard-sphere systems which are confined to 1D and it describes the hard-sphere crystal very well [77]. In later work, it has been argued that the third term with ϕ according to Eq. (4.22) yields also the presently best FMT (among those which use the PY equation of state) for hard-sphere *mixtures* [98]. Given these merits we choose Tarazona's ϕ rather than the original one of Rosenfeld for the following calculations. This holds also for our definition of onFMT which we henceforth take to be the special case of edFMT [Eq. (4.21) supplemented by Eq. (4.22)] with $\zeta = 0$, in contrast to the "original" onFMT proposed in Refs. [29,30] which uses Rosenfeld's ϕ. However, in the situations which we consider no crystals or extremely confined fluids are involved such that the differences arising from the different expressions for the third term are expected to be negligible. We have checked

that this is indeed the case; more precisely, these differences are clearly dominated by the influence of the value of ζ in Eq. (4.21). It would be in any case very interesting to study whether the excess free energy density $\Phi_{\rm ed}$ with ϕ from Eq. (4.22) is suitable for the description of crystals composed of hard non-spherical particles such as the gyroid cubic phase of hard pear-shaped particles [125] or the simple monoclinic phase of hard ellipsoids of revolution [126] which have been discovered recently in numerical simulations.

The fact that our improved deconvolution Eq. (4.15) for the non-spherical particles gives rise to the tensorial weighted density $\overleftrightarrow{n}_2$ is particularly valuable as this establishes a connection between the two distinctly different manners of constructing a FMT. One the one hand, there is Rosenfeld's original approach [22] in which the low-density limit of the excess free energy is considered and from this the building blocks (which are the six weighted densities n_0, n_1, n_2, n_3, $\overrightarrow{n}_1$, and $\overrightarrow{n}_2$) for the excess free energy density $\Phi_{\rm RF}$ are identified. On the other hand, in later work, Tarazona and Rosenfeld [84] construct the functional based on zero dimensional cavities and dimensional crossover which leads to the introduction of the additional tensorial weighted density $\overleftrightarrow{n}_2$ for hard spheres [77]. In the spirit of Rosenfeld's original approach, our work provides a motivation for introducing $\overleftrightarrow{n}_2$ which comes out simply as an additional building block from considering our *improved* expression Eq. (4.16) for the low-density limit of $\Phi_{\rm ed}$. While the weighted density $\overleftrightarrow{n}_1$ vanishes for spheres and cannot be included in the third term of $\Phi_{\rm ed}$ for dimensional reasons, the weighted density $\overleftrightarrow{n}_2$ is non-zero even for spheres and has the correct dimension[2] to be incorporated. Thus the motivation for using $\overleftrightarrow{n}_2$ is provided following the lines of Ref. [22]. *How* $\overleftrightarrow{n}_2$ has to be incorporated into $\Phi_{\rm ed}$ cannot be answered in this way. Here the arguments of Refs. [77, 84, 98] are necessary in order to obtain the correct form of the numerator ϕ. In conclusion, the use of $\overleftrightarrow{n}_2$ for constructing the functional for hard sphere systems can be viewed in some sense as a consequence of stabilizing the theory against small deformations of the constituents from sphericity. For slightly non-spherical particles the use of $\overleftrightarrow{n}_2$ is in order for a proper deconvolution of f_{ij}. As $\overleftrightarrow{n}_2$ is non-vanishing also for spheres, the requirement of continuity imposes the use of $\overleftrightarrow{n}_2$ also for the hard-sphere fluid/crystal.

[2]Note here that the dimension of n_α is (length)$^{\alpha-3}$ and the dimension of $\Phi_{\rm ed}$ is (length)$^{-3}$.

4.2 Comparison with data from simulations

4.2.1 Isotropic-nematic transition

For the calculation of the isotropic-nematic transition as obtained from edFMT we consider a bulk fluid of spherocylinders (length L, diameter D) with particle density ρ. The spherocylinders are assumed to be distributed as a function of their azimuthal angle ϑ according to the distribution function $g(\cos\vartheta)$. The orientation dependent density distribution is thus given by $\rho(\varpi) = \rho f(\varpi) = \rho g(\cos\vartheta)$. From the requirement of normalization we can conclude that

$$\frac{1}{4\pi}\int_0^{2\pi} \mathrm{d}\varphi \int_0^{\pi} \mathrm{d}\vartheta \sin\vartheta \; g(\cos\vartheta) = \frac{1}{2}\int_{-1}^{1} \mathrm{d}(\cos\vartheta) g(\cos\vartheta) = \int_0^1 \mathrm{d}x g(x) \stackrel{!}{=} 1\,. \quad (4.23)$$

Here we have used that due to their symmetry spherocylinders with orientation ϑ cannot be distinguished from those with orientation $\pi - \vartheta$. We can therefore assume without loss of generality that $g(x) = g(-x)$. The formula for the weighted densities, Eq. (4.2), reduces to

$$n_\alpha = \int \mathrm{d}\varpi n_\alpha(\varpi) = \frac{1}{4\pi}\int_0^{2\pi} \mathrm{d}\varphi \int_0^{\pi} \mathrm{d}\vartheta \sin\vartheta \; n_\alpha(\varpi)\,, \quad (4.24)$$

where the weighted densities from Appendix C have to be used with $f(\varpi) = g(\cos\vartheta)$. The φ-integrations can be carried out immediately for all the weighted densities, while the ϑ-integrations involve the distribution $g(x)$ and lead to a distribution dependence of the tensorial weighted densities via the second moment $I_2 \doteq \int_0^1 \mathrm{d}x x^2 g(x)$. A simple calculation yields

$$\begin{aligned}
&n_3 = \rho\left(\frac{\pi}{4}LD^2 + \frac{\pi}{6}D^3\right)\,, \qquad n_2 = \rho\left(\pi LD + \pi D^2\right)\,,\\
&n_1 = \rho\left(\frac{L}{4} + \frac{D}{2}\right)\,, \qquad n_0 = \rho\,,\\
&(\overleftrightarrow{n}_1)_{11} = (\overleftrightarrow{n}_1)_{22} = \rho\frac{L}{16}\left(3I_2 - 1\right)\,,\\
&(\overleftrightarrow{n}_1)_{33} = -\rho\frac{L}{8}\left(3I_2 - 1\right)\,,\\
&(\overleftrightarrow{n}_2)_{11} = (\overleftrightarrow{n}_2)_{22} = \rho\left(\frac{\pi}{4}LD\left(1 + I_2\right) + \frac{\pi}{3}D^2\right)\,,\\
&(\overleftrightarrow{n}_2)_{33} = \rho\left(\frac{\pi}{2}LD\left(1 - I_2\right) + \frac{\pi}{3}D^2\right)\,.
\end{aligned} \quad (4.25)$$

The non-diagonal elements of the tensorial weighted densities as well as the vectorial weighted densities vanish. One can easily check that we have $\mathrm{Tr}\overleftrightarrow{n}_1 = 0$ and $\mathrm{Tr}\overleftrightarrow{n}_2 = n_2$ which was shown above to hold also for general $\rho(\mathbf{r}, \varpi)$.

The grand potential Ω of the fluid is given according to Eqs. (2.26) and (2.27) by the expression[3]

$$\Omega/V = \Phi_{\rm id} + \Phi_{\rm ed} - \mu\rho\,, \tag{4.26}$$

where

$$\begin{aligned}\Phi_{\rm id} &= \int {\rm d}\varpi \rho(\varpi) \left(\ln(\rho(\varpi)\Lambda^3) - 1\right) \\ &= \rho\left(\ln(\rho\Lambda^3) - 1\right) + \rho\int_0^1 {\rm d}x g(x)\ln g(x)\end{aligned} \tag{4.27}$$

is the free energy density of the non-interacting spherocylinders (ideal gas) and $\Phi_{\rm ed}$ is the edFMT excess free energy density [Eq. (4.21) with Eq. (4.22)] evaluated for the weighted densities given above in Eq. (4.25). For given fixed volume V, chemical potential μ and particle number density $\rho = \frac{N}{V}$ the equilibrium orientational distribution $g(x)$ must minimize the grand potential Ω, i.e., the variation $\delta\Omega/\delta g$ must vanish. A straightforward calculation shows that this is equivalent to

$$g(x) = \text{const.} \times \exp\left(-\frac{1}{\rho}\frac{\partial\Phi_{\rm ed}}{\partial I_2}\,x^2\right) \tag{4.28}$$

with a constant which is chosen such that normalization of $g(x)$ is guaranteed. This can be cast into the equivalent normalized form

$$g(x) = \frac{\alpha}{\mathcal{D}(\alpha)}\exp\left(-\alpha^2(1-x^2)\right) \tag{4.29}$$

where $\mathcal{D}(\alpha)$ is Dawson's integral

$$\mathcal{D}(\alpha) = \exp(-\alpha^2)\int_0^\alpha {\rm d}u \exp(u^2) \tag{4.30}$$

and α satisfies the condition

$$\alpha^2 = -\frac{1}{\rho}\frac{\partial\Phi_{\rm ed}}{\partial I_2}\,. \tag{4.31}$$

Note that the r.h.s. of Eq. (4.31) depends on α through the second moment I_2 of $g(x)$. From Eq. (4.29) one obtains that

$$I_2 = \frac{\frac{\alpha}{\mathcal{D}(\alpha)} - 1}{2\alpha^2} = \frac{1}{3} + \frac{4}{45}\alpha^2 + \mathcal{O}(\alpha^4)\,. \tag{4.32}$$

Obviously, Eq. (4.29) is equivalent to $g(x) \propto \exp(-\alpha^2\sin^2\vartheta)$. This orientational distribution, which *follows* here from the excess free energy $\Phi_{\rm ed}$, has been used as an empirical input for the description of the nematic phase in previous work [127].

[3]In order to lighten the expressions we omit henceforth the factor $k_{\rm B}T$ which converts the units of $\Phi_{\rm id}$ and $\Phi_{\rm ed}$ into those of energy densities.

In order to complete our calculation of the isotropic-nematic transition we make Eq. (4.31) more explicit by inserting the expression for Φ_{ed}. This leads to

$$\alpha^2 = A(3I_2 - 1) - B(3I_2 - 1)^2 \,, \tag{4.33}$$

where

$$\begin{aligned} A &= \frac{3}{16} \frac{\zeta\eta\ell^2}{(1-\eta)\left(\frac{\ell}{4}+\frac{1}{6}\right)} \,, \\ B &= \frac{3}{512} \frac{\eta^2\ell^3}{(1-\eta)^2\left(\frac{\ell}{4}+\frac{1}{6}\right)^2} \,. \end{aligned} \tag{4.34}$$

Here $\ell = \frac{L}{D}$ is the spherocylinder aspect ratio and $\eta = n_3$, as defined in Eq. (4.25), is the spherocylinder packing fraction. Obviously, the isotropic distribution ($\alpha = 0$) is always a solution of Eq. (4.33), see also Eq. (4.32). One can also see immediately, that for onFMT ($\zeta = 0$) it follows that $A = 0$ and thus no solution with $\alpha \neq 0$ exists. Note that the term proportional to B is due to Tarazona's modification [Eq. (4.22)] of the third term of Rosenfeld's original FMT [29, 30]. The latter FMT has $B = 0$. We now come back to the edFMT excess free energy Φ_{ed} which allows us to choose $\zeta > 0$. The analysis of the generic case shows that for small η the only solution is the one with $\alpha = 0$. At a certain "critical" packing fraction η_{cr} a second solution of Eq. (4.33) with $\alpha > 0$ sets in discontinuously. For η slightly larger than η_{cr} two different solutions with $\alpha > 0$ exist. The one corresponding to the lower value of α runs into $\alpha = 0$ when η is increased up to some η_{unst}. For $\eta > \eta_{\mathrm{unst}}$ two solutions exist: one with $\alpha = 0$ and one with $\alpha > 0$. It should be noted that Eq. (4.33) is invariant under the transformation $\alpha \to -\alpha$ which reflects the symmetry of Eq. (4.29). The solutions of Eq. (4.33) correspond to extrema in the free energy (or, equivalently, the grand potential) considered as a function of α. It can be shown that for $\eta < \eta_{\mathrm{cr}}$ a single minimum at $\alpha = 0$ exists. At $\eta = \eta_{\mathrm{cr}}$ a second minimum at $\alpha > 0$ appears corresponding to the nematic phase. The local maximum between the two minima is connected with the intermediate solution of Eq. (4.33) which therefore does not correspond to a (meta-)stable physical state. Upon increasing η the intermediate maximum moves towards $\alpha = 0$, where it gets located as $\eta = \eta_{\mathrm{unst}}$. For $\eta > \eta_{\mathrm{unst}}$ the free energy displays a local *maximum* at $\alpha = 0$, indicating that the isotropic phase is definitely unstable, and a minimum at $\alpha > 0$, corresponding to the stable nematic phase.

The orientational distribution, Eq. (4.29), allows in principle also for purely imaginary α which refers to a (rather odd) orientational distribution $g(\cos\vartheta)$ where more particles with $\vartheta \simeq \frac{\pi}{2}$ than those with $\vartheta \simeq 0$ can be found in the system. Equation (4.33) has indeed such a purely imaginary solution which emerges continuously

from the isotropic solution ($\alpha = 0$) when η is increased beyond η_{unst}. It can be shown, however, that the corresponding phase is unstable w.r.t. the nematic phase in the relevant range of η. The range of η is limited from above due to the fact that for sufficiently large η the stable phase is the smectic one [128]. The smectic phase has to be described by a spatially *heterogeneous* density distribution $\rho(\mathbf{r}, \varpi)$ and it is thus not covered by the assumptions made on $\rho(\mathbf{r}, \varpi)$ in this section.

Finally, we calculate the isotropic-nematic coexistence line by solving simultaneously for ρ_{iso} and ρ_{nem} the equations

$$\mu_{\text{iso}}(\rho_{\text{iso}}) = \mu_{\text{nem}}(\rho_{\text{nem}}) \,, \qquad p_{\text{iso}}(\rho_{\text{iso}}) = p_{\text{nem}}(\rho_{\text{nem}}) \,, \tag{4.35}$$

where $\mu_{\text{iso/nem}}$ and $p_{\text{iso/nem}}$ are the chemical potential and the pressure of the respective phase as functions of the particle density. Using the edFMT free energy $\Phi_{\text{id}} + \Phi_{\text{ed}}$ of the hard-spherocylinder fluid [cf. Eq. (4.26)] we obtain the chemical potentials

$$\mu_{\text{iso}} = \left.\frac{\partial(\Phi_{\text{id}} + \Phi_{\text{ed}})}{\partial \rho}\right|_{\alpha=0} , \qquad \mu_{\text{nem}} = \left.\frac{\partial(\Phi_{\text{id}} + \Phi_{\text{ed}})}{\partial \rho}\right|_{\alpha=\alpha_{\text{nem}}(\rho)} , \tag{4.36}$$

where $\alpha_{\text{nem}}(\rho) > 0$ is the appropriate solution of Eq. (4.33). The pressure is obtained as the negative of the grand potential density

$$p_{\text{iso}} = -(\Phi_{\text{id}} + \Phi_{\text{ed}})_{\alpha=0} + \mu_{\text{iso}}\rho \,, \qquad p_{\text{nem}} = -(\Phi_{\text{id}} + \Phi_{\text{ed}})_{\alpha=\alpha_{\text{nem}}(\rho)} + \mu_{\text{nem}}\rho \,. \tag{4.37}$$

Note that the calculation of μ_{nem} in Eq. (4.36) would in principle require an additional contribution $(\partial(\Phi_{\text{id}}+\Phi_{\text{ed}})/\partial\alpha)\times(\partial\alpha_{\text{nem}}/\partial\rho)$ arising from the ρ-dependence of α_{nem}. However, due to the fact that the orientational distribution $g(x)$ minimizes the grand potential Ω it follows that $\partial\Omega/\partial\alpha = 0$ and thus also $\partial(\Phi_{\text{id}} + \Phi_{\text{ed}})/\partial\alpha$ vanishes.

In Fig. 4.4 we show results for the isotropic-nematic transition for the parameter $\zeta = \frac{5}{4}$ and $\zeta = 1.6$. The first value was chosen as it provides the best description of the isotropic fluid on the microscopic level (see Section 4.1.3) while $\zeta = 1.6$ was determined empirically in order to obtain the best fit to the simulation data by Bolhuis and Frenkel [128] at moderate aspect ratios L/D. With $\zeta = \frac{5}{4}$ we obtain qualitative agreement with the simulations while $\zeta = 1.6$ yields good agreement for moderate aspect ratios. However, when L/D grows large the difference of ρ_{iso} and ρ_{nem} at coexistence is seriously underestimated by the theory based on the edFMT excess free energy density Φ_{ed}. This might be partially attributed to the fact that the error made in approximating the second virial coefficient B_2 by v_{FMT} [Eq. (4.19)] grows with increasing L. For not too long spherocylinders, however, the isotropic-nematic transition is well described by the theory with the empirical $\zeta = 1.6$ which is located

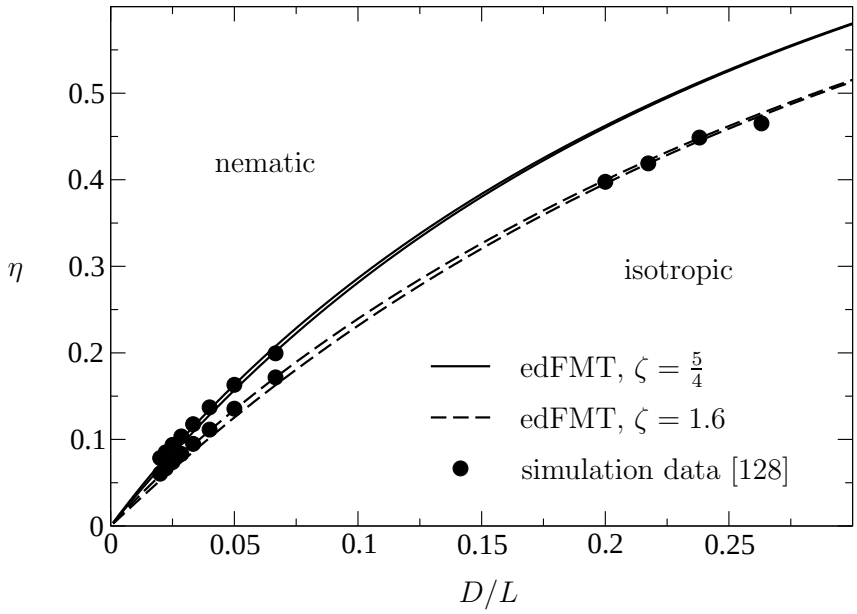

Figure 4.4: Results for the isotropic-nematic transition of hard spherocylinders (length L, diameter D) as obtained from the edFMT excess free energy density Φ_{ed} [Eq. (4.21)] with $\zeta = \frac{5}{4}$ and $\zeta = 1.6$, respectively. For comparison we show simulation data obtained by Bolhuis and Frenkel [128]. The lower (upper) line or symbol indicates the density of the isotropic (nematic) phase at coexistence. The simulation data for modest aspect ratios L/D gives only one point at the transition. η is the spherocylinder packing fraction.

right in the middle of the predicted interval $\left[\frac{5}{4}; 2\right]$ (see Section 4.1.3). One might consider obtaining a more accurate non-empirical value for ζ by using in Eq. (4.20) some appropriate orientational distribution $g(x)$. Then, in turn, one has $\zeta = \zeta[g(x)]$ and the minimization of $\hat{\Omega}$ gets more involved such that the distribution $g(x)$ can no longer be calculated analytically. We do not pursue this road further.

To conclude, we have shown that the edFMT excess free energy Φ_{ed} provides a good description of the location of the isotropic-nematic transition of the hard-spherocylinder fluid. Our theory has to be viewed in contrast with the previous FMTs for non-spherical particles: Rosenfeld's onFMT [29, 30] (corresponding to $\zeta = 0$) does not yield a stable nematic phase at all and the DFT by Cinacchi and Schmid [114], which yields an isotropic-nematic transition, is no longer based on one-center convolutions which makes it computationally more demanding.

4.2.2 Inhomogeneous isotropic hard-spherocylinder fluid

Our edFMT for the non-spherical particles fluids, which is given by Eq. (4.21) supplemented by Eq. (4.22), is derived from considerations in the spirit of Rosenfeld's original FMT [22]. In consequence one can expect the new functional to inherit the ability of yielding accurate results for inhomogeneous fluids without requiring any empirical fitting. Note that our theory contains the new parameter ζ which can *a priori* be chosen freely. However, we provided arguments in Section 4.1.3 that $\zeta = \frac{5}{4}$ should be the most suitable for the isotropic spherocylinder fluid while the nematic fluid should require some larger $\zeta \in \left[\frac{5}{4}; 2\right]$. In Section 4.2.1 we showed that $\zeta = 1.6$ yields the best fit to simulation data for the isotropic-nematic transition for spherocylinders with moderate aspect ratios. For the sake of clearness, we mention again that onFMT corresponds to setting $\zeta = 0$ in Eq. (4.21) which makes it slightly different from Rosenfeld's FMT for non-spherical particle fluids [29, 30] as we use Tarazona's expression Eq. (4.22) for the third term in Eq. (4.21). We have checked that for the calculations performed in the following the effect of the different expressions for the third term is significantly smaller than the effect due to our different choices of ζ.

In order to study the performance of the edFMT for describing inhomogeneous fluids of non-spherical particles we consider hard-spherocylinder fluids at a planar hard wall. We have performed canonical Monte-Carlo (MC) simulations for three systems which differ in the length to diameter ratios $\ell = L/D$ and the bulk packing fractions $\eta = (n_3)_{\text{bulk}}$ of the spherocylinders. Distinguishing the systems by Roman numbers, we used $\ell_{\text{I}} = 2.5$, $\eta_{\text{I}} \simeq 0.346$; $\ell_{\text{II}} = 5.0$, $\eta_{\text{II}} \simeq 0.271$; $\ell_{\text{III}} = 10.0$, $\eta_{\text{III}} \simeq 0.127$. We have simulated fluids contained between two distant planar hard walls located at $z = 0$ and $z = z_{\max}$ with lateral extensions $x_{\max}$ and $y_{\max}$ in the x- and y-directions where we applied periodic boundary conditions. The dimensions for system I are: $z_{\max} = 5.0(L + D)$, $x_{\max} = y_{\max} = 4.0(L + D)$; for system II: $z_{\max} = 4.0(L + D)$, $x_{\max} = y_{\max} = 4.0(L + D)$; and for system III: $z_{\max} = 4.0(L + D)$, $x_{\max} = y_{\max} = 3.0(L+D)$. We have checked that errors caused by the finite extension of the systems can be neglected. In particular the fluid-mediated interaction between the two planar walls is sufficiently small for the chosen values of $z_{\max}$ as to not affect the data. We have performed 100 independent runs for system I and 50 for systems II and III. Each run extended over 10^6 MC steps and at each MC step every particle was selected once on average. The acceptance rate for particle moves was between 40% and 70% being larger the smaller the packing fraction of the system was. The statistical error of the MC data which we show below could be estimated to amount to $\lesssim 1\%$.

The packing fractions had to be kept below certain thresholds beyond which the isotropic hard-spherocylinder fluid wets the wall with a nematic layer (having

a nematic director which lies perpendicular to the wall normal) [129–131]. This wetting scenario is of course amenable to a description with the present edFMT but the corresponding biaxial geometry would complicate the numerical treatment for the minimization of the density functional [Eq. (2.26) with $\mathcal{F}_{\rm ex}$ calculated from $\Phi_{\rm ed}$]. We have therefore restricted ourselves to the uniaxial geometry corresponding to densities below the wetting transition. The particle density is then a function only of the distance z between the center of the spherocylinder and the wall and of the angle $\vartheta \in [0, \pi/2]$ between the cylinder axis and the wall normal. For the numerical minimization of the functional the angle ϑ is discretized as $\vartheta_j = (j - 1)/(\nu - 1) \times \pi/2$, $j = 1, \ldots, \nu$, and the system is treated as a ν-component fluid in which each component has a fixed orientation ϑ_j. We have chosen $\nu = 25$ which makes a reasonable compromise between accuracy and efficiency of the calculation. The spatially varying densities $\rho_j(z)$ corresponding to the respective component have to be smeared out with the different weight functions [Eqs. (4.1), (4.13), and (4.14)] which have to be evaluated for the given orientation ϑ_j. The procedure is expressed formally by Eq. (4.2), where the integration with respect to the orientations gets absorbed in the sum over the ν components. In practice, the calculation requires a "slicing" of the spherocylinder with orientation ϑ_j along planes lying perpendicular to the hard wall. In the given system these are the iso-ρ planes. Roughly speaking, the contribution which a given slice, say at distance z' from the wall, makes to the weighted density $n_\alpha(z)$ is proportional to $\omega_j^{(\alpha)}(z' - z)\rho_j(z')\Delta z$, where $\omega_j^{(\alpha)}(z' - z)$ is an analytically calculated factor and Δz is the interval length corresponding to the discretization in the z-direction. In our calculation $\Delta z = D/100$. We spare the reader the details of calculating the factors $\omega_j^{(\alpha)}(z' - z)$ and only mention that the cut surfaces along the iso-ρ planes correspond either to circles (arising from the capping spheres), ellipses (arising from the cylindrical body), or a combination of both circle and ellipse segments. The minimization of the density functional Eq. (2.26) with the excess free energy density $\Phi_{\rm ed}$ [Eq. (4.21)] is achieved by solving the corresponding Euler-Lagrange equations via iteration. At each step of the iteration, this requires a convolution of the different weight functions $\omega_j^{(\alpha)}$ with the respective partial derivative $\partial\Phi_{\rm ed}/\partial n_\alpha$ which has to be performed in addition to the calculation of the weighted densities $n_\alpha(z)$.

The simulation results for the spherocylinders with $L/D = 2.5$ are shown in Fig. 4.5 (upper panel) for four different orientations ϑ_j. Note that in order to compare with DFT calculations, where $\nu = 25$ fixed orientations are assumed, we have sampled the simulation data such that all the spherocylinders with $\vartheta \in [\vartheta_j - \Delta\vartheta/2, \vartheta_j + \Delta\vartheta/2]$

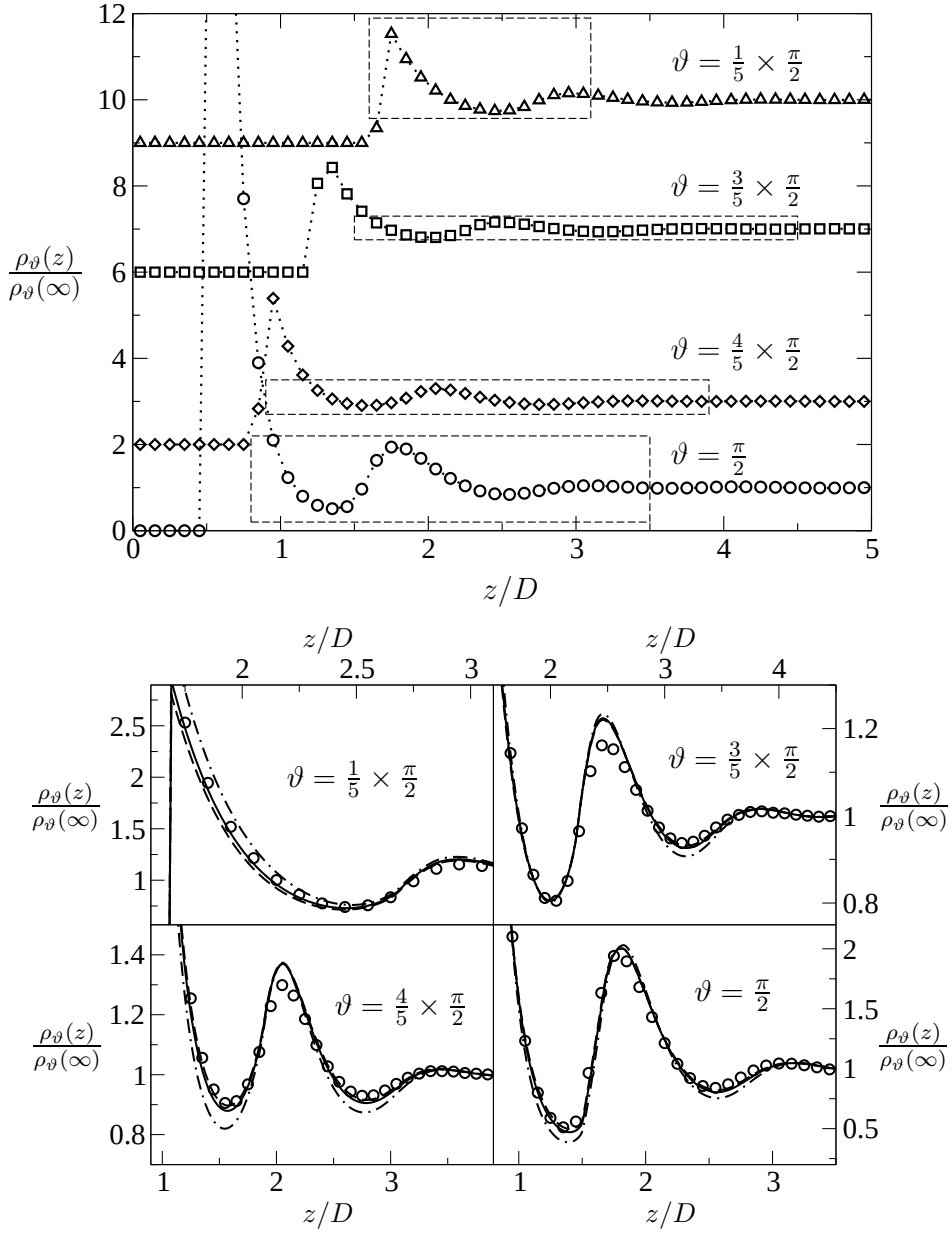

Figure 4.5: Upper panel: Density profiles $\rho_\vartheta(z)$ from MC simulations for a fluid of hard spherocylinders with length-to-diameter ratio $L/D = 2.5$ and bulk packing fraction $\eta \simeq 0.346$ at a hard planar wall which is located in the x-y plane at $z = 0$. The angle between the cylinder axis of the spherocylinder and the surface normal of the wall is denoted by ϑ. Density profiles were obtained for 25 different orientations $\vartheta \in [0, \pi/2]$ only four of which are plotted (see the main text for details). The data have been shifted vertically for clarity. The dotted curves serve as a guide to the eye while the dashed boxes indicate areas which are reconsidered in the lower panel. The peak of the profile for $\vartheta = \pi/2$ has a height of about 25.5. Lower panel: For the areas indicated in the upper panel, we compare the MC data (open circles) with the outcome of the minimization of three different FMT density functionals. These are: onFMT which has $\zeta = 0$ (dashed-dotted lines), edFMT with parameter $\zeta = 1.6$ (dashed lines), and edFMT with parameter $\zeta = \frac{5}{4}$ (solid lines).

and $\Delta\vartheta = \pi/2/(\nu-1)$,[4] are attributed to the density profile $\rho_j(z)$. As a consequence the profiles from the simulations do not jump discontinuously at low z from zero to finite contact values as this is the case for the orientationally discrete DFT results. Instead, there is some interval in which the density increases steeply but continuously. Obviously, the vanishing of the profiles for low z corresponds to the range which is inaccessible to the center of the spherocylinder due to the hard wall. For $L/D = 2.5$ the jump in the profile must occur at $z = 0.5D$ for $\vartheta = \pi/2$ and at $z = 1.75D$ for $\vartheta = 0$ which is consistent with the data. One can observe that spherocylinders which lie parallel to the wall (i.e. $\vartheta \approx \pi/2$) are preferentially adsorbed at the hard wall. This behavior can be interpreted as a precursor of the nematic wetting which occurs at higher bulk packing fractions.

In Fig. 4.5 (lower panel) we compare the MC data with the results from the different FMT density functionals by zooming into the regions which are indicated in the upper panel of the figure. The FMTs describe the MC data quite well for all the different choices of the parameter ζ. In particular, the wavelength of the oscillations is very well captured. While the case $L/D = 2.5$ does not allow one to decide whether edFMT with $\zeta = \frac{5}{4}$ or $\zeta = 1.6$ yields the better description, one can already notice that onFMT ($\zeta = 0$) performs slightly worse as it overestimates the contact density for small ϑ and it underestimates the density at the minima of the oscillations for larger ϑ. As an aside, we mention that underestimating the contact density in a certain range of ϑ must go in hand with overestimating it in another range of ϑ, as long as the bulk pressure is yielded correctly by the theory. This is a consequence of the contact theorem for fluids at hard walls [132] which states that the pressure is obtained as $p = k_\mathrm{B}T\sum_{j=1}^{\nu}\rho_j^\mathrm{c}$, where ρ_j^c is the density of orientation ϑ_j at contact with the hard wall. As the FMTs discussed here are non-local theories they satisfy the contact theorem. Since the bulk pressure p does not depend on ζ, the sum $\sum_{j=1}^{\nu}\rho_j^\mathrm{c}$ yields the same result irrespective of the choice of ζ.

The simulation data for the spherocylinders with $L/D = 5.0$ are plotted in Fig. 4.6 (upper panel). The comparison with FMT results, which we carry out in the lower panel of Fig. 4.6, reveals now clearly the failure of onFMT which grossly overestimates the density profiles with low ϑ while it systematically underestimates the density of the spherocylinders with large ϑ. Concerning the edFMTs with $\zeta = \frac{5}{4}$ and $\zeta = 1.6$ one can see that the former yields a slightly better description of the simulation data—at least for the part of the profiles which is close to the wall. Taking the whole z-range of the profiles into consideration one can argue that both edFMTs describe the data

[4]The "boundary" intervals with $j = 1$ and $j = \nu$ are not centered around $\vartheta_1 = 0$ and $\vartheta_\nu = \pi/2$. These intervals are given by $[0, \Delta\vartheta/2]$ and $[\pi/2 - \Delta\vartheta/2, \pi/2]$.

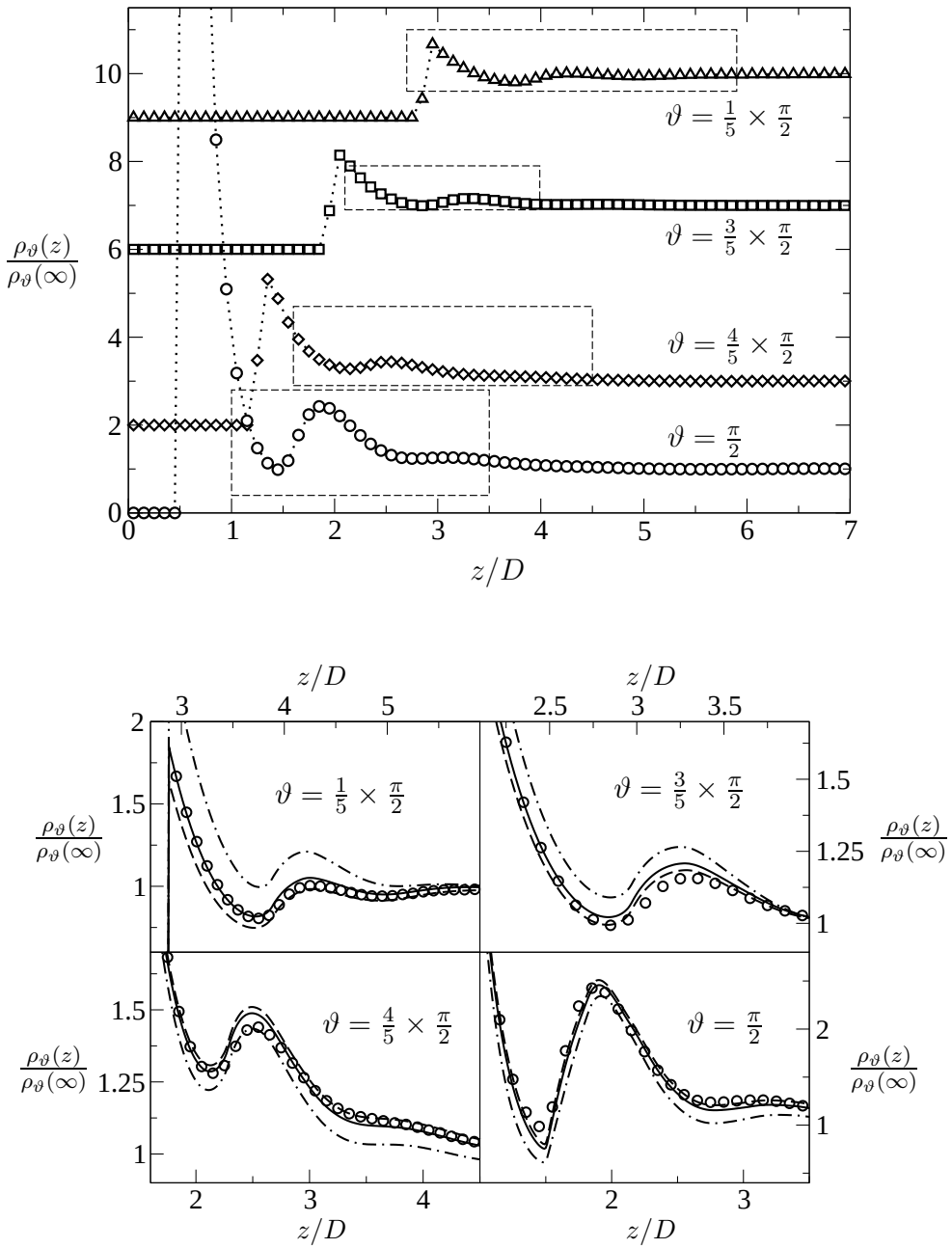

Figure 4.6: Same as Fig. 4.5 but with $L/D = 5.0$ and $\eta \simeq 0.271$. The peak of the profile for $\vartheta = \pi/2$ has a height of about 26.0.

equally well.

Finally we show in Fig. 4.7 (upper panel) the simulation results for a fluid composed of spherocylinders with $L/D = 10.0$ which are the most elongated which we have considered. The detailed comparison with the FMTs in the lower panel of Fig. 4.7 reveals again the same systematic failure of onFMT as in the two previous cases. However, it now becomes possible to clearly discriminate between the edFMTs with $\zeta = \frac{5}{4}$ and $\zeta = 1.6$. While the latter underestimates the data for the orientations for which onFMT overestimates them and vice versa, the edFMT with $\zeta = \frac{5}{4}$ gives a very accurate description of the data over the whole range of distances from the wall and for all spherocylinder orientations. This agreement is particularly encouraging as $\zeta = \frac{5}{4}$ is precisely the value which was obtained in Section 4.1.3 from the requirement that the *isotropic* low-density bulk fluid is optimally described. Apparently the suitability of the value $\zeta = \frac{5}{4}$ for the isotropic fluid survives beyond the low-density limit and in the inhomogeneous fluid.

4.3 Conclusion

Based on a suitable expression of the Mayer f-function for convex hard bodies, which we derive from the Gauss-Bonnet formula, we have introduced a new deconvolution of the Mayer f-function in terms of weight functions. The latter extends a previous deconvolution [29, 30] by the introduction of two tensorial weight functions one of which has already been used in the related context of hard sphere crystals [77]. The second tensorial weight function depends on the deviatoric curvature (i.e. the difference of principal curvatures) and is therefore non-zero only for non-spherical bodies. Using the new deconvolution, we have constructed a FMT free energy functional for the general inhomogeneous hard-body fluid, the extended-deconvolution FMT (edFMT), which can be compared with Rosenfeld's FMT for non-spherical particles (onFMT) [29, 30]. In the following, we summarize the virtues of the new theory.

- edFMT does not require any input apart from the weighted densities, which follow from the deconvolution of the known low-density limit of the excess free energy functional. In principle, the deconvolution can be performed exactly such that the Onsager limit is reproduced for long rods. However, in order to guarantee that the theory can be efficiently treated numerically, we introduce an suitable approximate deconvolution which leaves us with a single free parameter ζ. For an isotropic bulk fluid of hard rods we obtain analytically that $\zeta = \frac{5}{4}$ is optimal, while one can argue that the nematic phase requires some $\zeta \in \left[\frac{5}{4}; 2\right]$. Comparison with simulation data for the isotropic nematic transition

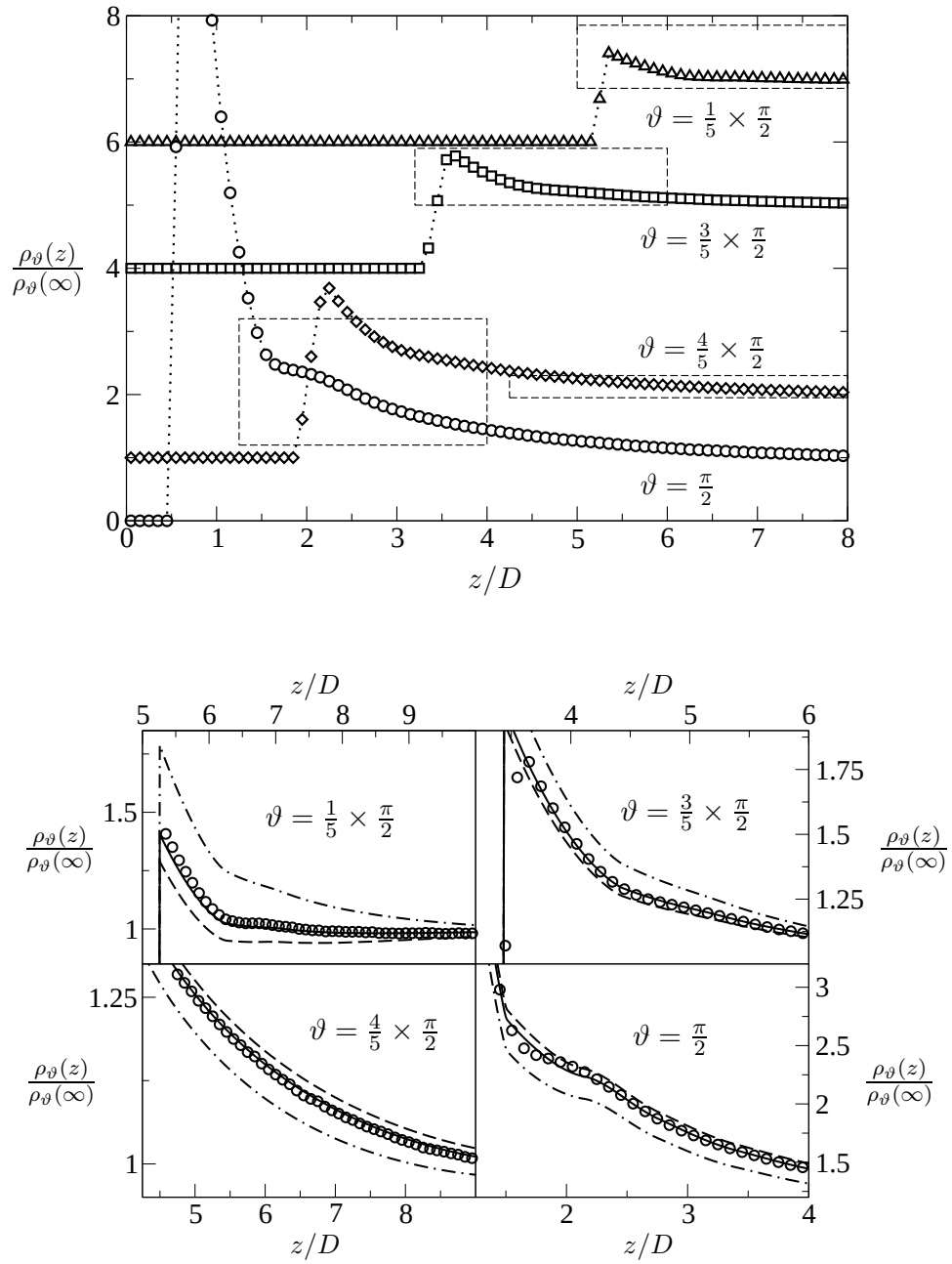

Figure 4.7: Same as Fig. 4.5 but with $L/D = 10.0$ and $\eta \simeq 0.127$. The peak of the profile for $\vartheta = \pi/2$ has a height of about 13.5.

[128] yields indeed $\zeta = 1.6$.

- edFMT yields a stable nematic phase for the hard-spherocylinder fluid—an essential feature of fluids of non-spherical particles which was completely missed by the previous onFMT. Using the parameter $\zeta = 1.6$ the isotropic-nematic transition is located in good agreement with simulation data [128] for not too long spherocylinders.

- edFMT improves upon onFMT with regard to the description of the inhomogeneous isotropic hard-spherocylinder fluid, as we show by comparison with data from Monte-Carlo simulations. In this context, we find the analytical value of $\zeta = \frac{5}{4}$ confirmed.

- In contrast to other FMTs for non-spherical particles [114, 120–123], edFMT is based on weighted densities which can be calculated from one-center convolutions and which depend only on the properties of *one* of the fluid components each. This makes the theory conveniently tractable numerically.

- In the isotropic bulk fluid, edFMT, as its predecessor onFMT, yields the exact second virial coefficient unlike previous theories, which are based on the expansion in some small parameter (e.g. the rod thickness [122]).

- When applied to the hard-sphere fluid, edFMT reduces to Rosenfeld's FMT for hard spheres [22]. However, only one of the tensorial weighted densities vanishes in the limit of spherical particles. The other one is the tensorial weighted density introduced by Tarazona [77] for the description of the hard-sphere crystal. Our work provides thus a motivation for the use of this weighted density for the construction of the functional. If one intends to construct a theory which is continuous for small deviations from sphericity the extended deconvolution *imposes* the use of Tarazona's tensorial weighted density also for spherical particles.

- Our theory is open for further extentions which lead to better agreement with Onsager's limit by the use of tensorial weighted densities with higher rank. Different from other approaches [120–123], these extentions do not require sophisticated geometrical arguments but instead simply follow from expanding our exact expression for the Mayer f-function in a Taylor series.

We want to conclude by mentioning some possible future developments and studies related to edFMT. Obviously, it would be interesting to investigate how the present edFMT performs when applied to phases other than the inhomogeneous isotropic and

the bulk nematic, which have been studied in the present work. In this context, crystalline phases are of particular interest as these are potentially affected by spurious divergences in the free energy functional [98]. It seems moreover worthwhile to study the relation between edFMT and other FMTs which are compatible with Onsager's limit (e.g. spheres and infinitely thin needles [120]) in view also of finding additional arguments for the appropriate choice of ζ. Furthermore, the introduction of tensorial weighted densities of higher rank and the expected related improvement of the performance of the resulting edFMT for long rods might be investigated. Finally, a comparison of the edFMT with different closure relations of the Ornstein-Zernike equation in the spirit of Ref. [133] may be illuminating.

With the DFT for the general hard-body fluid at hand we can proceed to the calculation of solvation free energies of a model protein which is contained in Chapter 5. To this end we shall examine the FMT for non-spherical particles in the light of morphological thermodynamics (see Section 5.1).

Chapter 5

Protein solvation

Predicting native structures of proteins in their cellular environment is a long standing task which has challenged researchers from diverse fields such as biology, chemistry, informatics, and physics. Although principal secondary motifs, namely the α-helix and the β-sheet, have been observed experimentally since the early 1930's [1] and a correct model of these structures in terms of covalent and hydrogen bonds has been presented in 1951 by Pauling and coworkers [2,3], to date no algorithm exists which is able to calculate for an arbitrary input sequence of amino acids how the protein folds, i.e., which secondary motifs different parts of the sequence assume and how these are located in space relative to each other. The reasons for this shortcoming are manifold, including the number of different amino acids (20) with their individual properties, the incomplete knowledge of the details of their interactions, effects coming from the interaction with the solvent, and, notably, the limitations set by the calculation power of today's computers.

Strong interest in the determination of native states is due to the fact that knowledge of a protein's tertiary structure is crucial for understanding its function [6]. Stunningly, tertiary structure of proteins in living organisms can be reduced to an estimated number of only 1,000 basic protein folds [9]. Considering in addition that folds are obtained from the secondary motifs according to a set of "constructional rules" and taking into account their stability against mutation it has been argued that the basic folds might be viewed as primary natural forms which one can speculate to obey physical laws in the spirit of a Platonian model of life [10]. Taking the idea of certain robust motifs in protein folding as a guideline, Banavar and Maritan introduced a simple geometrical model for protein folding which they show to reproduce many of the basic building blocks of real proteins [11,12]. In their model, the protein backbone is viewed as a impenetrable, flexible tube with finite thickness. This has two important consequences: locally, an effective three body interaction is introduced

by the limited local curvature and, globally, a specific interaction of *cylindrical* segments takes effect. While the first feature can in principle be modeled by a chain of tethered spheres with an appropriate three neighbor potential, the second property is genuine to the tube model. To complete the model, an attractive potential perpendicular to the tube axis is introduced mimicking the effect of hydrophobic amino acids. These ingredients are sufficient to drive the model protein into the marginally compact regime where it displays conformations which closely resemble basic folds of real proteins. As the model does not include any chemical details, the results can be considered indeed as "Platonian folds".

The purpose of our investigation is to devise how the solvent effects can be calculated directly rather than taking them into account via the detour of an attractive potential in the above tube model. These solvent effects are crucial for folding [134], in particular due to solvent entropy [24]. Concerning the latter aspect, we are able to extend the results of a recent study by Snir and Kamien [14] to more realistic solvent configurations. For an efficient calculation of solvation free energies we employ the concept of morphological thermodynamics which combines Hadwiger's theorem from integral geometry with DFT for classical fluids (Section 5.1). Both the improved FMT for spheres (Section 3.3) and the FMT for non-spherical particles (Chapter 4) will prove particularly valuable in this context. The proteins are represented within the tube model of Banavar and Maritan with the difference that we do *not* make use of any net attraction between segments of the tube which would imitate the solvent-mediated tendency of the protein to adopt compact conformations. Morphology requires the calculation of certain geometric measures of the protein in a given conformation. This is the subject of Section 5.2.1 where we also give the precise definition of the tube model for the protein. We consider two different types of solvent. In order to study effects which are due to the solvent entropy alone we perform calculations for the hard-sphere solvent (Section 5.2.2). The influence of hydrophilic and hydrophobic side chains is discussed in Section 5.2.3 where we consider a square-well solvent, i.e., a fluid with inter-molecular attraction which can be viewed as a first approximation of water which is *the* solvent in biological systems. Summary and conclusion for this chapter are presented in Section 5.3.

5.1 Morphological thermodynamics

Hadwiger's theorem

We start our presentation of morphological thermodynamics by introducing Hadwiger's theorem from integral geometry. To this end, consider a body $\mathcal{B}$ (a closed

and bounded set) in $\mathbb{R}^3$ which is going to represent, at a later stage, the protein immersed in the solvent. Concerning a characterization of $\mathcal{B}$ in terms of simple numbers, the volume $V(\mathcal{B})$ of $\mathcal{B}$ appears to be an obvious choice. $V(\mathcal{B})$ has a number of familiar (and obvious) properties, which include: (i) *motion invariance*, i.e., for every rotation and translation g we have $V(g\mathcal{B}) = V(\mathcal{B})$; (ii) *continuity*, i.e., for every sequence of bodies $\mathcal{B}_n$ which converges (w.r.t. the Hausdorff metric) to $\mathcal{B}$ for $n \to \infty$ we have that $V(\mathcal{B}_n) \to V(\mathcal{B})$; and (iii) *additivity*, *i.e.*, for the union $\mathcal{B}_1 \cup \mathcal{B}_2$ of two bodies $\mathcal{B}_1$ and $\mathcal{B}_2$ we have $V(\mathcal{B}_1 \cup \mathcal{B}_2) = V(\mathcal{B}_1) + V(\mathcal{B}_2) - V(\mathcal{B}_1 \cap \mathcal{B}_2)$ where $\mathcal{B}_1 \cap \mathcal{B}_2$ is the intersection of $\mathcal{B}_1$ and $\mathcal{B}_2$.

For a more precise description of $\mathcal{B}$ we include the surface area $A(\mathcal{B})$ into our consideration. The question arises whether properties (i), (ii), and (iii) hold for $A(\mathcal{B})$ as well. It turns out that motion invariance and additivity are still fulfilled, while continuity is violated [23]. As an example, take $\mathcal{B}$ to be a torus which we approximate by a series of tori $\mathcal{B}_n$ which are not closed but have a small opening becoming narrower and narrower with increasing n. Then we have that the $\mathcal{B}_n$ converge to $\mathcal{B}$ but $A(\mathcal{B}_n)$ does not converge to $A(\mathcal{B})$ due to the opening of the tori $\mathcal{B}_n$ which gives a finite, additional contribution to the surface area. However, we can weaken the requirement of continuity by asking it to hold only in the case of sets $\mathcal{B}_n$ and $\mathcal{B}$ which are *convex*. This property is termed *conditional continuity* and it is fulfilled for both $V(\mathcal{B})$ and $A(\mathcal{B})$.

Refining the characterization of $\mathcal{B}$ further leads us to introducing the integral mean curvature $C(\mathcal{B})$ and the integral Gaussian curvature $X(\mathcal{B})$ which are defined as

$$C(\mathcal{B}) = \int\limits_{\partial\mathcal{B}} \mathrm{d}\mathbf{r}\, \frac{1}{2}\left(\frac{1}{R_I} + \frac{1}{R_{II}}\right), \quad X(\mathcal{B}) = \int\limits_{\partial\mathcal{B}} \mathrm{d}\mathbf{r}\, \frac{1}{R_I R_{II}}. \tag{5.1}$$

Here R_I and R_{II} denote the (position-dependent) principal radii of curvature which are defined on the surface $\partial\mathcal{B}$ of $\mathcal{B}$. $C(\mathcal{B})$ has the dimension of a length while $X(\mathcal{B})$ is dimensionless. $X(\mathcal{B})/4\pi$ equals the Euler characteristic χ of $\mathcal{B}$. For instance, $\chi = 1$ for all bodies $\mathcal{B}$ which are topologically equivalent to a sphere. One can show that $C(\mathcal{B})$ and $X(\mathcal{B})$, like $V(\mathcal{B})$ and $A(\mathcal{B})$, have the properties of motion invariance, conditional continuity, and additivity. As an aside, we mention that the four measures which we have introduced are (up to constant factors) the Minkowski measures of the body $\mathcal{B}$.

The remarkable result which was obtained by Hadwiger is that in three dimensions $V(\mathcal{B})$, $A(\mathcal{B})$, $C(\mathcal{B})$, and $X(\mathcal{B})$ are, except for linear combinations, the *only* measures of $\mathcal{B}$ with the above properties. This result leads to Hadwiger's theorem: *every functional φ, defined on the set of bodies $\mathcal{B}$ in $\mathbb{R}^3$, and having the properties of motion*

invariance, conditional continuity, and additivity, can be cast to the form $\varphi(\mathcal{B}) = c_V V(\mathcal{B}) + c_A A(\mathcal{B}) + c_C C(\mathcal{B}) + c_X X(\mathcal{B})$ *with constant (i.e. geometry-independent) coefficients* c_V, c_A, c_C, *and* c_X [23].

Application to fluids

Although proved about fifty years ago, Hadwiger's theorem has not been exploited for physics before the mid-1990's when it was used in the field of complex fluids for a study of microemulsions [20]. A further early study where the term "morphological thermodynamics" appeared is about the phase behavior of composite media [135]. Only recently, detailed quantitative analysis has settled the approach in the field of hard-sphere fluids [93] and simple fluids with intermolecular attraction [97, 136].

The idea behind morphological thermodynamics, also termed the morphometric approach, is to identify a physical quantity of interest which can take the place of the functional φ appearing in Hadwiger's theorem. In the present study, this quantity is the solvation free energy F_{sol} of a protein under consideration. As mentioned above, the protein is going to play the role of the body $\mathcal{B}$ in the theorem. The crucial point, however, for applying Hadwiger's theorem is to check whether the assumptions made about φ are fulfilled in the present physical context, i.e., for F_{sol}. To this end, imagine a protein immersed in a solvent. Concerning motion invariance we note that F_{sol} does not depend on the protein's orientation and position as long as the bulk solvent itself has rotational and translational invariance. This is the case for all the solvents which are considered in the following. Conflicts with this assumption would arise, e.g., in nematic liquids, magnetic liquids or liquids which experience an anisotropic external potential. The second property of φ is conditional continuity. As an example where continuity of F_{sol} is violated consider a close packing of spheres (the solvent) around a large convex body $\mathcal{B}$ (the solute). It is then possible to choose $\mathcal{B}$ such that the elements of a sequence $\mathcal{B}_n$ (converging to $\mathcal{B}$) allow for packing more solvent spheres into the system then this is possible for $\mathcal{B}$. Hence F_{sol} would vary discontinuously in the limit $\mathcal{B}_n \to \mathcal{B}$. However, in the case where close-packed spheres figure as the solvent already the requirement of motion invariance is violated. For solvents which are in the liquid phase we do not see how conditional continuity could be violated. Finally, additivity of φ is required. Additivitity can actually be understood as a generalization of the thermodynamic concept of extensivity to finite-sized objects. In this sense additivity provides the crucial link between the functional φ from Hadwiger's theorem and the thermodynamic quantity F_{sol}. But does F_{sol} obey additivity? A counter-example is readily constructed: consider an extended protein in a configuration displaying a loop which causes two segments

of the backbone to approach closely in space while their distance measured along the protein backbone is large. The essence of the example, i.e. the confinement of a portion of the solvent induced by distant parts of the backbone, is captured in a simple model where we replace the single solute protein by a complex which consists of two disjoint spheres. Applied to this setup, additivity implies that F_{sol} is independent of the distance between the two spheres immersed in the solvent. It is, however, a well known fact that the two bodies do experience a solvent mediated force (solvation force) when their distance becomes comparable to the correlation length of the solvent [137]. Thus, additivity can only be fulfilled if the distance between the solute spheres is large compared to the correlation length of the solvent. As a consequence, additivity breaks down for fluids possessing long-ranged correlations, e.g., fluids near the critical point and situations of wetting or drying (for details on the latter aspect see Refs. [138–140]). As far as the solvents considered in this work are concerned, correlations decay rapidly, i.e., within a few particle diameters. Therefore, we can assume additivity to hold approximatively. The related error will be analyzed at the end of this section.

With these remarks concerning the assumptions of Hadwiger's theorem in mind, we apply the theorem to the solvation free energy F_{sol} of a protein in a given conformation to which we assign the volume V, the surface are A, the integral mean curvature C and the integral Gaussian curvature X. Adopting a physically motivated notation for the coefficients, the morphometric form for F_{sol} reads

$$F_{\mathrm{sol}} = pV + \sigma A + \kappa C + \bar{\kappa} X. \tag{5.2}$$

According to the theorem, the coefficients are independent of the geometry of the protein conformation which is considered. In the present context, we identify p as the solvent pressure and σ as the interfacial tension related to the solvent covering a planar segment of the protein surface. The bending rigidity κ characterizes the influence on F_{sol} of curving the protein surface. Finally, $\bar{\kappa}$ couples to the topological invariant X which, roughly speaking, counts the cavities and holes containing portions of solvent which are disconnected from the bulk fluid in the given protein configuration. This contribution, which becomes important for the study of fluids in porous media [141], will turn out to be irrelevant for our study of the model protein. All coefficients have in common that they are related to solvent properties depending only on the temperature and the chemical potential and, except for the pressure p, on the specific interaction between the protein and the solvent. The quantities p, σ, κ, and $\bar{\kappa}$ are referred to as *thermodynamic coefficients* which emphasizes their independence of the solute geometry.

Thermodynamic coefficients for the hard-sphere solvent

Morphometry is obviously a very useful tool for the calculation of the solvation free energy F_{sol} of complexly shaped solutes as the form Eq. (5.2) allows one to divide the calculation into two tasks. Instead of performing DFT calculations involving the solvent under the potentially complicated external potential V_{ext}, which is induced by the solute (cf. the functional Ω [Eq. (2.26)]), the thermodynamic coefficients can be obtained from DFT calculations in a simple test geometry where solutes with simple shapes (spheres of different radii, for instance) are considered. This task completed, the geometric measures for a range of complexly shaped solutes (or solute configurations) can be computed, independently of the solvent properties. Finally, the two ingredients are combined according to Eq. (5.2) in order to yield the solvation free energy F_{sol}. For instance, the morphometric approach has been applied successfully to the calculation of F_{sol} for various conformations of a protein represented in the fused-spheres model [142] and to the thermodynamics of fluids which are contained in porous media [141].

In the case where contributions due to solvent *entropy* are studied it is expedient to use as a solvent the simple hard-sphere fluid. For the hard-sphere fluid the application of morphometric thermodynamics is even more favorable than in the general case which we have sketched above. This is due to the fact that accurate *analytical* expressions for the thermodynamic coefficients can be derived from FMT for the hard-sphere fluid. Thus it is not even necessary to perform DFT calculations in the simple test geometry from which the coefficients can be extracted. This advantage is particularly valuable when one is interested in F_{sol} for various solvent conditions (for hard spheres the relevant parameter which regulates solvent conditions is the packing fraction η). The calculation of the analytical expressions for p, σ, κ, and $\bar{\kappa}$ is shown in the following.

As we have mentioned earlier in this work the connection between the morphometric form [Eq. (5.2)] and FMT can be established by making use of the generalized FMTs for fluids consisting of arbitrarily shaped hard particles (see Chapter 4). In a first step, we denote by Φ a FMT free energy density of the general hard body fluid which we shall specify at a later stage. For the moment we make the only assumption that Φ is a function of the weighted densities $n_0, \ldots, n_3$, calculated with the weight functions from Eq. (4.1), which allow also for fluid components with shapes other than the spherical one. For the following calculations only the bulk expression for Φ is required. As the vectorial weighted densities $\overrightarrow{n}_1$ and $\overrightarrow{n}_2$ vanish in the bulk we do not need to include them into the set of variables of Φ. The same holds for the tensorial weighted density $\overleftrightarrow{n}_1$ [Eq. (4.13)] which vanishes in the case of the isotropic

bulk fluid. There, also the weighted density $\overleftrightarrow{n}_2$ [Eq. (4.14)] can be expressed by the scalar quantity n_2 so that accounting for a dependence of Φ on $\overleftrightarrow{n}_2$ would not yield any additional information. It can be shown, moreover, that for the isotropic bulk fluid Tarazona's third term for Φ [Eq. (4.21) with Eq. (4.22)] and Rosenfeld's original expression for the third term [Eq. (3.16)] are equivalent. In conclusion, for the following derivation it suffices to assume that Φ is a function only of $n_0, \ldots, n_3$.

For the derivation of the thermodynamic coefficients p, σ, κ and $\bar{\kappa}$ we follow the ideas of Refs. [88, 124] which make use of the applicability of FMT to mixtures. The basic idea is to consider the complex of the hard-sphere solvent (radius R, packing fraction η) on the one hand and the solute body $\mathcal{B}$ on the other hand as two components of a binary bulk mixture. As only a single solute particle $\mathcal{B}$ is contained in the system the corresponding particle number density $\rho_{\mathcal{B}}$ vanishes for the infinite system, i.e. $\rho_{\mathcal{B}} \to 0$. Using moreover that F_{sol} is precisely the excess chemical potential $\mu_{\mathcal{B}}^{\mathrm{ex}}$ of species $\mathcal{B}$, which is obtained as the partial derivative of the mixture excess free energy density Φ with respect to $\rho_{\mathcal{B}}$, we find

$$\begin{aligned} \beta F_{\mathrm{sol}} &= \beta\mu_{\mathcal{B}}^{\mathrm{ex}} = \lim_{\rho_{\mathcal{B}}\to 0} \frac{\partial\Phi}{\partial\rho_{\mathcal{B}}} \\ &= \frac{\partial\Phi}{\partial n_3}\,\tilde{V} + \frac{\partial\Phi}{\partial n_2}\,\tilde{A} + \frac{1}{4\pi}\frac{\partial\Phi}{\partial n_1}\,\tilde{C} + \frac{1}{4\pi}\frac{\partial\Phi}{\partial n_0}\tilde{X}\,. \end{aligned} \tag{5.3}$$

The result is obtained similarly to Eq. (3.12) which we have calculated for the derivation of Rosenfeld's FMT for spheres. It should be emphasized, however, that identifying in Eq. (5.3) the volume $\tilde{V}$, the surface area $\tilde{A}$, the integral mean curvature $\tilde{C}$, and the integral Gaussian curvature $\tilde{X}$ of the *non-spherical* body $\mathcal{B}$ becomes possible only with the generalization of the weighted densities $n_0, \ldots, n_3$ to non-spherical particles (see Eq. (4.1) for the corresponding weight functions). Different from Eq. (3.12), the partial derivatives of Φ in Eq. (5.3) are evaluated for the one-component hard-sphere fluid (radius R, packing fraction η) which is a consequence of considering the solute component at infinite dilution ($\rho_{\mathcal{B}} \to 0$).

We have decorated the geometric measures of the solute body $\mathcal{B}$ with tildes in order to indicate that these are calculated with respect to the *physical* surface of $\mathcal{B}$. It should, however, be noted that the effect of $\mathcal{B}$ onto the solvent has to be translated into the action of an external potential V_{ex} which is defined with respect to the centers of the solvent particles. In other words, the relevant surface for the calculation of the geometric measures figuring in Eq. (5.3) is given by the *parallel* surface of $\mathcal{B}$ which lies at a distance R (solvent particle radius) to the physical surface of $\mathcal{B}$. The parallel surface delimits the space which is accessible to the solvent spheres. This is meaningful in particular when portions of the solvent are trapped in cavities formed by the solute. In this scenario, the parallel surface vanishes for cavities which are

so small that they cannot hold a solvent particle. Obviously, such a cavity does not contribute to F_{sol} which underlines why the use of the parallel surface is appropriate. A concrete example illustrating these arguments is presented at the end of this section where we discuss the limits of morphological thermodynamics. For convex solutes the geometric measures V, A, C, and X, as obtained for the parallel surface of $\mathcal{B}$ at distance R, can be calculated from $\tilde{V}$, $\tilde{A}$, $\tilde{C}$, and $\tilde{X}$ by applying Steiner's formula [23]:

$$\begin{aligned} V &= \tilde{V} + R\tilde{A} + R^2\tilde{C} + \tfrac{1}{3}R^3\tilde{X}\,, \\ A &= \tilde{A} + 2R\tilde{C} + R^2\tilde{X}\,, \\ C &= \tilde{C} + R\tilde{X}\,, \\ X &= \tilde{X}\,. \end{aligned} \tag{5.4}$$

Steiner's formula can be used in order to match the result for F_{sol} as obtained from the FMT excess free energy in Eq. (5.3) with the initial morphometric form given in Eq. (5.2). As a result, we can identify the thermodynamic coefficients, calculated for the parallel surface, with certain linear combinations of the partial derivatives of Φ. We find that

$$\begin{aligned} \beta p &= \frac{\partial\Phi}{\partial n_3}\,, \\ \beta\sigma &= \frac{\partial\Phi}{\partial n_2} - R\frac{\partial\Phi}{\partial n_3}\,, \\ \beta\kappa &= \frac{1}{4\pi}\frac{\partial\Phi}{\partial n_1} - 2R\frac{\partial\Phi}{\partial n_2} + R^2\frac{\partial\Phi}{\partial n_3}\,, \\ \beta\bar{\kappa} &= \frac{1}{4\pi}\frac{\partial\Phi}{\partial n_0} - \frac{R}{4\pi}\frac{\partial\Phi}{\partial n_1} + R^2\frac{\partial\Phi}{\partial n_2} - \frac{1}{3}R^3\frac{\partial\Phi}{\partial n_3}\,. \end{aligned} \tag{5.5}$$

The relation for the pressure is precisely the scaled particle relation [Eq. (3.13)] which we have used in Chapter 3 for the derivation of Rosenfeld's FMT. In the following, we refer to the above analytical results for the thermodynamic coefficients as the outcome of the "bulk route".

We give the explicit results for the coefficients only for the case of the new excess free energy density Φ_{WBII} [Eq. (3.43)]:

$$\begin{aligned} \frac{\beta p_{\mathrm{WBII}}}{\rho} &= \frac{1+\eta+\eta^2-\eta^3}{(1-\eta)^3}\,, \\ \frac{\beta\sigma_{\mathrm{WBII}}}{R\rho} &= -\frac{1+2\eta+8\eta^2-5\eta^3}{3(1-\eta)^3} - \frac{\ln(1-\eta)}{3\eta}\,, \\ \frac{\beta\kappa_{\mathrm{WBII}}}{R^2\rho} &= \frac{4-10\eta+20\eta^2-8\eta^3}{3(1-\eta)^3} + \frac{4\ln(1-\eta)}{3\eta}\,, \\ \frac{\beta\bar{\kappa}_{\mathrm{WBII}}}{R^3\rho} &= \frac{-4+11\eta-13\eta^2+4\eta^3}{3(1-\eta)^3} - \frac{4\ln(1-\eta)}{3\eta}\,. \end{aligned} \tag{5.6}$$

We want to highlight that the pressure p_{WBII} equals precisely the quasi-exact CS pressure [Eq. (3.19)]. This is an important consequence of constructing the novel mixture equation of state [Eq. (3.34)], which underlies the WBII version of FMT, based on the requirement of self-consistency [see Eq. (3.32)]. In contrast, the original White-Bear version of FMT, which is based on the a different mixture generalization of the CS pressure [the BMCSL equation of state, Eq. (3.25), to be precise] does not possess this feature of self-consistency, i.e. the derivative of Φ_{WB} with respect to n_3 does *not* yield exactly the CS pressure [25].

As we have mentioned earlier, results for the thermodynamic coefficients can be obtained alternatively by performing DFT calculations for solutes in a simple test geometry. The test geometry we choose here is the case where the solute particle $\mathcal{B}$ is a single hard sphere $\mathcal{S}$ of radius R_{s} immersed in a pure fluid of hard spheres with radius R and bulk density ρ_{bulk}. The solvation free energy F_{sol} equals the change in grand potential $\Delta\Omega$ due to the insertion of the sphere $\mathcal{S}$. In order to obtain $\Delta\Omega$ we minimize the density functional Ω [Eq. (2.26)] using an excess free energy $\mathcal{F}_{\mathrm{ex}}$ which is calculated from a given FMT expression (Φ_{RF}, Φ_{WB}, or Φ_{WBII}). The solute enters the calculations via the use of an appropriate external potential in the functional Ω. Using the equilibrium density profile $\rho(\mathbf{r})$ one can calculate $\Delta\Omega = \Omega[\rho(\mathbf{r})] - \Omega[\rho_{\mathrm{bulk}}]$. By performing the calculation for different radii R_{s} of the solute sphere the function $F_{\mathrm{sol}}(R_{\mathrm{s}}) = \Delta\Omega(R_{\mathrm{s}})$ is obtained numerically. The extraction of the thermodynamic coefficients p, σ, κ, and $\bar{\kappa}$ from the values $F_{\mathrm{sol}}(R_{\mathrm{s}})$ as obtained by minimizing the functional Ω is achieved by fitting Eq. (5.2) to the numerical DFT data. This fit was performed for DFT data (using Φ_{WB} or Φ_{WBII}) in the range $R_{\mathrm{s}} \in [2R, 10R]$ for various values of the packing fraction of the fluid. Indeed, we find the assumption made by Eq. (5.2) concerning the R_{s}-dependence of F_{sol} clearly confirmed and in accordance with previous results [93]. The thermodynamic coefficients which result from the fitting of Eq. (5.2) to the numerical DFT data are referred to in the following as obtained via the "minimization route".

We now compare the results from the bulk and minimization routes as obtained for the different versions Φ_{WB} and Φ_{WBII} of FMT. In Fig. 5.1 we show our results for the thermodynamic coefficients calculated from the new functional Φ_{WBII}. The agreement for p is perfect by construction of the equation of state, Eq. (3.34), and very good for the surface tension σ. The analytical result for σ has already been considered in Section 3.2 where a comparison with simulation data revealed σ_{WBII} to be of high accuracy for intermediate and high packing fractions of the hard-sphere solvent. At low packing fractions, however, we found a small deviation from the exact low density limit of σ [83]. Only for the bending rigidities κ and $\bar{\kappa}$ a slight inconsistency between

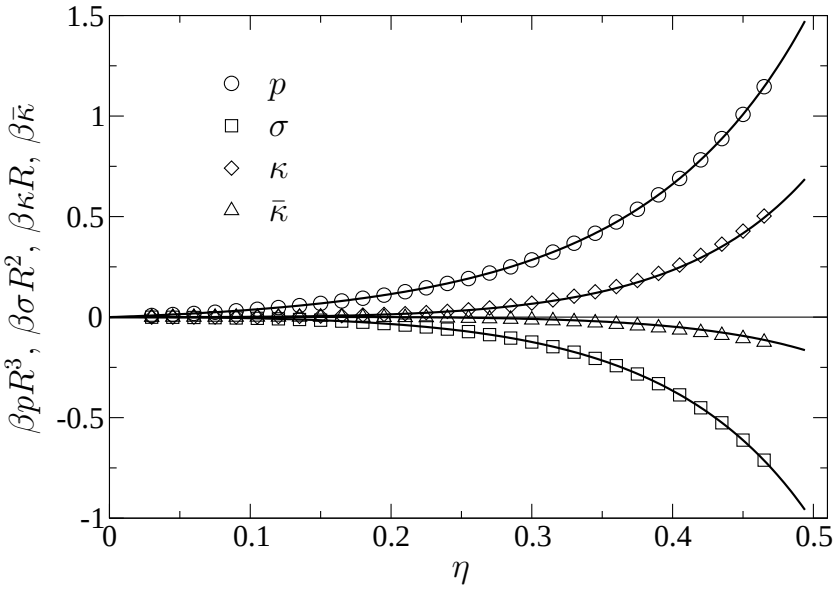

Figure 5.1: Results for the four thermodynamic coefficients p, σ, κ, and $\bar{\kappa}$ of the hard-sphere fluid are shown as obtained from the new excess free energy density Φ_{WBII}, Eq. (3.43). The analytical expressions given in Eqs. (5.6) are denoted by the lines, while the results from the minimization route are given by the symbols. η is the packing fraction. At $\eta \approx 0.494$ the hard-sphere fluid freezes.

the bulk and the minimization route appears. However, this inconsistency remains below 1% at high values of η and we conjecture from the very good agreement of σ_{WBII} with simulation data that also κ_{WBII} and $\bar{\kappa}_{\mathrm{WBII}}$ deliver accurate expressions for the thermodynamic coefficients of the hard-sphere fluid. With Eq. (5.6) we have obtained a set of analytical expressions for the thermodynamic coefficients which are more accurate than previous suggestions, namely the results calculated from the original White-Bear version or those from Rosenfeld's FMT.

As an illustration, we plot in Fig. 5.2 the difference of various results for the four thermodynamic coefficients, p, σ, κ, and $\bar{\kappa}$, from the analytical expressions [Eq. (5.6)] of the WBII version. Again, we find a high degree of self-consistency of the new functional Φ_{WBII} (symbols, except the crosses in Fig. 5.2). In contrast, the inconsistency of the original White-Bear version, which can be read off from the distance between the dashed line and the crosses in Fig. 5.2, is considerably larger and appears even for the pressure. The analytical expressions derived in the bulk route from Φ_{WB} are therefore of lower quality than Eqs. (5.6), which manifests itself

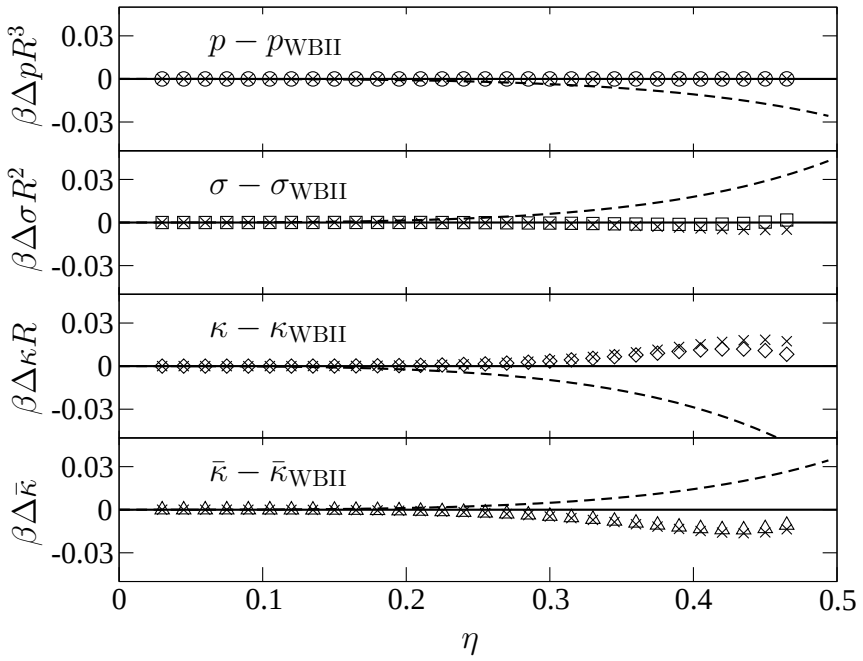

Figure 5.2: Various results for the four thermodynamic coefficients, p, σ, κ, and $\bar{\kappa}$. Shown are the differences of these coefficients obtained by various routes and theories to the analytical WBII results [Eq. (5.6)], cf. the lines in Fig. 5.1. The symbols (except the crosses) denote the WBII results from the minimization route. For comparison, we also show results from the original White-Bear version: those from the bulk route are plotted as dashed lines while the crosses denote the outcome of the minimization route.

also in their poorer agreement with simulations (see Section 3.2). The fact that the results from the minimization route are so close for the two versions of FMT is a direct consequence of the strong similarity of the corresponding density profiles. This observation can be rationalized by noting that for the pure fluid the contact values of the density profile at a planar wall (and hence the bulk pressure) coincide for both versions of FMT as the underlying one-component equation of state is the CS expression in both cases. Concerning the thermodynamic coefficients as obtained from Rosenfeld's excess free energy density Φ_{RF} [Eq. (3.16)], we mention that p_{RF} follows the PY compressibility result [Eq. (3.18)] which quantitatively differs from simulations so that the analytical expressions from the bulk route only yield a semi-quantitative description of the thermodynamic coefficients beyond the low-density

limit. Surprisingly, the agreement between the bulk and the minimization route is comparable to that of Φ_{WB} except for the pressure where Φ_{RF} is consistent by construction [97]. Intuitively, one might expect a better agreement for Φ_{RF} than for Φ_{WBII} because the former is self-consistent on the level of the pressure for arbitrary mixtures and not just for the pure fluid. The interesting observation that consistency between the bulk and minimization route is relatively low for Φ_{RF} will be encountered again in the following where we consider the contact density of the hard-sphere fluid at a curved hard wall.

The contact density of the hard-sphere fluid at a hard wall is connected to the normal derivative of the grand potential Ω [93]. The case of interest here is again a hard-sphere fluid (radius R, packing fraction η) around a sphere $\mathcal{S}$ with radius R_{s}. Due to the symmetry of the problem, the normal derivative of Ω reduces to a derivative with respect to R_{s} at constant chemical potential. It can be calculated from the density functional $\Omega[\rho(\mathbf{r})]$, where $\rho(\mathbf{r})$ is the equilibrium density profile. This leads us to

$$\frac{\partial\Omega}{\partial R_{\mathrm{s}}} = \int \mathrm{d}\mathbf{r}\, \frac{\delta\Omega[\rho(\mathbf{r})]}{\delta\rho}\frac{\partial\rho(\mathbf{r})}{\partial R_{\mathrm{s}}} + \int \mathrm{d}\mathbf{r}\, \rho(\mathbf{r})\frac{\partial V_{\mathrm{ext}}(\mathbf{r})}{\partial R_{\mathrm{s}}}\,. \tag{5.7}$$

The first integral vanishes due to the equilibrium condition for $\rho(\mathbf{r})$, i.e. $\delta\Omega/\delta\rho = 0$. The derivative of the external potential gives rise to a δ-peak located at a distance R from the physical hard wall (cf. the introduction of the parallel surface above), and one finds [143]

$$\beta\,\frac{\partial\Omega}{\partial R_{\mathrm{s}}} = 4\pi(R_{\mathrm{s}}+R)^2\rho_{\mathrm{c}} \tag{5.8}$$

where ρ_{c} is the contact value of the density of the fluid at the sphere $\mathcal{S}$. Using the morphometric form Eq. (5.2) for F_{sol}, the grand potential Ω of the fluid containing the sphere $\mathcal{S}$ is $\Omega(R_{\mathrm{s}}) = -pV_{\mathrm{tot}} + F_{\mathrm{sol}}$, where V_{tot} is the total volume of the system which is independent of R_{s}. When the morphometric expression for $\Omega(R_{\mathrm{s}})$ is inserted into Eq. (5.8) one obtains for the contact density ρ_{c}

$$\rho_{\mathrm{c}} = \beta p + \frac{2\beta\sigma}{R_{\mathrm{s}}+R} + \frac{\beta\kappa}{(R_{\mathrm{s}}+R)^2}\,. \tag{5.9}$$

For $R_{\mathrm{s}} \to \infty$ the planar wall contact theorem $\rho_{\mathrm{c}} = \beta p$ is recovered and for finite values of R_{s} the contact density is lowered as has to be expected for a convex surface.

We show results for the contact density ρ_{c} of a hard-sphere fluid with packing fraction $\eta = 0.4$ as a function of the radius R_{s} in Fig. 5.3. The symbols are the contact densities obtained from the density profiles which were calculated by minimizing numerically the density functional Eq. (2.26) which uses one the three FMT excess free energy densities. The lines in Fig. 5.3 show the morphometric prediction according to Eq. (5.9) with the analytical expressions for the thermodynamic coefficients

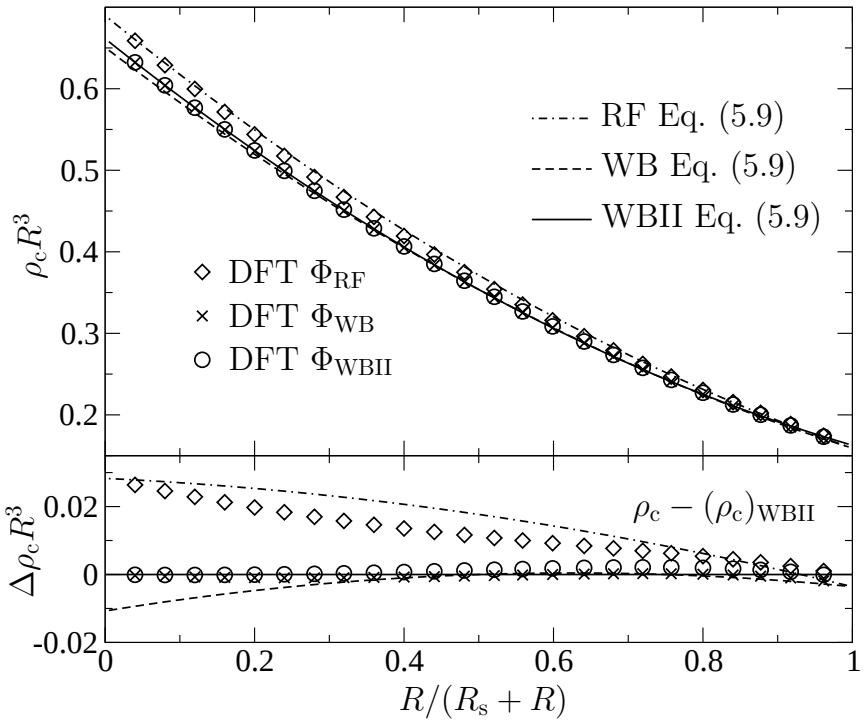

Figure 5.3: Contact value $\rho_{\rm c}$ of the density of a hard-sphere fluid (radius R, packing fraction $\eta = 0.4$) at a single sphere with radius $R_{\rm s}$. We show results obtained from the excess free energy densities $\Phi_{\rm RF}$ [Eq. (3.16)], $\Phi_{\rm WB}$, and $\Phi_{\rm WBII}$ [Eq. (3.43) and below], respectively. We compare results from the numerical minimization of the density functional Eq. (2.26) (symbols) with the morphometric prediction (lines) according to Eq. (5.9).

from the different versions of FMT (see the above explanation of the bulk route). Our first observation is that the numerical results from $\Phi_{\rm WB}$ and $\Phi_{\rm WBII}$ are nearly indistinguishable and indeed in the planar wall limit, $R_{\rm s} \to \infty$, the data coincide by construction of the functionals. Taking this fact into account, it is understandable that the results for $\rho_{\rm c}$ at finite values of $R_{\rm s}$ are very similar. The numerical data for $\Phi_{\rm RF}$ tends towards the PY pressure for $R_{\rm s} \to \infty$ which is known to overestimate the actual pressure in the hard-sphere fluid for sufficiently high values of η. In the limit $R_{\rm s} \to 0$ (point-like object) the data from the three versions of FMT are close.

Comparing with the analytical predictions from morphometry, we find very good agreement between the results from $\Phi_{\rm WBII}$ over the whole interval of $R_{\rm s}$. Only for very small radii $R_{\rm s}$ a slight deviation is visible. Therefore, the new functional im-

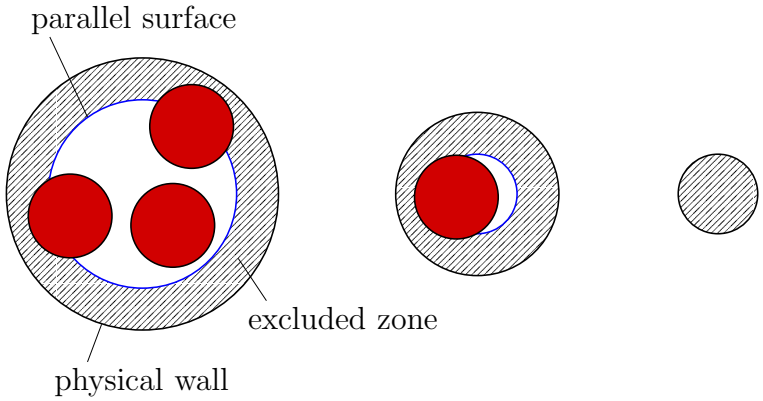

Figure 5.4: 2D sketch of solvent particles (in red) inside a cavity. When the size of the cavity is decreased, a singular point is reached at which the solvent has to be squeezed out of the cavity. This singularity is reflected by the vanishing of the parallel surface (in blue) which is constructed at distance R (solvent radius) from the physical wall.

proves upon the results obtained from the original White Bear version of FMT, which performs well at small radii, but leads to some error at large values of R_s due to the the pressure inconsistency of Φ_WB. As mentioned above for the thermodynamic coefficients, a rather poor agreement in the case of Rosenfeld's FMT is also observed for the contact density. While the approach is consistent for large values of R_s by construction of the functional, in the range of smaller values of R_s a deviation is clearly visible. This behavior has been observed previously [88]. We find this fact remarkable because it shows that, from the point of view of self-consistency on the level of σ, κ, and $\bar{\kappa}$, the new hard-sphere mixture equation of state [Eq. (3.34)] is better suited for an implementation within FMT than the PY mixture equation of state Eq. (3.17) itself. This is even more surprising as the latter is characterized by full consistency for mixtures on the level of the pressure p, while pressure consistency of Eq. (3.34) is guaranteed only for the one-component fluid.

Limits of morphological thermodynamics

We have mentioned above that the morphometric form for F_sol [Eq. (5.2)] constitutes, in principle, an excellent tool for efficient free energy calculations over a large set of protein configurations. The task of determining solvent properties can be shifted to a simple test geometry and has to be completed only once. The computational effort for obtaining the four geometric measures and combining them according to Eq. (5.2) is significantly lower than performing calculations which treat the solvent in a complex

geometry. But how accurate is the morphometric form for $F_{\rm sol}$? Recent calculations using DFT of the hard-sphere fluid have shown that morphometry is accurate within the (small) numerical error for the case of solved particles having simple *convex* shapes [93]. This result is very encouraging but it should be realized that the breakdown of additivity [property (iii) in Hadwiger's theorem] occurs for solute particles with concave regions which are necessary to induce a confinement of the solvent. We have therefore designed a more rigorous test for morphometry. We consider the interfacial tension γ of a hard-sphere fluid (radius R, packing fraction $\eta = 0.38$) which is contained *inside* a cylinder (radius $R_{\rm cyl}$). γ is defined as $\gamma = \frac{1}{A}(\Omega - \Omega_{\rm bulk})$ where $\Omega = -pV_{\rm tot} + F_{\rm sol}$ is the grand potential of the system *with* the solute and $\Omega_{\rm bulk} = -p(V_{\rm tot} - V)$ is the grand potential of the bulk reference system (V and A are the solute volume and surface area, respectively). Using the morphometric form for $F_{\rm sol}$ [Eq. (5.2)] in the above expression for γ one finds

$$\gamma = \sigma + \frac{\kappa C}{A} + \frac{\bar{\kappa} X}{A} = \sigma - \frac{\kappa}{2(R_{\rm cyl} - R)}\,. \tag{5.10}$$

In the last step, we have used that $X = 0$ in the cylindrical geometry (as one of the principal curvatures vanishes) and we have moreover plugged in the results for C and A in the given geometry. As we have mentioned earlier, the measures V, A, C, and X have to be calculated with respect to the parallel surface which, for the cylindrical pore considered here, is depicted in Fig. 5.1. The parallel wall is given as the surface of a cylinder with a radius $R_{\rm cyl} - R$. Therefore, we have $C = -\frac{A}{2(R_{\rm cyl}-R)}$ and the singular point $R_{\rm cyl} = R$, where the parallel surface vanishes and the solvent has to be squeezed out of the cavity, is reflected, mathematically, in the singularity of Eq. (5.10). The observed property that the parallel surface vanishes in regions which are not accessible for the solvent holds also in arbitrary geometries and is a simple consequence of the fact that the parallel surface is constructed such that it delimits the space accessible to the centers of the solvent particles. On the level of the geometric measures, the singular point where the parallel surface vanishes (i.e. $R_{\rm cyl} = R$ for the cylinder) is marked by the discontinuity of a geometric measure (X in spherical geometry, C in cylindrical geometry). In the present example, C is a negative constant for $R_{\rm cyl} \geq R$ and $C = 0$ for $R_{\rm cyl} < R$. As we shall see in the next section, the need to consider the parallel surface makes calculations of the geometric measures more involved, but it guarantees us to capture important features of the underlying physics.

Coming back to the calculation of γ in the cylindrical pore, we note that, as an alternative to Eq. (5.10), γ can be calculated with DFT using the defining relation $\gamma = \frac{1}{A}(\Omega[\rho(\mathbf{r})] - \Omega_{\rm bulk})$, where $\Omega[\rho(\mathbf{r})]$ is the density functional evaluated for the

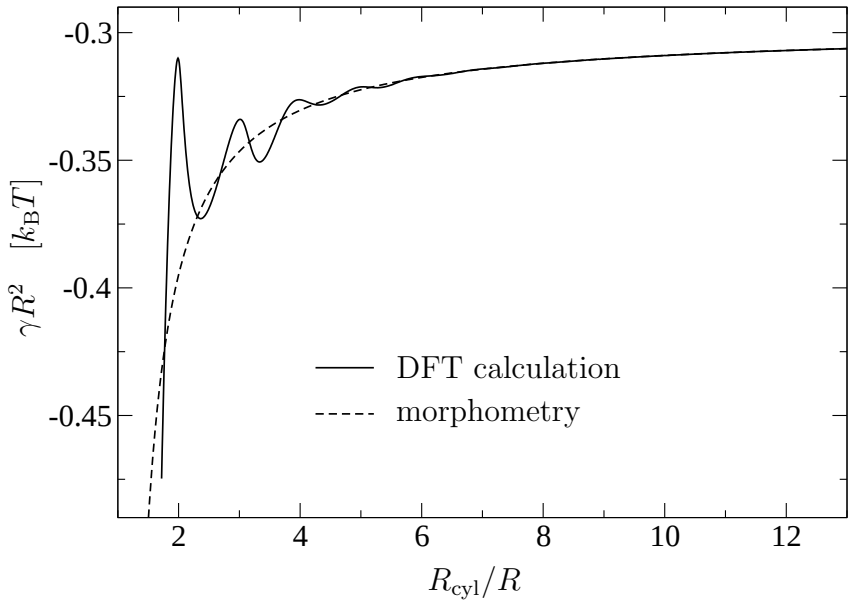

Figure 5.5: Interfacial tension γ of a hard-sphere fluid (radius R, packing fraction $\eta = 0.38$) inside a cylinder with radius R_{cyl}. The results from DFT calculations (WBII of FMT) oscillate around the prediction from morphometry, Eq. (5.10).

equilibrium density distribution $\rho(\mathbf{r})$. We have obtained data for γ using the WBII functional [Eq. (2.26) with $\mathcal{F}_{\text{ex}}$ calculated from Eq. (3.43)].

The results from the two approaches are compared in Fig. 5.5. The thermodynamic coefficients σ and κ have been obtained by fitting Eq. (5.10) to the DFT data for $R_{\text{cyl}} \in [10R, 20R]$. The morphometric prediction is excellent for $R_{\text{cyl}} > 7R$, only for smaller cylinder radii deviations from the DFT data appear, which become more pronounced for narrower cylinders. This is in agreement with our previous remark that morphomotry is supposed to perform well also for confined fluids as long as the length scale of the confinement is large compared to the correlation length of the fluid. Even for narrow cylinders we find the deviations reasonably small compared to the absolute value of γ and morphometry still captures the *trend* of γ which would persist after smoothing the DFT data by averaging out the characteristic oscillations which are caused by packing effects of the solvent particles. The capability of predicting the general trend suggests an explanation for the success of morphometry in a recent calculation of F_{sol} for protein G where confinement on the scale of the solvent correlation length is strongly present [142]. However, concerning the following results for the model protein, which are obtained using morphometry, we note that characteristic oscillations in situations of extreme confinement are not reproduced but their contribution to F_{sol} is sufficiently small so as not to affect the overall behavior.

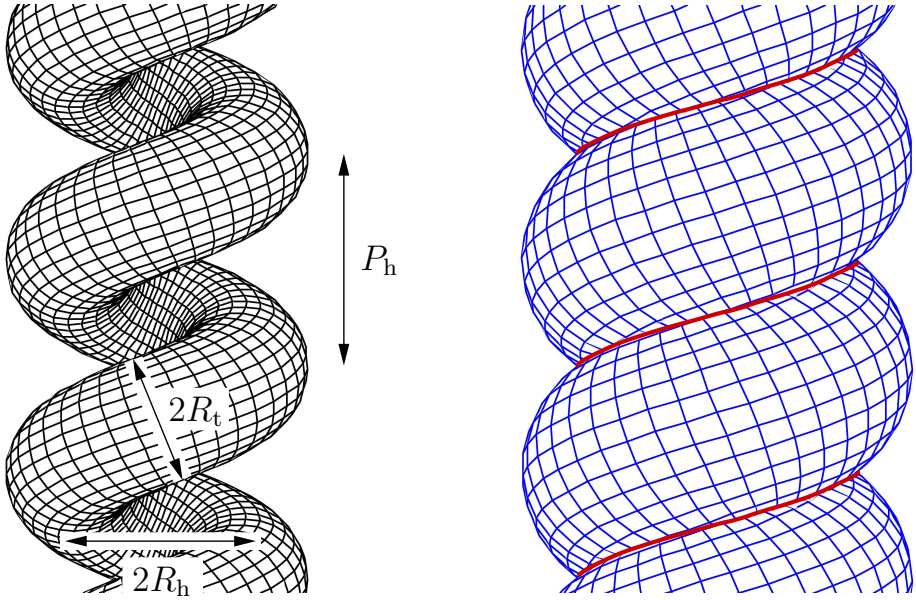

Figure 5.6: Left: helical conformation of a protein in the tube model. Right: a possible parallel surface for the same conformation. Due to self-intersection one or several helical intersection lines (in red) appear giving rise to additional contributions to the integral mean and Gaussian curvatures.

5.2 Results for a model protein

5.2.1 Geometric measures

We have calculated the geometric measures for a broad range of protein conformations in the tube model covering two principal secondary motives, namely helices and β-sheets. When the contributions from turns are neglected, β-sheets are attained in the limit of helices with infinite radius where all the calculations can be performed analytically using elementary geometry. We therefore focus here on the more involved case of truly helical conformations.

Helical tube conformations are obtained from a helical curve which is determined by two numbers: the pitch P_{h} and the radius R_{h}. The standard parametrization of the right-handed helical curve is

$$x = R_{\mathrm{h}} \cos\tau\,, \quad y = R_{\mathrm{h}} \sin\tau\,, \quad z = P_{\mathrm{h}}\tau/2\pi\,, \tag{5.11}$$

where $\tau \in (-\infty, +\infty)$. The corresponding conformation of the tube with radius R_{t} is given by the set of all the points having a distance lower than or equal to R_{t} from the helical curve (see left of Fig. 5.6). Obviously, for given parameters P_{h} and R_{h} there

exists a specific value of R_t such that tubes with larger radius cannot be realized in this helical conformation as they would self-intersect. An examination of the helical close-packing problem shows that two regimes can be distinguished [144]. Consider a situation where the tube radius R_t is kept fixed. Then for large helix radius R_h the close-packing is obtained by reducing P_h to the point below which consecutive turns of the helix would start to intersect. In the limit $R_\mathrm{h} \to \infty$ of this regime the geometry of a β-sheet is recovered. Following the line of these turn-to-turn distance limited close-packed helices while decreasing R_h causes the helical centerline of the tube to bend more and more strongly. A point is reached where the radius of curvature of the helical curve equals the tube radius R_t. Further decrease of R_h would cause the tube to bend so strongly that is would self-intersect *locally*. In this curvature limited regime P_h has to be chosen larger than according to the *global* turn-to-turn distance constraint in order to avoid self-intersection. The crossover between the two regimes occurs at $R_\mathrm{h}^* \simeq 0.8622 R_\mathrm{t}$ and $P_\mathrm{h}^* \simeq 2.166 R_\mathrm{t}$ corresponding to a pitch to radius ratio $c^* = P_\mathrm{h}^*/R_\mathrm{h}^* \simeq 2.512$. These parameters define one peculiar helix from the set of close-packed helices which marks the crossover point between the two regimes. This helix is termed "optimal" as it appears in packing problems of tubes subject to local compactness conditions [145]. Strikingly, the geometry of helical conformations of many real proteins appears closely related to that of the optimal helix [145].

As we have discussed above, the geometric measures for a helical conformation R_h, P_h, R_t and solvent particles with hard-core radius R must be calculated for the body resulting from a parallel shift of the surface by the distance R. The right of Fig. 5.6 shows an example for such a parallel body. Self-intersection, which is absent in the helical protein conformation, occurs for the parallel body and complicates the calculation of the geometric measures. Given that the equations for the determination of intersection lines (see Fig. 5.6) are transcendental we do not attempt an analytical calculation of the geometric measures and perform the volume, surface and curvature integrations numerically. The question remains, however, how intersection lines must be treated in this context. Clearly, possible line contributions must originate from the integrals of curvature. For their calculation we apply the following regularization of the intersection line. Imagine a small sphere with radius ϵ which is rolled along the groove with an intersection line at its bottom. In this way two lines tracking the points of contact between the small sphere and the parallel surface are drawn. These define the vicinity of the intersection line. The regular surface is constructed by "filling" the groove in the vicinity of the intersection line such that the contact between the small sphere and the modified surface is extended over the whole vicinity. In the limit $\epsilon \to 0$ the contributions of the vicinity to the integral curvatures converge

to finite numbers. In particular, for the helical geometry we obtain the following line contributions to the integral mean and Gaussian curvatures (per unit length of the intersection line)

$$C_{\text{line}} = -(\pi/2 - \theta/2)\,, \quad X_{\text{line}} = -2\varkappa_{\text{line}} \cos(\theta/2)\,. \tag{5.12}$$

Here θ is the opening angle of the intersection line groove and $\varkappa_{\text{line}}$ denotes the curvature of the intersection line. Our expressions are consistent with the result for the case of two intersecting spheres [146].

Results for the geometric measures of the close-packed helical conformations are shown in Fig. 5.7. Note that the integral Gaussian curvature always vanishes, which expresses the fact that the parallel body of a helix is topologically equivalent either to a solid or a hollow cylinder. For an easy comparison of the results for different solvent radii R we have subtracted the (R-dependent) values of the volume and the surface area corresponding to a β-sheet, V_β and A_β. These are approached in the limit $R_{\text{h}} \to \infty$. For the integral mean curvature this subtraction is unnecessary as $C_\beta \equiv 0$. The figure focuses on the turn-to-turn distance limited regime ($R_{\text{h}} > R_{\text{h}}^*$) while only the onset of the curvature limited regime is shown. There, the geometric measures quickly approach V_{str}, A_{str}, and C_{str} which are the values for a stretched tube, i.e., a tube with a straight center line. This behavior reflects the fact that for $R_{\text{h}} < R_{\text{h}}^*$ the pitch P_{h} must be strongly increased compared to the turn-to-turn distance limited regime which causes the surface of the tube to be more exposed to the solvent. The values $\Delta V_{\text{str}}^\beta = (V_{\text{str}} - V_\beta)/(R_{\text{t}}^3 \tilde{L})$ and $\Delta A_{\text{str}}^\beta = (A_{\text{str}} - A_\beta)/(R_{\text{t}}^2 \tilde{L})$ are tabulated in the figure. In our calculations $\tilde{L} = L/R_{\text{t}}$ is the dimensionless length of the tube which is considered in the limit $L \to \infty$ such that contributions coming from the end points of the tube are negligible. For the integral mean curvature, the R-dependence drops out and one finds $C_{\text{str}}/(R_{\text{t}}\tilde{L}) = \pi$.

We discuss some of the main features of the curves here, coming back to them in the context of solvation free energies for the different solvents. The curves for the volume V have their global minimum at $R_{\text{h}} = R_{\text{h}}^*$ when R is small. At $R = R_{\text{uw}} \simeq 0.0835 R_{\text{t}}$ the minimum starts to move to $R_{\text{h}} > R_{\text{h}}^*$ while its absolute value with respect to V_β remains roughly unchanged. This trend persists even for R larger than shown in Fig. 5.7. The value of V at $R_{\text{h}} = R_{\text{h}}^*$ increases with R for $R > R_{\text{uw}}$ exceeding V_β at $R_{\text{h}} \simeq 0.1373 R_{\text{t}}$. The results for the surface area A at small R behave similar to the volume results. Above $R = R_{\text{s}} \simeq 0.0465 R_{\text{t}}$ an interval appears where the surface area decays almost linearly. This is followed by an increase to the level of A_β which is connected to the linear part with a cusp. The cusp moves to larger R_{h} when R is increased. It is situated at a larger value of R_{h} than the minimum of the corresponding volume curve. Exactly at the location of the cusp, the results for

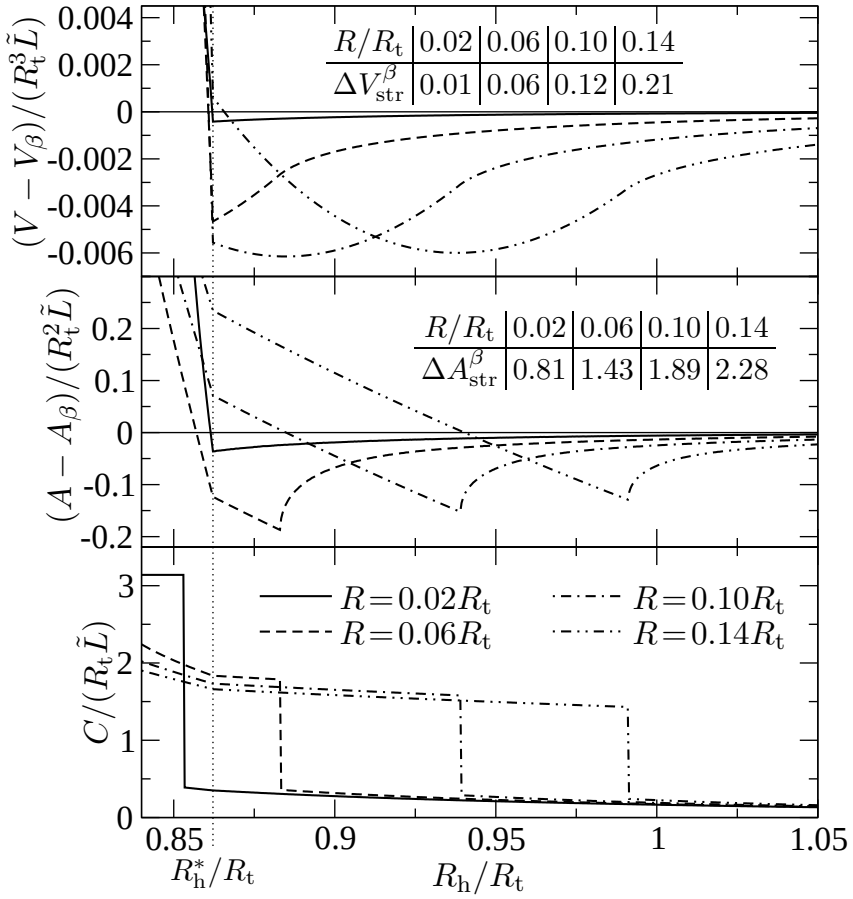

Figure 5.7: Volume V, surface area A, and integral mean curvature C for a range of close-packed helical tube conformations. Calculations are performed on the parallel body at different distances R (radius of solvent hard core). The integral Gaussian curvature X vanishes, consistent with the given topology. The helices with $R_h < R_h^*$ are curvature limited close-packed; those with $R_h > R_h^*$ are turn-to-turn distance limited close-packed. The limit $R_h \to \infty$ corresponds to the β-sheet conformation.

the integral mean curvature C display at discontinuity where $C/(R_\mathrm{t}\tilde{L})$ drops from a value between 1.5 and 2.0 to almost zero. It is instructive to compare this behavior with the case of a hollow cylinder mentioned in Section 5.1 where the discontinuity of C indicates that the solvent has to be squeezed out from the cylindrical cavity. It turns out that in the helical geometry the meaning of the discontinuity is the same. Given $R > R_\mathrm{s}$ and $R_\mathrm{h} > R_\mathrm{h}^*$ only the exterior of the helix can be probed by the solvent particles if R_h is below the location of the discontinuity. If R_h is increased above the discontinuity the space near the central axis of the helix grows large enough to hold the solvent particles. This observation reveals an interesting meaning of the threshold value R_s. A particle with this or a smaller size can enter even the cavity formed by the optimal close-packed helix. The curves of C for $R < R_\mathrm{s}$ display a jump at $R_\mathrm{h} < R_\mathrm{h}^*$. This corresponds to a connection between the cavity and the bulk being established due to the increase of the pitch P_h in the curvature limited regime. For solvent sizes slightly above R_s the situation is even more complex. There, a small interval of values for R_h below R_h^* exists where a cavity accessible to the solvent particles forms again (not shown). However, for sufficiently small helix radii R_h the cavity always connects to the bulk and $C/(R_\mathrm{t}\tilde{L}) \to \pi$.

5.2.2 Hard-sphere solvent

In recent work, Snir and Kamien have calculated the solvation free energy F_sol of helical conformations of molecules in the tube model for a hard-sphere solvent [14, 15]. They obtain results within the Asakura-Oosawa model [16] which neglects the interactions between solvent particles completely. Therefore, F_sol is directly proportional to the volume V of the protein calculated for the parallel body. More precisely $F_\mathrm{sol} = pV$ where $p = \rho k_\mathrm{B}T$ is the solvent pressure obtained from the solvent particle number density ρ. The simplicity of the Asakura-Oosawa model allows us to read off the results for F_sol directly from the volume curves of different helical conformations in Fig. 5.7.[1] Accordingly, for solvent particles smaller than R_uw the optimal close-packed helix, which is characterized by $R_\mathrm{h} = R_\mathrm{h}^*$ and $P_\mathrm{h} = P_\mathrm{h}^*$, has the lowest free energy. When the solvent particles are larger, the minimal free energy is assumed for some $R_\mathrm{h} > R_\mathrm{h}^*$. This was interpreted in Ref. [14] such that larger solvent particles lead to a favoring of sheetlike folding, i.e., they cause the helix to unwind. It should be noted that the Asakura-Oosawa model is valid only at low solvent densities ρ. In this regime, however, the solvent part of the protein's free energy is small as it is proportional to ρ. Employing the morphometric form of F_sol [Eq. (5.2)] allows us to

[1] The figure is restricted to the set of close-packed helices. A complete scan of the configuration space of helices shows that minima in V are always assumed on this set.

obtain reliable results for the hard-sphere solvent beyond the low-density limit.

It should be mentioned that the Asakura-Oosawa model constitutes indeed a special case of the morphometric form for $F_{\rm sol}$, namely the case where p equals the pressure of the ideal gas and the higher thermodynamic coefficients σ, κ, and $\bar{\kappa}$ are set to zero which is their correct value in the uncorrelated ideal gas. In order to treat the hard-sphere solvent beyond the low-density limit extrapolations for the thermodynamic coefficients to higher densities are required. Conveniently, accurate analytical expressions for the coefficients as functions of the hard-sphere fluid packing fraction η are available from the recent WBII version of FMT as we have shown in Section 5.1. The coefficients are plotted in Fig. 5.1. In particular, the pressure p is the quasi-exact CS expression and the result for the planar wall surface tension σ has been shown to compare very well with data from computer simulations. For $\eta \to 0$, the expressions reduce to those of the ideal gas: p is linear in η, σ quadratic, and κ cubic.

The fact that we have the coefficients available as functions of η through simple analytical expressions is particular valuable as it allows us to perform a detailed scan over the range of all possible solvent densities. We calculate the solvation free energy $F_{\rm sol}$ according to Eq. (5.2) for the set of close-packed helices for different solvent conditions which are determined via the solvent packing fraction η and the solvent particle radius R. As a result, we discern three different parameter regions where $F_{\rm sol}$ is minimal (i) for the *optimal helix* with $R_{\rm h} = R_{\rm h}^*$, (ii) for the *β-sheet* with $R_{\rm h} \to \infty$, and, (iii) for certain finite values $R_{\rm h} > R_{\rm h}^*$ which we refer to as *unwound helix*. These regions are plotted as a function of η and R in Fig. 5.8.

In the limit $\eta \to 0$ the result of Snir and Kamien is recovered: below $R = R_{\rm uw}$ the optimal helix minimizes $F_{\rm sol}$, above the minimum is assumed for an unwound helical configuration ($R_{\rm h} > R_{\rm h}^*$). However, taking into account also the diagram beyond vanishing solvent packing fraction η shows that the statement that larger solvent particles lead to a favoring of β-sheets can hardly be sustained. On the contrary, the only region where the β-sheet minimizes $F_{\rm sol}$ is situated at *small* solvent particles ($R \approx 0.05 R_{\rm t}$) with *large* packing fractions $\eta \gtrsim 0.3$. The nature of the regime of unwound helices at large solvent particles can be inferred from the curves of $F_{\rm sol}$ shown in Fig. 5.9(d). As has to be expected from the Asakura-Oosawa results by Snir and Kamien, the curves display a minimum at $R_{\rm h} > R_{\rm h}^*$ originating from the volume contribution. However, the minimum is separated from the sheetlike configuration by an energy barrier arising from the surface contribution (cf. Fig. 5.7) which enters into the calculation of $F_{\rm sol}$ with a negative sign as $\sigma < 0$ [see Eq. (5.2)]. Therefore the picture conveyed in Ref. [14] that increasing the solvent particle size

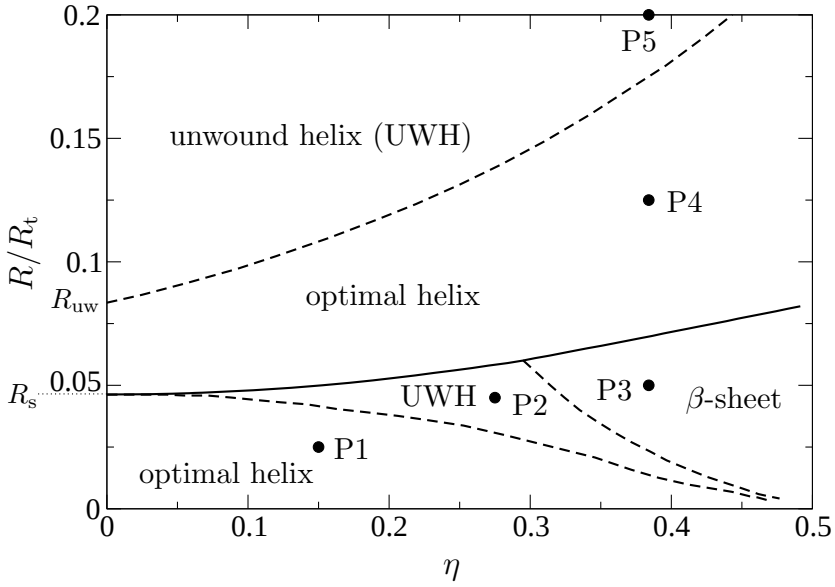

Figure 5.8: Diagram of the different protein structures which minimize $F_{\rm sol}$ in a hard-sphere solvent with packing fraction η and solvent radius R. At the full line the transition occurs discontinuously in $R_{\rm h}$ while it is continuous in $R_{\rm h}$ at the dashed lines. In the limit $\eta \to 0$ there is no transition at $R = R_{\rm s}$. The solvent configurations indicated by dots are discussed in Fig. 5.9.

R leads *continuously* to a sheetlike geometry is misleading. Note further that the effect of the surface area contribution is to stabilize the optimal helix conformation with respect to the unwound helix as can be seen from the transition line which increases from $R = R_{\rm uw}$ at $\eta = 0$ to $R > 0.2R_{\rm t}$ at large η. The discontinuities of the curves in Fig. 5.9 are due to the contribution from the integral mean curvature. In consequence, it locates the characteristic helix radius which divides two qualitatively different regimes. Helices with larger radius $R_{\rm h}$ contain in their interior solvent which is disconnected from the bulk. In contrast, the cavities offered by helices with radii smaller than the location of the jump position are so narrow that they cannot hold solvent particles. Coming from large helix radii $R_{\rm h}$ the discontinuity corresponds to the point where the solvent has to be squeezed out from the inner part of the helix. Once this is completed, the system can easily relax towards smaller radii $R_{\rm h}$ and eventually meet the the optimal helix configuration as in Fig. 5.9(c). Note that the discontinuity in $F_{\rm sol}$ is a consequence of assuming a hard body interaction between the protein tube and the solvent particles. It would be smeared out if soft interaction potentials were used. Figure 5.9 shows characteristic free energy curves for all the different regions of the diagram in Fig. 5.8. From the curves the presence of

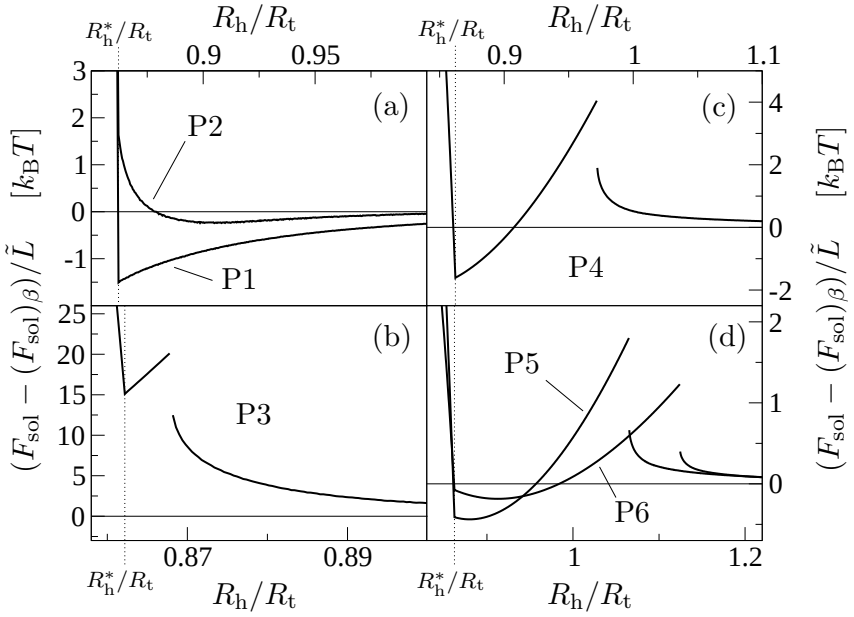

	P1	P2	P3	P4	P5	P6
η	0.15	0.275	0.384	0.384	0.384	0.384
R/R_t	0.025	0.045	0.05	0.125	0.2	0.25
ΔF^β_{str}	43.73	39.13	49.36	13.87	7.30	5.39

Figure 5.9: F_{sol} for the different solvent configurations which are indicated in the diagram Fig. 5.8, except P6. F_{sol} is shown for configurations along the line of close-packed helices with a focus on the turn-to-turn distance limited regime ($R_h > R_h^*$). In the curvature limited regime ($R_h < R_h^*$) the values ΔF^β_{str}, given in the table, are reached.

continuous (in R_h) and discontinuous transition lines between the regions in Fig. 5.8 can be understood. In order to assess the stability of the helical conformations shown in Fig. 5.9 we have checked that increasing the pitch of the close-packed helices by $0.02R$ leads to higher F_{sol} in all the cases. In the table which is given with Fig. 5.9 we compare F_{sol} for the β-sheet with the value corresponding to a stretched tube by calculating the quantity $\Delta F^\beta_{str} = ((F_{sol})_{str} - (F_{sol})_\beta)/(k_BT\tilde{L})$. As an interesting result, the large values of ΔF^β_{str} prove that in the hard-sphere solvent both the optimal helix and the β-sheet are clearly favorable energetically compared to the stretched tube configuration which is devoid of any economic packing. Finally, we note that the free energy curves become flatter with increasing R. Therefore, if additional contributions to the overall protein free energy, which can be formulated in a first

approach in terms of a bending stiffness [14], are taken into account, the results for $F_{\rm sol}$ cease to determine the protein configuration for solvent particles much larger than those included in Fig. 5.8. This observation has to be seen as an additional restriction of the unwinding hypothesis of Ref. [14] which assumes a solvent driven tendency of sheet formation in the range of large solvent particles.

5.2.3 Square-well solvent

Contrary to the hard-sphere solvent, where accurate analytical expressions for the thermodynamic coefficients are available, this is not the case for more complicated solvents. However, the morphometric approach is still viable as we show exemplarily for the square-well fluid which can serve as a crude model for water [136]. The square-well fluid is obtained by adding to the hard-sphere interaction a constant attractive potential

$$w_{\rm sw}(|\mathbf{r}-\mathbf{r}'|) = \begin{cases} -\epsilon_{\rm sw} & \text{if } |\mathbf{r}-\mathbf{r}'| \leq R_{\rm sw} \\ 0 & \text{otherwise} \end{cases} \tag{5.13}$$

acting between particles at positions $\mathbf{r}$ and $\mathbf{r}'$. We use $R_{\rm sw} = 3R$, where R is the hard core radius of the particles. The square-well potential can be included in the density functional $\Omega[\rho]$ [Eq. (2.26)] via a corresponding excess free energy functional $\mathcal{F}^{\rm ex}_{\rm sw}[\rho]$ which adds to the excess free energy functional for the hard sphere part of the interaction. Making a simple mean field approximation we use

$$\mathcal{F}^{\rm ex}_{\rm sw}[\rho] = \frac{1}{2}\iint {\rm d}\mathbf{r}{\rm d}\mathbf{r}'\rho(\mathbf{r})\rho(\mathbf{r}')w_{\rm sw}(|\mathbf{r}-\mathbf{r}'|)\,. \tag{5.14}$$

The hard core interaction is implemented through the WBII excess free energy functional [cf. Eq. (3.43)] such that the thermodynamic coefficients for hard spheres shown in Fig. 5.2 are reproduced in the limit of vanishing square-well interaction strength $\epsilon_{\rm sw} = 0$. Making use of the minimization route, which we have explained in Section 5.1, we can access the thermodynamics coefficients for $\epsilon_{\rm sw} > 0$. To this end the equilibrium grand potential Ω is obtained from the numerical minimization procedure of the functional $\Omega[\rho]$ for different solute particles which enter the calculations through the external potential. When the solute particles are chosen to be simply spheres of different radii the calculation of the corresponding Ω, and hence $F_{\rm sol}$, can be performed efficiently. The thermodynamic coefficients are extracted by fitting the morphometric form Eq. (5.2) for $F_{\rm sol}$, which is a cubic polynomial in the radius of the solute sphere, to the numerical data. We find that the quality of the fit is excellent. For solute spheres with sizes in the range of $2R$ and $10R$ the coefficients are determined with a standard error below 1%. Our results for the packing fraction

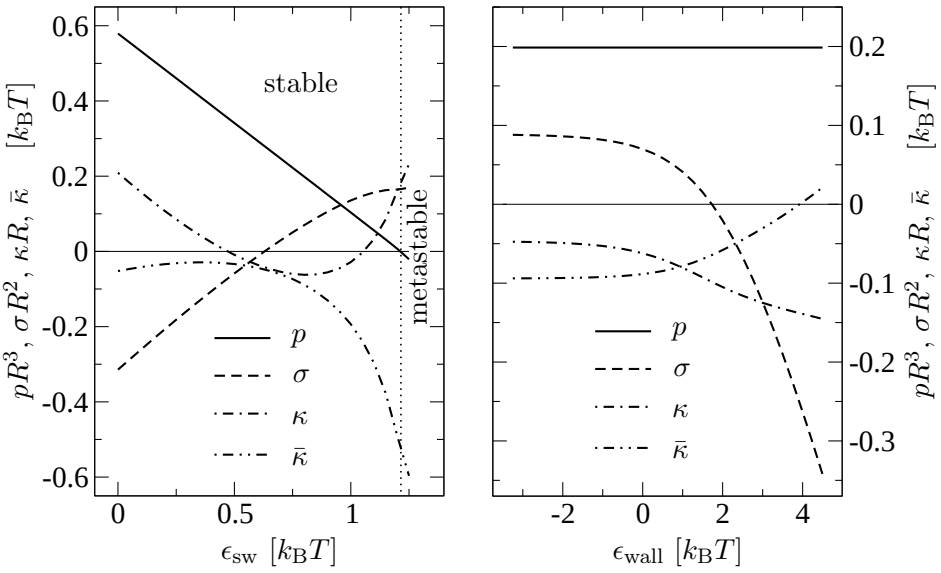

Figure 5.10: Left: thermodynamic coefficients of a square-well fluid as a function of ϵ_{sw}, the strength of the attraction between particles. Right: thermodynamic coefficients for a square-well fluid ($\epsilon_{sw} = 0.8k_BT$) at a wall acting through a short-ranged potential of strength ϵ_{wall} on the fluid.

$\eta = 0.384$, which corresponds to 55.5 Molar of water with an assumed hard core radius of $R = 1.4$ Å, are shown on the left of Fig. 5.10. The critical point of the given square-well fluid being located at $\eta_{cr} = 0.130$ and $\epsilon_{sw} = 0.785k_BT$ we can attribute the fluid to the liquid part of the phase diagram when ϵ_{sw}, the attraction between solvent particles, is larger than $0.785k_BT$. Upon increasing ϵ_{sw} at constant temperature T, the pressure of the fluid decreases linearly, consistent with the analytical result from the underlying density functional. At $\epsilon_{sw} = 1.215k_BT$ the liquid becomes metastable with respect to the gas phase with $\eta_g = 0.005$. Slightly above, at $\epsilon_{sw} = 1.218k_BT$, the pressure of the liquid vanishes. Both σ and κ change sign when ϵ_{sw} is increased. The increase in σ means that building up an interface at a neutral surface becomes more costly energetically. In particular, the square-well fluid retreats from the neutral wall in contrast to the hard-sphere fluid which is adsorbed.

In order to go beyond a neutral wall which corresponds to a protein surface without any specific interaction with the solvent, we determine thermodynamic coefficients for a square-well fluid with $\eta = 0.384$ and $\epsilon_{sw} = 0.8k_BT$ subject to a wall potential V_{wall} adding to the potential of the hard wall. We choose V_{wall} to be constant with a value $-\epsilon_{wall}$ over a short range of $d_{wall} = R/10$ in front of the hard wall. The motivation for choosing V_{wall} short-ranged is that otherwise one would have to expect also strong

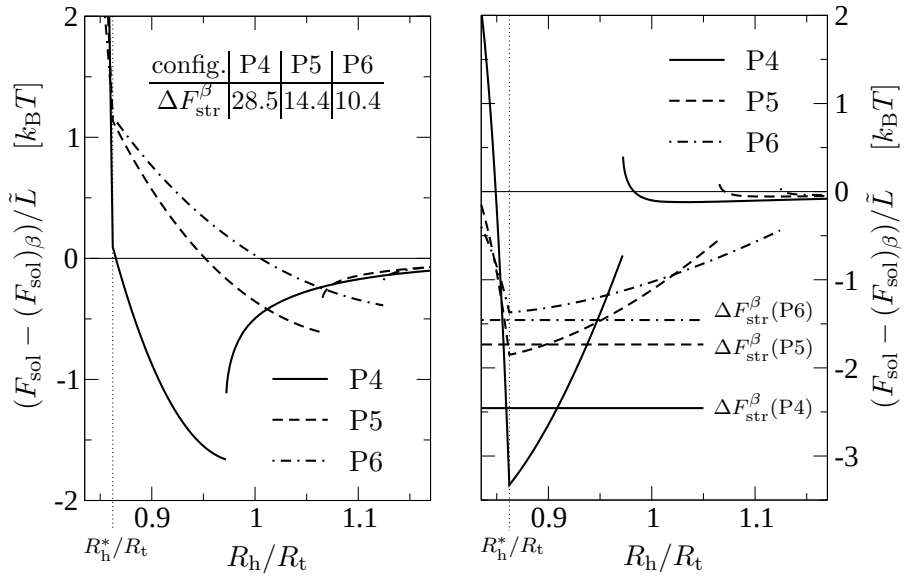

Figure 5.11: Left: $F_{\rm sol}$ for a hydrophobic protein ($\epsilon_{\rm wall} = -3.0k_{\rm B}T$) in a square-well fluid with $\epsilon_{\rm sw} = 0.8k_{\rm B}T$. The solvent packing fraction is $\eta = 0.384$ and the solvent particle radii are $R = 0.125R_{\rm t}$ (P4), $R = 0.2R_{\rm t}$ (P5), and $R = 0.25R_{\rm t}$ (P6). Right: $F_{\rm sol}$ for a hydrophilic protein ($\epsilon_{\rm wall} = 3.0k_{\rm B}T$) in the same solvents. The curves for $F_{\rm sol}$ assume their global maxima for some $R_{\rm h} < R^*_{\rm h}$ (not shown).

interactions between different parts of the protein. This would potentially give rise to important contributions to the free energy which are of other origin that the solvent. The results for different strengths $\epsilon_{\rm wall}$ of the wall potential are shown on the right of Fig. 5.10. Obviously, a repulsive wall ($\epsilon_{\rm wall} < 0$) does not have much effect on the coefficients. This can be explained by the fact that at $\epsilon_{\rm sw} = 0.8k_{\rm B}T$ the square-well fluid retreats even from the neutral wall such that an additional repulsion over a short range acts only on a rather small amount of liquid. In conclusion, the hydrophobicity of the wall ($\epsilon_{\rm wall} < 0$) is in fact basically equivalent to a neutral wall. In the case of a hydrophilic wall ($\epsilon_{\rm wall} > 0$) the sign of σ becomes negative again as in the case of the hard-sphere solvent. In contrast, κ, which is positive for the hard spheres, remains negative when $\epsilon_{\rm wall}$ is increased. The corresponding picture is that the square-well fluid at a hydrophilic wall likes convex domains as $V_{\rm wall}$ is experienced then over a lager volume. The hard-sphere fluid on the other hand likes concave domains which allow the fluid to maximize its excess adsorption. The implications of this difference for the value of $F_{\rm sol}$ turn out to be far-reaching.

In order to illustrate the influence of the sign of κ we turn to our results for a hydrophilic protein ($\epsilon_{\rm wall} = 3.0k_{\rm B}T$) in a square-well solvent ($\epsilon_{\rm sw} = 0.8k_{\rm B}T$) which are

shown on the right of Fig. 5.11. The curves are rather similar to those for the neutral protein in a hard-sphere solvent [cf. Fig. 5.9(c)] reflecting the similar ratio and signs of p and σ. Due to the different sign of κ, however, at the discontinuity the curves jump from lower to higher F_{sol} in the case considered here. This has two important effects. First, the β-sheet is shifted to a level which is situated energetically much higher than the optimal helix. The second, crucial effect of negative κ is to lower the energetic level of the stretched tube, which maximizes C, to values which lie close to the minimum belonging to the optimal helix. For large solvent particles the stretched tube is even more favorable compared to the helical conformation. If a bending stiffness is included in the tube model, helical conformations require additional energy compared to the stretched tube which compensates for the slight disadvantage of the stretched tube in terms of F_{sol} even for the smaller solvent particles. Our results suggest that the tendency of a protein to arrange in a compact configuration (its fold) is undermined by a prominent presence of hydrophilic groups. Note that if in the hydrophilic setup the sign of κ was inverted, the curves would become qualitatively the same as for the neutral protein in a hard-sphere solvent. In particular, F_{sol} of the helix and the β-sheet would be shifted below the level of the stretched tube conformation.

On the other hand, we can identify hydrophobicity of certain side chains as a driving force for protein folding. This is reflected in our results for the hydrophobic protein ($\epsilon_{\mathrm{wall}} = -3.0 k_{\mathrm{B}}T$) in a square-well solvent ($\epsilon_{\mathrm{sw}} = 0.8 k_{\mathrm{B}}T$) which we show on the left of Fig. 5.11. From the large values of $\Delta F^{\beta}_{\mathrm{str}}$ a strong tendency to arrange into a compact configuration can be read off (cf. the values given in Fig. 5.9). The configuration with lowest F_{sol}, however, is no longer the optimal helix but a helical conformation with a larger radius corresponding to the point where the cavity formed by the helical tube has precisely the size at which it could in principle hold the solvent particles. However, the influence of the discontinuity of C is such that the minimum is assumed on the branch of F_{sol} which corresponds to an empty cavity. In other words, the helix is widened up to the point where the solvent particles fit into the cavity but as a consequence of hydrophobicity the solvent does not enter the cavity. One can speculate that this widened helical conformation with its empty cavity provides space for hydrophobic side chains to be shielded from the solvent. For reasons of clarity, we have not included in Fig. 5.11 the curves corresponding to a slightly increased pitch. They are always situated at higher values of F_{sol} attesting for the stability of the close-packed helical conformations both in the hydrophobic and hydrophilic case.

5.3 Conclusion

In Section 5.1 of this chapter we have introduced the morphometric approach to the solvation free energy $F_{\rm sol}$ of a solute which in the present investigation is a protein represented in the tube model of Banavar and Maritan [11, 12] (see Fig. 5.6). The morphometric form of $F_{\rm sol}$ [Eq. (5.2)] allows for a very efficient calculation of solvation free energies as solvent properties and the potentially complex solute geometry are treated *separately*, rather than performing DFT calculations involving the solvent under the complicated external potential which is induced by the solute. The approach has been shown to be very reliable for simple convex solutes in a hard-sphere solvent [93] while deviations due to packing effects occur when a convex solute strongly confines portions of the solvent. Also in Section 5.1 we have investigated a confined fluid which allows us to estimate that deviations of the morphometric prediction from the full DFT calculations have only a minor effect on our results for the solvation free energy of the model protein.

In order to assess the effect of solvent entropy on how the protein folds we have considered in Section 5.2.2 a hard-sphere solvent for which the thermodynamic properties are given through accurate analytical expressions thanks to the novel hard-sphere equation of state [Eq. (3.34)] and the corresponding density functional [Eq. (3.43)]. This allows us to perform a scan over a large range of solvent configurations which are characterized by the solvent radius R and packing fraction η. Therefore we are able to extend recent results by Snir and Kamien [14,15] to solvents beyond the limit of vanishing packing fraction. While their results for $\eta \to 0$ are recovered in our approach, contributions to $F_{\rm sol}$ due to solvent surface tension σ and bending rigidity κ [see Eq. (5.2)] become important for $\eta > 0$. The influence of these additional contribution sheds new light on the results of Snir and Kamien and we find that their conclusion that increasing the size of the solvent particles "leads to the favoring of sheetlike folding" [14] should be questioned. Mainly three findings of our work challenge their statement: First, the only regime where the β-sheet minimizes $F_{\rm sol}$ is situated at *small* solvent particles with packing fractions $\eta > 0.3$. Second, large solvent particles are indeed identified to lead to helical conformations which have slightly larger radii than the so-called optimal helix. But these helical conformations have still lower $F_{\rm sol}$ than the β-sheet and are separated from the sheetlike conformation through an energy barrier which arises from the surface area contribution. Third, in order to obtain a pronounced unwinding of the helix, the size of the solvent particles has to be increased considerably. We show that for large solvent particles the curves of $F_{\rm sol}$ become quite flat such that energetic contributions of other origin than the solvent determine the protein folding.

In Section 5.2.3 we apply our method to a more complex solvent with intermolecular attraction and we include specific interactions between the protein and the solvent. To be more specific, we study hydrophobic and hydrophilic proteins in a square-well fluid which can serve as a crude model for water. We find that for a protein with a predominance of hydrophilic groups the tendency to adopt a compact folded state is extremely weak. This can be attributed to the influence of the integral mean curvature of the protein surface which enters Eq. (5.2) with opposite sign compared to the hard-sphere case. Moreover, the role of hydrophobic side chains as a driving force for folding is reflected in our results. Compact protein configurations, helices as well as the β-sheet, are shown to lead to F_{sol} much smaller than for the stretched (unfolded) protein configuration.

In conclusion, we have used the background provided by morphological thermodynamics in order to calculate F_{sol} for a protein in the tube model of Banavar and Maritan efficiently. The method has been employed for the hard-sphere fluid, which allows to assess entropic effects, and for the square-well fluid, which provides a crude model of water and which allows for studying the role of hydrophobic and hydrophilic amino acids. Future work could be centered around including more chemical details of given amino acid sequences. This might be realized by partitioning the protein surface into domains which, as a function of the corresponding amino acid, expose different interactions with the solvent. It should be noted that in this approach additional line contributions to F_{sol} stemming from the domain boundaries are to be expected. A further interesting topic of future research lies in the study of protein folding under confinement which might constitute a challenging test of the morphometric approach for F_{sol} as packing effects of the solvent are more important when the protein is located in the crowded environment of the cell.

Chapter 6

Summary and Outlook

The aim of this thesis has been to study the influence of different solvent conditions on protein folding. Given that protein function is crucially determined by the secondary and tertiary structure which are assumed under physiological conditions, it is most worthwhile to investigate the influence of the solvent, as a major characteristics of the cellular environment, on how a protein folds. Our focus for this study is on the entropic effects caused by the solvent, the essence of which is captured already if the solvent is chosen to be the relatively well understood hard-sphere fluid. However, even for this idealized model solvent free energy calculations in the potentially complex geometries provided by different protein conformations risk to become time consuming if high accuracy and an extensive scan of solvent properties are required. We devise a method for calculating the solvation free energy F_{sol} which makes use of the results of the so-called morphological thermodynamics based on Hadwiger's theorem from integral geometry [23]. The concept has been applied in statistical physics since the mid-1990's [20, 135] and rather recently in the context of the hard-sphere fluid [93]. The basic equation for F_{sol} within morphological thermodynamics is rather simple. The theory states that

$$F_{\mathrm{sol}} = pV + \sigma A + \kappa C + \bar{\kappa} X \,, \tag{6.1}$$

where p, σ, κ, and $\bar{\kappa}$ are properties of the solvent[1] which depend on the solvent temperature, the chemical potential, and the specific interaction of a given domain of the protein with the solvent. However, these thermodynamic coefficients are *independent* of the protein conformation. The latter is encoded in the geometric measures V, A, C, and X which can be attributed to an arbitrary given protein conformation.[2]

[1] To be more specific, p is the pressure, σ the planar wall surface tension, and κ and $\bar{\kappa}$ are the bending rigidities of the solvent.

[2] These geometric measures are the volume V, the surface area A, the integral mean curvature C, and the integral Gaussian curvature X of the protein for a given conformation.

The obvious advantage of Eq. (6.1) is that it allows one to avoid the treatment of solvents in the complex geometries which can be induced by the protein. Instead, solvent properties have to be calculated only *once* in test geometries which use solutes of simple shape. In a second step, the geometric measures for different protein conformations can be computed relatively easily and they can be finally joined with the solvent properties according to the simple equation Eq. (6.1) in order to yield F_{sol}. It should be mentioned, however, that Eq. (6.1) for F_{sol} constitutes merely an approximation to the exact solvation free energy. In the case of the hard-sphere solvent this approximation has been shown to be extremely accurate for simple convex solutes [93] but there are deviations from the exact results if concave solutes, which give rise to solvent confinement, are considered. In Section 5.1, which belongs to the last chapter of the present work, we give an introduction to morphological thermodynamics together with a discussion of its strengths and limitations. The preceding Chapters 2 to 4 are to a large extent preparatory to our setting up of the morphological approach to F_{sol} but they can be appreciated also independently of the biologically inspired applications in Chapter 5.

In Chapter 2 we present a rigorous calculation of the statistical mechanics of a system of particles confined to one dimension (1D) with arbitrary pair potentials acting between next neighbors. The formal solution of the 1D system is known since the 1950's [42, 43] but so far it has not been, to our knowledge, connected with experiments. We use a surprisingly simple relation resulting from the exact solution which allows for an unambiguous solution of the inverse problem which consists in recovering the pair interaction potential between the particles from a measured pair distribution function. The procedure is applied to data from measurements on a system of charge-stabilized colloids which are confined to 1D using an optical tweezer. As expected, given that the underlying theory is exact, we find excellent agreement between theory and experiment. Thus the 1D system provides one of the rare cases in which experimental results can be reproduced one-to-one by theory due to the fact that in 1D the statistical mechanics is exactly solvable.

The solvability of the 1D case enables us to illustrate our introduction to density functional theory of classical fluids (DFT), which we provide in Section 2.3, with the exact result for the excess (over the ideal gas) free energy functional $\mathcal{F}_{\mathrm{ex}}^{\mathrm{1D}}$ for the 1D hard-sphere mixture [64]. The expression for $\mathcal{F}_{\mathrm{ex}}^{\mathrm{1D}}$ is valuable for mainly two reasons. First, it proves that DFT provides a means of accessing conveniently the exact thermodynamics of the 1D hard-sphere system under arbitrary external potentials for which a calculation based on evaluating the partition function is barely manageable. This constitutes a motivation for using DFT also in the 3D case for

which free energy calculations have to be performed for various external potentials resulting from the presence of the solute (i.e. a protein or a simpler object in a test geometry). Second, we can analyze the structure of $\mathcal{F}_{\rm ex}^{\rm 1D}$ in some detail which provides us with the appropriate tools for the construction of approximations for the excess free energy functional $\mathcal{F}_{\rm ex}^{\rm 3D}$ of the hard-sphere fluid in 3D. Given the relative simplicity of the 1D result this approach allows us to spare the reader some of the details of the more cumbersome calculations related to the 3D functionals.

The construction of $\mathcal{F}_{\rm ex}^{\rm 3D}$ is undertaken in Chapter 3 following the lines of Rosenfeld's seminal work from 1989 [22]. From a close inspection of the exactly known low-density limit of $\mathcal{F}_{\rm ex}^{\rm 3D}$ a set of six weighted densities can be identified. These are the four scalar functions $n_0(\mathbf{r}), \ldots, n_3(\mathbf{r})$ and the two vectorial functions $\overrightarrow{n}_1(\mathbf{r})$ and $\overrightarrow{n}_2(\mathbf{r})$ which all depend on the spatial coordinates $\mathbf{r}$ and which are obtained by smearing out the density profiles of the multi-component hard-sphere mixture. Using an exact relation for the pressure from scaled-particle theory [27, 28] the approximate excess free energy density $\Phi_{\rm RF}$ [Eq. (3.16)] can be constructed as a function of the weighted densities. This defines Rosenfeld's fundamental measure theory (FMT) for the hard-sphere mixture. Remarkably, although based on completely unrelated premises, FMT renders the results for the pressure and the pair direct correlation function as they are obtained by solving the Ornstein-Zerneke integral equation with the Percus-Yevik (PY) closure [45]. In particular, for the pressure the PY compressibility result

$$\frac{p_{\rm PY}}{k_{\rm B}T} = \frac{n_0}{1-n_3} + \frac{n_1 n_2}{(1-n_3)^2} + \frac{n_2^3}{12\pi(1-n_3)^3} \tag{6.2}$$

follows from $\Phi_{\rm RF}$. The pressure $p_{\rm PY}$ is a function of the bulk values of the weighted densities which are given by

$$n_0 = \sum_{i=1}^{\nu} \rho_i \,, \quad n_1 = \sum_{i=1}^{\nu} R_i \rho_i \,, \quad n_2 = \sum_{i=1}^{\nu} 4\pi R_i^2 \rho_i \,, \quad n_3 = \sum_{i=1}^{\nu} \frac{4\pi}{3} R_i^3 \rho_i \tag{6.3}$$

for a ν-component fluid of spheres with particle number densities ρ_i and radii R_i. In particular n_0 is the total particle number density and n_3 equals the total packing fraction of the hard-sphere mixture. The vectorial weighted densities vanish in the homogeneous bulk fluid.

While at moderate packing fractions the pressure $p_{\rm PY}$ is in good agreement with simulation data for the one-component hard-sphere fluid, it overestimates the actual pressure by about 7% close to the freezing transition of the fluid. This has been cured for the one-component fluid by an empirical correction of the equation of state which gives rise to the Carnahan-Starling (CS) pressure $p_{\rm CS}$ [79]. In order to make $p_{\rm CS}$ useable within the context of FMT it has to be expressed in terms of the weighted

densities $n_0, \ldots, n_3$ which is equivalent to generalizing p_{CS} to hard-sphere mixtures. This is the purpose of Section 3.2 where we introduce a systematic expansion of the pressure in terms of powers of n_3. By maximizing consistency with the exact relation from scaled-particle theory, which we have mentioned above, we obtain without any fitting the Boublík-Mansoori-Carnahan-Starling-Leland (BMCSL) pressure p_{BMCSL} [80, 81] if the expansion is pursued to first order. Including the next higher order leads unambiguously to the recently proposed extended CS (eCS) pressure p_{eCS} [82]. The third order of the expansion renders the new equation of state

$$\frac{p^{(3)}}{k_{\mathrm{B}}T} = \frac{n_0}{1-n_3} + \frac{n_1 n_2 \left(1 + \frac{1}{3}n_3^2\right)}{(1-n_3)^2} + \frac{n_2^3 \left(1 - \frac{2}{3}n_3 + \frac{1}{3}n_3^2\right)}{12\pi(1-n_3)^3} \tag{6.4}$$

which, different from p_{BMCSL} and p_{eCS}, is fully consistent with scaled-particle theory for the one-component hard-sphere fluid. Besides this virtue, the comparison with simulation data for the pressure and the chemical potential of various hard-sphere mixtures as well as for the surface tension and adsorption shows that $p^{(3)}$ improves both on p_{BMCSL} and p_{eCS}. In Section 3.3 we describe how the novel equation of state $p^{(3)}$ can be incorporated into the framework of FMT such that the strengths of $p^{(3)}$ can be exploited also for inhomogeneous fluids within DFT. The resulting excess free energy density is denoted by Φ_{WBII} [Eq. (3.43)] and it is referred to as the White Bear version of FMT Mark II (WBII).

It has been shown previously [88] that the morphological form for F_{sol} [Eq. (6.1)] is perfectly compatible with the structure of FMT if the latter is extended to fluids which are composed of arbitrarily shaped hard particles. Such a generalized FMT has been proposed by Rosenfeld in 1994 [29, 30]. This *o*riginal *n*on-spherical FMT (onFMT) is introduced in Chapter 4. While onFMT reproduces properties of isotropic fluids quite well (e.g. the theory yields the exact second virial coefficient) it fails completely in describing the nematic phase which is always disfavored free energetically by onFMT. In order to cure this shortcoming we make use of the Gauss-Bonnet theorem [31] to derive an exact expression for the low-density limit of $\mathcal{F}_{\mathrm{ex}}$ in terms of integrals which extend over the surface of the intersection of two hard bodies. Approximations to the exact result can be deconvoluted in terms of weight functions which, for the simplest approximation, gives rise to the weighted densities $n_0(\mathbf{r}), \ldots, n_3(\mathbf{r})$ and $\overrightarrow{n_1}(\mathbf{r})$ and $\overrightarrow{n_2}(\mathbf{r})$ which follow from some straightforward adaptation of the corresponding weighted densities for spheres to the generally shaped hard particles. When the approximation to the exact result is improved by including the lowest-order expansion of the curvature asymmetry term, two additional *tensorial* weighted densities $\overleftrightarrow{n_1}(\mathbf{r})$ and $\overleftrightarrow{n_2}(\mathbf{r})$ can be identified which can be represented as 3×3-matrices. The excess free energy density Φ_{ed} which follows from

the extended set of weighted densities can be easily constructed and the corresponding theory is termed *e*xtended *d*econvolution FMT (edFMT). In Section 4.2 we show that edFMT improves upon onFMT with respect to several issues. First, edFMT is able to predict the isotropic-nematic transition as we show by comparison with data from computer simulations of hard spherocylinders [128]. The theory agrees well with the data for spherocylinders with moderate aspect ratios. Second, the description of the *inhomogeneous* isotropic hard-spherocylinder fluid is enhanced by edFMT compared to onFMT. In order to demonstrate this we have performed Monte Carlo simulations of different hard-spherocylinder fluids with length-to-diameter ratios up to 10.0 subjected to the external potential induced by a planar hard wall which gives rise to the inhomogeneity of the fluid. Moreover, edFMT provides a motivation for employing the weighted density $\overleftrightarrow{n}_2$, which unlike $\overleftrightarrow{n}_1$ does not vanish for spheres, also for the construction of an FMT for the hard-sphere systems. Thereby, a link between Rosenfeld's low-density limit based approach and the work by Tarazona [77], who previously introduced $\overleftrightarrow{n}_2$ in order to obtain a proper FMT for the hard-sphere *crystal*, can be established.

With the improved FMT version WBII and the generalization of FMT to fluids of non-spherical particles at hand we can push the high degree of efficiency, which results from employing the morphometric form of F_{sol} [Eq. (6.1)], even further. Matching F_{sol} as obtained from the excess free energy density Φ_{WBII} (or, more precisely, the corresponding FMT for non-spherical particles) with Eq. (6.1) provides us with analytical expressions for the thermodynamic coefficients p, σ, κ, and $\bar{\kappa}$ as functions of the hard-sphere packing fraction η and the hard-sphere radius R [Eq. (5.6)]. A comparison with the aforementioned calculation of the coefficients for simple solute geometries by means of a full DFT treatment reveals the high accuracy and consistency of the analytical expressions which are superior to earlier results (see Section 5.1). For the calculation of F_{sol} in the biologically inspired system this means that a wide range of solvent characteristics (η, R) can be covered conveniently.

We have mentioned at the beginning of the summary that our motivation for investigating the hard-sphere solvent is to study the effect of solvent *entropy*. The question remains what the appropriate counterpart to the hard-sphere solvent is regarding the protein representation. A simple protein model has been proposed some time ago by Banavar and Maritan [11, 12, 145] who modeled the protein backbone as an impenetrable, flexible tube with a well-defined diameter. Their model protein was shown to display various secondary motifs similar to those occurring in real proteins if the tube is subjected to local compactness conditions [145] or to an effective attractive potential between different tube segments mimicking the hydrophobic effect [12].

However, the direct influence of the solvent on bio-molecules represented in the tube model has been investigated only recently by Snir and Kamien [14, 15]. They have studied the effects on chain-like molecules due to solvent entropy which leads them to the conclusion that increasing the size of the solvent particles causes helical chain conformations to unwind such that sheetlike conformations appear to be favored. However, the results of Snir and Kamien are valid only in the limit of infinitely diluted hard-sphere solvents. Using the morphometric form [Eq. (6.1)] for the solvation free energy F_{sol} and the new analytical results for the thermodynamic coefficients for the hard-sphere solvent we are able to extend these previous results to the more relevant case of arbitrary solvent densities (see Section 5.2.2). It turns out that sheetlike folding is associated with *small* solvent particles at *large* solvent densities in contrast to the previous unwinding hypothesis which locates the β-sheet in the domain of large solvent particles. We can, however, confirm even for high solvent densities Snir's and Kamien's result that large solvent particles lead to a favoring of helices which are packed somewhat loosely. Nevertheless, we can show that these loose helical conformations are always separated from the sheetlike conformation by an energy barrier which disproves the unwinding hypothesis even in the limit of very large solvent particles for which the solvent entropy ceases to be significant anyway.

In order to study the influence of hydrophobicity and hydrophilicity on protein folding it is expedient to use a solvent with intermolecular attraction which is an essential feature of water models. We show that a treatment of such a solvent is feasible in the context of morphological thermodynamics (see Section 5.2.3). Our model fluid is the simple square-well fluid which is obtained by adding a constant, short-ranged attractive potential to the hard-sphere repulsion. The attraction can be treated by perturbation theory leading to a simple modification of the underlying DFT. Thermodynamic coefficients for Eq. (6.1) can, however, no longer be obtained analytically from the density functional as in the case of FMT for hard spheres which is a consequence of the lack of a good DFT for square-well mixtures. Nevertheless, Eq. (6.1) can still be applied with thermodynamic coefficients obtained from full DFT calculations in a simple test geometry. Besides the attraction between the solvent particles, our model also includes characteristic interactions of the solute with the solvent particles. In this way thermodynamic coefficients corresponding either to hydrophilic amino acids (solute-solvent attraction) or hydrophobic amino acids (solute-solvent repulsion) can be obtained within the numerical procedure. Our results for the solvation free energy F_{sol} of the protein in the tube model confirm the role of hydrophobic amino acids as a driving force for protein folding while we find no tendency of the protein to fold in the hydrophilic scenario.

In the remainder of this chapter we indicate possible routes for future research concerning the issues which have been investigated in this thesis. We have shown that the exact 1D density functional for the hard-sphere mixture provides an excellent basis for the derivation of approximative theories in higher dimensions. It would be of great interest if analogous results for mixtures of particles with arbitrary interaction potentials could be derived. In the literature there are in fact some examples of exact 1D DFTs for particles with more complicated interactions than the hard-body repulsion (see Ref. [147] and references therein). However, these functionals do not possess the structural simplicity of the hard-sphere analog such that to date it is not clear if they can be useful for obtaining results in higher dimensions. In particular, an improved theory for the general mixture might provide analytical expressions for the thermodynamic coefficients for fluids more complex than the hard-sphere fluid. In turn, this would facilitate the calculation of F_{sol} within morphological thermodynamics.

In view of the derivation of equations of state for the hard-sphere mixture, which has led us in this work to the improved expression $p^{(3)}$ [Eq. (6.4)] for the pressure, we note that basically two routes for further improvement are conceivable. First, an improved expression for the underlying equation of state for the one-component fluid can be employed and, second, the degree of consistency can be enhanced by requiring full thermodynamic consistency not only for the pure fluid but also for mixtures. The first issue might lead one to use the Kolafa equation of state (quoted in Ref. [148]) which is rather simple and slightly better than the Carnahan-Starling equation of state or more elaborate expressions as obtained from detailed fitting of simulation data [149,150]. While for sure these modifications would give rise to equations of state for mixtures which are rather cumbersome as compared to the expression for $p^{(3)}$, it is expected that the performance for multi-component mixtures and highly asymmetric mixtures is mainly determined by the second issue, i.e., the degree of consistency. We have, however, already checked in the course of deriving $p^{(3)}$ that a remaining degree of freedom cannot be used in order to extend consistency to the level of the binary mixture. Thus, it seems that such intrinsic limitations of the description are due to the restricted set of four weighted densities $n_0, \ldots, n_3$ [Eq. (6.3)]. Work aimed at investigating these limitations and possibly extending the set of variables might take into consideration a related study by Tarazona *et al.*, who discuss the intrinsic limitations of FMT [98].

Several aspects of FMTs for fluids of hard bodies with arbitrary shapes might be interesting to study in the future. The exact expression for the low-density limit of the excess free energy functional [Eq. (3.1) with Eq. (4.7)] can serve to identify

additional tensorial weighted densities of higher rank than that of $\overleftrightarrow{n}_1$ and $\overleftrightarrow{n}_2$ which allow for matching Onsager's limit for particles with large aspect ratios more closely. Such an extension should improve the FMT for these particles, in particular the size of the density gap at the isotropic-nematic transition should be predicted more precisely (cf. Section 4.2.1). However, the addition of tensorial weighted densities of higher rank to the FMT would complicate and impede the numerical treatment of spatially inhomogeneous systems, which, at moderate densities and aspect ratios, are already very well described by the present improved theory. As a very interesting test the present FMT could be applied to systems of non-spherical particles in the high-density regime such as the gyroid structure which has been found recently for compressed pear-shaped particles [125]. This application would allow to assess whether Tarazona's modification of Rosenfeld's FMT, which avoids spurious divergencies of the density functional occurring for the hard-sphere crystal, is sufficient for a reliable description also of crystals of general hard bodies. More extensive work in this direction might consist in mapping out complete phase diagrams of different hard-body fluids with the new FMT and compare the results with the outcome of numerical simulations. Moreover, a comparison of the edFMT with results from integral equations as obtained in Ref. [133] might be illuminating.

Given the complexity of biological systems, many aspects concerning the issue of protein solvation remain to be investigated. Extentions of the present study can be distinguished according to whether they concern the protein or the solvent characteristics. The protein description can be refined by modelling a given amino acid sequence, in a first approach, in terms of hydrophilic and hydrophobic patches on the protein tube. The solvation free energy can then still be calculated within morphological thermodynamics but one has to care about additional contributions to the geometric measures stemming from the boundary lines between different patches. Such a procedure may lead to an understanding of the folds of concrete proteins while the results, however, would no longer be of general character such as the effects due to solvent entropy which have been calculated in Chapter 5. Further refinement of the protein description can be obtained by including internal energetic contributions due to hydrogen bonds between amino acids from different parts of the protein backbone or, less specifically, by introducing a bending stiffness of the protein backbone into the model in the spirit of Ref. [14]. As far as the solvent description is concerned, improvement can obviously be realized by using models of water which are more realistic than the simple square-well fluid. We emphasize that Eq. (6.1) is applicable also for more complex solvents, but in this case DFT is likely to be insufficient for the calculations of thermodynamic coefficients. This is due to the aforementioned lack of

a good DFT for attractive interactions which makes accurate density functionals for more complex water models difficult to obtain. However, it seems practicable to determine F_{sol} from numerical simulations of complex solvents containing solutes with simple shapes and use the data for the calculation of the thermodynamic coefficients. A further extention of the investigation, which concerns the solvent description in the more general sense of the description of the surrounding medium, could be centered around studying protein folding in confinement. As a matter of fact, protein folding occurs in the often crowded environment of the cell where the assumption of confinement is realistic. This has motivated studies of protein folding in nanopores where confinement has been shown to either stabilize or destabilize the folded state, depending on whether the pore is permeable to the solvent [151, 152]. It would be highly interesting to study the issue with the help of morphological thermodynamics. The application of Eq. (6.1) to portions of the solvent which are confined between the protein and the walls of some container would provide an additional stringent test of the performance of the morphometric approach to F_{sol}.

Appendix A

Geodesic curvature of the intersection line

Given are two convex bodies $\mathcal{B}_i$ and $\mathcal{B}_j$ with an intersection $\mathcal{B}_i \cap \mathcal{B}_j \neq \varnothing$. Let the intersection line $\mathcal{C} = \partial\mathcal{B}_i \cap \partial\mathcal{B}_j$ be parametrized with unit velocity via $\mathbf{r} = \mathbf{r}(s)$. We calculate the geodesic curvatures κ_i^{g} and κ_j^{g} of $\mathcal{C}$ on the surfaces $\partial\mathcal{B}_i$ and $\partial\mathcal{B}_j$ in the point $\mathbf{r}(s=0)$. Without loss of generality we can assume $\mathbf{r}(s=0) = 0$. The equations describing $\partial\mathcal{B}_i$ and $\partial\mathcal{B}_j$ in the vicinity of $\mathbf{r} = 0$ can be written as Taylor expansions

$$-\mathbf{n}_\tau \mathbf{r} = \frac{1}{2}\kappa_\tau^I (\mathbf{v}_\tau^I \mathbf{r})^2 + \frac{1}{2}\kappa_\tau^{II} (\mathbf{v}_\tau^{II} \mathbf{r})^2 + \text{h.o.t.} \quad , \qquad \tau = i, j\,. \tag{A.1}$$

Here $\mathbf{n}_\tau$ is the outward normal on the respective surface, and κ_τ^I and κ_τ^{II} denote the principal curvatures. The unit vectors $\mathbf{v}_\tau^I$ and $\mathbf{v}_\tau^{II}$ indicate the directions of principal curvatures. It will become clear in the following that the higher order terms in $\mathbf{v}_\tau^I \mathbf{r}$ and $\mathbf{v}_\tau^{II} \mathbf{r}$ (h.o.t.) are irrelevant for the calculation of κ_τ^{g}. In particular, as $\mathcal{C}$ is contained in $\partial\mathcal{B}_i$ and $\partial\mathcal{B}_j$ the parametrization $\mathbf{r}(s)$ must obey the equations

$$-\mathbf{n}_\tau \mathbf{r}(s) = \frac{1}{2}\kappa_\tau^I (\mathbf{v}_\tau^I \mathbf{r}(s))^2 + \frac{1}{2}\kappa_\tau^{II} (\mathbf{v}_\tau^{II} \mathbf{r}(s))^2 + \text{h.o.t.} \quad , \qquad \tau = i, j\,. \tag{A.2}$$

Taking the first and second derivatives on both sides of Eq. (A.2) w.r.t. s yields equations for $\mathbf{r}'(s)$ and $\mathbf{r}''(s)$:

$$-\mathbf{n}_\tau \mathbf{r}'(s) = \kappa_\tau^I (\mathbf{v}_\tau^I \mathbf{r}(s))(\mathbf{v}_\tau^I \mathbf{r}'(s)) + \kappa_\tau^{II} (\mathbf{v}_\tau^{II} \mathbf{r}(s))(\mathbf{v}_\tau^{II} \mathbf{r}'(s)) + \text{h.o.t.} \quad , \qquad \tau = i, j\,, \tag{A.3}$$

$$\begin{aligned} -\mathbf{n}_\tau \mathbf{r}''(s) = {} & \kappa_\tau^I (\mathbf{v}_\tau^I \mathbf{r}'(s))^2 + \kappa_\tau^I (\mathbf{v}_\tau^I \mathbf{r}(s))(\mathbf{v}_\tau^I \mathbf{r}''(s)) \\ & + \kappa_\tau^{II} (\mathbf{v}_\tau^{II} \mathbf{r}'(s))^2 + \kappa_\tau^{II} (\mathbf{v}_\tau^{II} \mathbf{r}(s))(\mathbf{v}_\tau^{II} \mathbf{r}''(s)) + \text{h.o.t.} \quad , \qquad \tau = i, j\,. \end{aligned} \tag{A.4}$$

Evaluating the equations at $s = 0$ leads to a vanishing of the higher order terms and we obtain the simple equations

$$-\mathbf{n}_\tau \mathbf{r}'(0) = 0 \quad , \qquad \tau = i, j \,, \tag{A.5}$$

$$-\mathbf{n}_\tau \mathbf{r}''(0) = \kappa_\tau^I (\mathbf{v}_\tau^I \mathbf{r}'(0))^2 + \kappa_\tau^{II} (\mathbf{v}_\tau^{II} \mathbf{r}'(0))^2 \quad , \qquad \tau = i, j \,. \tag{A.6}$$

As $\mathcal{C}$ is parametrized with unit velocity it follows immediately from Eq. (A.5) that

$$\mathbf{r}'(0) = \pm \frac{\mathbf{n}_i \times \mathbf{n}_j}{|\mathbf{n}_i \times \mathbf{n}_j|} \doteq \mathbf{t} \,. \tag{A.7}$$

Using in the next step that $\mathbf{r}'(s)\mathbf{r}''(s) \equiv 0$ due to the constant velocity and that in addition Eq. (A.6) holds, we can construct $\mathbf{r}''(0)$ from its projections in the directions of $\mathbf{n}_i$, $\mathbf{n}_j$, and $\mathbf{t}$. The result is

$$-\mathbf{r}''(0) = \frac{M_i - M_j \mathbf{n}_i \mathbf{n}_j}{|\mathbf{n}_i \times \mathbf{n}_j|^2} \, \mathbf{n}_i + \frac{M_j - M_i \mathbf{n}_i \mathbf{n}_j}{|\mathbf{n}_i \times \mathbf{n}_j|^2} \, \mathbf{n}_j \,, \tag{A.8}$$

where we have introduced the shorthand

$$M_\tau = \kappa_\tau^I (\mathbf{v}_\tau^I \mathbf{t})^2 + \kappa_\tau^{II} (\mathbf{v}_\tau^{II} \mathbf{t})^2 \quad , \qquad \tau = i, j \,. \tag{A.9}$$

The curvature κ and principal normal $\mathbf{n}$ of $\mathcal{C}$ at $s = 0$ are given by $\kappa = |\mathbf{r}''(0)|$ and $\mathbf{n} = \mathbf{r}''(0)/|\mathbf{r}''(0)|$. By definition, the geodesic curvature of $\mathcal{C}$ on $\partial\mathcal{B}_\tau$ is given by $\kappa_\tau^{\mathrm{g}} = \sigma_\tau \kappa \sin\omega_\tau$, where $\omega_\tau \in [0, \pi]$ is the angle between $\mathbf{n}_\tau$ and $\mathbf{n}$. The sign of κ_τ^{g} is $\sigma_\tau = +1$ if the projection of $\mathbf{n}$ onto the tangent plane of $\partial\mathcal{B}_\tau$ points inwards the bounded surface S [cf. Eq. (4.4)], and $\sigma_\tau = -1$ if it points outwards. With Eq. (A.8) and the definition of κ_τ^{g} we calculate

$$\kappa_i^{\mathrm{g}} = \sigma_i |\mathbf{n}_i \times \mathbf{r}''(0)| = \sigma_i \frac{|M_j - M_i \mathbf{n}_i \mathbf{n}_j|}{|\mathbf{n}_i \times \mathbf{n}_j|} \tag{A.10}$$

and κ_j^{g} is given by the same expression with $i \leftrightarrow j$. For the determination of σ_i we calculate the projection of $\mathbf{r}''(0)$ onto the tangent plane of $\partial\mathcal{B}_i$ which is the plane perpendicular to $\mathbf{n}_i$:

$$(\mathbf{r}''(0))_{\mathrm{proj}} = \mathbf{r}''(0) - (\mathbf{n}_i \mathbf{r}''(0)) \, \mathbf{n}_i = -\frac{M_j - M_i \mathbf{n}_i \mathbf{n}_j}{|\mathbf{n}_i \times \mathbf{n}_j|^2} \big(\mathbf{n}_j - (\mathbf{n}_i \mathbf{n}_j) \mathbf{n}_i \big) \,. \tag{A.11}$$

The direction pointing outwards the surface $S = \partial\mathcal{B}_i$ is indicated by the projection of $\mathbf{n}_j$ onto the tangent plane of $\partial\mathcal{B}_i$ which is simply $(\mathbf{n}_j)_{\mathrm{proj}} = \mathbf{n}_j - (\mathbf{n}_i \mathbf{n}_j) \mathbf{n}_i$. A comparison with $(\mathbf{r}''(0))_{\mathrm{proj}}$ and the definition of σ_i show that we must choose $\sigma_i = \mathrm{sgn}(M_j - M_i \mathbf{n}_i \mathbf{n}_j)$. It follows for κ_i^{g}, and with similar arguments for κ_j^{g}, that

$$\kappa_i^{\mathrm{g}} = \frac{M_j - M_i \mathbf{n}_i \mathbf{n}_j}{|\mathbf{n}_i \times \mathbf{n}_j|} \,, \quad \kappa_j^{\mathrm{g}} = \frac{M_i - M_j \mathbf{n}_i \mathbf{n}_j}{|\mathbf{n}_i \times \mathbf{n}_j|} \,. \tag{A.12}$$

The sum $\kappa_i^{\mathrm{g}} + \kappa_j^{\mathrm{g}}$, which appears in Eq. (4.5), gives rise to the expression

$$\kappa_i^{\mathrm{g}} + \kappa_j^{\mathrm{g}} = (M_i + M_j)\frac{1 - \mathbf{n}_i\mathbf{n}_j}{|\mathbf{n}_i \times \mathbf{n}_j|}\,. \tag{A.13}$$

Finally, we express M_τ from Eq. (A.9) differently. From the fact that $\mathbf{v}_\tau^I$ and $\mathbf{v}_\tau^{II}$ constitute an orthonormal basis of the tangent plane of $\partial\mathcal{B}_\tau$ it follows for the unit vector $\mathbf{t}$ that $(\mathbf{v}_\tau^I\mathbf{t})^2 + (\mathbf{v}_\tau^{II}\mathbf{t})^2 = 1$. This allows us to formulate M_τ in terms of the mean curvature $H_\tau = \frac{1}{2}(\kappa_\tau^I + \kappa_\tau^{II})$ and the deviatoric curvature $\Delta\kappa_\tau = \frac{1}{2}(\kappa_\tau^I - \kappa_\tau^{II})$:

$$\begin{aligned} M_\tau &= \kappa_\tau^I(\mathbf{v}_\tau^I\mathbf{t})^2 + \kappa_\tau^{II}(\mathbf{v}_\tau^{II}\mathbf{t})^2 \\ &= \frac{1}{2}(\kappa_\tau^I + \kappa_\tau^{II})\big((\mathbf{v}_\tau^I\mathbf{t})^2 + (\mathbf{v}_\tau^{II}\mathbf{t})^2\big) + \frac{1}{2}(\kappa_\tau^I - \kappa_\tau^{II})\big((\mathbf{v}_\tau^I\mathbf{t})^2 - (\mathbf{v}_\tau^{II}\mathbf{t})^2\big) \\ &= H_\tau + \Delta\kappa_\tau\big((\mathbf{v}_\tau^I\mathbf{t})^2 - (\mathbf{v}_\tau^{II}\mathbf{t})^2\big)\,. \end{aligned} \tag{A.14}$$

Using further the definition of $\mathbf{t}$ [Eq. (A.7)] and the fact that $\mathbf{n}_\tau$, $\mathbf{v}_\tau^I$ and $\mathbf{v}_\tau^{II}$ are orthonormal, relations like the following can be derived:

$$(\mathbf{v}_i^I\mathbf{t})^2 = \frac{(\mathbf{v}_i^I(\mathbf{n}_i \times \mathbf{n}_j))^2}{|\mathbf{n}_i \times \mathbf{n}_j|^2} = \frac{(\mathbf{v}_i^{II}\mathbf{n}_j)^2}{1 - (\mathbf{n}_i\mathbf{n}_j)^2}\,. \tag{A.15}$$

Thus we obtain

$$M_i = H_i - \frac{\Delta\kappa_i}{1 - (\mathbf{n}_i\mathbf{n}_j)^2}\big((\mathbf{v}_i^I\mathbf{n}_j)^2 - (\mathbf{v}_i^{II}\mathbf{n}_j)^2\big) \tag{A.16}$$

and the corresponding expression with $i \leftrightarrow j$. Plugging this into Eq. (A.13) we arrive at the final result

$$\kappa_i^{\mathrm{g}} + \kappa_j^{\mathrm{g}} = H_i\,\frac{1 - \mathbf{n}_i\mathbf{n}_j}{|\mathbf{n}_i \times \mathbf{n}_j|} - \Delta\kappa_i\,\frac{(\mathbf{v}_i^I\mathbf{n}_j)^2 - (\mathbf{v}_i^{II}\mathbf{n}_j)^2}{(1 + \mathbf{n}_i\mathbf{n}_j)|\mathbf{n}_i \times \mathbf{n}_j|} + (i \leftrightarrow j)\,. \tag{A.17}$$

Appendix B

Intersection of two delta-shells

Consider first the case of two planes with normal vectors $\mathbf{n}_i$ and $\mathbf{n}_j$ with an intersection line which runs through the origin. We call F the integral of the function $f(x,y,z)$ along the intersection line which is defined as

$$F = \iiint \mathrm{d}x\,\mathrm{d}y\,\mathrm{d}z\, f(x,y,z)\,\delta(c_i n_i^x x + c_i n_i^y y + c_i n_i^z z)\,\delta(c_j n_j^x x + c_j n_j^y y + c_j n_j^z z) \quad \text{(B.1)}$$

where c_i and c_j are arbitrary non-zero constants. We perform the z-integration and use that, according to the second delta-function, $z = z(x,y) = -\frac{n_j^x}{n_j^z}x - \frac{n_j^y}{n_j^z}y$ must hold. This leads to

$$F = \iint \mathrm{d}x\,\mathrm{d}y\,\frac{f(x,y,z(x,y))}{|c_j||n_j^z|}\,\delta\!\left[c_i\left(n_i^x - \frac{n_i^z n_j^x}{n_j^z}\right)x + c_i\left(n_i^y - \frac{n_i^z n_j^y}{n_j^z}\right)y\right]. \quad \text{(B.2)}$$

Performing now the y-integration yields

$$F = \int \mathrm{d}x\,\frac{f(x,y(x),z(x))}{|c_i||c_j||n_i^y n_j^z - n_j^y n_i^z|} \quad \text{(B.3)}$$

where

$$y(x) = -\frac{n_i^x n_j^z - n_i^z n_j^x}{n_i^y n_j^z - n_i^z n_j^y}\,x \qquad \text{and} \qquad z(x) = -\frac{n_i^y n_j^x - n_i^x n_j^y}{n_i^y n_j^z - n_i^z n_j^y}\,x\,. \quad \text{(B.4)}$$

In a last step we parametrize the intersection line by its arclength s. Using that $\mathrm{d}s = \sqrt{1 + y'(x)^2 + z'(x)^2}\,\mathrm{d}x$ we arrive at the final result

$$F = \int \mathrm{d}s\,\frac{f(x(s),y(s),z(s))}{|c_i||c_j||\mathbf{n}_i \times \mathbf{n}_j|}\,. \quad \text{(B.5)}$$

Consider now the intersection of two bodies centered at $\mathbf{r}_i$ and $\mathbf{r}_j$ which are parametrized via $\mathbf{R}_i(\hat{\mathbf{r}})$ and $\mathbf{R}_j(\hat{\mathbf{r}})$ as shown in Fig. 4.1. We calculate the contribution of a given point $\mathbf{r}_0$ of the intersection line to the convolution $\omega_i^{(1)} \otimes \omega_j^{(2)}$ in order to demonstrate the validity of Eq. (4.9). For the convolutions $\overrightarrow{\omega}_i^{(1)} \otimes \overrightarrow{\omega}_j^{(2)}$ and

$\overleftrightarrow{\omega}_i^{(1)} \otimes \overleftrightarrow{\omega}_j^{(2)}$ essentially the same arguments apply. From Eqs. (3.6) and Eq. (4.1) we know that

$$\omega_i^{(1)} \otimes \omega_j^{(2)} = \int \mathrm{d}\mathbf{r} \frac{H_i}{4\pi} \delta\big(|\mathbf{R}_i(\widehat{\mathbf{r}-\mathbf{r}_i})| - |\mathbf{r}-\mathbf{r}_i|\big) \big/ \big(\mathbf{n}_i \cdot (\widehat{\mathbf{r}-\mathbf{r}_i})\big) \times \delta\big(|\mathbf{R}_j(\widehat{\mathbf{r}-\mathbf{r}_j})| - |\mathbf{r}-\mathbf{r}_j|\big) \big/ \big(\mathbf{n}_j \cdot (\widehat{\mathbf{r}-\mathbf{r}_j})\big)\,, \tag{B.6}$$

where we suppress in the notation the dependences of H_i, $\mathbf{n}_i$, and $\mathbf{n}_j$ on the spacial coordinates. For clarity, we have denoted the scalar product by the dot. It is useful to apply a transformation $\mathbf{r} \to \mathbf{r}_0 + \delta\mathbf{r}$ such that the integration is performed w.r.t. $\delta\mathbf{r}$. By definition of $\mathbf{r}_0$ the point $\delta\mathbf{r} = 0$ corresponds to a zero of the arguments A_i and A_j of the two delta-functions in Eq. (B.6). For the contribution of the point $\mathbf{r}_0$ to the convolution, A_i and A_j are relevant only to lowest order in $\delta\mathbf{r}$. We therefore calculate $A_i = |\mathbf{R}_i(\widehat{\mathbf{r}_0 - \mathbf{r}_i + \delta\mathbf{r}})| - |\mathbf{r}_0 - \mathbf{r}_i + \delta\mathbf{r}|$ in more detail. By definition $\mathbf{R}_i(\widehat{\mathbf{r}_0 - \mathbf{r}_i + \delta\mathbf{r}}) = \lambda(\mathbf{r}_0 - \mathbf{r}_i + \delta\mathbf{r})$ with positive $\lambda \in \mathbb{R}$ which is itself a function of $\mathbf{r}_0 - \mathbf{r}_i + \delta\mathbf{r}$. To lowest order in $\delta\mathbf{r}$ the curvature of the intersecting surfaces is not relevant. We can thus reach the point $\mathbf{R}_i(\widehat{\mathbf{r}_0 - \mathbf{r}_i + \delta\mathbf{r}})$ in the vicinity of $\mathbf{R}_i(\widehat{\mathbf{r}_0 - \mathbf{r}_i}) = \mathbf{r}_0 - \mathbf{r}_i$ simply by moving within the tangent plane of the surface i which is spanned by $\mathbf{v}_i^I$ and $\mathbf{v}_i^{II}$. In other words $\mathbf{R}_i(\widehat{\mathbf{r}_0 - \mathbf{r}_i}) + \mu_I \mathbf{v}_i^I + \mu_{II}\mathbf{v}_i^{II} = \mathbf{R}_i(\widehat{\mathbf{r}_0 - \mathbf{r}_i + \delta\mathbf{r}})$ or, equivalently, $\mathbf{r}_0 - \mathbf{r}_i + \mu_I \mathbf{v}_i^I + \mu_{II}\mathbf{v}_i^{II} = \lambda(\mathbf{r}_0 - \mathbf{r}_i + \delta\mathbf{r})$. This relation can be solved for λ by taking the scalar product of both sides with $\mathbf{n}_i$. As $\mathbf{n}_i\mathbf{v}_i^I = \mathbf{n}_i\mathbf{v}_i^{II} = 0$ we obtain that

$$\lambda - 1 = -\frac{\mathbf{n}_i \delta\mathbf{r}}{\mathbf{n}_i \cdot (\mathbf{r}_0 - \mathbf{r}_i)} \tag{B.7}$$

It follows that

$$\begin{aligned} A_i &= |\mathbf{R}_i(\widehat{\mathbf{r}_0 - \mathbf{r}_i + \delta\mathbf{r}})| - |\mathbf{r}_0 - \mathbf{r}_i + \delta\mathbf{r}| \\ &= \lambda|\mathbf{r}_0 - \mathbf{r}_i + \delta\mathbf{r}| - |\mathbf{r}_0 - \mathbf{r}_i + \delta\mathbf{r}| \\ &= -\frac{\mathbf{n}_i\delta\mathbf{r}}{\mathbf{n}_i \cdot (\mathbf{r}_0 - \mathbf{r}_i)} |\mathbf{r}_0 - \mathbf{r}_i + \delta\mathbf{r}| \\ &= -\frac{\mathbf{n}_i\delta\mathbf{r}}{\mathbf{n}_i \cdot (\widehat{\mathbf{r}_0 - \mathbf{r}_i})} + \mathcal{O}(\delta\mathbf{r}^2)\,. \end{aligned} \tag{B.8}$$

In consequence, at the point $\mathbf{r}_0$ Eq. (B.6) becomes

$$\begin{aligned} \omega_i^{(1)} \otimes \omega_j^{(2)} &= \int \mathrm{d}(\delta\mathbf{r}) \frac{H_i}{4\pi} \delta\bigg(-\frac{\mathbf{n}_i\delta\mathbf{r}}{\mathbf{n}_i \cdot (\widehat{\mathbf{r}_0 - \mathbf{r}_i})}\bigg) \big/ \big(\mathbf{n}_i \cdot (\widehat{\mathbf{r}_0 - \mathbf{r}_i})\big) \\ &\qquad \times \delta\bigg(-\frac{\mathbf{n}_j\delta\mathbf{r}}{\mathbf{n}_j \cdot (\widehat{\mathbf{r}_0 - \mathbf{r}_j})}\bigg) \big/ \big(\mathbf{n}_j \cdot (\widehat{\mathbf{r}_0 - \mathbf{r}_j})\big) \\ &= \int \frac{H_i}{4\pi} \frac{\mathrm{d}s}{|\mathbf{n}_i \times \mathbf{n}_j|}\,, \end{aligned} \tag{B.9}$$

where we have used the equality of Eqs. (B.1) and (B.5) in the last step. This completes the demonstration of the statement made in Eq. (4.9).

Appendix C

Second virial coefficient for spherocylinders

Consider a bulk fluid which is composed of spherocylinders with length L and diameter D (see Fig. 4.2). Due to translational invariance the particle density is a function of the spherocylinder orientation ϖ only, i.e., $\rho(\mathbf{r}, \varpi) = \rho(\varpi) = \rho f(\varpi)$ with constant bulk density ρ and orientational distribution $f(\varpi)$. The scalar weighted densities for fixed orientation ϖ can be calculated from Eq. (4.1) and Eq. (4.2). Independent of the shape of the particles which are considered, one finds the relations

$$n_3(\varpi) = \rho f(\varpi) v \,, \qquad n_2(\varpi) = \rho f(\varpi) a \,, \tag{C.1}$$

where v and a are the volume and the surface area of the particles under consideration. Using the expression for spherocylinders yields

$$n_3(\varpi) = \rho f(\varpi) \left(\frac{\pi}{4} L D^2 + \frac{\pi}{6} D^3 \right) \,, \qquad n_2(\varpi) = \rho f(\varpi) \left(\pi L D + \pi D^2 \right) \,. \tag{C.2}$$

For the calculation of n_1 and n_0 the contributions of the surface area of the spherocylinder have to be weighted with the mean and Gaussian curvatures which are $H = \frac{1}{D}$ and $K = 0$ for the cylinder and $H = \frac{2}{D}$ and $K = \frac{4}{D^2}$ for the capping hemispheres. Applying further the required division by 4π (see Eq. (4.1)) yields

$$n_1(\varpi) = \rho f(\varpi) \left(\frac{L}{4} + \frac{D}{2} \right) \,, \qquad n_0(\varpi) = \rho f(\varpi) \,. \tag{C.3}$$

The vectorial weighted densities $\overrightarrow{n}_1(\varpi)$ and $\overrightarrow{n}_2(\varpi)$ vanish in the bulk fluid. The calculation of the tensorial weighted densities $\overleftrightarrow{n}_1(\varpi)$ and $\overleftrightarrow{n}_2(\varpi)$ is a bit more involved than for the scalar weighted densities. We write the orientation ϖ in a more explicit fashion by using spherical coordinates (ϑ, φ). The orientation ϖ is then

encoded in the matrix

$$\mathcal{R} = \begin{pmatrix} \cos\varphi\cos\vartheta & -\sin\varphi & \cos\varphi\sin\vartheta \\ \sin\varphi\cos\vartheta & \cos\varphi & \sin\varphi\sin\vartheta \\ -\sin\vartheta & 0 & \cos\vartheta \end{pmatrix} . \tag{C.4}$$

The matrix $\mathcal{R}$ corresponds to a rotation mapping the vector $(0,0,1)^{\mathrm{T}}$ onto $(\cos\varphi\sin\vartheta, \sin\varphi\sin\vartheta, \cos\vartheta)^{\mathrm{T}}$ which points into the direction ϖ. Consider first a spherocylinder which is orientated along the $(0,0,1)^{\mathrm{T}}$-direction. A contribution to $\overleftrightarrow{n}_1(\varpi)$ is only made by the cylinder and not by the capping hemispheres which have a deviatoric curvature $\Delta\kappa = 0$ [see Eq. (4.13)]. The directions of principal curvature of the cylinder are given by $\mathbf{v}^I = (-\sin\varphi', \cos\varphi', 0)^{\mathrm{T}}$ ($\varphi' \in [0, 2\pi]$) and $\mathbf{v}^{II} = (0,0,1)^{\mathrm{T}}$ with a corresponding deviatoric curvature $\Delta\kappa = \frac{1}{D}$. According to Eq. (4.13) and Eq. (4.2) the weighted density $\overleftrightarrow{n}_1(\varpi)$ can be obtained by using these vectors $\mathbf{v}^I$ and $\mathbf{v}^{II}$ as

$$\overleftrightarrow{n}_1(\varpi) = \rho f(\varpi)\frac{L}{4}\int_0^{2\pi}\frac{\mathrm{d}\varphi'}{2\pi}\left((\mathcal{R}\mathbf{v}^I)(\mathcal{R}\mathbf{v}^I)^{\mathrm{T}} - (\mathcal{R}\mathbf{v}^{II})(\mathcal{R}\mathbf{v}^{II})^{\mathrm{T}}\right) , \tag{C.5}$$

where the integrals are calculated as

$$\begin{aligned} &\int_0^{2\pi}\frac{\mathrm{d}\varphi'}{2\pi}(\mathcal{R}\mathbf{v}^I)(\mathcal{R}\mathbf{v}^I)^{\mathrm{T}} \\ &= \frac{1}{2}\begin{pmatrix} \sin^2\varphi + \cos^2\varphi\cos^2\vartheta & -\sin\varphi\cos\varphi\sin^2\vartheta & -\cos\varphi\sin\vartheta\cos\vartheta \\ -\sin\varphi\cos\varphi\sin^2\vartheta & \cos^2\varphi\sin^2\vartheta + \cos^2\vartheta & -\sin\varphi\sin\vartheta\cos\vartheta \\ -\cos\varphi\sin\vartheta\cos\vartheta & -\sin\varphi\sin\vartheta\cos\vartheta & \sin^2\vartheta \end{pmatrix} \end{aligned} \tag{C.6}$$

and

$$\begin{aligned} &\int_0^{2\pi}\frac{\mathrm{d}\varphi'}{2\pi}(\mathcal{R}\mathbf{v}^{II})(\mathcal{R}\mathbf{v}^{II})^{\mathrm{T}} = (\mathcal{R}\mathbf{v}^{II})(\mathcal{R}\mathbf{v}^{II})^{\mathrm{T}} \\ &= \begin{pmatrix} \cos^2\varphi\sin^2\vartheta & \sin\varphi\cos\varphi\sin^2\vartheta & \cos\varphi\sin\vartheta\cos\vartheta \\ \sin\varphi\cos\varphi\sin^2\vartheta & \sin^2\varphi\sin^2\vartheta & \sin\varphi\sin\vartheta\cos\vartheta \\ \cos\varphi\sin\vartheta\cos\vartheta & \sin\varphi\sin\vartheta\cos\vartheta & \cos^2\vartheta \end{pmatrix} . \end{aligned} \tag{C.7}$$

Concerning the calculation of $\overleftrightarrow{n}_2(\varpi)$ we note that both the cylindrical body and the capping hemispheres do contribute in this case. The surface normal of the hemispheres is given by $\mathbf{n}_{\mathrm{hs}} = (\cos\varphi'\sin\vartheta', \sin\varphi'\sin\vartheta', \cos\vartheta')^{\mathrm{T}}$ with $\varphi' \in [0, 2\pi]$ and $\vartheta' \in [0, \pi]$. As we are dealing with the translational invariant bulk fluid the hemispheres can be considered as being connected to form a single sphere which simplifies the choice of the parameter region for φ' and ϑ'. The cylindrical body of

the $(0,0,1)^{\mathrm{T}}$-oriented spherocylinder has the surface normal $\mathbf{n}_{\mathrm{cyl}} = (\cos\varphi', \sin\varphi', 0)^{\mathrm{T}}$ with $\varphi' \in [0, 2\pi]$. Using Eq. (4.14) and Eq. (4.2) we find that

$$\overleftrightarrow{n}_2(\varpi) = \rho f(\varpi)\pi LD \int_0^{2\pi} \frac{\mathrm{d}\varphi'}{2\pi} (\mathcal{R}\mathbf{n}_{\mathrm{cyl}})(\mathcal{R}\mathbf{n}_{\mathrm{cyl}})^{\mathrm{T}} + \rho f(\varpi)\pi D^2 \int_0^{\pi} \mathrm{d}\vartheta' \frac{\sin\vartheta'}{4\pi} \int_0^{2\pi} \mathrm{d}\varphi' (\mathcal{R}\mathbf{n}_{\mathrm{hs}})(\mathcal{R}\mathbf{n}_{\mathrm{hs}})^{\mathrm{T}}\,, \tag{C.8}$$

where

$$\int_0^{2\pi} \frac{\mathrm{d}\varphi'}{2\pi} (\mathcal{R}\mathbf{n}_{\mathrm{cyl}})(\mathcal{R}\mathbf{n}_{\mathrm{cyl}})^{\mathrm{T}} = \int_0^{2\pi} \frac{\mathrm{d}\varphi'}{2\pi} (\mathcal{R}\mathbf{v}^I)(\mathcal{R}\mathbf{v}^I)^{\mathrm{T}}\,, \quad \text{see Eq. (C.6)}, \tag{C.9}$$

and

$$\int_0^{\pi} \mathrm{d}\vartheta' \frac{\sin\vartheta'}{4\pi} \int_0^{2\pi} \mathrm{d}\varphi' (\mathcal{R}\mathbf{n}_{\mathrm{hs}})(\mathcal{R}\mathbf{n}_{\mathrm{hs}})^{\mathrm{T}} = \frac{1}{3} \cdot \mathbb{1}\,. \tag{C.10}$$

Here $\mathbb{1}$ denotes the unit matrix.

Using the fact that $n_\alpha = \int \mathrm{d}\varpi n_\alpha(\varpi)$ we obtain from Eq. (4.16) the low-density limit of the free energy density

$$\Phi_{\mathrm{ed}} = n_0 n_3 + n_1 n_2 - \overrightarrow{n}_1 \overrightarrow{n}_2 - \zeta \mathrm{Tr}[\overleftrightarrow{n}_1 \overleftrightarrow{n}_2] + \mathcal{O}(\rho^3) \tag{C.11}$$

$$= \iint \mathrm{d}\varpi \mathrm{d}\varpi' \big(n_0(\varpi) n_3(\varpi') + n_1(\varpi) n_2(\varpi') - \overrightarrow{n}_1(\varpi) \overrightarrow{n}_2(\varpi') - \zeta \mathrm{Tr}[\overleftrightarrow{n}_1(\varpi) \overleftrightarrow{n}_2(\varpi')] \big) + \mathcal{O}(\rho^3) \tag{C.12}$$

$$= \frac{\rho^2}{2} \iint \mathrm{d}\varpi \mathrm{d}\varpi' f(\varpi) f(\varpi') v_{\mathrm{FMT}}(\varpi, \varpi') + \mathcal{O}(\rho^3). \tag{C.13}$$

which proves Eq. (4.19). The equality of Eqs. (C.12) and (C.13) follows from some algebra involving the above expressions for the weighted densities $n_\alpha(\varpi)$ and the relation that

$$\sin\gamma = \left| \begin{pmatrix} \cos\varphi \sin\vartheta \\ \sin\varphi \sin\vartheta \\ \cos\vartheta \end{pmatrix} \times \begin{pmatrix} \cos\varphi' \sin\vartheta' \\ \sin\varphi' \sin\vartheta' \\ \cos\vartheta' \end{pmatrix} \right| \tag{C.14}$$

where γ is the angle between the directions ϖ and ϖ'.

Zusammenfassung

Proteine erfüllen in Organismen eine Vielzahl von ganz unterschiedlichen Aufgaben. Proteine treten beispielsweise als Enzyme in Erscheinung, indem sie als Katalysator bei biochemischen Reaktionen wirken, sowie als Transportproteine, indem sie lebenswichtige Substanzen wie den Sauerstoff im Blut transportieren. Auf der makrokopischen Skala wird die Wirkung von so genannten Motorproteinen sichtbar, die für die Kontraktion der Muskeln verantwortlich sind und somit das Ausüben von Kräften ermöglichen. Als letztes Beispiel sei hier die Bedeutung von Proteinen für die Stabilisierung der Körperzellen genannt, welche ihre Form dank des durch Aktin und Tubulin gebildeten Zytoskelettes aufrecht erhalten können, sowie die Stabilisierung fester Stukturen wie Haare und Nägel durch Keratin.

Erstaunlicherweise werden diese "Alleskönner" der Zelle aus einem überschaubaren Baukasten von nur 20 Aminosäuren (plus Selenocystein), welche zu linearen Ketten zusammengefügt sind, gebildet. Unter physiologischen Bedingungen nehmen Proteine einen wohldefinieren kompakten Zustand ein, der als Tertiärstruktur des Proteins bezeichnet wird und in dem die Abschnitte der Polypeptidkette entsprechend gewisser Sekundärmotive gefaltet sind und diese sich gegeneinander in charakteristischer Weise anordnen. Die wichtigsten Sekundärmotive der Proteinfaltung sind die α-Helix und das β-Faltblatt, die experimentell erstmals 1931 von Astbury nachgewiesen [1] aber erst 1951 durch Pauling in einem atomaren Modell korrekt entschlüsselt wurden [2,3]. Das große Interesse an einem vollständigen Verständnis der Proteinfaltung ergibt sich aus der Tatsache, dass die Tertiärstruktur eines Proteins dessen Funktion ganz entscheidend bestimmt [6]. Außerdem erweisen sich gefaltete Proteine als erstaunlich stabil gegen Versuche, sie zu entfalten, abgesehen von eventuellen kleineren Änderungen der physiologischen Struktur, welche die Ausübung der Proteinfunktion unterstützen. Jedoch hat sich herausgestellt, dass, obwohl das Problem der Vorhersage von Tertiärstrukturen als Eingabe nichts weiter als die Sequenz der Aminosäuren verlangt, eine verlässliche Berechnung der physiologischen Struktur noch nicht befriedigend gewährleistet werden kann [7].

Heute existiert bereits eine große Anzahl von bekannten Proteinstrukturen, die als

Prüfstein für Algorithmen zur Strukturvorhersage dienen können. Mittels Röntgenkristallografie und NMR-Spektroskopie wurden bis zum Jahr 2006 etwa 35.000 Proteinstrukturen ermittelt, welche in der Protein Data Bank (www.rcsb.org) archiviert sind [8]. Interessanterweise kann diese große Zahl von Proteinen in Familien eingeteilt werden, innerhalb derer die Proteine nach ihrer Tertiärstruktur eng miteinander verwandt sind und auch häufig ähnliche Funktionen ausüben [9]. Die Zahl dieser Familien wird auf nur etwa 1.000 geschätzt und es wird vermutet, dass die Proteine innerhalb einer Familie auf einen gemeinsamen Ahnen zurückgeführt werden können [9]. Außerdem wurde bemerkt, dass die den Familien zugrunde liegenden fundamentalen Tertiärstrukturen aus den diversen Sekundärmotiven gemäß einer Reihe von "Bauvorschriften" zusammengesetzt sind und dass sie stabil gegen Mutationen der zugehörigen Aminosäuresequenz sowie gegen molekulare Turbulenz in der Zelle sind [10]. Diese Tatsachen haben Wissenschafter dazu bewogen, diese fundamentalen Proteinstrukturen als primäre natürliche Formen, welche durch unabänderliche Gesetze regiert werden, zu beschreiben [10]. In diesem Sinne wurde argumentiert, dass unbeschadet Darwins Evolutionslehre gewisse Züge der Proteinfaltung im Rahmen eines platonischen Modelles verstanden werden können, welches unabänderliche Formen und ebensolche Gesetze, nach denen diese Formen zusammengefügt werden, involviert [10].

Diese Idee gewisser stabiler "platonischer" Proteinstrukturen diente Banavar und Maritan als Motivation für die Formulierung eines vereinfachten Modells der Proteinfaltung [11, 12]. Sie stellen die Polypeptidkette durch einen biegsamen undurchdringlichen Schlauch mit vorgegebenem endlichen Radius dar, was in einem einfachen Bild durch einen Gartenschlauch veranschaulicht werden kann. Diese Schlauchdarstellung des Proteins stellt einerseits sicher, dass die chemischen Bestandteile der verschiedenen Aminosäuren genügend Raum haben, während andererseits lokal die Richtung der Polypeptidkette durch die Schlauchachse vorgegeben wird, was in anderen Modellierungen, wie der anhand verbundener Kugeln, so nicht gegeben ist. Die Eigenschaft eines Proteins unter physiologischen Bedingungen eine kompakte Tertiärstruktur anzunehmen, die hauptsächlich dadurch zu Stande kommt, dass in einer kompakten Konfiguration hydrophobe Aminosäuren bevorzugt im Innern des Proteins vom Lösungsmittel abgeschirmt werden [13], wird bei Banavar und Maritan dadurch abgebildet, dass sie eine effektive attraktive Wechselwirkung zwischen den verschiedenen Segmenten des Schlauches einführen. Indem man den Schlauchradius und die Reichweite des attraktiven Potentials aufeinander abstimmt, kann das Modellprotein in die so genannte marginal kompakte Phase gebracht werden, wo der Proteinschlauch verschiedene Sekundärmotive annimmt, wie zum Beispiel die

α-Helix, das β-Faltblatt und β-Schleifen [11, 12]. Bedenkt man, dass das Banavar-Maritan-Modell keinerlei Informationen über chemische Details *bestimmter* Proteine beinhaltet, so zeigt sich, dass die erhaltenen Motive einen universellen Charakter besitzen und daher in der Tat in dem Sinne gewisser primärer mutationsstabiler Formen, welche als Bausteine für die Tertiärstruktur dienen, verstanden werden können.

Ein Nachteil des Ansatzes von Banavar und Maritan besteht darin, dass die Wirkung des Lösungsmittels (in erster Linie Wasser), das durch den hydrophoben Effekt Proteine zur Bildung kompakter Strukturen veranlasst, nur *indirekt* anhand der effektiven attraktiven Wechselwirkung zwischen verschiedenen Teilen des Proteinschlauches erfasst wird. In der vorliegenden Arbeit wird hingegen die Wirkung des Lösungsmittels auf Proteine im Schlauchmodell *unmittelbar* berechnet, wodurch es möglich wird, das Auftreten gewisser Sekundärmotive mit konkreten Lösungsmitteleigenschaften in Verbindung zu bringen. Insbesondere wird dabei die Entropie des Lösungsmittels behandelt, deren Zunahme durch die Bildung eines kompakten physiologischen Zustandes von Bedeutung für die Proteinfaltung ist [24]. Zu dem Zeitpunkt, da diese Untersuchung begonnen wurde, war bereits ein erster Schritt in diese Richtung im Schlauchmodell unternommen worden. Snir und Kamien haben 2005 durch das Lösungsmittel hervorgerufene entropische Effekte auf kettenartige Moleküle untersucht, welche sie im Schlauchmodell darstellen und als Lösungmittel eine verdünnte Harte-Kugel-Flüssigkeit annehmen [14, 15]. Im Limes niedriger Dichte ist es möglich, die Entropie des Lösungsmittels (welche für harte Kugeln der einzig relevante Beitrag zur freien Energie ist) im so genannten Asakura-Oosawa-Modell [16] zu erhalten, das ursprünglich zur Berechnung von entropischen Kräften zwischen parallelen Platten entwickelt wurde. Snirs und Kamiens Ergebnisse führen die Autoren zu dem Schluss, dass große Lösungsmittelteilchen β-Faltblatt-artige Proteinkonfigurationen begünstigen während für kleine Lösungsmittelteilchen Helix-Strukturen bevorzugt sind. Da jedoch ihre Ergebnisse erst im Limes verschwindender Dichte exakt werden, erschien es sinnvoll, die Untersuchungen in den Bereich realistischer Lösungsmitteldichten auszuweiten.

In der vorliegenden Arbeit werden zu diesem Zweck Methoden der Dichtefunktionaltheorie (DFT) für klassische Flüssigkeiten [17–19] verwendet, welche in den Rahmen der so genannten morphologischen Thermodynamik eingebettet werden. Das Konzept der morphologischen Thermodynamik baut auf dem Satz von Hadwiger aus der Integralgeometrie [23] auf, der seit Mitte der 1990er Jahre Anwendung in der Statistischen Physik gefunden hat [20]. Vor wenigen Jahren wurden erstmals auch Harte-Kugel-Flüssigkeiten im Rahmen der morphologischen Thermodynamik untersucht [93]. Die wichtigste Gleichung der Theorie, die in dieser Arbeit zur Anwendung

kommt, ist der so genannte morphometrische Ansatz für die Lösungsenergie F_{sol} eines Proteins. Diese liest sich

$$F_{\text{sol}} = pV + \sigma A + \kappa C + \bar{\kappa} X \,, \tag{1}$$

wobei p, σ, κ und $\bar{\kappa}$ Eigenschaften des Lösungsmittels sind, während V, A, C und X als geometrische Maße für eine bestimmte Proteinkonfiguration charakteristisch sind. Die so genannten thermodynamischen Koeffizienten p, σ, κ und $\bar{\kappa}$ hängen nur von der Temperatur und dem chemischen Potential des Lösungsmittels sowie der Protein-Lösungsmittel-Wechselwirkung ab. Es können p als Druck, σ als Oberflächenspannung an einer planaren Wand sowie κ und $\bar{\kappa}$ als Biegesteifigkeiten identifiziert werden. Die geometrischen Maße V, A, C und X erhält man als Integrale über das Volumen beziehungsweise die Oberfläche des Proteins in einer gegebenen Konfiguration. Es sind V das Volumen des Proteins, A der Flächeninhalt der Oberfläche, C das Oberflächenintegral der mittleren Krümmung und X das Oberflächenintegral der Gaußschen Krümmung. Entscheidend für die Bedeutung von Gl. (1) ist die Tatsache, dass die thermodynamischen Koeffizienten *nicht* von der gegeben Proteinkonfiguration abhängen.

Offensichtlich bietet Gl. (1) für die Berechnung von F_{sol} einen entscheidenen Vorteil gegenüber einer numerischen DFT Rechnung, welche das Lösungsmittel in dem in der Regel komplizierten externen Potential, das durch das Protein induziert wird, zu bewältigen hat. Während eine solche DFT-Rechnung bereits für einfache Lösungsmittel zeitaufwendig sein kann, besonders wenn eine hohe numerische Genauigkeit verlangt ist, erlaubt Gl. (1), die thermodynamischen Koeffizienten zunächst in einer einfachen Testgeometrie (zum Beispiel anhand sphärischer gelöster Teilchen) zu berechnen. Anschließend können in einer relativ einfachen numerischen Rechnung die geometrischen Maße für verschiedene Proteinkonfigurationen erhalten werden, welche dann letztendlich mit den thermodynamischen Koeffizienten gemäß Gl. (1) linear kombiniert werden, woraus sich F_{sol} ergibt. Diese alternative Rechnung benötigt keine Behandlung des Lösungsmittels in komplizierten Geometrien und ist deshalb wesentlich schneller als die volle DFT Rechnung. Es sollte jedoch angemerkt werden, dass Gl. (1) lediglich eine Näherung für F_{sol} darstellt von der allerdings gezeigt worden ist, dass sie im Fall einfacher konvexer gelöster Teilchen extrem genau ist [93]. Es ist aber zu beachten, dass es im Falle von konkaven gelösten Teilchen, bei denen Teile des Lösungsmittels durch das Protein eingeschränkt werden, zu merklichen Abweichungen der morphometrischen Form für F_{sol} von Ergebnissen der vollen DFT-Rechnungen kommt. Im Abschnitt 5.1, der sich im letzten Kapitel dieser Arbeit vor Zusammenfassung und Ausblick (Kapitel 6) befindet, geben wir eine Einführung in das Konzept der morphologischen Thermodynamik in deren Rahmen wir auch die Stärken und

Schwächen dieses approximativen Ansatzes diskutieren. Die voranstehenden Kapitel 2 bis 4 stellen zu großen Teilen eine Vorbereitung des morphometrischen Ansatzes für F_{sol} dar; sie enthalten jedoch auch wichtige Resultate, die unabhängig von der biologisch inspirierten Anwendung in Kapitel 5 von Bedeutung sind. Die Arbeit beginnt mit Kapitel 1, in dem eine kurze Einführung in das Thema gegeben und der Aufbau der Arbeit erläutert wird.

Im Kapitel 2 stellen wir eine exakte Berechnung von Eigenschaften eindimensionaler (1D) Systeme vor, die sich den Methoden der Statistischen Mechanik bedient. Es wird dabei eine Wechselwirkung zwischen den Teilchen des Systems durch ein beliebiges Potential, welches zwischen nächsten Nachbarn wirkt, angenommen. Die formale Lösung dieses Problems ist seit den 1950er Jahren bekannt [42, 43] sie wurde aber unseres Wissens bisher noch nicht mit experimentellen Ergebnissen in Verbindung gebracht. Wir verwenden einen erstaunlich einfachen Zusammenhang, der aus der exakten Lösung folgt und mit Hilfe dessen wir eine eindeutige Lösung für das inverse Problem, welches darin besteht, das Paar-Wechselwirkungspotential aus gemessenen Paar-Verteilungsfunktionen zu bestimmen, angeben können. Die Methode wird auf Messdaten von kolloidalen Suspensionen, deren Teilchen mit Hilfe optischer Fallen auf 1D eingeschränkt sind, angewendet. Da die zugrunde liegende Theorie exakt ist, findet man, wie erwartet, eine sehr gute Übereinstimmung zwischen Theorie und Experiment. Damit stellen die 1D Systeme den seltenen Fall dar, dass experimentelle Ergebnisse eins-zu-eins durch eine exakte Theorie nachvollzogen werden können, welche insbesondere die Probleme bei der Lösung des inversen Problems, die in höheren Dimensionen auftreten, zu vermeiden erlaubt.

Die Lösbarkeit des 1D Systems erlaubt uns auch, unsere Einführung in die DFT, welche wir im Abschnitt 2.3 geben, mit Hilfe des exakten Ergebnisses für das Überschuss (das heißt über das ideale Gas hinausgehende) Freie-Energie-Funktional $\mathcal{F}_{\mathrm{ex}}^{\mathrm{1D}}$ für die 1D Harte-Kugel-Mischung zu illustrieren. Aus zwei Gründen ist der Ausdruck für $\mathcal{F}_{\mathrm{ex}}^{\mathrm{1D}}$ für uns wertvoll. Erstens lässt sich damit zeigen, dass DFT ein geeignetes Mittel ist, um die exakten Eigenschaften des 1D Harte-Kugel-Systems mit beliebigen externen Potentialen zu erhalten. Für beliebige externe Potentiale ist die herkömmliche Rechnung, die eine Auswertung der Zustandssumme vornimmt, nicht praktikabel. Diese Beobachtung liefert uns eine Motivation dafür, DFT auch für 3D Systeme zu verwenden, wo wir im Rahmen der biologischen Fragestellung freie Energien für diverse externe Potentiale, die aus der Gegenwart des gelösten Proteins (oder eines einfacheren Teilchens in einer Testgeometrie) resultieren, berechnen müssen. Zweitens analysieren wir die Struktur von $\mathcal{F}_{\mathrm{ex}}^{\mathrm{1D}}$ im Detail, was uns mit den Werkzeugen ausstattet, die für die Konstruktion von Näherungen für das Überschuss-Freie-

Energie-Funktional $\mathcal{F}_{\rm ex}^{\rm 3D}$ für die Harte-Kugel-Flüssigkeit in 3D äußerst hilfreich sind. Da das Funktional in 1D relativ einfach ist, erlaubt uns diese Vorgehensweise, dem Leser einige verwandte länglichere Rechnungen für die 3D Funktionale zu ersparen.

Die Konstruktion von $\mathcal{F}_{\rm ex}^{\rm 3D}$ wird in Kapitel 3 gemäß Rosenfelds bahnbrechender Arbeit aus dem Jahr 1989 [22] vorgenommen. Anhand einer genauen Betrachtung des exakt bekannten Limes von $\mathcal{F}_{\rm ex}^{\rm 3D}$ im Fall niedriger Dichte lassen sich sechs gewichtete Dichten identifizieren. Dies sind die vier skalaren Funktionen $n_0(\mathbf{r}), \ldots, n_3(\mathbf{r})$ und die zwei vektoriellen Funktionen $\overrightarrow{n}_1(\mathbf{r})$ und $\overrightarrow{n}_2(\mathbf{r})$, die alle von den räumlichen Koordinaten $\mathbf{r}$ abhängen und die durch ein Ausschmieren der Dichteprofile der gegebenen mehrkomponentigen Harte-Kugel-Mischung über einen Bereich, der der Kugelgröße entspricht, erhalten werden. Unter Verwendung einer exakten Relation aus der Scaled-Particle-Theorie [27, 28] kann eine approximative Überschuss-Freie-Energie-Dichte $\Phi_{\rm RF}$ [Gl. (3.16)] als Funktion der gewichteten Dichten konstruiert werden. Dies definiert Rosenfelds Fundamentalmaßtheorie (FMT) für die Harte-Kugel-Mischung. Bemerkenswerterweise liefert FMT den gleichen Druck und die gleiche direkte Paar-Korrelationsfunktion, wie man sie aus der Lösung der Ornstein-Zerneke-Integralgleichung unter Verwendung der Percus-Yevick (PY) Näherung erhält, obwohl FMT auf gänzlichen anderen Voraussetzungen aufgebaut ist. Insbesondere folgt für den Druck das PY-Kompressibilitäts-Ergebnis

$$\frac{p_{\rm PY}}{k_{\rm B}T} = \frac{n_0}{1-n_3} + \frac{n_1 n_2}{(1-n_3)^2} + \frac{n_2^3}{12\pi(1-n_3)^3} \tag{2}$$

aus $\Phi_{\rm RF}$. Der Druck $p_{\rm PY}$ ist eine Funktion der Bulk-Werte der gewichteten Dichten, die durch

$$n_0 = \sum_{i=1}^{\nu} \rho_i\,, \quad n_1 = \sum_{i=1}^{\nu} R_i\rho_i\,, \quad n_2 = \sum_{i=1}^{\nu} 4\pi R_i^2\rho_i\,, \quad n_3 = \sum_{i=1}^{\nu} \frac{4\pi}{3} R_i^3\rho_i \tag{3}$$

gegeben sind, wobei der Index i die unterschiedlichen Komponenten einer ν-komponentigen Flüssigkeit bezeichnet, welche durch die Teilchenzahldichten ρ_i und die Kugelradien R_i charakterisiert sind. Insbesondere ist n_0 die gesamte Teilchenzahldichte und n_3 ist die gesamte Packungsdichte der Harte-Kugel-Mischung. Die vektoriellen gewichteten Dichten verschwinden in der homogenen Bulk-Flüssigkeit.

Während der Druck $p_{\rm PY}$ in guter Übereinstimmung mit Simulationsergebnissen für einkomponentige Harte-Kugel-Flüssigkeiten bei nicht zu hohen Dichten ist, so überschätzt $p_{\rm PY}$ den tatsächlichen Druck in der Nähe des flüssig-fest-Übergangs um circa 7%. Diese Ungenauigkeit wurde im Fall der einkomponentigen Flüssigkeit durch eine empirische Modifikation der Zustandsgleichung korrigiert, welche auf den Carnahan-Starling (CS) Druck $p_{\rm CS}$ führte [79]. Um $p_{\rm CS}$ auch im Rahmen der FMT

nutzbar zu machen, ist es nötig, die CS Zustandsgleichung als Funktion der gewichteten Dichten $n_0, \ldots, n_3$ auszudrücken, was gleichbedeutend mit einer Verallgemeinerung von p_{CS} für Harte-Kugel-*Mischungen* ist. Dies geschieht im Abschnitt 3.2 dieser Arbeit mit Hilfe einer systematischen Entwicklung des Druckes nach Potenzen von n_3. Indem wir die Konsistenz mit einer bereits oben erwähnten exakten Relation aus der Scaled-Particle-Theorie maximieren, erhalten wir ohne empirische Anpassung von Parametern den Boublík-Mansoori-Carnahan-Starling-Leland (BMCSL) Druck p_{BMCSL} [80, 81], wenn wir die Entwicklung in erster Ordnung durchführen. Eine Hinzunahme der nächst höheren Ordnung führt in eindeutiger Weise auf den vor einiger Zeit vorgeschlagenen erweiterten CS (eCS) Druck p_{eCS} [82]. Indem wir die Entwicklung in dritter Ordnung betrachten, können wir die neue Zustandsgleichung

$$\frac{p^{(3)}}{k_{\mathrm{B}}T} = \frac{n_0}{1-n_3} + \frac{n_1 n_2 \left(1 + \frac{1}{3}n_3^2\right)}{(1-n_3)^2} + \frac{n_2^3 \left(1 - \frac{2}{3}n_3 + \frac{1}{3}n_3^2\right)}{12\pi(1-n_3)^3} \tag{4}$$

herleiten, die im Gegensatz zu p_{BMCSL} und p_{eCS} im Falle der einkomponentigen Harte-Kugel-Flüssigkeit vollständig konsistent mit der Scaled-Particle-Theorie ist. Neben dieser wichtigen Eigenschaft zeigt sich, dass $p^{(3)}$ eine deutlich bessere Übereinstimmung mit Simulationsergebnissen für den Druck und das chemische Potential verschiedener Harte-Kugel-Mischungen sowie für die Oberfächenspannung und die Adsoption liefert als p_{BMCSL} und p_{eCS}. Im Abschnitt 3.3 beschreiben wir, wie die neue Zustandsgleichung $p^{(3)}$ in den Rahmen der FMT eingearbeitet werden kann, wodurch ihre Stärken auch für inhomogene Flüssigkeiten mittels DFT nutzbar werden. Die resultierende Überschuss-Freie-Energie-Dichte wird mit Φ_{WBII} [Gl. (3.43)] bezeichnet und die dadurch definierte Theorie wird die White-Bear-Version der FMT Mark II (WBII) genannt.

Es wurde bereits früher gezeigt, dass die morphometrische Form für F_{sol} [Gl. (1)] uneingeschränkt kompatibel mit der Struktur der FMT ist [88], vorausgesetzt, dass eine Verallgemeinerung der FMT für Flüssigkeiten aus beliebig geformten harten Teilchen verwendet wird. Eine solche FMT wurde durch Rosenfeld im Jahr 1994 vorgeschlagen [29, 30]. Diese originale nicht-sphärische FMT (onFMT) wird im Kapitel 4 vorgestellt. Während onFMT Eigenschaften isotroper Flüssigkeiten recht gut reproduziert (beispielsweise liefert die Theorie den exakten zweiten Virialkoeffizient), so versagt sie bei der Beschreibung der nematischen Phase, die gemäß onFMT immer eine höhere freie Energie als die isotrope Phase hat. Um diesen gravierenden Mangel zu beheben, bedienen wir uns des Gauß-Bonnet-Theorems [31] mit Hilfe dessen wir einen exakten Ausdruck für $\mathcal{F}_{\mathrm{ex}}$ im Limes niedriger Dichten herleiten, der sich in Form von Integralen über die Oberfläche des Schnittes von Paaren harter Körper schreibt. Näherungen an dieses exakte Ergebnis können als Summe

von Faltungen so genannter Gewichtsfunktionen geschrieben werden, was für die einfachste Näherung zu den gewichteten Dichten $n_0(\mathbf{r}), \ldots, n_3(\mathbf{r})$ sowie $\overrightarrow{n}_1(\mathbf{r})$ und $\overrightarrow{n}_2(\mathbf{r})$ führt, die sich durch einfache Anpassungen der entsprechenden gewichteten Dichten für die harten Kugeln an die beliebig geformten Teilchen ergeben. Verbessert man die Näherung an das exakte Ergebnis, indem man den aufgrund von Krümmungsasymetrie auftretenden Beitrag in niedrigster Ordnung berücksichtigt, so erhält man zwei zusätzliche *tensorielle* gewichtete Dichten $\overleftrightarrow{n}_1(\mathbf{r})$ und $\overleftrightarrow{n}_2(\mathbf{r})$, die als 3×3-Matrizen dargestellt werden können. Die Überschuss-Freie-Energie-Dichte Φ_{ed}, die sich mit dem erweiterten Satz von gewichteten Dichten ergibt, kann leicht konstruiert werden und die entsprechende Theorie wird Extended-Deconvolution-FMT (edFMT) genannt. Wir zeigen im Abschnitt 4.2, dass edFMT in mehrfacher Hinsicht eine Verbesserung bezüglich onFMT bringt. Erstens ist edFMT in der Lage, den Isotrop-Nematisch-Übergang vorherzusagen, wie wir anhand eines Vergleiches mit Daten aus Computersimulationen von Harte-Sphärozylinder-Flüssigkeiten [128] zeigen. Die Theorie erzielt gute Übereinstimmung mit den Simulationen für nicht zu lange Sphärozylinder. Zweitens liefert edFMT eine bessere Beschreibung der *inhomogenen* isotropen Harte-Sphärozylinder-Flüssigkeit als dies durch onFMT erzielt wird. Um dies zu zeigen, führen wir Monte-Carlo-Simulationen von verschiedenen Harte-Sphärozylinder-Flüssigkeiten mit Länge-zu-Durchmesser-Verhältnissen bis zu 10.0 durch, die in Kontakt mit einer planaren harten Wand sind, welche die Inhomogenität der Flüssigkeit hervorruft. Außerdem stellt edFMT eine Motivation dar, die tensorielle gewichtete Dichte $\overleftrightarrow{n}_2(\mathbf{r})$, die anders als $\overleftrightarrow{n}_1(\mathbf{r})$ im Spezialfall von harten Kugeln nicht verschwindet, auch für die Konstruktion einer FMT für Harte-Kugel-Systeme zu verwenden. Dadurch kann ein neuer Zusammenhang zwischen Rosenfelds FMT, die auf der Untersuchung des Grenzfalls niedriger Dichte fußt, und den Arbeiten Tarazonas [77], der bereits früher auf ganz anderem Wege $\overleftrightarrow{n}_2(\mathbf{r})$ einführte, um eine reguläre FMT für den Harte-Kugel-Kristall zu erhalten, hergestellt werden.

Mit Hilfe der verbesserten FMT-Version WBII und der Verallgemeinerung der FMT für Flüssigkeiten aus nicht-sphärischen Teilchen lässt sich die hohe Effizienz, die aus der Verwendung der morphometrischen Form für F_{sol} [Gl. (1)] folgt, noch weiter steigern. Vergleicht man F_{sol}, wie es aus der Überschuss-Freien-Energiedichte Φ_{WBII} (oder, genauer, aus der entsprechenden FMT für nicht-sphärische Teilchen) folgt, mit Gl. (1), so erhält man geschlossene Ausdrücke für die thermodynamischen Koeffizienten p, σ, κ und $\bar{\kappa}$ als Funktionen der Packungsdichte η und des Radius R der harten Kugeln [Gl. (5.6)]. Ein Vergleich dieser Ausdrücke mit den Ergebnissen für die thermodynamischen Koeffizienten, wie sie aus der vollen DFT-Rechnung in einer einfachen Testgeometrie (spärische gelöste Teilchen) folgen, zeigt die ho-

he Genauigkeit und Konsistenz der analytischen Ausdrücke, die früheren Resultaten überlegen sind (siehe Abschnitt 5.1). Für die Berechnung von F_{sol} im Rahmen der biologisch inspirierten Fragestellung bedeutet das, dass ein großer Bereich von Lösungsmittelkonfigurationen (η, R) mit hoher Effizienz und Genauigkeit abgedeckt werden kann.

Wie eingangs bemerkt erlaubt uns der morphometrische Ansatz für F_{sol} die Untersuchung von Snir und Kamien [14, 15] für ein Protein, das im Schlauch-Modell dargestellt wird und in einer stark verdünnten Harte-Kugel-Flüssigkeit gelöst ist, auf den relevanten Bereich beliebiger höherer Dichten des flüssigen Lösungsmittels auszuweiten. Im Gegensatz zu der Folgerung von Snir und Kamien, die die Bildung von β-Faltblättern mit großen Lösungsmittelteilchen und die von Helices dagegen mit kleinen Lösungsmittelteilchen assoziieren, finden wir, dass die einzigen Lösungsmittelkonfigurationen für die das β-Faltblatt stabil ist, in dem Bereich *kleiner* Lösungsmittelteilchen bei gleichzeitig *hoher* Lösungsmitteldichte lokalisiert sind. Wir können allerdings Snirs und Kamiens Ergebnis, dass große Lösungsmittelteilchen zu einer Bevorzugung von Helices, die weniger dicht gepackt sind, führen, auch in dem Bereich hoher Lösungsmitteldichten bestätigen. Diese Beobachtung wurde durch Snir und Kamien in dem Sinne eines Unwinding-Übergangs, der die Helixstruktur in die Faltblattstruktur überführt, interpretiert. Unsere Ergebnisse zeigen jedoch, dass diese weniger dicht gepackten Helix-Konfigurationen von der Faltblatt-Konfiguration durch eine Energiebarriere getrennt sind, was die Unwinding-Hypothese selbst in dem Grenzfall sehr großer Lösungsmittelteilchen, in dem sowieso die Lösungsmittelentropie an Bedeutung verliert, widerlegt.

Um den Einfluss hydrophiler und hydrophober Aminosäuren auf die Proteinfaltung zu untersuchen, ist es nützlich, ein Lösungsmittel mit attraktiver Wechselwirkung zwischen den Teilchen zu betrachten, da diese ein entscheidener Faktor des wichtigsten Lösungsmittels in der Natur, nämlich Wasser, ist. Wir zeigen, dass auch ein solches Lösungsmittel im Rahmen der morphologischen Thermodynamik behandelt werden kann (siehe Abschnitt 5.2.3). Exemplarisch verwenden wir als Modell-Lösungsmittel eine einfache Square-Well-Flüssigkeit, die man erhält, indem man ein kurzreichweitiges attraktives Wechselwirkungspotential konstanter Stärke zu dem repulsiven Harte-Kugel-Wechselwirkungspotential hinzufügt. Diese attraktive Wechselwirkung kann mittels Störungstheorie behandelt werden, was zu einem einfachen Zusatzterm in dem Dichtefunktional der zugehörigen DFT führt. Allerdings können anhand dieses Dichtefunktionals keine analytischen Ausdrücke für die thermodynamischen Koeffizienten, die in Gl. (1) auftreten, berechnet werden, was eine Konsequenz der Ermangelung einer guten DFT für Square-Well-Mischungen ist. Glei-

chung (1) kann dennoch für die Berechnung von F_{sol} verwendet werden, indem man die thermodynamischen Koeffizienten anhand von numerischen DFT-Rechnungen in einer einfachen Testgeometrie (sphärische gelöste Teilchen) bestimmt. Zusätzlich zu der attraktiven Wechelwirkung zwischen den Lösungsmittelteilchen erweitern wir das Modell um charakteristische Wechselwirkungen zwischen dem gelösten Molekül und den Lösungsmittelteilchen. Auf diesem Wege können thermodynamische Koeffizienten ermittelt werden, die entweder hydrophilen Aminosäuren (attraktive Wechselwirkung zwischen dem gelösten Molekül und dem Lösungsmittel) oder hydrophoben Aminosäuren (repulsive Wechselwirkung zwischen dem gelösten Molekül und dem Lösungsmittel) entsprechen. Unsere Ergebnisse für F_{sol} von Proteinen im Schlauchmodell bestätigen die Rolle von hydrophoben Aminosäuren als eine treibende Kraft für die Proteinfaltung während wir in dem Fall hydrophiler Aminosäuren keine Tendenz der Proteine zur Herausbildung von kompakten Tertiärstrukturen beobachten.

Das abschließende Kapitel 6 der Arbeit enthält eine Zusammenfassung der Ergebnisse und einen Ausblick auf mögliche zukünftige Untersuchungen, die im Zusammenhang mit den Themen dieser Arbeit stehen. Wir gehen hier nur auf den Teil des Ausblicks ein, der die biologisch inspirierte Fragestellung der Arbeit betrifft. Erweiterungen der vorliegenden Untersuchung können danach unterschieden werden, ob sie die Modellierung des Proteins oder die des Lösungsmittels betreffen. Die Beschreibung des Proteins lässt sich verfeinern, indem konkrete gegebene Aminosäuresequenzen durch eine Partitionierung des Proteinschlauches in hydrophile und hydrophobe Bereiche abgebildet werden. Die Lösungsenergie F_{sol} kann in diesem Fall noch immer durch die morphometrische Form Gl. (1) berechnet werden, wobei allerdings unter Umständen zusätzliche Linienbeiträge zu den geometrischen Maßen, welche von den Grenzlinien zwischen den unterschiedlichen Bereichen herrühren, berücksichtigt werden müssen. Ein solches Vorgehen kann helfen, die Tertiärstruktur gegebener Proteine zu verstehen, während die Ergebnisse jedoch ihren allgemeinen Charakter, den sie in der Untersuchung entropischer Lösungsmitteleffekte in Kapitel 5 haben, verlieren würden. Weitere Verfeinerungen des Proteinmodells könnten die Hinzunahme innerer energetischer Beiträge durch Wasserstoffbrückenbindungen zwischen verschiedenen Bereichen des Proteins oder, allgemeiner, die Einführung einer Biegesteifigkeit der Polypeptidkette im Stil von Ref. [14] umfassen. Eine offensichtliche Verbesserungmöglichkeit der Beschreibung des Lösungsmittels stellt die Verwendung von Modellen für Wasser da, die realistischer als die einfache Square-Well-Flüssigkeit sind. Es soll betont werden, dass Gl. (1) auch für solche komplexeren Lösungsmittel verwendbar ist, wobei jedoch voraussichtich eine Berechnung der thermodynamischen Koeffizienten durch DFT unzureichend ist. Dies ergibt sich aus der bereits erwähnten

Ermangelung guter Störungstheorien für attraktive Wechselwirkungen, wodurch es schwierig ist, Dichtefunktionale für komplexere Wassermodelle zu erhalten. Es erscheint jedoch machbar, F_{sol} anhand von numerischen Simulationen für einfach geformte gelöste Moleküle in kompexen Lösungsmitteln zu bestimmen und mit Hilfe dieser Daten die thermodynamischen Koeffizienten zu berechnen. Eine andere Erweiterung der Untersuchung, welche die Beschreibung des Lösungsmittels in dem allgemeineren Sinne der Beschreibung des umgebenden Mediums betrifft, könnte sich mit der Proteinfaltung in Gegenwart von äußeren räumlichen Einschränkungen befassen. Tatsächlich findet die Faltung von Proteinen in der gedrängten Zellumgebung statt, so dass die Annahme räumlicher Einschränkung realistisch sein kann. Frühere Arbeiten haben gezeigt, dass räumliche Einschränkung in gewissen Situationen eine entscheidende Auswirkung auf die Proteinfaltung hat [151, 152] und es wäre von großem Interesse, diesen Aspekt im Rahmen der morphologischen Thermodynamik zu untersuchen. Die Anwendung von Gl. (1) auf Teile des Lösungmittels, die zwischen dem Protein und einem äußeren Behälter eingeschränkt sind, würde einen weiteren anspruchsvollen Test der Leistungsfähigkeit des morphometrischen Ansatzes für F_{sol} bedeuten.

Bibliography

[1] W.T. Astbury and A. Street, Phil. Trans. Roy. Soc. A **230**, 75 (1931).

[2] L. Pauling, R.B. Corey, and H.R. Branson, Proc. Natl. Acad. Sci. USA **37**, 205 (1951).

[3] L. Pauling and R.B. Corey, Proc. Natl. Acad. Sci. USA **37**, 729 (1951).

[4] C. Park, L.W. Schultz, and R.T. Raines, Biochemistry **40**, 4949 (2001).

[5] R.A. Sayle, E.J. Milner-White, Trends Biochem. Sci. **20**, 374 (1995).

[6] G.A. Petsko and D. Ringe, *Protein Structure and Function* (New Science Press, London, 2004).

[7] O. Schueler-Furman, C. Wang, P. Bradley, K. Misura, and D. Baker, Science **310**, 638 (2005).

[8] G.D. Rose, P.J. Fleming, J.R. Banavar, and A. Maritan, Proc. Natl. Acad. Sci. USA **103**, 16623 (2006).

[9] C. Chothia, Nature **357**, 543 (1992).

[10] M. Denton and C. Marshall, Nature **410**, 417 (2001).

[11] J.R. Banavar and A. Maritan, Rev. Mod. Phys. **75**, 23 (2003).

[12] J.R. Banavar, T.X. Hoang, A. Maritan, F. Seno, and A. Trovato, Phys. Rev. E **70**, 041905 (2004).

[13] G.D. Rose and S. Roy, Proc. Natl. Acad. Sci. USA **77**, 4643 (1980).

[14] Y. Snir and R.D. Kamien, Science **307**, 1067 (2005).

[15] Y. Snir and R.D. Kamien, Phys. Rev. E **75**, 051114 (2007).

[16] S. Asakura and F. Oosawa, J. Chem. Phys. **22**, 1255 (1954).

[17] C. Ebner, W.F. Saam, and D. Stroud, Phys. Rev. A **14**, 2264 (1976).

[18] A.J.M. Yang, P.D. Fleming III, and J.H. Gibbs, J. Chem. Phys. **64**, 3732 (1976).

[19] R. Evans, Adv. Phys. **28**, 143 (1979).

[20] C.N. Likos, K.R. Mecke, and H. Wagner, J. Chem. Phys. **102**, 9350 (1995).

[21] J. Wu, AIChE J. **52**, 1169 (2006).

[22] Y. Rosenfeld, Phys. Rev. Lett. **63**, 980 (1989).

[23] H. Hadwiger, *Vorlesungen über Inhalt, Oberfläche und Isoperimetrie* (Springer, Berlin, 1957).

[24] Y. Harano, R. Roth, and M. Kinoshita, Chem. Phys. Lett. **432**, 275 (2006).

[25] R. Roth, R. Evans, A. Lang, and G. Kahl, J. Phys.: Condens. Matter **14**, 12063 (2002).

[26] Y.-X. Yu and J. Wu, J. Chem. Phys. **117**, 10156 (2002).

[27] H. Reiss, H.L. Frisch, E. Helfand, and J.L. Lebowitz, J. Chem. Phys. **32**, 119 (1960).

[28] H. Reiss, in *Statistical Mechanics and Statistical Methods in Theory and Application*, edited by U. Landman (Plenum Press, New York, 1977).

[29] Y. Rosenfeld, Phys. Rev. E **50**, R3318 (1994).

[30] Y. Rosenfeld, Mol. Phys. **86**, 637 (1995).

[31] I. Chavel, *Riemannian geometry – A modern introduction* (Cambridge Univeristy Press, Cambridge, 2006).

[32] E.H. Lieb and D.C. Mattis, eds., *Mathematical Physics in One Dimension. Exactly Solvable Models of Interacting Particles* (Academic Press, New York, 1966).

[33] V. Privman, *Nonequilibrium Statistical Mechanics in One Dimension* (Cambridge University Press, Cambridge, 1997).

[34] B. Schmittmann and R.K.P. Zia, in *Phase Transitions and Critical Phenomena*, edited by C. Domb and J. Lebowitz (Academic, London, 1995).

[35] J. Krug, Phys. Rev. Lett. **67**, 1882 (1991).

[36] B. Derrida, M.R. Evans, V. Hakim, and P. Pasquier, J. Phys. A: Math. Gen **26**, 1493 (1993).

[37] J.K. Holt, H.G. Park, Y. Wang, M. Stadermann, A.B. Artyukhin, C.P. Grigoropoulos, A. Noy, and O. Bakajin, Science **312**, 1034 (2006).

[38] M. Whitby and N. Quirke, Nat. Nanotechnol. **2**, 87 (2007).

[39] K. Hahn, J. Kärger, and V. Kukla, Phys. Rev. Lett. **76**, 2762 (1996).

[40] C. Lutz, M. Kollmann, P. Leiderer, and C. Bechinger, J. Phys.: Condens. Matter **16**, S4075 (2004).

[41] C. Lutz, M. Kollman and C. Bechinger, Phys. Rev. Lett **93**, 026001 (2004).

[42] F. Gürsey, Proc. Cambridge Phil. Soc. **46**, 182 (1950).

[43] Z.W. Salsburg, R.W. Zwanzig, and J.G. Kirkwood, J. Chem. Phys. **21**, 1098 (1953).

[44] G.P. Brenan and R. Evans, Mol. Phys. **73**, 789 (1991).

[45] J.-P. Hansen and I.R. McDonald, *Theory of simple liquids*, (Academic, London, 1986).

[46] A.P. Lyubartsev and A. Laaksonen, Phys. Rev. E **52**, 3730 (1995).

[47] V. Lobaskin, M. Brunner, C. Bechinger, and H.H. von Grünberg, J. Phys.: Condens. Matter **15**, 6693 (2003).

[48] M. Brunner, J. Dobnikar, H.H. von Grünberg, and C. Bechinger, Phys. Rev. Lett. **92**, 078301 (2004).

[49] C. Russ, M. Brunner, C. Bechinger, and H.H. von Grünberg, Europhys. Lett. **69**, 468 (2005).

[50] T.T.M. Võ, L.-J. Chen and M. Robert, J. Chem. Phys. **119**, 5607 (2003).

[51] J. Baumgartl and C. Bechinger, Europhys. Lett. **71**, 487 (2005).

[52] L.P. Faucheux, G. Stolovitzky, and A. Libchaber, Phys. Rev. E **51**, 5239 (1995).

[53] L. Belloni, J. Phys.: Condens. Matter **12**, R549 (2000).

[54] B. Derjaguin, Kolloid-Z. **69**, 155 (1934); Acta Physicochim. **10**, 333 (1939).

[55] E.J.W. Verwey and J.Th.G. Overbeek, *Theory of the Stability of Lyophobic Colloids* (Elsevier, Amsterdam, 1948).

[56] G.M. Bell, S. Levine, and L.N. McCartney, J. Colloid Interface Sci. **33**, 335 (1970).

[57] L. Belloni, Colloids Surfaces A: Physicochem. Eng. Aspects **140**, 227 (1998).

[58] M. Brunner, C. Bechinger, W. Strepp, and H.H. von Grünberg, Europhys. Lett. **58**, 926 (2002).

[59] M. Brunner, C. Bechinger, U. Herz and H.H. von Grünberg, Europhys. Lett. **63**, 791 (2003).

[60] P. Hohenberg and W. Kohn, Phy. Rev. **136**, B864 (1964).

[61] N.D. Mermin, Phys. Rev. **137**, A1441 (1965).

[62] P. Tarazona, Mol. Phys. **52**, 81 (1984).

[63] Y. Singh, J.P. Stoessel, and P.G. Wolynes, Phys. Rev. Lett. **54**, 1059 (1985).

[64] T.K. Vanderlick, H.T. Davis, and J.K. Percus, J. Chem. Phys. **91**, 7136 (1989).

[65] R. Evans, in *Fundamentals of Inhomogeneous Fluids*, edited by D. Henderson (Marcel Dekker, New York, 1992).

[66] Y. Rosenfeld, Phys. Rev. A **42**, 5978 (1990).

[67] E. Kierlik and M.L. Rosinberg, Phys. Rev. A **42**, 3382 (1990).

[68] S. Phan, E. Kierlik, M.L. Rosinberg, B. Bildstein, and G. Kahl, Phys. Rev. E **48**, 618 (1993).

[69] R. Roth and S. Dietrich, Phys. Rev. E **62**, 6926 (2000).

[70] Y. Rosenfeld, J. Chem. Phys. **89**, 4272 (1988).

[71] M.S. Wertheim, Phys. Rev. Lett. **10**, 321 (1963).

[72] E. Thiele, J. Chem. Phys. **39**, 474 (1963).

[73] J.L. Lebowitz, Phys. Rev. **133**, A895 (1964).

[74] W.G. Hoover and F.H. Ree, J. Chem. Phys. **49**, 3609 (1968).

[75] Y. Rosenfeld, M. Schmidt, H. Löwen, and P. Tarazona, J. Phys.: Condens. Matter **8**, L577 (1996).

[76] Y. Rosenfeld, M. Schmidt, H. Löwen, and P. Tarazona, Phys. Rev. E **55** 4245 (1997).

[77] P. Tarazona, Phys. Rev. Lett. **84** 694 (2000).

[78] A. Malijevský and J. Veverka, Phys. Chem. Chem. Phys. **1**, 4267 (1999).

[79] N.F. Carnahan and K.E. Starling, J. Chem. Phys. **51**, 635 (1969).

[80] T. Boublík, J. Chem. Phys. **53**, 471 (1970).

[81] G.A. Mansoori, N.F. Carnahan, K.E. Starling, and T.W. Leland, J. Chem. Phys. **54**, 1523 (1971).

[82] A. Santos, S.B. Yuste, and M. López de Haro, Mol. Phys. **96**, 1 (1999).

[83] A. Bellemans, Physica **28**, 493 (1962).

[84] P. Tarazona and Y. Rosenfeld, Phys. Rev. E **55**, R4873 (1997).

[85] M. Barošová, M. Malijevský, S. Labík, and W.R. Smith, Mol. Phys. **87**, 423 (1996).

[86] C. Barrio and J.R. Solana, Physica A **351**, 387 (2005).

[87] A. Malijevský, S. Labík, and A. Malijevský, Phys. Chem. Chem. Phys. **6**, 1742 (2004).

[88] P. Bryk, R. Roth, K.R. Mecke, and S. Dietrich, Phys. Rev. E **68**, 031602 (2003).

[89] D. Henderson and M. Plischke, Proc. R. Soc. Lond. A **400**, 163 (1985).

[90] J.R. Henderson and F. van Swol, Mol. Phys. **51**, 991 (1984).

[91] M. Heni and H. Löwen, Phys. Rev. E **60**, 7057 (1999).

[92] J.A. Barker and D. Henderson, Rev. Mod. Phys. **48**, 587 (1976).

[93] P.-M. König, R. Roth, and K.R. Mecke, Phys. Rev. Lett. **93**, 160601 (2004).

[94] R. Roth, J. Phys.: Condens. Matter **17**, S3463 (2005).

[95] P.-M. König, P. Bryk, K. Mecke, and R. Roth, Europhys. Lett. **69**, 832 (2005).

[96] P. Bryk, R. Roth, M. Schoen, and S. Dietrich, Europhys. Lett. **63**, 233 (2003).

[97] P.-M. König, doctoral thesis, ITAP, University of Stuttgart, Stuttgart (2005).

[98] J.A. Cuesta, Y. Martínez-Ratón, and P. Tarazona, J. Phys.: Condens. Matter **14**, 11965 (2002).

[99] W.B. Russel, D.A. Saville, and W.R. Schowalter, *Colloidal Dispersions* (Cambridge University Press, Cambridge, 1989).

[100] D.F. Evans and H. Wennerström, *The Colloidal Domain: Where Physics, Chemistry, Biology, and Technology Meet*, 2nd ed. (Wiley-VCH, New York, 1999).

[101] C. Graf, D.L.J. Vossen, A. Imhof, and A. van Blaaderen, Langmuir **19**, 6693 (2003).

[102] D. van der Beek, A.V. Petukhov, S.M. Oversteegen, G.J. Vroege, and H.N.W. Lekkerkerker, Eur. Phys. J. E **16**, 253 (2005).

[103] J.-W. Kim, R.J. Larsen, and D.A. Weitz, Adv. Mater. **19**, 2005 (2007).

[104] H. Graf and H. Löwen, Phys. Rev. E **59**, 1932 (1999).

[105] G.H. Koenderink, G.A. Vliegenthart, S.G.J.M. Kluijtmans, A. van Blaaderen, A.P. Philipse, and H.N.W. Lekkerkerker, Langmuir **15**, 4693 (1999).

[106] K. Lin, J.C. Crocker, A.C. Zeri, and A.G. Yodh, Phys. Rev. Lett. **87**, 088301 (2001).

[107] P.G. Bolhuis, A. Stroobants, D. Frenkel, and H.N.W. Lekkerkerker, J. Chem. Phys. **107**, 1551 (1997).

[108] S.C. McGrother, R.P. Sear, and G. Jackson, J. Chem. Phys. **106**, 7315 (1997).

[109] L. Onsager, Ann. NY Acad. Sci. **51**, 627 (1949).

[110] G.J. Vroege and H.N.W. Lekkerkerker, Rep. Prog. Phys. **55**, 1241-1309 (1992).

[111] P. Padilla and E. Velasco, J. Chem. Phys. **106**, 10299 (1997).

[112] J.D. Parsons, Phys. Rev. A **19**, 1225 (1979).

[113] S.-D. Lee, J. Chem. Phys. **87**, 4972 (1987).

[114] G. Cinacchi and F. Schmid, J. Phys.: Condens. Matter **14**, 12223 (2002).

[115] R. Hołyst and Poniewierski, Phys. Rev. A **38**, 1527 (1988).

[116] P. Tarazona, Phil. Trans. R. Soc. Lond. A **344**, 307 (1993).

[117] H. Graf and H. Löwen, J. Phys.: Condens. Matter **11**, 1435 (1999).

[118] Y. Mao, P. Bladon, H.N.W. Lekkerkerker, and M.E. Cates, Mol. Phys. **92**, 151 (1997).

[119] J.A. Cuesta, Phys. Rev. Lett. **76**, 3742 (1996).

[120] M. Schmidt, Phys. Rev. E **63**, 050201(R) (2001).

[121] J.M. Brader, A. Esztermann, and M. Schmidt, Phys. Rev. E **66**, 031401 (2002).

[122] A. Esztermann and M. Schmidt, Phys. Rev. E **70**, 022501 (2004).

[123] A. Esztermann, H. Reich, and M. Schmidt, Phys. Rev. E **73**, 011409 (2006).

[124] S.M. Oversteegen and R. Roth, J. Chem. Phys. **122**, 214502 (2005).

[125] L.J. Ellison, D.J. Michel, F. Barmes, and D.J. Cleaver, Phys. Rev. Lett. **97**, 237801 (2006).

[126] P. Pfleiderer and T. Schilling, Phys. Rev. E **75**, 020402(R) (2007).

[127] J.P. Straley, Mol. Cryst. Liquid Cryst. **24**, 7 (1973).

[128] P. Bolhuis and D. Frenkel, J. Chem. Phys. **106**, 666 (1997).

[129] R. van Roij, M. Dijkstra, and R. Evans, Europhys. Lett. **49**, 350 (2000).

[130] M. Dijkstra, R. van Roij, and R. Evans, Phys. Rev. E **63**, 051703 (2001).

[131] M. Dijkstra and R van Roij, J. Phys.: Condens. Matter **17**, S3507 (2005).

[132] R. Hołst, Mol. Phys. **68**, 391 (1989).

[133] D.L. Cheung, L. Anton, M.P. Allen, and A.J. Masters, Phys. Rev. E **73**, 061204 (2006).

[134] C.M. Dobson, Nature **426**, 884 (2003).

[135] K.R. Mecke, Fluid Phase Equilib. **150/151**, 591 (1998).

[136] R. Roth and K.M. Kroll, J. Phys.: Condens. Matter **18**, 6517 (2006).

[137] J. Israelachvili, Acc. Chem. Res. **20**, 415 (1987).

[138] R. Evans, R. Roth, and P. Bryk, Europhys. Lett. **62**, 815 (2003).

[139] R. Evans, J.R. Henderson, and R. Roth, J. Chem. Phys. **121**, 12074 (2004).

[140] M.C. Stewart and R. Evans, Phys. Rev. E **71**, 011602 (2005).

[141] K. Mecke and C.H. Arns, J. Phys.: Condens. Matter **17**, S503 (2005).

[142] R. Roth, Y. Harano, and M. Kinoshita, Phys. Rev. Lett. **97**, 078101 (2006).

[143] J.R. Henderson, Mol. Phys. **50**, 741 (1983).

[144] S. Przybył and P. Pierański, Eur. Phys. J. E **4**, 445 (2001).

[145] A. Maritan, C. Micheletti, A. Trovato, and J.R. Banavar, Nature **406**, 287 (2000).

[146] K.R. Mecke, T. Buchert, and H. Wagner, Astron. Astrophys. **288**, 697 (1994).

[147] J. Buschle, P. Maass, and W. Dieterich, J. Phys. A: Math. Gen. **33**, L41 (2000).

[148] T. Boublík and I. Nezbeda, Coll. Czech. Chem. Commun. **51**, 2301 (1986).

[149] J.J. Erpenbeck and W.W. Wood, J. Stat. Phys. **35**, 321 (1984).

[150] T. Coussaert and M. Baus, J. Chem. Phys. **109**, 6012 (1998).

[151] E.J. Sorin and V.S. Pande, J. Am. Chem. Soc.**128**, 6316 (2006).

[152] D. Lucent, V. Vishal, and V.S. Pande, Proc. Natl. Acad. Sci. USA **104**, 10430 (2007).

Danksagung

An dieser Stelle möchte ich mich bei allen, die auf ganz unterschiedlichen Wegen zum Gelingen der Arbeit beigetragen haben, bedanken. Insbesondere gilt mein Dank

- *Prof. Dr. S. Dietrich* für den Vorschlag des interessanten Themas, bereichernde Diskussionen und die Ermöglichung einer aktiven Partizipation an der wissenschaftlichen Community.

- *Prof. Dr. U. Seifert* für die Übernahme des Zweitberichtes zu dieser Arbeit.

- *Dr. R. Roth* für seine Einführung in die Dichtefunktionaltheorie sowie für die Vermittlung zur Bearbeitung des Themas wichtiger Konzepte. Von den Diskussionen mit ihm und der guten Zusammenarbeit habe ich in hohem Maße profitiert.

- *Prof. Dr. C. Bechinger* und *Dr. C. Lutz* für die gute Zusammenarbeit im Rahmen der experimentellen Realisierung eindimensionaler Kolloidsysteme.

- *Prof. Dr. K. Mecke* für das Teilen fruchtbarer Ideen aus den Bereichen Differentialgeometrie und Morphometrie.

- meinem Kollegen und Freund *Hartwig* für zahllose engagierte bis hitzige Diskussionen zu Fragen aus Physik, Gesellschaft und Politik. Die Sache Schwaben vs. Preußen konnte dabei allerdings trotz Anstrengungen nicht endgültig entschieden werden.

- meinem Kollegen und Freund *Carlo* für den gemeinsamen Urlaub in Italien und die vielen bildreichen, witzigen Erklärungen und Schilderungen deiner Heimat. Dein tragischer Tod hat mich tief erschüttert.

- *Darek* und *Wille* für die Erweiterung meines kulturellen Horizontes; *Wille* und *Hartwig* dafür, dass sie meine Bekanntschaft mit *Herrn Luis Lehle* möglich gemacht haben.

- *Moni* und *Roland* dafür, dass sie ihre Schwäche für original österreichischen Apfelstrudel gerne mit mir teilen.
- *Dr. Gambassi* für die großzügige Vermittlung eines unbezahlten Arbeitseinsatzes auf einer toskanischen Olivenplantage; einer anderen Italienerin und einer Spanierin.
- *Frau A. Geigle* für ihre Unterstützung bei organisatorischen Fragen, ihre Urlaubsgrüße und die Schulung meines Verständnisses der schwäbischen Sprache.
- allen Mitgliedern der Abteilung Dietrich für die gute Atmosphäre.
- meinen "unphysikalischen" Freunden.
- meinen Eltern und Geschwistern.